Experimental Investigation of Membrane Materials used in Multilayer Surfacing Systems for Orthotropic Steel Deck Bridges

Tzimiris, George

DOI
10.4233/uuid:503a9595-508b-4901-86ab-c6ce7429fb67

Publication date
2017

Document Version
Final published version

Citation (APA)
Tzimiris, G. (2017). *Experimental Investigation of Membrane Materials used in Multilayer Surfacing Systems for Orthotropic Steel Deck Bridges*. [Dissertation (TU Delft), Delft University of Technology]. https://doi.org/10.4233/uuid:503a9595-508b-4901-86ab-c6ce7429fb67

Experimental Investigation of Membrane Materials used in Multilayer Surfacing Systems for Orthotropic Steel Deck Bridges

By

Georgios Tzimiris

Experimental Investigation of Membrane Materials used in Multilayer Surfacing Systems for Orthotropic Steel Deck Bridges

Proefschrift

ter verkrijging van de graad van doctor
aan de Technische Universiteit Delft,
op gezag van de Rector Magnificus Prof. ir. K.Ch.A.M. Luyben,
voorzitter van het College voor Promoties,
in het openbaar te verdedigen op maandag 27 februari 2017 om 10.00 uur

door

Georgios TZIMIRIS

Master of Science with distinction in Road Engineering and Management, University of Birmingham, UK
Geboren te Thessaloniki, Greece

Dit proefschrift is goedgekeurd door de promotor:
Prof. dr. A. Scarpas

Copromotor:
Dr. X. Liu

Samenstelling promotie- commissie:

Rector Magnificus	Voorzitter
Prof. dr. A. Scarpas	Technische Universiteit Delft
Dr. X. Liu	Technische Universiteit Delft

Onafhankelijke leden:

Prof. dr. M. Veljkovic	Technische Universiteit Delft
Assistant Prof. dr. E. Manthos	Aristotle University of Thessaloniki, Greece
Prof. dr. ir. S.M.J.G. Erkens	Technische Universiteit Delft
Dr. ir. R. Hofman	Dienst Water Verkeer en Leefomgeving, Rijkswaterstaat

Published and distributed by:
G.Tzimiris
Email: g.tzimiris@gmail.com

ISBN 978-94-92516-45-9

Printed in the Netherlands

Acknowledgements

During the five years' study in TU-Delft, many people gave me their guidance, encouragement and support when I faced difficulties, without their effort, this research would never have been completed. Therefore, this moment is a good opportunity for me to express my sincere gratitude to all of them.

This research project was funded by Rijkswaterstaat, an agency of the Dutch Ministry for Infrastructure and the Environment.

I am especially grateful to my promoter Prof. Tom Scarpas who not only had helped me to get the opportunity to carry out this research here, but also encouraged, supported and advised me during this study. My sincere gratitude to Dr. Xueyan Liu, my daily supervisor, who has given me ample support, guidance and encouragement in all the key moments during my PhD. His tireless effort and constructive comments on this dissertation are highly appreciated.

I wish to express my sincere thanks to my colleague Dr Jinlong Li for his great help with numerical implementations and simulations.

I'm particularly grateful to Dr. Zao Su who helped us for the preparation and testing of all associated membrane products in order to have a first idea of their mechanical properties.

The sample preparation for the five point bending tests took place at BAS research and technology company in the Netherlands, so the author wish to express his honest thanks for their support.

I would like to thank all the colleagues of the Road Engineering Section. The extensive laboratory work could not have been successfully finished without the arrangement and support provided by Jan-Willem Bientjes, Marco Poot, John Hermsen and Arjan van Rhijn.

Summary

In the Netherlands asphaltic surfacings on orthotropic steel deck bridges (OSDB) mostly consist of two structural layers. The upper layer consists of what is known as very open porous asphalt (ZOAB) for noise reduction. For the lower layer Guss Asphalt (GA) is used. Earlier investigations have shown that the bonding characteristics of membrane layers to the surrounding materials have a very strong influence on the overall response of the steel bridge decks.

Rijkswaterstaat, an agency of the Dutch Ministry of Infrastructure and the Environment, has commissioned Delft University of Technology to investigate and rank the performance of various commercially available membranes.

In order to obtain insight into the response of membranes and their interaction with the surrounding materials on orthotropic steel decks, a project of evaluation of the performance of modern surfacing systems on OSDBs has been undertaken. Currently, there are various kinds of membranes provided by various companies. Thereby it was necessary to examine the bonding strength of these membrane products and to develop a ranking methodology.

The research project focused on membrane performance and the effects hereof on the bridge deck as a whole. The methodology used was a multi-phase approach, which consisted of three main phases.

In Phase 1, a Membrane Adhesion Test (MAT) device was developed at Delft University of Technology for the characterization of the adhesive bonding strength of membranes with the surrounding materials on OSDBs on the basis of a fundamentally sound, mechanistic methodology. Several membrane products were tested monotonically in this phase.

In Phase 2, the MAT device was utilised for investigation of the fatigue response of the various membrane products on various substrates and under two different temperature conditions and three different cyclic load levels. A ranking methodology consisting of a combination of experimental (via MAT) and computational investigations was also developed and utilized for the ranking of the various membrane products.

In Phase 3 of the project, four typical Dutch multilayer surfacing systems, constructed with five selected membrane products from Phase 1 and 2, were studied by means of five-point bending (5PB) beam tests and FE simulations. The findings of the 5PB beam tests were used for calibration and validation of the finite element predictions and for further ranking of the performance of the various membranes in Dutch OSDBs.

On the basis of the project results, the top two ranking membranes were selected for subsequent testing by means of the LINTRACK facility available at Delft University of Technology.

Samenvatting

In Nederland bestaan asfaltwegdekken op orthotrope stalendekbruggen (OSDB) voornamelijk uit twee lagen. De bovenste laag bestaat uit zogeheten zeer open asfaltbeton (ZOAB) voor geluidsreductie. Voor de onderste laag wordt Guss Asfalt (GA) gebruikt. Eerdere onderzoeken hebben aangetoond dat de bindingseigenschappen van de membraanlagen van de omringende materialen een zeer sterke invloed hebben op de totale respons van de stalen brugdekken.

Rijkswaterstaat, een agentschap van het Nederlandse Ministerie van Infrastructuur en Milieu, heeft de Technische Universiteit Delft opdracht gegeven om de prestaties van de verschillende in de handel verkrijgbare membranen te onderzoeken en te rangschikken.

Om inzicht te krijgen in de respons van membranen en hun interactie met de omringende materialen op orthotrope stalen brugdekken, is een project uitgevoerd voor de evaluatie van de prestaties van moderne deklaagsystemen op OSDBs. Momenteel zijn er verschillende membranen beschikbaar bij verschillende bedrijven. Daarvoor was het noodzakelijk de bindingssterkte van deze membraanproducten te onderzoeken en een rankingmethode te ontwikkelen.

Het onderzoek richtte zich op membraanprestaties en de effecten daarvan op het brugdek als geheel. De gebruikte methode was een meerfasenaanpak, die bestond uit drie hoofdfasen.

In Fase 1 werd een Membraan Adhesion Test (MAT) apparaat ontwikkeld aan de Techische Universiteit Delft voor de karakterisering van de adhesieve bindingssterkte van membranen met de omringende materialen op OSDBs op basis van een grondige fundamentele mechanistische methode. Meerdere membraanproducten werden in deze fase monotoon getest.

In Fase 2, werd het MAT-apparaat gebruikt voor onderzoek naar de vermoeiingsrespons van de verschillende membraanproducten op verschillende substraten onder twee verschillende temperatuuromstandigheden en drie verschillende cyclische belastingsniveaus. Een rankingmethodologie bestaande uit een combinatie van experimenteel (via MAT) en computeronderzoek werd ook ontwikkeld en gebruikt voor de rangschikking van de verschillende membraanproducten.

In Fase 3 van het project, werden vier typisch Nederlandse meerlaagse deklaagsystemen, gebouwd met de vijf geselecteerde membraan producten uit Fase 1 en 2, bestudeerd door middel van vijfpuntsbuigproeven (5PB) en FE simulaties. De bevindingen van de 5PB tests werden gebruikt voor de kalibratie en validatie van de eindige elementen voorspellingen en voor de verdere ranking van de prestaties van de verschillende membranen in Nederlandse OSDBs.

Table of Contents

1 Introduction

Orthotropic steel decks are widely applied in long span bridges, movable bridges and shorter span road and rail bridges due to their favourable properties. These properties are low deadweight, lots of plastic reserve in case of overload and aesthetic advantages. Nowadays, more than 1000 orthotropic steel deck bridges have been built in Europe, out of which 86 are in The Netherlands.

In the last three decades, several problems were reported in relation to asphalt surfacing materials on orthotropic steel deck bridges such as rutting, cracking, loss of bond between the surfacing system and steel deck. The severity of the problems is enhanced by the considerable increase in traffic in terms of number of trucks, heavier wheel loads, wide-base tires etc.

The Ministry of Transport, Public Works and Water Management (RWS) in The Netherlands is facing a growing challenge in maintaining network capacity. The combined length of orthotropic steel deck bridges in the primary road network is limited; however, the consequences of repairs of the steel deck plate or the overlaying surfacing structure to network capacity are dramatic. The service life of asphaltic surfacing structures on orthotropic steel deck bridges is limited to an average of 5 years.

For the surfacing system, asphalt concrete surfacing structures have distinct advantages when compared to alternative surfacing structures: fast installation, good driving comfort, low noise levels, relatively cheap construction costs, and homogeneity in road surface. Therefore, improvement of the performance of asphaltic surfacing structures on orthotropic steel deck bridges is of the utmost importance.

In The Netherlands an asphaltic surfacing structure mostly consists of two structural layers. The upper layer consists of Porous Asphalt (PA) for noise reduction. For the lower layer is used Guss Asphalt (GA). Earlier investigations have shown that the bonding strength of membrane layers to the surrounding materials has a strong influence on the structural response of orthotropic steel bridge decks. The most important requirement for the application of membrane materials is that the membrane adhesive layer shall be able to provide sufficient bond to the surrounding materials.

The Transport Research Centre (DVS) of the Ministry of Transport, Public Works and Water Management (RWS) commissioned Delft University of Technology to investigate the performance of various commercially available membranes.

In order to obtain insight into the response of membranes and their interaction with the surrounding materials on orthotropic steel decks, a project of evaluation of the performance of modern surfacing systems on orthotropic steel deck bridges has been undertaken. Currently, there are various kinds of membranes provided by various companies. Thereby it is necessary to examine the bonding strength of these membrane products, and develop a ranking methodology.

As mentioned before, the following research questions are formulated:

1. *What are the physical quantities that can be used to quantify the membrane bonding strength?*

Apparently, these should be representative and independent of membrane geometry and applied loads. From fracture mechanics, strain energy release rate can be chosen as such parameter to characterize bond conditions at the membrane substrate interface. Strain energy release rate can be measured by using different specimen geometries.

2. *Which device should be utilized to obtain the strain energy release rate?*

A number of techniques have been developed in the past to quantify the adhesive strength between a membrane and the associated substrate. Combining advantages and drawbacks from these traditional tests, a new setup called Membrane Adhesion Test (MAT) was developed to measure the strain energy release rate.

In this MAT setup, a piston with a cylindrical head replaces the shaft in order to reduce the stress concentration. The membrane debonds with the rise of the piston once it reaches its critical energy release rate. The advantage of the MAT is that properties like adhesive fracture energy and the basic mechanical characteristics of the membrane can be determined from a single test.

3. *How to get strain energy release rate from MAT tests?*

The strain energy release rate of the membrane in a MAT test can be calculated on the basis of the displacement of piston and the applied force.

4. *How to rank the membrane products from MAT tests?*

From the MAT tests, the strain energy release rate can be obtained for each membrane with different substrates. Larger strain energy release rate represents better bonding strength. In addition, one thing should be paid attention to is that one membrane layer has two interfaces with the different surrounding materials; thereby the recommended best-performing membrane should demonstrate optimum response for both interfaces. This ranking also shows the importance of computing the right quantity of the strain energy release rate.

Most membranes are made by bitumen-based materials, thus they are viscous and sensitive to the surrounding materials. In this project, a visco-elastic Zener model is utilized to model membrane materials. Relaxation tests have been done in order to determine the necessary material parameters for the membrane constitutive model.

1.1 Merwedebrug - bridge of concern

The Merwedebrug (Figure 1.1), part of Highway A27 near Gorinchem, the Netherlands, was opened on March 15 1961. It has been playing a very important role in connecting the Randstad and North Brabant, and it is representative due to heavy load traffic every day. Our initial proposed research program came from the need of a surfacing structure for that bridge with prolonged service life.

Figure 1.1 The Merwede bridge, Gorinchem

The design of the surfacing system has been changed during the years. In the past, the upper layer consisted of either GA or Dense Asphalt Concrete (DAC) and a membrane product was applied between the steel and the GA layer.

Later on, a new type of surfacing structure was applied: membrane, GA, membrane, polymer modified Porous Asphalt, PA. Within half year this structure developed ravelling. According to experts, the additional cause of the poor performance was the 10 mm deck plate which is too thin for the current traffic.

In 2000, damage became so severe that the upper membrane and the PA were removed and replaced by PA 0/8.

In 2005, the PA surface layer was replaced with DAC. The applied structure consisted of a lower membrane, GA, an upper membrane and a surface layer of DAC. In 2009, it was decided that the structure required reconstruction.

Prior to the reconstruction works it was estimated that about 10% of GA needed to be replaced. Cracking and alligator cracking already indicated poor performance caused by poor membrane adhesion in the existing structure. A schematic figure of the new design of the bridge is shown in Figure 1.2.

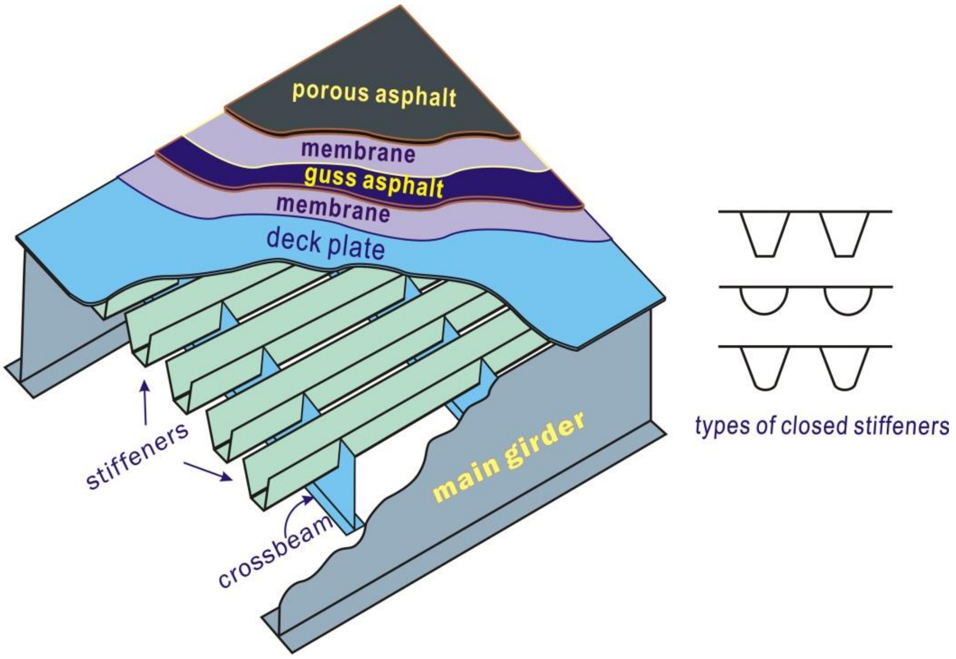

Figure 1.2 schematic of Merwedebrug, Gorinchem

1.2 Types of distress in orthotropic steel bridges surfacing

The considerable increase in traffic volume and magnitude of the traffic loads have resulted in many reported problems in orthotropic steel bridge decks. This happened because those changes were not expected during the design of the bridges, even more the assumption of linear elastic material behaviour was too optimistic for the response of the bridge structure. Problems taking place in the surfacing are described below.

1.2.1 Permanent deformation

Both Porous and Guss asphalt are sensitive to rutting due to the nature of the mixture, and the high amount of bitumen and the stability is provided by the mortar Figure 1.3. High loads induce high repeated compressive stresses and finally permanent deformation. The use of modified bitumen will make the mix more stable and but unfortunately the more stable mix increases the changes of cracking. Furthermore tangential forces (caused by braking) give high shear stresses, which lead to permanent deformation in the form of corrugation. Finally, the pavement on bridges tends to move, because of the traffic moving from the stiffer parts of the pavement (above the steel stiffeners) to the more flexible parts (between the stiffeners). Medani, (2006)

Figure 1.3 Rutting on pavement

1.2.2 Fatigue Cracking

Fatigue cracking of pavements materials is very common damage type in surfacing on orthotropic steel bridge decks. Mainly it is caused by repeated stresses (shear or tensile) induced by traffic, environment and poor construction. Above the stiffeners, they start on top of the surface, finally growing through the asphalt and reaching the steel, Figure 1.4. When the bond between steel and asphalt is too weak, they may also start between the stiffeners at the bottom of the surfacing. When the cracks reach the steel deck, it rusts and may lead to debonding. Medani, (2006)

Figure 1.4 Fatigue cracking

1.2.3 Loss of bond between steel plate and surfacing

It is very important that there is bond between the steel plate and surfacing. Experience has shown that loss of the bond indicates failure of the pavement a short time thereafter [*Medani, 2006*]. The loss of bond has various causes:

- The difference in transverse stresses on top of the steel plate and the bottom of the asphaltsurfacing causes shear stresses.
- Acceleration or braking vehicles cause shear stresses.
- When a bridge deck has some slope, the shear stresses increase.
- The expansion coefficient of asphalt differs from steel.
- Vibrations in the deck, caused by the passing traffic will weaken the bond.
- The high temperature during application of the surfacing causes high strains on top of the steelplate, leading to residual stresses after cooling down.

1.2.4 Other damages

1.2.4.1 Blistering and Potholes

That is a local expansion/swell of a waterproof layer and occurs when a waterproof layer is laid on a layer that contains water. When asphalt is laid on such a layer, water evaporates forming bubbles and will be seen at the surface as isolated lumps resulting the appearance of potholes, damages Figure 1.5.

Figure 1.5 Localised surfing damages

1.2.4.2 Disintegration.

This includes ravelling (loss of stone particles from surface due to the nature of the mix) and potholes, Figure 1.6. It is caused by cracking, loss of bonding and/or a combination of other distress mechanism. Ravelling can seriously reduce the skid resistance of the pavement and hence endangers the safety of road users. Sometimes distress is characterized by means of the mechanisms causing the distress. These are facilitated by the action of mechanisms reducing the pavement strength, i.e. decrease of the bond strength between the plate and the surface layer, ageing of bitumen, weathering of aggregate materials (chemical decomposition caused by oxygen, water, heat and/or solar radiation) and strength reduction of bituminous materials because of low viscosity at high temperatures.

Figure 1.6 Distress modes

Once the bond between the steel deck and surfacing is destroyed, the failure of the pavement is merely a matter of time. There are several reasons behind the destruction/weakening of the bonding layer among which are:

• The high shear stresses between the pavement and the deck produced by accelerating or braking wheel loads which weaken and hence destroy the bond.

• The rather high application temperature of the mix. This can increase the temperature of the steel plate and may result in high strains at its topside.

• Vibrations set up in the deck by fast moving traffic also weaken the bond.

• The shear forces (both in the longitudinal and transverse directions) increase with the increase of the slope of the bridge deck. These shear forces may result in cracks at the elevated points of the structure. Preventive maintenance is defined as a planned strategy of cost-effective treatments applied at the proper time to preserve and extend the useful life of a bridge. There are several rehabilitation methods for steel bridge pavements: replacement of the asphalt surface layer and/ or removing the whole pavement and reconstructing again

1.3 Thesis description

The overall objective of this research is the development of a methodology that can be utilized for the ranking of waterproofing membrane systems for orthotropic steel bridge with asphalt concrete deck. Asphalt surfed deck consisting of a bottom layer of “Guss” asphalt and top layer of porous asphalt (ZOAB) are considered.

Six membrane manufacturers have participated in this experimental program. There are total eight types of membrane products that are the most commonly used for waterproofing in orthotropic steel bridge constructions have been tested at TU-Delft with the MAT device on different substrates. The effects of temperature on bonding characteristics of membrane are investigated.

In this phase of this project, the monotonic tests on all membranes that are included in this research project have been completed and the results of these tests are presented and analyzed in this Thesis. Once the potential of all membrane products are clear by the monotonic tests, in the second phase of our tests, the fatigue testing of the selected membranes from the monotonic tests will be carried out.

In Chapter 2 a literature review is introduced. In this chapter, the commonly used methods for testing membrane debonding strength are briefly introduced.

In Chapter 3, details of the Membrane Adhesion Test (MAT) have been described to characterize the adhesive characteristics of the various membranes with the surrounding materials. Analytical constitutive relations of MAT test have been derived.

In Chapter 4, experimental results for each membrane interface tested at different temperature conditions are presented. The values of strain energy release rate for each membrane interface are compared, as well as the relationship between the membrane debonding force and the piston elevated height. Meanwhile, the rates of membrane debonding propagation are also included. From these results, the temperature influence on the strain energy release rate of membrane interface is discussed. In the last part of this Chapter, in order to rank various membrane products, comparisons of strain energy release rate for different membranes under the same test condition are shown.

In Chapter 5, experimental results of the selected membrane products on various substrates tested at two different temperature conditions and three different cyclic loading levels are presented. The values of dissipated work for each membrane interface are compared, as well as the relationship between the membrane debonding length. The first part of this Chapter presents the results from the tests conducted at 10^0C under three different load levels (P_{max}= 150N, 250N and 350N). The second part includes the tests conducted at 30^0C at one load level (P_{max}=100N). In the last part of this chapter a methodology has been developed in order to predict the service life of the membranes.

Finally in Chapter 6 in order to investigate the integral response of the typical Dutch asphalt surfacing layers with the selected membrane products from MAT tests, the TUD five-point bending (5PB) beam tests were performed at TU Delft. Four membrane products ranked from MAT tests (Liu & Scarpas, 2012) were utilized as the top and bottom membrane layers in the 5PB beams. Several displacement sensors have been used in order to detect the initiation of cracks where they are most likely to appear. Strain gauges have been used in order to monitor the significant changes in strain on the porous asphalt (ZOAB) and Guss asphalt layer during the fatigue tests. Shear displacements between the asphalt layers are monitored and presented.

Furthermore, the fatigue damage in 5PB beam test is related to the amount of dissipated work computed by using the measurement of actuator load and loading plate deformation during the loading cycle. The dissipated work, which is equivalent to the lost part of the total potential energy of the beam, has been utilized to explain the incremental damage during the testing

Conclusions and recommendations are described in Chapter 7.

Appendix I shows the tables of comparison among the membrane products.

In appendix II, the strain energy release rate of each specimen type is shown together with the adjusted maximum relative opening displacement.

In appendix III, the comparisons of the test results among different interfaces with different membrane products are summarized

1.3.1 Schematic diagram of research description

PHASE 1	MAT Monotonic tests

4.

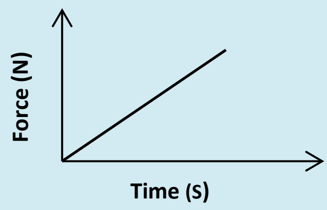

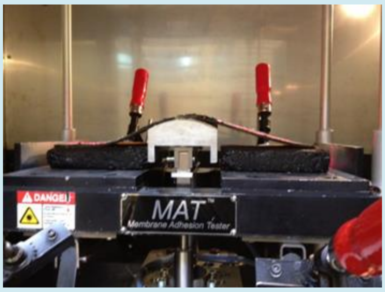

PHASE 2	MAT Cyclic tests

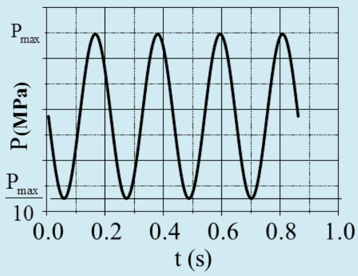

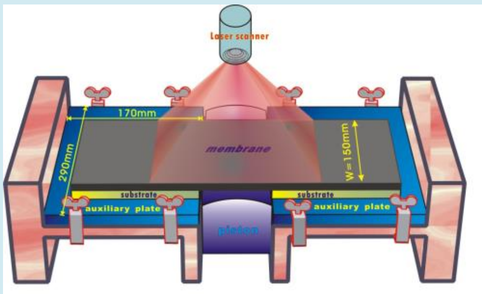

PHASE3	The 5point bending test

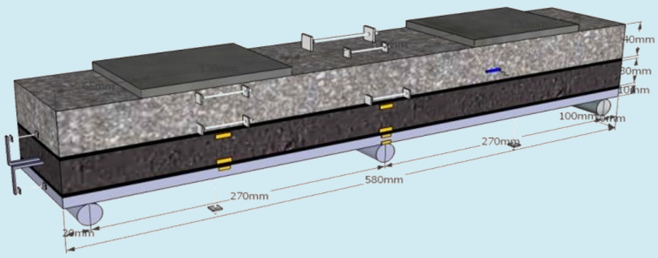

2 Multilayer surfacing systems

Orthotropic steel deck bridges (OSDB) were first introduced 1950 over the Neckar River in Mannheim, Germany, and since then they become a popular economical alternative mainly due to lower mass, ductility, thinner sections, rapid bridge installation, and cold-weather construction (Gurney,1992).

Nowadays more than 1000 orthotropic steel bridges have been built in Europe, out of which 86 are in the Netherlands. In the Netherlands, an asphaltic surfacing structure for orthotropic steel bridge decks mostly consists of two structural layers. The upper layer consists of porous asphalt (PA) because of reasons related to noise reduction. For the lower layer a choice between mastic asphalt (MA), or guss asphalt (GA), can be made.

Mostly, various membrane layers are involved, functioning as bonding layer, isolation layer as well as adhesion layer. The asphalt surfacing structures for OSDBs is a complicated and yet not properly solved technical problem. The high flexibility and large local deformations, wind and earthquake forces, temperatures and other natural factors make the problem even more complicated. Due to high flexibility of OSDBs, fatigue cracking, rutting, delaminating and other damage types are commonly reported and these severely destroy the performance of steel bridges. fatigue damage can also occur at the interface regions between the membrane layers and the surfacing layers but, also, within the membrane materials. It is necessary to study into the damage mechanism, distributions, evolution etc. in the surfacing systems on OSDBs. Laboratory or in-site field tests of damages on bridge pavements are quite costly in time as well as the budget. A material subjected to cyclic loading will accumulate damage and it will fail when the accumulated damage exceeds a threshold. (Miner 1945) was one of the first to relate failure of a material to damage. Since then, a multitude of methods have been developed for quantification of damage. (Kim and Little 1990) and (Lee and Kim 1998).

2.1 Research on surfacing materials

The majority of OSDBs around the world, are paved with asphalt mixtures. Asphalt surfacings are light and have good performance. Creep properties, the influence of temperature and fatigue properties (including reflection cracks) are some important issues associated with the durability of asphalt bridge surfacing systems. Earlier study on the performance of asphalt mixtures was focused on general characteristics of bitumen and asphalt mixtures.

Heukelom, (1966) was one of the first who studied methods for testing the modulus of asphalt mixtures. He used the nomoograph method to obtain the modulus of asphalt, then took this modulus into a formula to converge into the modulus of the asphalt mixture. This method is based on the concept that only by knowing the properties of asphalt can be known the properties of the asphalt mixture.

Hadly (1971) applied the direct tensile test to asphalt mixtures. Deacoene (1989) measured the dynamic modulus of asphalt mixtures by fatigue bending tests. He applied sinusoidal cyclic loads onto small sample beams made from asphalt mixtures. Formulae were given to calculate the dynamic modulus at certain temperatures.

Based on the stress and strain characteristics of steel bridges under traffic loads and temperature changes, Huang and Ren (1994) suggested one kind of EVA modified asphalt binder with improved deformation ability under low temperatures and better stability at high temperatures. Based on material properties such as Marshall stability, flexural strength at low temperatures, creep properties at higher temperatures, fatigue strength under repeated loads etc., they comprehensively discussed and evaluated the performance of this modified asphalt mixture. This mixture was applied to bridges and main trunk roads later, which turned out to be quite good.

Monisimth (1994 & 1995) did fatigue tests on three kinds of asphalt mixtures and sixty-two sample beams, analysed the relationship between energy dissipation and the number of cyclic loading and established an equation that can relate the fatigue life to the total energy consumed. This equation even describes the elastic and viscous properties of the mixture, and the energy dissipation process.

Park, Kim and Schapery (1996) established the viscoelastic continuum model of an asphalt mixture by considering the influence of the damage rate. This model was able to determine the mechanical properties of an asphalt mixture under uniaxial loading and describes its correlation with time.

Xiong and Li (1997) did an experimental study on mixture properties such as dynamic stability, compressive strength, flexural strength and elastic modulus, especially the relations with variation of temperatures.

Wang and Tan (1998) managed to obtain the relationship between dynamic stability of surfacing and axle load. They presented a design method for a heavy loaded asphalt pavement. Zhang, Zhu and Tan (1998) proposed a statistical prediction equation of fatigue properties for asphalt mixes based on cumulative flow energy consumption obtained by creep tests. Jiang (1998) suggested an optimum proportion for SMA mixture based on the available types of aggregates and bitumen in China. Marshall test, rutting test, split test and the triaxial test were adopted to get the technical indicators of this SMA mixture. A comparison was done between the suggested SMA and other dense-graded SMA.

Tan and Zhao (1999) argued that the asphalt material is a typical viscoelastic material, its deformation were decided by Hooke elastic properties and Newton viscous properties. Based on the viscoelastic properties of an asphalt material, they decomposed its deformation under repeated loading and obtained the proportion between viscous and elastic.

Zhang and Li (1999) reviewed the origin and application of SMA, as well as its difference from traditional dense-graded mixtures. They also reviewed the design and test methods in the US and Europe at that time. Zeng and Chen (1999) concluded different requirements of bridge surfacing layers, argued that three key issues should be analysed during the design of a bridge surfacing structure and asphalt mixtures: the bridge structure, traffic loads and environmental conditions based on climate data. Additionally, they also introduced a design method of SMA mixture to satisfy the aforementioned requirements.

Wang (2000) discussed the selection of asphalt mixtures and the usage of bitumen by testing and empirical formula, as well as the correlation between experimental properties and paving performance.

Li, Sun and Ding (2001) studied a series of requirements for bridge surfacings, including high temperature stability, fatigue performance, resistance to shear deformations and drainage properties. They suggested some new materials and technologies to meet equirements such as crack resistance, stability, toughness, elasticity, aging resistance and drainage.

Zhang, Han and Wang (2001) analysed the working conditions of bridge surfacings, discussed the design of water proofing and adhesion materials, compared their performances and talked about the selection of modified asphalt materials and bonding materials etc.

Epoxy Asphalt Concrete is a polymer concrete with a 45-year history as an extremely durable bridge deck surfacing. It was originally developed by Shell Oil Company in the late 1950's as a jet fuel and jet blast resistant specialty pavement for airfield applications.

2.2 Deck surfacing materials

On top of the steel deck, normally an asphalt surfacing is applied. This surfacing has to meet the functional demands of various parties involved. Furthermore, it is desired that the material on top meets some structural properties as well. Those required properties are briefly discussed first of all, after which the usual built up of such a surfacing is described.

Functional properties

The asphalt surfacing serves four main purposes with regard to the functional requirements:

- Sufficient skid resistance. Therefore, the mix should have both a good macro texture

(sizes of the aggregate) and micro texture (roughness of the aggregate).

- Adequate water drainage is a very important demand, since a wet road gives less skid resistance. Usually, this is obtained by giving the transverse profile a cross slope of about 2 % so that the water can run off to the gutter. Also, giving the surfacing an open structure allows the water to infiltrate quickly, but for bridge decks this is undesirable since they should be protected to water
- Sufficient resistance against polishing.
- For driving comfort, the road surface should not have too much unevenness in both the

longitudinal and transverse direction.

Prevention of too much traffic noise is also a very important demand, especially when the road runs through densely populated areas. Two major aspects of the road surface are taken into account here. First, the texture of the surface determines how much the vehicle tyres vibrate. A greater aggregate size means greater vibrations and thus more noise production. Furthermore, the ability to absorb the produced noise plays a great role. A high porosity of the surface gives a better noise reduction.

Structural properties

The distinction between structural and functional properties is not always that clear. For example, nobody likes permanent deformation (as a functional property), but the resistance against this deformation should be reached by the structural properties of the surface layer. There are many structural requirements, but the most important ones are mentioned below:

- Especially for the case of a surface layer on a bridge, the surfacing should protect the steel deck from corrosion and therefore, a waterproofing layer is required. This becomes especially important when an open surface is desired for noise reduction and water drainage.
- There should be sufficient bonding between the asphalt surfacing and the steel deck.

- Resistance against permanent deformation is very important. Although the bridge deck will not deform like base layers and sub-grade, the asphalt surfacing should be stiff and stable enough to prevent rutting as much as possible.
- With regard to durability, ravelling of the surface layer should be prevented as much as possible.
- Furthermore, the resistance against fatigue cracking of the surface layer should be as high as possible. With this respect, it should be noted that bridge decks suffer very high strains compared to conventional road pavements.

In all those cases, the influence of the temperature should be taken into account. A material which is stiff enough at room temperature will lose a part of its stiffness at higher temperatures.

2.3 Research on asphalt mixtures

2.3.1 Porous asphalt

Porous asphalt (PA) is a bituminous mixture with high content of interconnecting voids that allow the passage of water and air in order to provide the compacted mixture with drain and noise-reducing features (Nikolaides,2015). It is mainly used for surface courses.

Porous asphalt was developed during 1960s in UK, initially for airfield surfaces courses in order to eliminate rainwater. Successful full scale trails on road application led PA to be used in highway pavements as well (Brown 1973, Daines 1992, Nicholls 1997). PA can successfully be laid over concrete surfaces (Nicholls 2001).

PA became more widespread in other countries as well, Holland, Switchrland, Italy and Spain started using it as a surface course. The PA production percentage amounted to 13% of the annual production for hot and warm mixture in 2010 in The Netherlands.

Since 2006 PA is not recommended as surface course in UK, mainly because of the premature failures and its high cost.

The surface of porous asphalt pavements has very good macro-texture and good anti-skidding coefficient, even when the surface is wet. In 1960s 10% of the accidents in United Kingdom were caused by wet surfaces (Maycock 1966)

One of the main advantages of PA is the noise reduction issue. The reduction measured was 3-4 dB(A) when the surface is dry and 7-8dB(A) is wet. (Nelson and Ross 1981). Similar results were found by (Phillips 1995) and the Belgium Road Research centre (Decoene 1989)

Weaknesses of PA are:

- Faster oxidation of bitumen
- Small mix tolerance to variation in bitumen content
- Less service life compared to other asphalt mixtures
- Loss of functionality caused by clogging
- Reduction of bearing capacity compared with other open-graded mixtures
- Higher requirements of salts during winter in order to avoid the formulation of ice.

Nowadays thin porous asphalt is also used by many countries in order to minimize these drawbacks. Morgan (2007) concluded that although the cost of the thin PA is higher when costs are expressed in terms of noise reduction achieved per unit spent, a thin PA layer may be more cost effective than single mitigation measures such as noise barrier.

2.3.2 Guss Asphalt mixture

Guss asphalt (GA) is a type of a Mastic asphalt with added coarse aggregate particles, perhaps one of the oldest mixture, developed in France and UK more than 100 years old. According to (Nikolaides,2015) the primary features of this mixture are:

- Its high filler content
- Its higher binder content
- It’s almost zero permeability
- Its use of harder bitumen
- Its high cost due to high binder content

2.3.3 Dense asphalt mixture

Asphalt concrete is a dense-graded HMA with a larger nominal maximum aggregate size intended for use as a base course or binder course. In addition to site paving benefits, AC can be advantageous because it can provide:

- A waterproof barrier to prevent fines infiltration into the subgrade and pavement structure. If water accumulates in the subgrade, the repetition of pavement loading can cause subgrade fines to migrate into the base and pavement structure. This can clog the base layer, which impedes drainage and create voids in the subgrade into which the pavement may settle.

- An alternative to untreated base material. Structurally, AC is about three times as strong as an untreated aggregate base. Therefore, it is possible to use thinner layers for the same structural support, which can save on excavation costs. In some cases a layer of aggregate base is still needed to provide material to fine grade and to provide a smooth surface on which to pave.

- A base course that can be opened to traffic immediately after placement. AC can support traffic as soon as it is compacted. Although an aggregate base may be able to support limited traffic after placement, the traffic must travel very slowly, automobile and windshield damage can result from loose aggregate kicked up by tires, and the aggregate base must typically be re-graded and compacted before the final wearing course can be paved.

2.4 Research on adhesion performance of interlayers

Goodman (1968) proposed a zero-thickness contact element which was able to simulate the cleftiness inside rocks. Desai (1984) proposed a thin contact element with a certain thickness. The mechanism of two-node contact element is simple, and it is easy to simulate in finite element analysis, but it can only roughly model the deformation at the contact interface. The zero-thickness Goodman element has a clear concept and can better reflect the development of contact shear stress and deformation at the interlayer, and nonlinear characteristics of contact interlayers could be simulated too. By direct shear tests, its parameter could be easily determined, and the shear contact behaviour could be considered to some extent. Its disadvantage is the large normal stiffness value in order to prevent excessive overshooting, which will often result in large normal stress errors. Also, the contact interface may fluctuate.

Contact was first brought out to study the interaction of soil and its surrounding materials (Clough & Duncan, 1973; Zong-Ze, Hong & Guo-hua, 1995). The embryonic form of a contact element is a two-node element. Two nodes are set at two sides of the same location at a contact interface (Zhang & Ge, 2005). The element is composed of normal and tangential springs with stiffness coefficients. When the interface cracked, the stiffness coefficients are set to be infinitely small to simulate the non-connection reaction between two sides; large stiffness coefficient values model the fully adhesive condition.

Surfacing systems with different surfacing materials or adhesive layers may have different forms of shear failure (Zaman, Desai & Drumm, 1984). Much work done to asphalt surfacing structures was based on the assumption that the surfacing overlay was fully bonded to the steel deck plate, without considering non-perfect bonding of interlayers. There were also several researchers that adopted the Goodman zero-thickness contact element to simulate the interlayer between the asphalt layer and the steel deck plate, neither perfectly smooth nor completely bonded (Huang, Wang & Chen, 1999; Xiao & Zha, 2000). Nishizawa et al. (2001) created a SLPE model to simulate steel bridge surfacing system, using prism element to model the asphalt surfacing layer, shell element to model a steel deck plate, and describing interlayers by Goodman contact elements.

Shen and Cao (1996) also found shear deformation occurring between surfacing layer and steel deck plate via experimental tests of a bridge surfacing system with 12 mm steel deck plate, polymer modified asphalt binder and 60 mm polymer modified asphalt concrete. Hameau (2001) tested the strain distributions of a multilayer surfacing system with a 10mm steel deck plate, 3mm rubber asphalt waterproofing and adhesive layer, and a 60 mm mastic asphalt pavement layer. Large shear slippage was found between the asphalt surfacing layer and the steel deck plate. The strain distribution inside the mastic asphalt layer was nonlinear. Huang and Li (2001) studied strain distributions of steel bridge surfacing structure with a 14 mm steel deck plate, epoxy asphalt adhesive layer and a 50 mm epoxy asphalt concrete layer. They argued that the strain distribution through the thickness of the surfacing layer was linear.

2.5 Membranes for orthotropic steel deck bridges

In the Dutch primary and secondary road network, many of the bridges with larger spans are OSDBs. In many cases two layered surfacing structures are placed. In these cases, a layer of Porous Asphalt (PA) is placed over a layer of Guss Asphalt (GA) placed on the steel deck bridge. Membranes are placed between the various layers for two main reasons:

1) to provide a watertight seal and

2) to provide some kind of durable bond between layers.

The second reason for membrane application is vaguely formulated. The reason for this is that there is no consensus on the mechanical function of membranes. In general, two views exist: 1) membranes are bonded to sliding layers that act to disconnect the various structural layers; 2) membranes are shear bonding layers that act to promote the composite action of the structure as a whole.

2.5.1 Types and functions of available membranes

2.5.1.1 Types of membranes

A membrane in bridge surfacing systems is defined as a thin impermeable layer that is used in conjunction with asphalt wearing surface to protect the deck plate from the penetration of moisture and deicing salts. Most Canadian provinces and many European countries require the use of membranes on new bridge decks. About 60% of the U.S. state agencies use them with greater usage on existing bridge decks than new bridges (Russell, 2012).

In literature, several groups of membranes could be identified based on certain distinctions, such as membranes with or without inlays (reinforced), preformed membranes (produced in a factory) or in-place formed membranes (liquid applied membranes).

Preformed membranes involve the application of a primer to the clean bridge deck to improve the adhesion of the membrane to the deck. Some preformed membranes include a self-adhesive backing on the membrane sheet. These sheets can be rolled into place and then bonded to the deck primer using a roller. Others are bonded to the deck by heating the membrane using either a hand torch or a machine. After the membrane is installed, a tack coat is applied to the top surface to increase bond with the asphalt overlay.

In-place formed membranes may be placed using either spray equipment or rollers and squeegees. These membranes are applied either hot or cold depending on the manufacturer requirements and they may or may not contain a reinforcing fabric.

Materials used to produce the membranes by various manufactures are rubberized asphalt, polymer-modified asphalt, modified bitumen, polymeric membrane, or bitumen and polymers (Russell, 2012).

In this dissertation, any layer between the steel deck and the asphalt layer, or between two asphalt layers, is termed a membrane. No distinction is made between preformed membranes prefabricated in a factory and in-place formed membranes. Similarly both membrane types with and without an inlay (reinforcing fabric) are considered membranes.

2.5.1.2 Functions of membranes

The following summarize the function of membranes in asphalt concrete surfacing structures.

1) Corrosion protection. The steel deck plate should be protected against corrosion. This function is achieved by several systems, where in most cases corrosion and waterproofing are more or less combined. Nunn and Morris (1974) reported a zinc-sprayed steel deck with one coat of etch primer. Primer bitumen and bitumen tack coat was used for the same purpose. Smith and Cullimore (1987) presented a cold setting coal tar epoxy system on the steel deck and lightly dressed with sand prior to setting. A three-coat system was applied on the shot blasted the steel top plate to satisfy corrosion and waterproofing requirements (Vincent, 2004). Héritier et al. (2005) discussed a primary bituminous fixing intended to protect metal from corrosion. Corrosion protection of the steel deck is trivial but essential (Huurman & van de Ven, 2008).

2) Watertight seal. Most researchers indicate that adhesive membranes are amongst others applied to provide a watertight seal protecting any underlying layer (steel, primer or asphalt concrete) against water infiltration.

3) Water discharge. Adhesive membranes can also be used as water discharging layers on bridge decks. This is more often observed in relation to concrete decks where a membrane may be used to discharge moisture entrapped during construction.

4) Mechanical functions. The mechanical function of a membrane always plays an important role. Even in situations where the membrane is applied for other reasons, the mechanical interaction with the whole structure is very important. The importance of relating the application of a membrane to the mechanical behaviour of the whole structure was overemphasized by many researchers (Touran & Okereke, 1991, Huurman, Medani, Scarpas & Kasbergen, 2003, Medani, 2006).

5) Resistance against thermal and mechanical attacks during paving. A last aspect that needs to be mentioned is the resistance against damage during construction especially when the temperature is high with mastics and hot mix asphalt overlays. Damage may occur due to compaction and other interactions.

2.5.2 Fracture mechanics tests on adhesive membranes

2.5.2.1 Pull out tests

A pull-out test was used to determine the tensile bond strength between the asphalt layers and the membranes, Figure 2.1. The pull-off adhesion strength and mode of failure of a coating from a substrate are important performance properties that are used in specifications. This test were first introduced for evaluating the pull-off adhesion strength of a coating on concrete. This test, is performed by applying a tensile force to a metal disk attached with epoxy to a cored asphalt section, Figure 2.1 on the right, measuring the force required to separate the pavement from the membrane. Failure will occur along the weakest plane within the system comprised of the test fixture, adhesive and substrate.

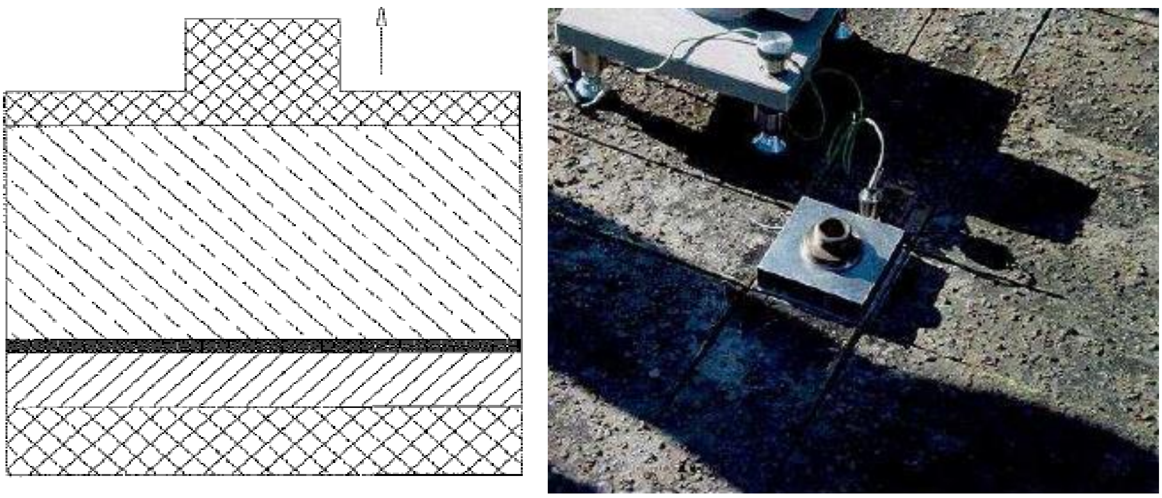

Figure 2.1 Tensile bond strength test (left: schematic diagram; right: in situ)

The tests are commonly used to determine the effects of temperature on the strength of adhesive membranes. However, for this test method, the possible debonding position can be at the top interface of the membrane or at the bottom interface or even across three materials layers. This will cause some ambiguity as to the actual debonding strength and mechanism.

2.5.2.2 Blister test

Adhesion measurements by the blister test were first done by Dannenberg in 1961, however his set up is quite different than the ones are used today. Dannenberg used a grooved restraining plate to limit the deflection of the blister. He found that an oblong blister rather than a circular blister had a more stable debonding pattern. (Williams 1969) was the one who introduced the test as we know using fracture mechanics in the analysis. The test specimen consists of a perforated substrate with a thin flexible overcoating. A fluid is injected at the interface through the perforation, thereby causing a progressive debonding of the overlayer, Figure 2.2. Gent and Lewandowski (1987) have discussed how the adhesion energy can be calculated from the geometry of the blister and the fluid pressure. Recently, the test has been reanalysed and applied to predict the bonding between bituminous sealant and aggregate (Fini, Al-Qadi, Masson and McGhee, 2010).

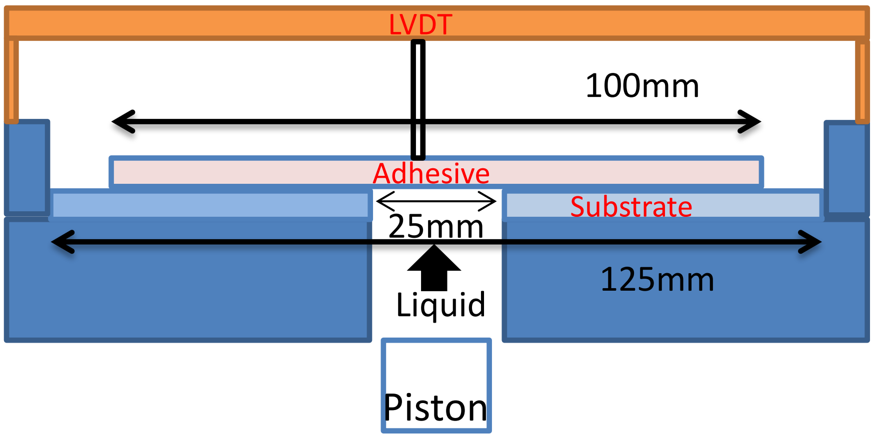

Figure 2.2 Schematic diagram of the blister geometry

In the blister test, hydraulic liquid with pressure p is injected into the centre of the substrate, the adhesive lifts off the substrate. A blister forms, whose radius stays fixed, until a critical pressure is reached. The blister test can measure interfacial fracture energy, which is a fundamental property of the interface. For viscoelastic material, interfacial fracture energy is expected to be time-dependent, although still geometry-independent, like the relaxation modulus.

The blister test offers several advantages over peel tests:

- there is no direct mechanical contact via fixtures or clamps to effect debonding,
- the small detachment angle and relatively low debonding rates minimize the dissipative effects in the overlayer.
- the fracture surface is axisymmetric, which minimizes the effect of sample nonuniformity, and
- the applied forces are uniform and symmetric without requiring tedious alignment.

In earlier tests, Lai and Dillard, (1994). Debonding were caused by applying hydrostatic pressure however a few problems were reported. One of these is that due to hydrostatic pressured blister test, the strain energy release rate increases as blister radius increases and debonding become unstable (Moreover, pressurized blister tests require sophisticated experimental equipment to monitor the simultaneous change in blister dimension and dissolved gases may invalidate such tests (Wan, 1999).

2.5.2.3 Shaft loaded blister test

The shaft loaded blister test (SLBT), first reported by (Williams,1969), who introduced the crack driving force via a central load acting on a spherically capped shaft, Figure 2.3. The shaft loaded blister test offers an alternative to pressured blister tests because a universal test machine can drive the shaft that induces displacements, better compliance measurements can also be obtained Jennings, Taylor and Ferris, (1995). The configuration is of particular interest due to the simpler experimental setup and has received a considerable amount of attention in the last 20 years.

Even though the blister test is widely used to measure mechanical properties of thin films, its application is limited because of the complicated fluid control system and the difficulty of simultaneously measuring both blister height and pressure (Lai and Dillard, 1994) and Wan, (1999). Therefore, The SLBT is a very good replacement of the traditional blister test, which a transverse load is applied to a thin film by a mechanical system where the load-shaft displacement data is easily obtainable experimentally. One drawback needs to be mentioned about this test is that, even with a spherically capped shaft, still there is a severe stress concentration around the loading point, which would affect the test accuracy.

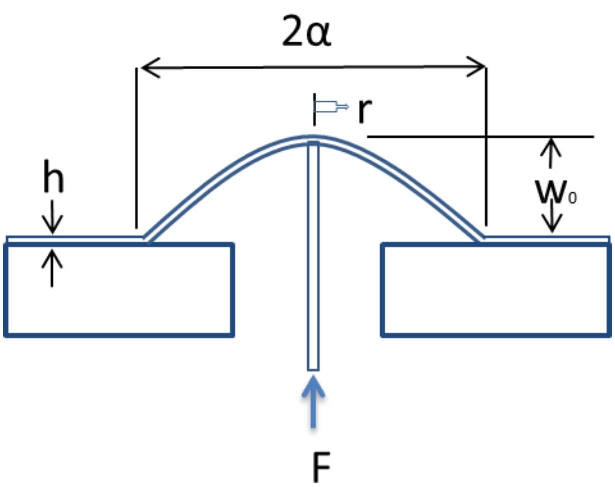

Figure 2.3 Schematic diagram of the shaft loaded blister test

2.5.2.4 Peeling test

The schematic diagram of a peeling test is shown in Figure 2.4. This test method is primarily intended for determining the relative peel resistance between flexible adherents by means of a specimen using a tension testing machine. The unbounded ends of the test specimen are clamped in the test grips of the tension testing machine and a load of a constant head speed is applied. A recording of the load versus the head movement or load versus distance peeled is made. Peel resistance over a specified length of the bond line after the initial peak is determined.

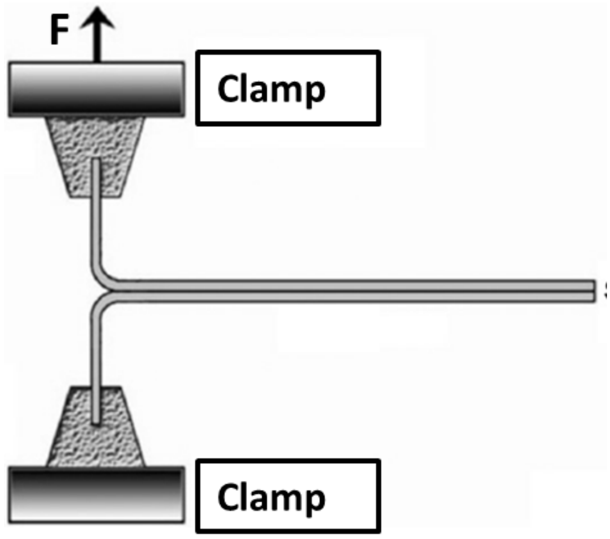

Figure 2.4 Schematic diagram of peeling test

The peeling test meets many of the criteria of the ideal adhesion test. Sample preparation is typically simple and straightforward. Another advantage of this test is that the rate of the delamination and the locus of failure can be controlled precisely. This stems from the fact that a very high stress concentration exists at the point where the delamination starts.

A drawback apply to the peeling test is that, large stress concentration or deformation occurs around the clamp area, making interpretation of the results unclear.

3 Theoretical background of MAT

3.1 Introduction

A number of techniques have been developed in the past to quantity the adhesive strength between membrane and the associated substrate. Among others, the blister tests, initially suggested by Dannenberg (1961) and discussed by Gent and Lewandowski (1987), is the most common used one. The test specimen in the blister test consists of a perforated substrate with a thin flexible bonded membrane. A fluid is injected at the interface through the perforation, thereby causing a progressive debonding of the membrane. However, blister tests have several drawbacks such as the strain energy release rate increases as blister radius increases and membrane debondings become unstable. The bulged area is anomalous and unpredictable especially when the substrate materials are harsh and porous, for example, cement concrete or porous asphalt concrete. It is vague about the physical or chemical effects of the pressurized liquid on interface between the two bonded materials.

Shaft loaded blister test (SLBT), first proposed by Williams (1969), is an alternative to the pressured blister test. A machine-driven shaft is utilized to induce central loads and displacements on membrane. Because of the slightly simpler setup and loading method, SLBT has its advantages over traditional blister test and received much attention in the last two decades. The main limitation of the SLBT is about the stress singularity caused by its shaft point load. Different kinds of shaft cap shapes are employed to improve this weakness. Most common way is using a spherically capped shaft or ball with certain radius, Liao and Wan (2001), Xu et al.(2003).

Peel tests are also commonly used to quantify the adhesive strength of membrane to the associated substrate. However the peel tests usually cause large permanent deformation at the loading point, which makes the calculation of energy release rate inaccurate. The majority of mechanical energy supplied in peeling is dissipated or stored in deforming the test specimen; relatively little energy actually contributes to the fracture process of the interface.

In recent years, considerable number of analytical solutions for blister tests, SLBT and peel tests have been proposed, Malyshev and Salganik (1965), Williams (1969), Storakers and Andersson (1988), Williams (1997) and C.Jin (2008).

In order to characterize adequately the adhesive bonding strength of the various membranes with surrounding materials on orthotropic steel bridge decks and collect the necessary parameters for FE modeling, a Membrane Adhesion Test (MAT) device has been developed by Delft University of Technology. This innovative MAT device has the following advantages. Due to a cylindrical loading piston head, the piston force can be applied uniformly on the membrane surface with negligible boundary effects. Cylindrical loading piston heads can be utilized with different radii to minimize damage on the test membrane. The energy release rate and membrane strain expressions can be easily determined. A laser scanning system is utilized to measure membrane deformation, hence the in-time membrane profile can be recorded.

In this chapter, details of the MAT device are presented. Meanwhile, the membrane products from different companies will be briefly introduced and manufacture process of specimen will be described. The final part presents the theoretical background of MAT and the theory behind the tests.

3.2 Apparatus

The schematic diagram of MAT setup can be shown as below, see Figure 3.1.

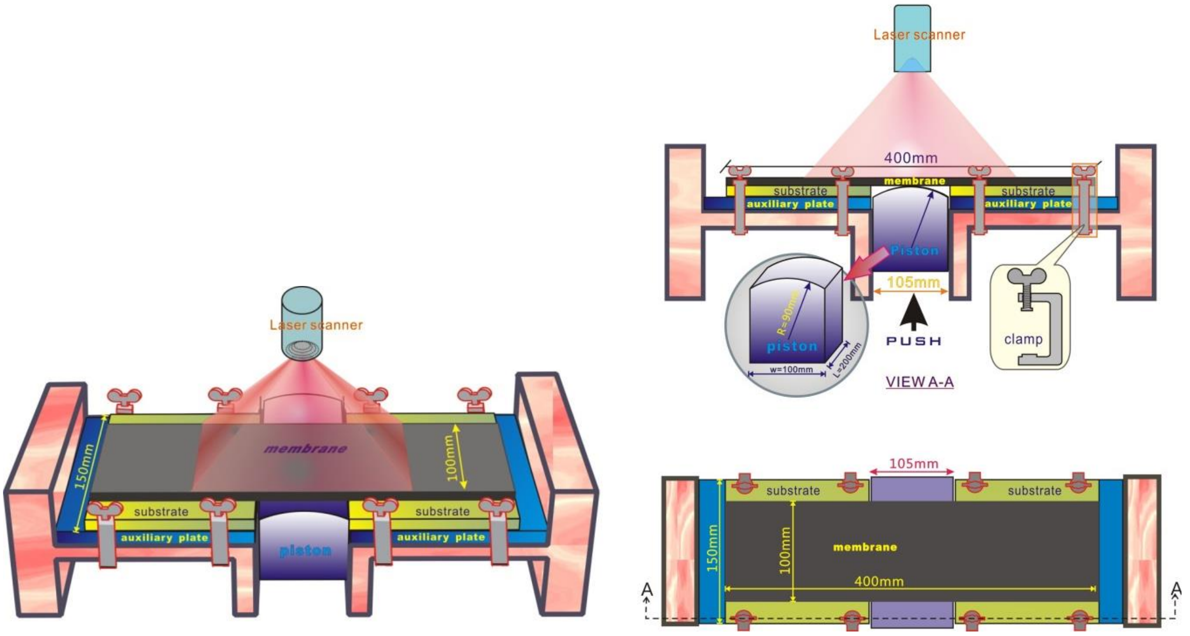

Figure 3.1 Schematic of Membrane Adhesion Test (MAT)

The action of the piston causes gradual debonding of the membrane from the substrate. A continuous measurement of the membrane deformation and load, provide a measure of the energy necessary for debonding and can be used to characterize adequately the adhesive bonding strength of the various membranes with substrates. The advantage of the MAT is that properties like adhesive fracture energy and the basic mechanical characteristics of the membrane can be determined from a single test.

The MAT loading actuator is computer controlled and is able to provide:

- Maximum force up to 5KN
- Piston travel to the maximum distance of 150mm

The actuator uses a specially designed roller screw mechanism for converting electric power into linear motion within the actuator.The laser scanning system senses the shape of the deformed membrane along 150 mm length. The laser scanner can be operated in temperature range of -10 ^{o}C to 55 ^{o}C. The control and data acquisition system is capable of measuring the load and deformation of the piston and adjusting the load or displacement applied by the loading device. The MAT set up is presented in Figure 3.2.

The test system requirements are summarized in Table 3-1.

Table 3-1 Test system minimum requirements

Load measure and control	Range of load cell 1: 0~5 kN Range of load cell 2: 0~0.5 kN Accuracy: 1% down to 5% of full load
Displacement measurement and control	Range:0~150mm Speed: 0~30mm/s Accuracy: 1%
Laser scanner	Range: 150mm width Frequency: up to 250Hz

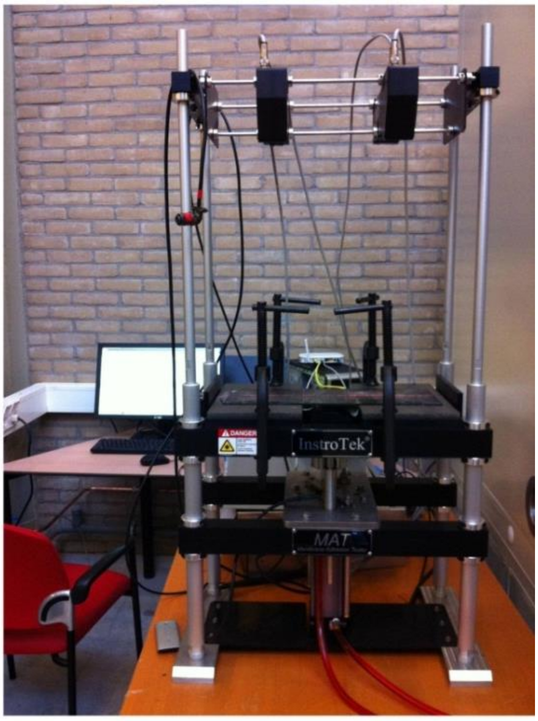

Figure 3.2 Set-up for MAT

3.3 List of membrane products and its mechanical properties

3.3.1 Product A1 and A2 from Company A

In this research, one of the involved participants to this project is company A with two membrane products A1 and A2.

Product A1 and A2 are highly performed waterproofing membrane manufactured with SBS elastomeric bitumen and internally reinforced with a non-woven polyester textile. These two products are implemented on concrete deck, steel deck, sand asphalt or asphalt concrete. In MAT test, product A1 is applied on the steel plate, while product A2 is applied on the Guss Aspahlt. Figure 3.3 is the real picture of product A1 (A2).

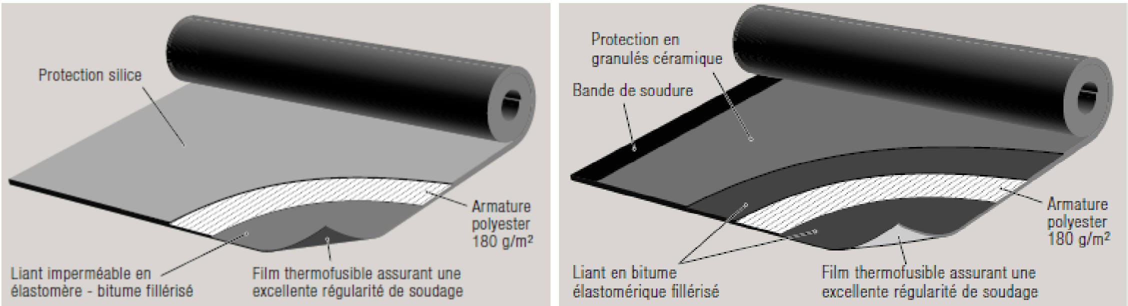

Figure 3.3 Product A1 (left) and A2 (right) from Company A

Product A1 and A2 can be bonded to the prepared substrate by melting the film on the membrane surface and softening of the bitumen. Details of the product specifications can be seen in Table 3-2.

Table 3-2 Specifications of product A1 and A2 from Company A

Test and specification	Units	Standard	A1		A2	
			Nominal values	Critical values	Nominal values	Critical values
Main surface thickness	mm	EN 1849-1	4	3.8	4.8	4.6
Longitudinal overlap thickness	mm	EN 1849-1			4	3.8
Longitudinal overlap width	mm	EN 1848-3			110	100
Tensile strength at break (20°C,100mm/min)	N/5cm	EN 12311-1	950	820	950	820
Elongation at break (20°C, 100mm/min)	%	EN 12311-1	40	35	40	35
Pull-off resistance (20°C, 1.65 m/min)	MPa	NF P 98 282			>0.4	
Cold temperature flexibility	°C	EN 1109	-15	-10	-15	-10
Dimensional stability	%	EN 1107-1			≤0.5	
Heat flow	°C	EN 1110			100	95
Static puncture resistance	kg	EN 12730				
Weight/sqm	kg		5.05	4.79	6.27	
Length × width	m×m		10×1	9.9×0.99	8(±10)	1(±0.1)
Weight/roll	kg		50.5	48	48.9	

3.3.2 Membrane B from Company B

Another involved participant to this project is the company B with one type of membrane. This membrane can be used as both bottom membrane and top membrane in Dutch steel bridge system.

Product B is used as moisture and insulation layer on the surfacing system. This membrane product is a high SBS modified isolation diaphragm which is reinforced with a strong support of polyester, see Figure 3.4. Specifications of product B are shown in Table 3-3.

Figure 3.4 Product B from Company B

Table 3-3 Specification of product B from Company B

Test and specifications	Units	Standard	B
Grammage	kg/m²	EN 1849-1	6
Thickness	mm		5.3±0.3
Waterproofing		EN 1928 (Method A)	
Flexibility at low temperature	°C	EN 1109	≤-20
Impact resistanct	mm	EN 1269 (Method B)	≥1000
Resistance to static load	kg	EN 12730 (Method A)	≥20
Extensibility in the cold with the same density	%	EN 13897	≥10
Sliding in the heat	°C	EN 1110	≥110
Dimensional stability	%	EN 1107-1	≤0.4
Flexibility at low temperature aftr aging	°C	EN 1296/EN 1109	≤-10
Extensibility in the cold with the same density after aging	%	EN 1296/EN 13897	≥5

3.3.3 Membrane C1 and C2 from Company C

There are two types of membranes from Company C, who is also an involved participant to this investigation. Product C1 is used only as bottom membrane, and product C2 can be applied for both top and bottom membrane layers in Dutch asphalt surfacing system on a steel bridge deck.

Figure 3.5 Product C1 (left) and C2 (right) from Company C

Product C1 is a single ply membrane with a total thickness of 2.4 mm, with non woven polyester fleece. This product is made for the single-ply sealing under stone mastic asphalt, mastic asphalt or bituminous concrete, see Figure 3.5 left.

Product C2 is a single ply membrane with a total thickness of 4.7 mm, which exists of a 1.5 mm strong fleece. This membrane is provided with a modified bituminous mass of 1.6 mm thickness on both sides. It is easy to lay as waterproofing membrane for bridges, and high resistance to traffic loading, see Figure 3.5 right.

The details of specifications for product C1 and C2 are shown in

Table 3-4.

Table 3-4 Specifications of product C1 and C2 from Company C

Test and specification	Units	Standard	C1	C2
Thickness	mm	EN 1859-2	2.4	4.7
Dimensions	m	EN 1849-2	1.00-7.5	1.00-7.5
Water tightness	6 bar/24 h	EN 1928-B	o.k.	0.k.
Cold bend test	^{o}C	EN 495-5	-40	-40
Heat stability	^{o}C		100	100
Tensile strength MD/TD	N/50 mm	ISO 527	1350/1150	1350/1150
Elongation at tensile strength MD/TD	%	ISO 527	50/70	50/70
Adehsive tensile strength/SMA	MPa	TP-BEL-B	1	1

3.3.4 Membrane D from Company D

Company D as another involved participant to this investigation has provided only one membrane product D, and it is claimed that it can be applied as both top and bottom membrane in Dutch asphalt surfacing system on a steel bridge deck.

Figure 3.6 Product D from Company D [13]

Product D consists of a self-adhesive bituminous compound, reinforced with an extra strong crossover glass-fiber mesh. This membrane can be applied on large damaged roads due to self-adhesion, see Figure 3.6. Generally, product D can be used for: reinforcing in case of subsidence and alligator skin cracks on damaged road surfaces; jointing membrane between different subgrades for road extensions; spreading loads over unstable cement subgrades in bituminous or standard mix.

The details of specifications for Membrane D are shown in Table 3-5.

Table 3-5 Specifications of product D from Company D

Test and specification	Units	Standard	D
Thickness	mm	EN 1849-1	3
Backing melting point	^{o}C	ASTM D 276	>400
Tensile strength long.	N/m	ISO 4606	>40000
Tensile strength trans.	N/m	ISO 4606	>24000
Elongation at break long.	%	ISO 4606	2
Elongation at break trans.	%	ISO 4606	1.6
Adhesion strength	N	ASTM D1000	>250

3.3.5 Membrane E from Company E

Membrane E, Figure3.7 is provided by Company E, and it is tested in this investigation as bottom membrane in steel deck bridge.

Figure 3.7 Product E from Company E

Membrane E consists of two coats with a film thickness of 1.5 mm per coat and a total thickness of 3.0 mm. This membrane is three-component spray-applied. The membrane consists of two liquid components and a hardener powder.

Specifications of product E are shown in Table 3-6.

Table 3-6 Specifications of product E from Company E

Test and specification	Units	Standard	E
Water vapor transmission	g/m2 day	ASTM E 96	6.6
Chloride transmission	%	TRRL Research	0.02
Adhesion to steel	MPa	BS3900:E10:1989	2
Tensile strength	MPa	ASTM D638	6.481
Elongation at break	%	ASTM D638	80
Tear strength	N/mm	BS903 Pt A3	60
Low temperature flexibility	^{o}C	DTp Technical	-25
Resistance to penetration	^{o}C	DTp Technical	80

3.3.6 Membrane F from Company F

Another involved participant to this project is the company F, Figure 3.8 with one type of membrane. This membrane can be used as both bottom membrane and top membrane in Dutch steel bridge system. Product F is a specially in-situ laid composite asphalt reinforcement system, it consists of a high strength glassfiber reinforcement grid with double strength in the transverse direction and a polymer modified bitumen.

The application of the modified bitumen provides an extremely good, though visco-elastic bond between both the steel bridge and the Guss asphalt as bottom membrane and between the Guss asphalt and the surface layer as top membrane, while ensuring waterproofed protection of the underlying structure for a considerable period of time. The specifications of product F are presented in Table 3-7 Specifications of product F from Company F Table 3-7

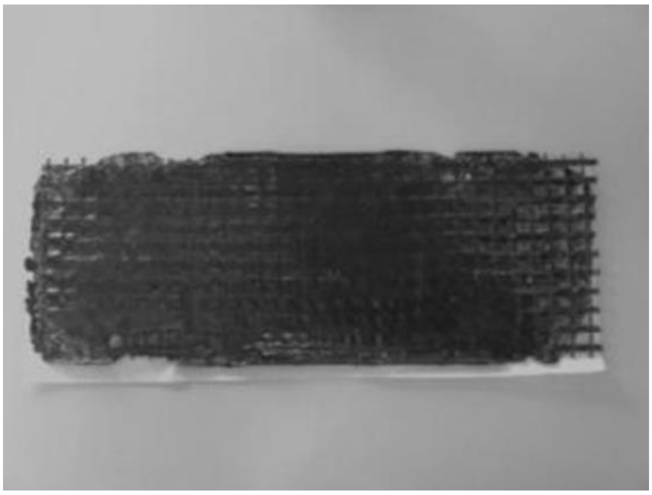

Figure 3.8 Product F from Company F

Table 3-7 Specifications of product F from Company F

Test and specification for the modified bitumen	Standard	F
Penetration at 25 °C	EN 1426	60 – 90
Softening Point R&B	EN 1427	≥100 °C
Cohesion Force-ductility at 5 °C Total energy till fracture	EN 13589 / EN 13703	≥15 J/cm2
Change of Mass after hardening	EN 12607-1	≤0.5% m/m
Retained penetration after hardening	EN 12607-1 / EN1426	≥ 60%
Increase in softening point after hardening	EN 12607-1 / EN1427	≤8 °C
Flash Point	EN ISO 2592	≥250 °C
Test and specification for the reinforcement		
Tensile strength (single rib testing)	NEN-EN 15381:2008	115 kN/m +/- 15 kN/m
in longitudinal direction		
in transverse direction		215 kN/m +/- 15 kN/m

3.4 Specimen preparation

In the Netherlands an asphaltic surfacing structure for orthotropic steel bridge decks mostly consists of two structural layers, see Figure 3.9. The upper layer consists of Porous Asphalt (PA) for noise reduction. For the lower layer a choice between Mastic Asphalt (MA) or Guss Asphalt (GA), can be made. In order to characterize the adhesive bonding strength of various membrane products utilized in the Dutch steel deck bridges, four types of specimen, i.e. steel-membrane specimen (SM1), Guss Asphalt Concrete-membrane specimen (GM1 and GM2) and Porous Asphalt-membrane specimen (PM2) were investigated first.

The preparation of the asphalt samples took place at Ooms civiel bv in Netherlands though the steel-membrane specimens were produced at TU-Delft.

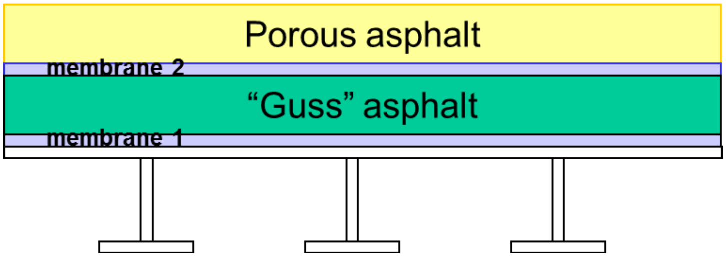

Figure 3.9 Schematic of a typical Dutch asphalt surfacing system on a steel bridge deck

3.4.1 Asphalt mixes

Guss asphalt (GA) for road surfacing was developed principally by German engineers in the 1950’s. It is estimated that 45% of all existing Autobahn surfaces in Germany are surfaced with Guss asphalt and that many of them are 30 years old or more. Since the 1970’s, the Dutch Ministry of Transport, Public Works and Water Management (RWS), which manages the main road network of the Netherlands, has been researching, developing, and applying porous asphalt to improve the safety of the nation's freeways and to reduce road noise. Therefore the upper layer of asphalt surfacing on Dutch OSDB consists of mainly Porous Asphalt (PA). Table 3-8 gives the mix composition of porous asphalt and Guss asphalt that have been utilized to make 5PB beam test samples. The average density of GA is ρ = 2320kg/m3 and for PA is ρ = 1980 kg/m3

Table 3-8 Specifications of asphalt mixtures

	Mass percentages (%)		
Guss asphalt	Targeted	Min	Max
C8	2.1	1.1	3.1
2mm	52	45	59
63µm	78	76	80
Bitumen MA 8	9.0 (%)		
SFB-5-20(JR)			
Porous asphalt			
C11.2		0	8.4
C8		51.0	63.0
C 5.6		71.0	83.0
2mm		81.0	89.0
63µm		94.0	97
Bitumen 50/50	4.9(%)		

3.4.2 Steel - Membrane 1 specimen (SM1)

Two pieces of square steel plates $150 \times 150mm$ with thickness 6 mm have been used. The steel plate has been cleaned in accordance with EN ISO 8503-1 before the application of the membrane. A wooden plug with dimensions $150 \times 105 \times 6mm$ has been placed as spacer between the two steel plates. The membrane has been cut in pieces with dimension $405 \times 105 \times 3mm$ and bonded to the steel plates using the glue side or melting the membrane. After adhesion membrane to steel plates, the wooden plate is removed. The process can be shown as Figure 3.10.

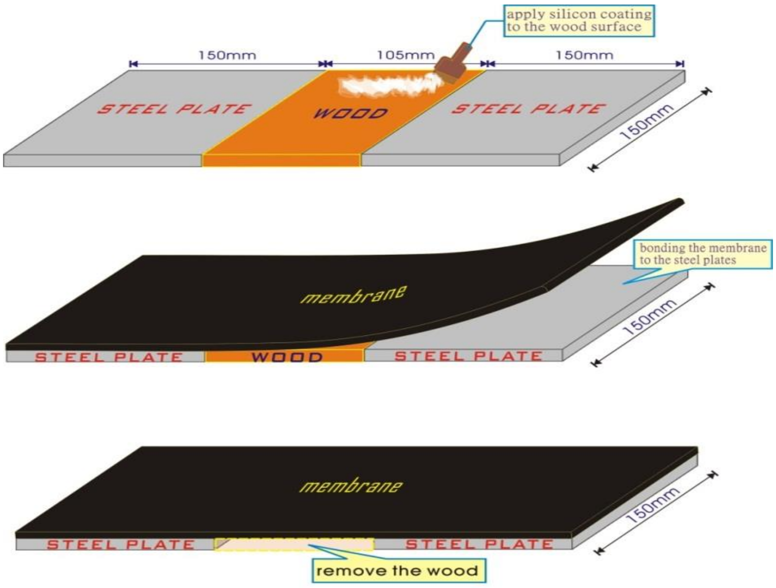

Figure 3.10 SM1 specimen preparation steps

The final SM1 sample is shown in Figure 3.11.

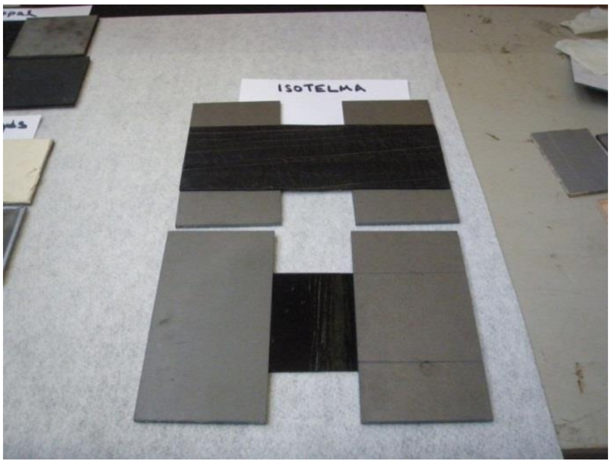

Figure 3.11 Final SM1 sample

3.4.3 Guss Asphalt – Membrane 1 specimen (GM1)

Because the GM system consists of two interfaces, one is the membrane on the bottom of the Guss Asphalt and another is the membrane on top of the Guss Asphalt. Therefore two types of GM specimens have been prepared. In this section, the bottom membrane connects to Guss Asphalt is considered. The membrane has been placed at the bottom of the mould with its sticky side facing the bottom of the mould. Over it, a wooden plug with dimensions $150\times105\times30$ mm has been placed as a spacer. For some specimens, the membrane should be melted before application. The process of GM1 sample preparation is illustrated in Figure 3.12.

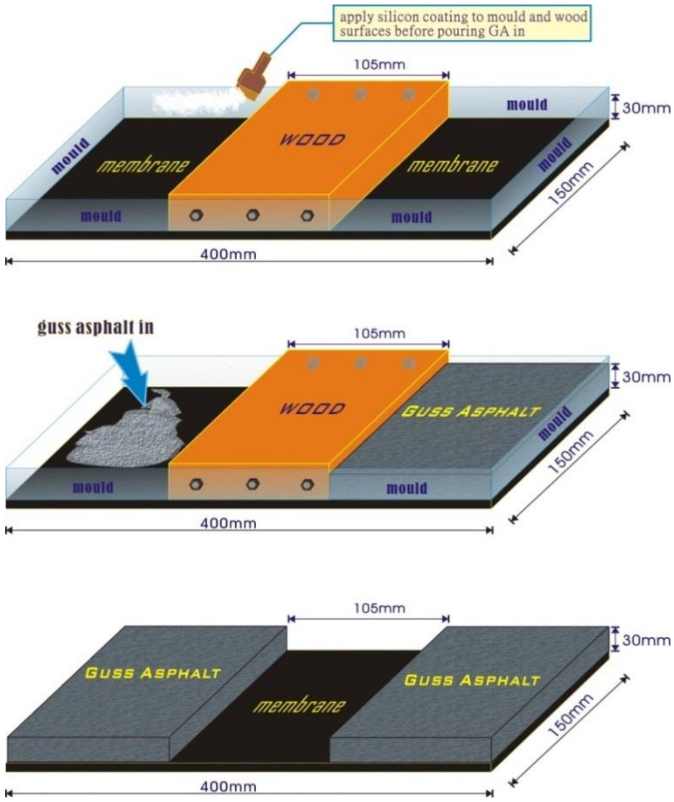

Figure 3.12 GM1 specimen preparation steps

The GA requires a minimum curing time of 14 days and a maximum of 8 weeks before testing. After curing of the Guss asphalt, the mould and the wooden plug have been removed. Figure 3.13 shows one sample of GM1.

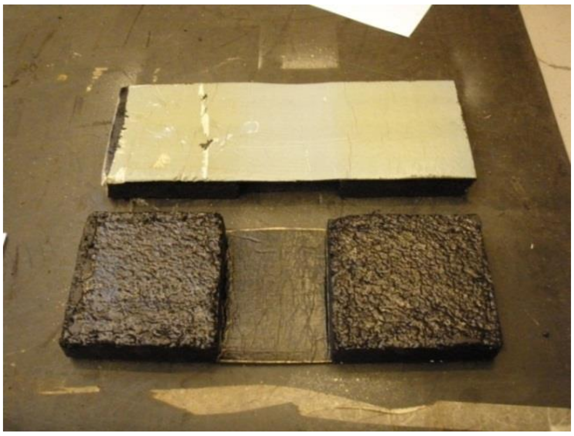

Figure 3.13 Final GM1 sample

3.4.4 Guss Asphalt – Membrane 2 specimen (GM2)

In this section, the top membrane adhered to GA is considered.

For the preparation of these specimens, the same mould and the same wooden plug (spacer) have been used as in the previous system. But in this case the asphalt and wooden plate are installed first and then the membrane is placed facing the asphalt with its sticky surface. After curing of the guss asphalt, silicon coating is applied on top of the wooden plug, so it can be removed after the application of the membrane. Finally, the membrane placed on top of the guss asphalt and the wooden plug has been removed.

The process of GM2 specimen preparation is illustrated in Figure 3.14.

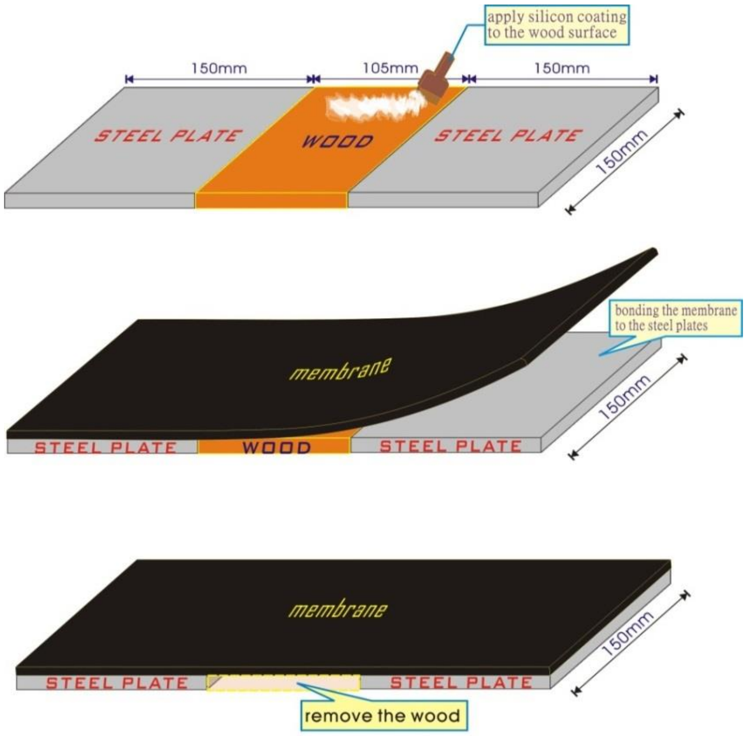

Figure 3.14 GM2 specimen preparation steps

Figure 3.15 is also one sample after GM2 specimen being finished.

Figure 3.15 Final GM2 sample

3.4.5 Porous Asphalt – Membrane 2 specimen (PM2)

For the preparation of PM specimen, a mould with dimension 400mm by 150mm by 45mm has been utilized. The tested membrane has been placed at the bottom of the mould with a wooden plug in place as a spacer, with its sticky side facing the bottom of the mould, see Figure 3.16.

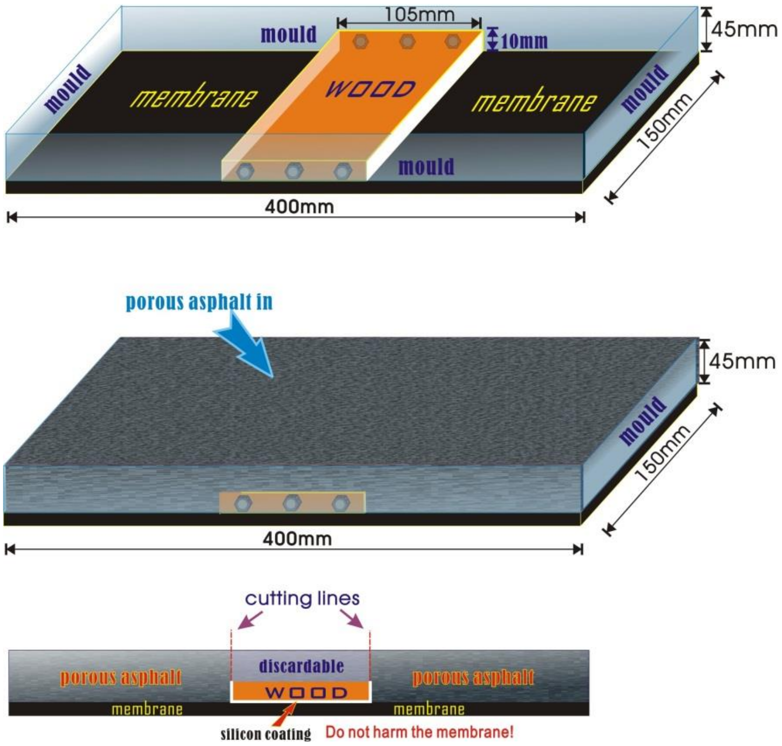

Figure 3.16 PM2 specimen preparation steps

The porous asphalt has been poured and compacted. After compaction, the excess asphalt on top of the wooden plug has been removed by careful saw cutting, see Figure 3.17.

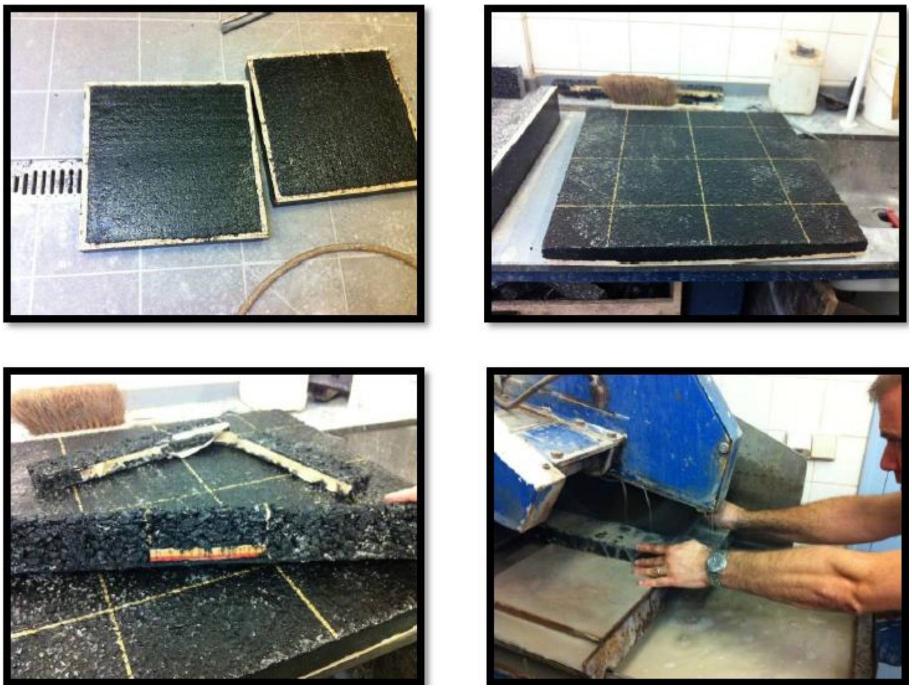

Figure 3.17 PM2 sample preparation and cutting

The porous asphalt requires a minimum curing time of 14 days and a maximum of 8 weeks before testing. Porous asphalt preparation has been performed in accordance with NEN-EN 12697-33. Figure 3.18 shows the final sample of PM2.

Figure 3.18 Final PM2 sample

Before testing, all samples were modified in order to place them on the MAT set up. 250mm of membrane of all prepared samples were cut and removed from each side along the length of the sample in order to clamp them on the set up. The final dimension of the membrane is 100mm by 150mm lying on steel, Guss or Porous asphalt interface with dimemsions of 150mm by 1500mm.

3.5 Theoretical background of MAT test

3.5.1 Introduction

In this chapter, details of the Membrane Adhesion Test (MAT) have been described to characterize the adhesive characteristics of the various membranes with the surrounding materials. Analytical constitutive relations of MAT test have been derived on the basis of Williams (1997).

3.5.2 Constitutive relations

In order to derive the constitutive relations of MAT device, a deformed thin membrane with thickness h and width b is shown in Figure 3.19. A central load F is applied to the membrane via a cylindrically capped piston with radius R. The deformed height of the center point at the outer surface of the membrane is H. There are two contact situations that may occur in the MAT tests. The first situation is that the piston partially contacts the membrane, see Figure 3.19. The second situation is the membrane contacts fully to the piston and the membrane will be stretched in straight after the kinks of the piston touch to the membrane, see Figure 3.20.

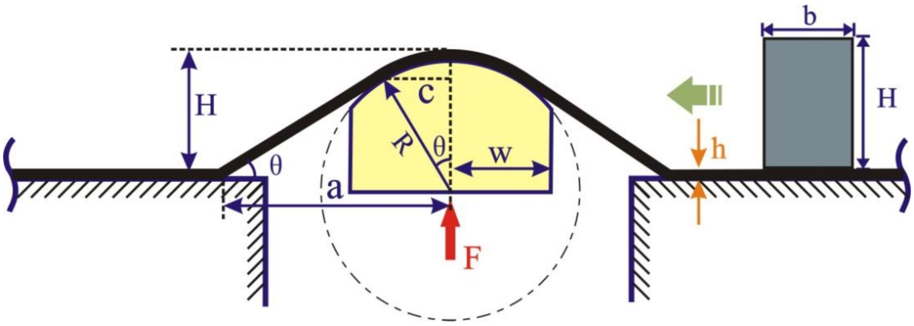

Figure 3.19 Cylindrically capped MAT (membrane contact partially to the piston head)

It depends on the stiffness and bonding strength of membrane, in most test cases, the membrane contacts partially to the cylindrical piston head before the bonding failure occurs. However, if the membrane is quite soft and the radius of the piston is relatively large, the second contact situation may occur, see Figure 3.20 below.

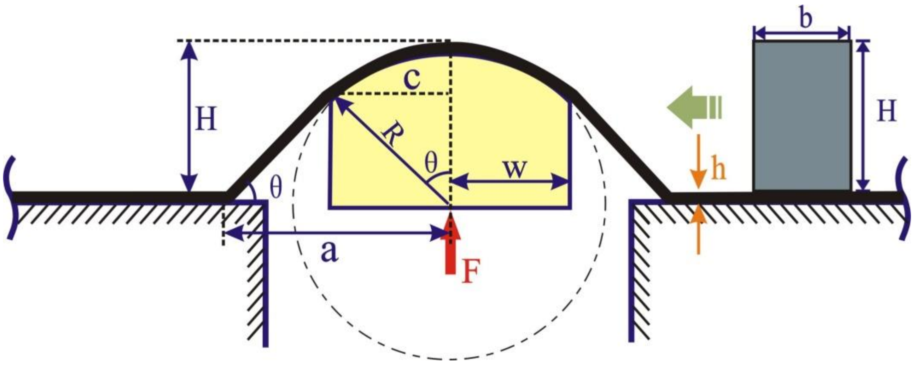

Figure 3.20 Cylindrically capped MAT (membrane contact fully to the piston head)

In order to get complete analytical solutions for MAT test, the following constitutive relations are derived on the basis of the aforementioned two contact situations.

Situation 1: Membrane contacts partially to the piston head:

Let us now consider a membrane bonded to a surface, but debonded over a length 2a as shown in Figure 3.21. There is a load point height at the centre of H giving a membrane strip angle of θ. With debonding process, H, a and θ change. The following relationship is valid:

$$\frac{H}{a} = \tan\theta - \frac{R}{a}\left(\frac{1-\cos\theta}{\cos\theta}\right) \qquad (\sin\theta \le \frac{W}{R}) \qquad (3.1)$$

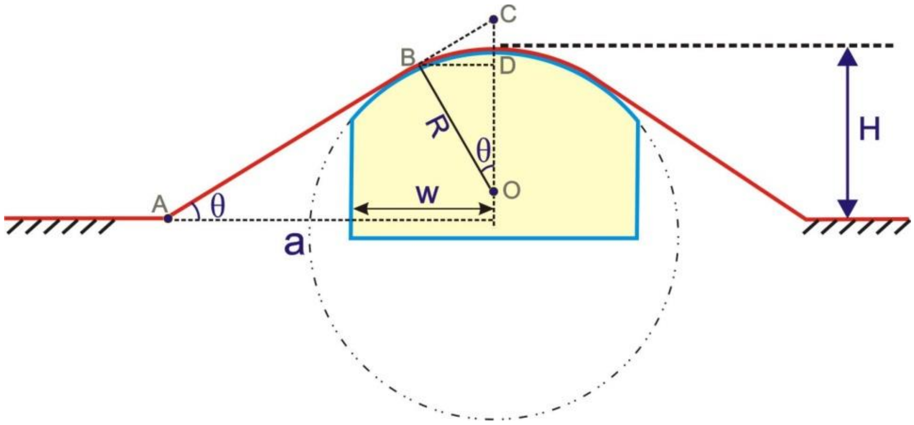

Figure 3.21 Membrane covers partially to piston head

The membrane original length is:

$$\overline{AO} = a$$

The deformed membrane length is:

$$\overline{AC} - \overline{BC} + BD = \frac{a}{\cos\theta} - R\tan\theta + R\theta$$

Thus, membrane strain is:

$$\begin{aligned}\varepsilon_1 &= \frac{\overline{AC} - \overline{BC} + BD - \overline{AO}}{\overline{AO}} \\ &= \frac{\dfrac{a}{\cos\theta} - R\tan\theta + R\theta - a}{a} \\ &= \left(\frac{1-\cos\theta}{\cos\theta}\right) + \frac{R}{a}(\theta - \tan\theta) \qquad \left(\sin\theta \le \frac{W}{R}\right)\end{aligned}$$

(3.2)

Situation 2: Membrane contacts fully to the piston head:

After the membrane touch the kinks of the piston, the loading point height H at the center of the membrane in Figure 3.22 can be defined by:

$$H = (a - W)\tan\theta + R - \sqrt{R^2 - W^2} \qquad (\sin\theta > \frac{W}{R}) \tag{3.3}$$

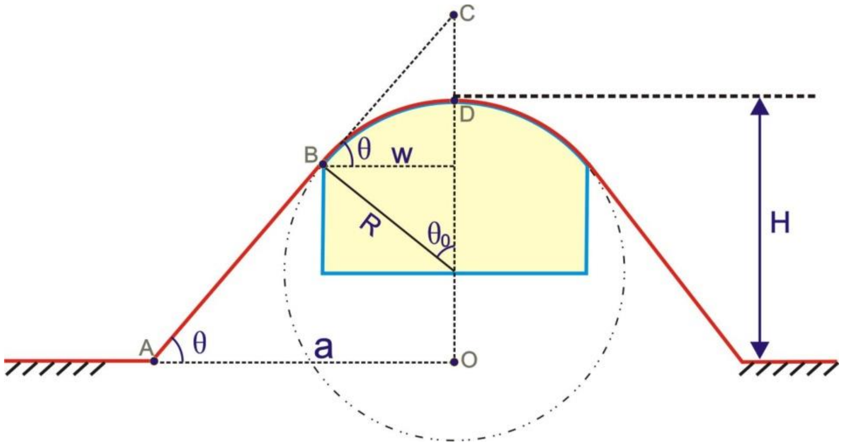

Figure 3.22 Membrane contacts fully to piston head

The membrane original length is:

$$\overline{AO} = a$$

The deformed membrane length is:

$$\overline{AC} - \overline{BC} + BD = \frac{a}{\cos\theta} - \frac{w}{\cos\theta} + R\theta_0$$

Thus, membrane strain is:

$$\begin{aligned} \varepsilon_2 &= \frac{\overline{AC} - \overline{BC} + BD - \overline{AO}}{\overline{AO}} \\ &= \frac{\frac{a}{\cos\theta} - \frac{w}{\cos\theta} + R\theta_0 - a}{a} \\ &= \left(\frac{1-\cos\theta}{\cos\theta}\right) - \frac{w}{a\cos\theta} + \frac{R\theta_0}{a} \qquad \left(\sin\theta > \frac{W}{R}\right) \end{aligned} \tag{3.4}$$

in which $\theta_0 = \arcsin\frac{w}{R}$.

The complete solutions of the load point height H and the membrane strain ε are summarized by the combinations of the aforementioned two contact situations:

$$H = \begin{cases} a\tan\theta - R\left(\frac{1-\cos\theta}{\cos\theta}\right) & \left(\sin\theta \le \frac{W}{R}\right) \\ (a-W)\tan\theta + R - \sqrt{R^2 - W^2} & \left(\sin\theta > \frac{W}{R}\right) \end{cases} \tag{3.5}$$

$$\varepsilon = \begin{cases} \left(\frac{1-\cos\theta}{\cos\theta}\right) + \frac{R}{a}(\theta - \tan\theta) & \left(\sin\theta \le \frac{W}{R}\right) \\ \left(\frac{1-\cos\theta}{\cos\theta}\right) - \frac{w}{a\cos\theta} + \frac{R\theta_0}{a} & \left(\sin\theta > \frac{W}{R}\right) \end{cases} \tag{3.6}$$

Figure 3.23 shows a comparison of membrane stain versus the membrane strip angle θ at different debonding length a.

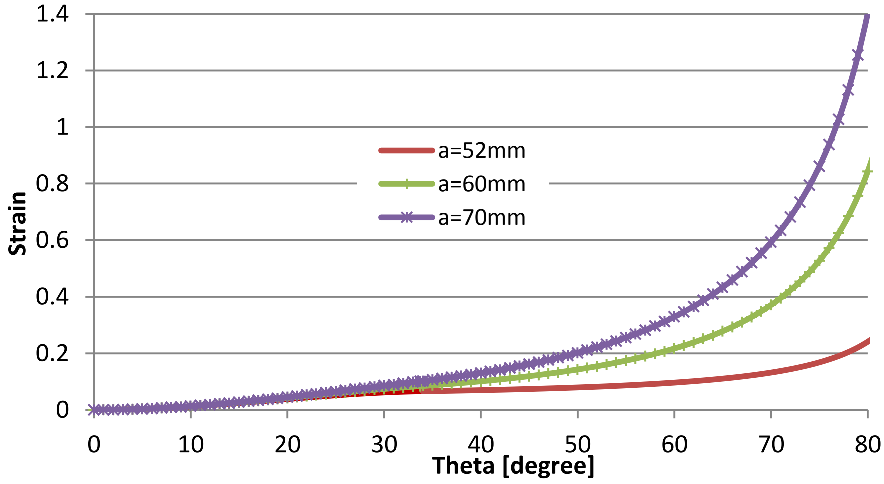

Figure 3.23 Example of ε-θ curves for MAT test (R=90mm, W=50mm)

Figure 3.24 shows a comparison of membrane stress versus the membrane strip angle θ with different membrane stiffness. It can be observed that, for elastic membrane material, the development of membrane tensile stress σ depends both on the membrane strain ε and its stiffness.

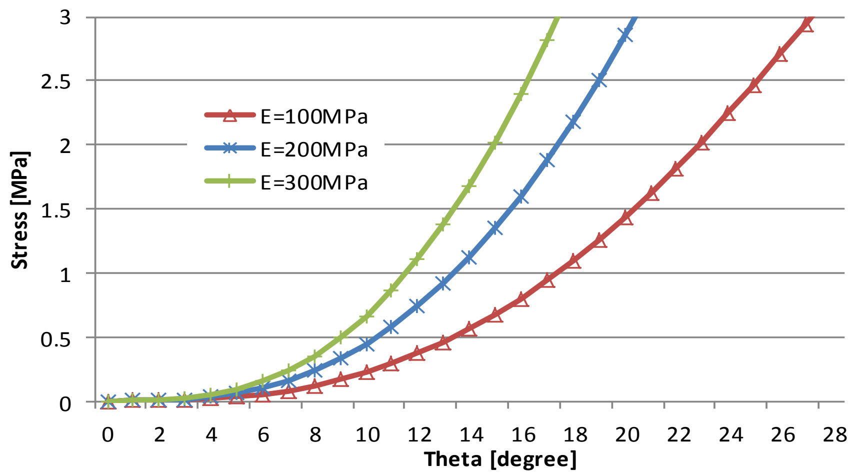

Figure 3.24 Example of σ-θ curves for MAT test (R=90mm, W=50mm, a=52mm)

In order to derive the relationship between actuator load F and the membrane strip angle θ, a schematic of force decomposition for MAT is illustrated in Figure 3.25

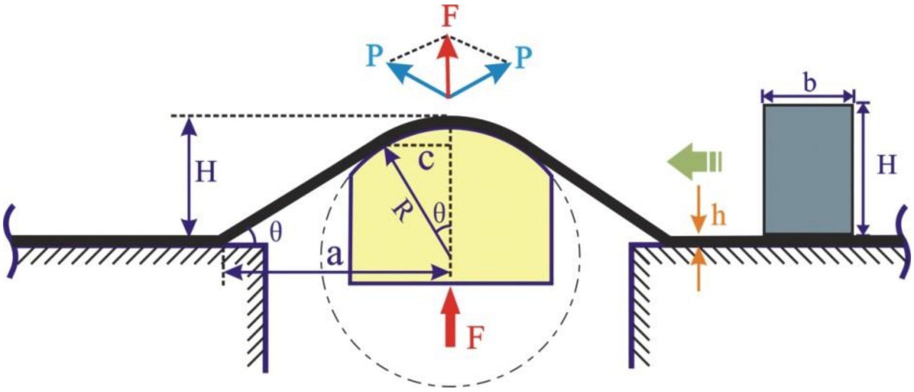

Figure 3.25 Force decomposition for MAT

Force along membrane strip is:

$$P = \frac{F}{2\sin\theta} = \sigma bh \tag{3.7}$$

where b is the width and h is the thickness of the membrane.

Actuator load F can be defined by:

$$F = 2\sigma bh\sin\theta \tag{3.8}$$

Furthermore, for elastic membrane, the actuator load for the aforementioned two contact situations can be expressed by:

$$F = 2bh\sigma\sin\theta$$
$$= \begin{cases} 2bh\sin\theta E\left[\left(\dfrac{1-\cos\theta}{\cos\theta}\right) - \dfrac{R}{a}(\tan\theta - \theta)\right] & \left(\sin\theta \le \dfrac{W}{R}\right) \\ 2bh\sin\theta E\left[\left(\dfrac{1-\cos\theta}{\cos\theta}\right) - \dfrac{W}{a\cos\theta} + \dfrac{R\theta_0}{a}\right] & \left(\sin\theta > \dfrac{W}{R}\right) \end{cases} \tag{3.9}$$

Figure 3.26 shows the variation of actuator load F versus the membrane strip angle θ by using Equation (3.9).

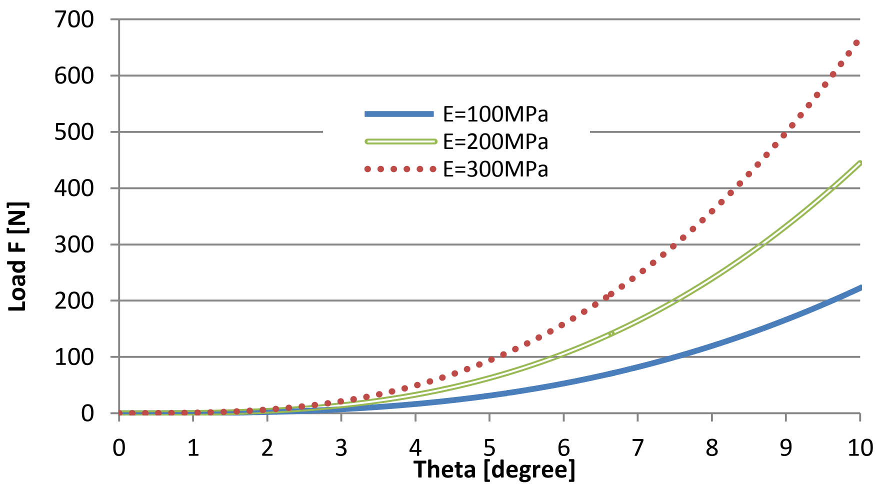

Figure 3.26 Example of F-θ curves (R=90mm, W=50mm, a=52mm)

3.6 Analytical solution of strain rate for MAT test

Before starting the MAT tests, two crucial questions needed to be answered. One is what piston loading speed should be utilized to debond the membrane from the substrate. Second one is what membrane strain rate will be resulted from such loading speed. In order to answer these questions, the analytical solutions of membrane strain rate for MAT test shall be derived. By FEM simulation of moving load, strain rate of membrane layers in reality could be obtained, see Section 5.4 in Chapter 5 for more details.

Differentiate Equation (3.5) with respect to time gives us

$$\dot{H} = \begin{cases} \left(\dfrac{a - R\sin\theta}{\cos^2\theta}\right)\dot{\theta} & \left(\sin\theta \le \dfrac{W}{R}\right) \\ \left(\dfrac{a - W}{\cos^2\theta}\right)\dot{\theta} & \left(\sin\theta > \dfrac{W}{R}\right) \end{cases} \tag{3.10}$$

Thus

$$\dot{\theta} = \begin{cases} \left(\dfrac{\cos^2\theta}{a - R\sin\theta}\right)\dot{H} & \left(\sin\theta \le \dfrac{W}{R}\right) \\ \dfrac{\cos^2\theta}{(a - W)}\dot{H} & \left(\sin\theta > \dfrac{W}{R}\right) \end{cases} \tag{3.11}$$

Differentiate Equation (3.6) with respect to time

$$\dot{\varepsilon} = \begin{cases} \dfrac{\left(R\sin\theta - a\right)\sin\theta}{a\cos^2\theta}\dot{\theta} & \left(\sin\theta \le \dfrac{W}{R}\right) \\ \dfrac{\sin\theta(a - W)}{a\cos^2\theta}\dot{\theta} & \left(\sin\theta > \dfrac{W}{R}\right) \end{cases} \tag{3.12}$$

Substitute Equation (3.11) into Equation (3.12)

$$\dot{\varepsilon} = \begin{cases} \dfrac{\sin\theta}{a}\dot{H} & \left(\sin\theta \le \dfrac{W}{R}\right) \\ \dfrac{\sin\theta}{a}\dot{H} & \left(\sin\theta > \dfrac{W}{R}\right) \end{cases} \tag{3.13}$$

For loading speed $\dot{H} = 10$mm/s, 15mm/s and 20mm/s, the corresponding strain rates are plotted in Figure 3.27 as below.

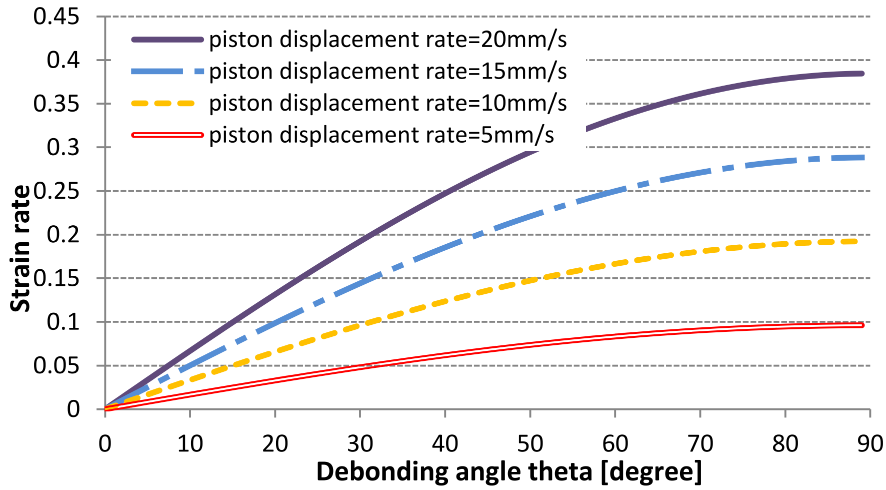

Figure 3.27 Analytical solution of strain rate for MAT test

Most MAT tests samples are debonded when the debonding angles are between 30 to 40 degrees. From Figure 3.27 above it can be seen that the strain rate in membrane corresponding to this angle range is around 0.05 when the piston displacement rate is around 5mm/s. Actually the strain rate 0.05 is obtained by FEM analysis . It represents the average strain rate occurring in Merwedebrug. Therefore, the piston displacement rate in MAT tests is chosen as 5mm/s.

3.7 Strain energy release rate G

Energy methods were employed in the earliest work on fracture mechanics, reported by Griffith (1920). This approach is expressed by a concept called the strain energy release rate, G. Later work led to the concept of a stress intensity factor K. G and K are directly related. See any book on fracture mechanics for details. We will employ G primarily since only one of these two concepts is generally needed. The general definition of energy release rate can be expressed as

$$G = \frac{d}{dA}(U_{ext} - U_s - U_d - U_k) \tag{3.14}$$

where

U_{ext} is the external work;

U_s is the strain energy;

U_d is the dissipated energy;

U_k is the kinetic energy;

A is the area create.

$$dU_{ext} = FdH$$

$$d(U_s + U_d) = 2(bh\int_0^{\varepsilon} \sigma d\varepsilon)da$$

$$dU_k = 0$$

It is assumed that the kinetic energy is zero due to slow peeling.

Combination of the above three equations, the energy release rate can be derived again and taken as blow.

$$G=\frac{dU_{ext}}{dA}-\frac{d(U_s+U_d)}{dA}=\frac{FdH}{2bda}-h\int_0^{\varepsilon}\sigma d\varepsilon \tag{3.15}$$

If the material is linear elastic, σ=Eε is valid. Then take Equation (3.8) into (3.15), another equation can be expressed as below.

$$h\int_0^{\varepsilon}\sigma d\varepsilon=\frac{F}{2b\sin\theta}\times\frac{1}{E\varepsilon}\times\int_0^{\varepsilon}E\varepsilon d\varepsilon=\frac{F}{2b\sin\theta}\frac{\varepsilon}{2} \tag{3.16}$$

Equation $\frac{dH}{da}=\frac{dH}{d\theta}\cdot\frac{d\theta}{da}$ can help the further deduction.

After combination of the aforementioned equations, dH/da can be derived as

$$\frac{dH}{da}=\frac{1+\varepsilon-\cos\theta}{\sin\theta} \tag{3.17}$$

Consider Equation (3.6) and (3.17), a final equation about G can be written as below.

$$G=\frac{F}{2b\sin\theta}\left(1-\cos\theta+\frac{\varepsilon}{2}\right) \tag{3.18}$$

But ε should be divided in two different equations as shown in Equation (3.6).

$$G=\begin{cases}\dfrac{F\left(a\cos\theta-2a\cos^2\theta+a+R\theta\cos\theta-R\sin\theta\right)}{4ab\sin\theta\cos\theta} & \left(\sin\theta\le\dfrac{W}{R}\right)\\[2ex] \dfrac{F\left(a\cos\theta-2a\cos^2\theta+a+R\theta_0\cos\theta-W\right)}{4ab\sin\theta\cos\theta} & \left(\sin\theta>\dfrac{W}{R}\right)\end{cases} \tag{3.19}$$

Since the actuator load F and membrane strip angle θ in Equation (3.19) can be measured directly via MAT test, hence G-value for each membrane bonded on different substrates can be determined.

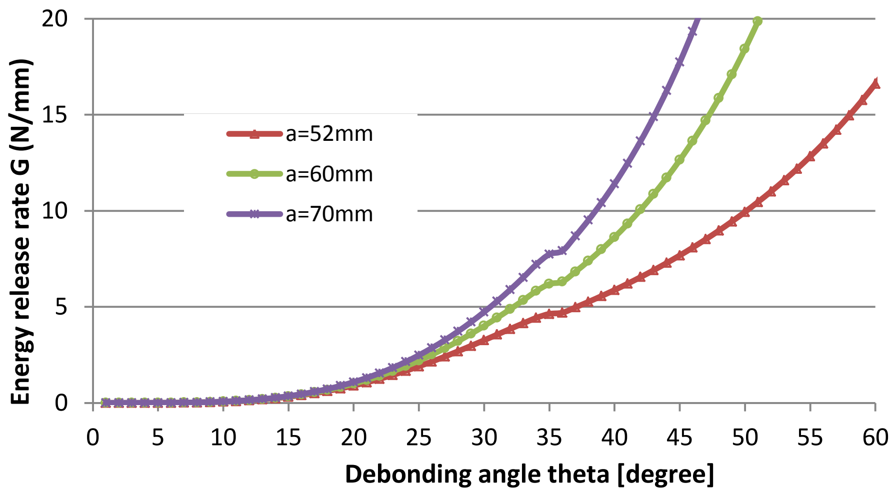

Figure 3.28 Example of G-θ curves (R=90mm, W=50mm, E=100MPa)

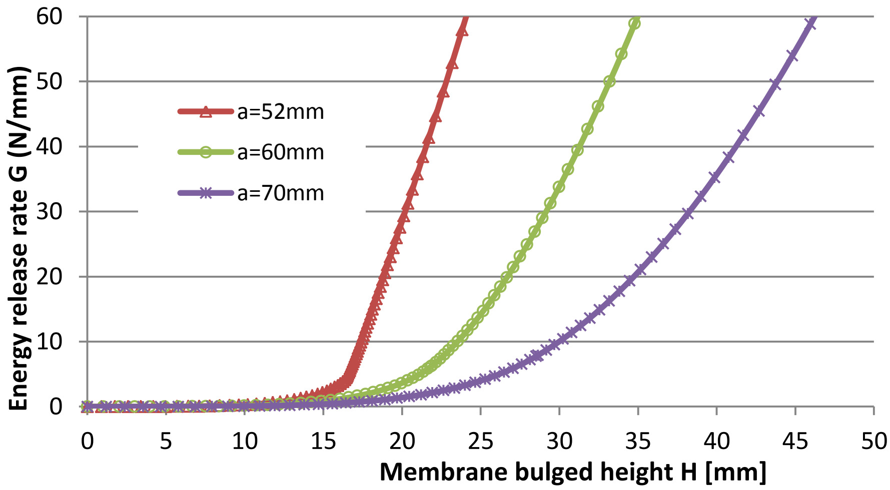

Figure 3.29 Energy release rate at different debonding widths and membrane bulge height (R=90mm, W=50mm, E=100MPa)

Figure 3.28 and Figure 3.29 show the analytical solution of the influences of the different initial gaps a=52mm, 60mm and 70mm in MAT device on the development of strain energy release rate G inside membrane material. It can be observed that, before membrane debonding, smaller initial gap in MAT device results the faster development of strain energy inside the membrane. According to Griffith criterion, for steady crack propagation, once the G value reaches a certain critical value, the crack extension will occur. This critical strain energy release rate will be utilized as a physical quantity controlling the behavior of the membrane bonding strength.

3.8 Material model of membrane products

In this project, the membranes products which are utilized for MAT test are mostly made by bitumen-based materials, thereby the mechanical responses of the membrane material are time dependent and temperature sensitive. In order to simulate the membrane response properly, a Visco-Elastic Zener model is utilized for the finite element studies. Figure 3.30 shows the mechanical analog of Visco-Elastic Zener model.

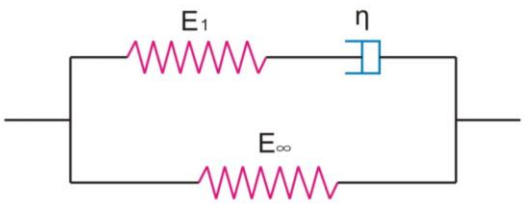

Figure 3.30 Schematic diagram of Zener model

From Figure 3.30 above, it is clear to see that the model consists of two parallel components. One is pure elastic component with modulus E_∞ and another is viscoelastic component which consists of a spring with modulus E_1 and a damper with viscosity coefficient η in series.

The total applied stress σ can be decomposed by the stresses in the two components. one is the stress σ_1 in the viscoelastic component and another is the stress σ_2 in the elastic component. It can be expressed as:

$$\sigma = \sigma_1 + \sigma_2 \tag{3.20}$$

Since the two components are in parallel, thus the two parts should have the same strain as:

$$\varepsilon_{total} = \varepsilon_1 = \varepsilon_2 \tag{3.21}$$

By consider the damper and spring in series, the strain in this viscoelastic component is additive, hence the following relations can be obtained

$$\varepsilon_1 = \varepsilon_{spring} + \varepsilon_{damper} \tag{3.22}$$

$$\sigma_1 = \sigma_{damper} = \sigma_{spring} \tag{3.23}$$

Taking the derivative of Eq. (3.22) with respect to time, a strain changes with time can be obtained as below

$$\frac{d\varepsilon_1}{dt} = \frac{d\varepsilon_{damper}}{dt} + \frac{d\varepsilon_{spring}}{dt} \tag{3.24}$$

Meanwhile, there are some relationships between stress and strain in both two parts.

$$\sigma_{damper} = \eta\dot{\varepsilon}_{damper} = \eta\frac{d\varepsilon_{damper}}{dt} \tag{3.25}$$

$$\sigma_{spring} = E_1\varepsilon_{spring} \tag{3.26}$$

Therefore, by combinations of Eq. (3.24), (3.25) and (3.26), a new expression of Eq. (3.24)is obtained.

$$\frac{d\varepsilon_1}{dt} = \frac{\sigma_{damper}}{\eta} + \frac{1}{E_1}\frac{d\sigma_{spring}}{dt} = \frac{\sigma_1}{\eta} + \frac{1}{E_1}\frac{d\sigma_1}{dt} \tag{3.27}$$

In current case, the natural conditions should be expressed as that ε_{damper} is equal to zero at the time t=0. By combination of Eq (3.22), (3.25) and (3.26), the following equations are derived

$$E_1(\varepsilon_1 - \varepsilon_{damper}) = \eta\dot{\varepsilon}_{spring} \tag{3.28}$$

$$\dot{\varepsilon}_{damper} + \frac{E_1}{\eta}\varepsilon_{damper} = \frac{E_1}{\eta}\varepsilon_1 \tag{3.29}$$

The solution of strain of damper can be obtained as below.

$$\varepsilon_{damper} = Ce^{-\frac{E_1}{\eta}t} + \varepsilon_1(1 - e^{-\frac{E_1}{\eta}t}) \tag{3.30}$$

At t=0, ε_{damper} =0 results C=0, hence

$$\varepsilon_{damper} = \varepsilon_1(1 - e^{-\frac{E_1}{\eta}t}) \tag{3.31}$$

$$\varepsilon_{spring} = \varepsilon_1 - \varepsilon_{damper} = \varepsilon_1 e^{-\frac{E_1}{\eta}t} \tag{3.32}$$

Therefore

$$\sigma_1 = E_1 \varepsilon_1 e^{-\frac{E_1}{\eta}t} = E_1 \varepsilon_{total} e^{-\frac{E_1}{\eta}t} \tag{3.33}$$

According to the relaxation test, the strain keeps constant, there is no elongation or shrinkage any more, which means that residual stresses caused by the elastic component will keep constant. Thus stress σ_2 can be expressed by

$$\sigma_2 = E_\infty \varepsilon_2 = E_\infty \varepsilon_{total} \tag{3.34}$$

By combinations of Eq. (3.20), (3.33) and (3.34), the total stress is expressed as follow

$$\sigma = E_\infty \varepsilon_{total} + E_1 \varepsilon_{total} e^{-\frac{E_1}{\eta}t} \tag{3.35}$$

If the total stress is plotted, a constant residual stress can be observed, see Figure 3.31.

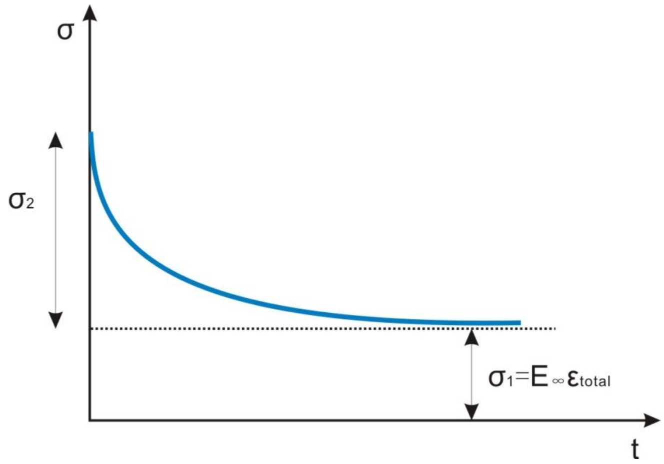

Figure 3.31 Stress versus time for relaxation test

3.8.1 Determination of material properties using relaxation tests

Relaxations tests have perfromed to Icopal B.V facilities in Groningen to five different membrane products for the model parameter determination according to specification EN 12311-1. The test set up and specimen geometry for the relaxation tests are shown in Figure 3.32. The membrane specimen is cut into dimension 30 x 5 cm strip (in long direction). Start tensile test till 15% of strain is reached, and then maintain the strain unchanged while recording the remaining tensile force against the time.

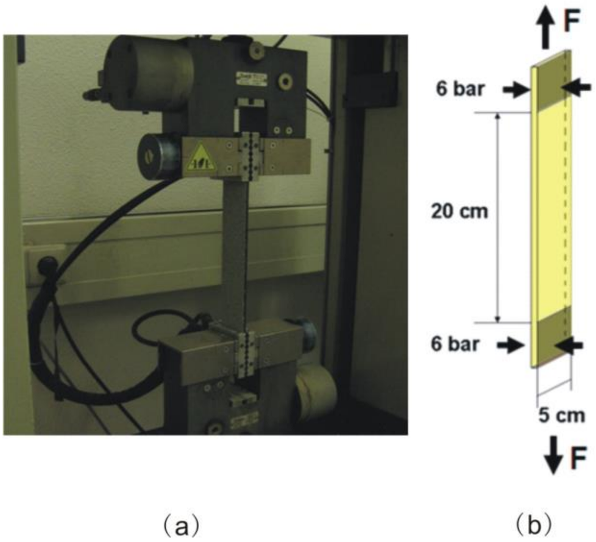

Figure 3.32 Strength and relaxation test at Icopal B.V facilities (a) test instrument and (b) schematic diagram

By using the theory of Zener model that is described in the previous section, the model parameters of E_∞ and E_1 as well as parameter η can be deductive through fitting curve by Origin program. And the parameters values will be used as input parameters in the CAPA-3D program for MAT test simulations, five-points bending test as well as bridge FE simulations by Li (2015).

3.8.1.1 Company A: A1 and A2 products

The model parameters of A1 can be obtained by fitting curves, shown in Table 3-9.

Table 3-9 Parameters from fitting curve of A1

Equation	$y = y_0 + A\exp(R_0 \times x)$		
Constants	y_0	A	R_0
fitted results	1.514	1.857	-0.0033
ε_t=0.15	$E_\infty=y_0/\varepsilon_t$	$E_1=A/\varepsilon_t$	$\eta=-E_1/R_0$
model parameters	10.09 N/mm^2	12.38 N/mm^2	3752 N/(mm^2·s)

Making use of Origin program, the fitting curve of A1 is shown in Figure 3.33.

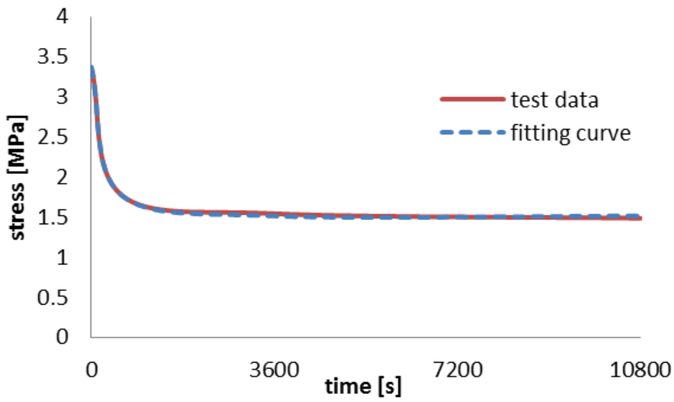

Figure 3.33 Fitting curve and test result curve of A1

The model parameters of A2 can be obtained by fitting curves, shown in Table 3-10.

Table 3-10 Parameters from fitting curve of A2

Equation	$y = y_0 + A \exp(R_0 \times x)$		
Constants	y_0	A	R_0
fitted results	1.314	1.714	-0.00299
ε_t=0.15	$E_\infty = y_0/\varepsilon_t$	$E_1 = A/\varepsilon_t$	$\eta = -E_1/R_0$
model parameters	8.76 N/mm^2	11.4 N/mm^2	3822 $N/(mm^2 \cdot s)$

Making use of Origin program, the fitting curve of A2 is shown in Figure 3.34

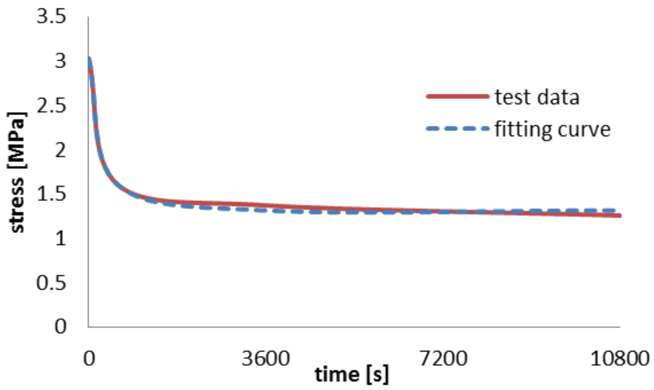

Figure 3.34 Fitting curve and test result curve of A2

3.8.1.2 Company B: B membrane product

The model parameters of product B can be obtained by fitting curves, shown in Table 3-11

Table 3-11 Parameters from fitting curve of product B

Equation	$y = y_0 + A\times\exp(R_0\times x)$		
Constants	y_0	A	R_0
fitted results	0.88859	1.37723	-0.02391
ε_t=0.15	$E_\infty=y_0/\varepsilon_t$	$E_1=A/\varepsilon_t$	$\eta=-E_1/R_0$
model parameters	5.924 N/mm^2	9.18 N/mm^2	384 $N/(mm^2\cdot s)$

Making use of Origin program, the fitting curve of product B is shown in Figure 3.35

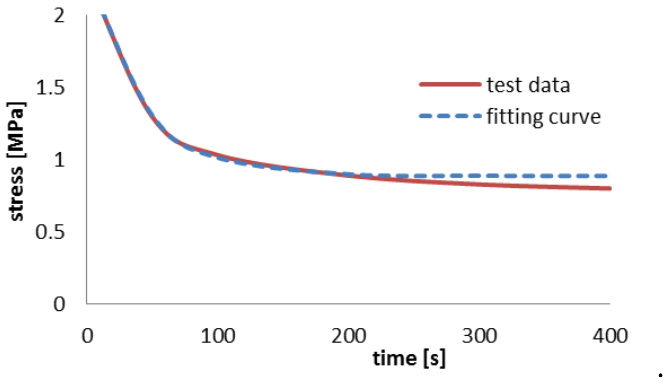

Figure 3.35 Fitting curve and test result curve of B

3.8.1.3 Company C: C1 membrane product

The model parameters of Lucobridge PV can be obtained by fitting curves, shown in Table 3-12

Table 3-12 Parameters from fitting curve of product C1

Equation	$y = y_0 + A\times\exp(R_0\times x)$		
Constants	y_0	A	R_0
fitted results	4.865	2.77233	-0.02745
ε_t=0.15	$E_\infty=y_0/\varepsilon_t$	$E_1=A/\varepsilon_t$	$\eta=-E_1/R_0$
model parameters	32.43 N/mm^2	18.48 N/mm^2	673.3 $N/(mm^2\cdot s)$

Making use of Origin program, the fitting curve of product C2 is shown in Figure 3.36

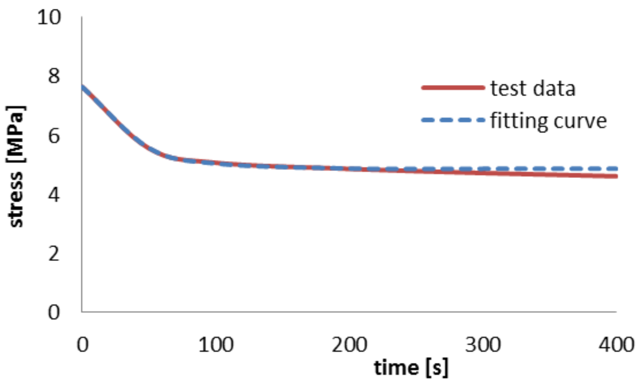

Figure 3.36 Fitting curve and test result curve of C1

3.8.1.4 Company C: C2 membrane product

The model parameters of product C2 can be obtained by fitting curves, shown in Table 3-13.

Table 3-13 Parameters from fitting curve of product C2

Equation	$y = y_0 + A \exp(R_0 \times x)$		
Constants	y_0	A	R_0
fitted results	1.44038	2.81359	-0.01972
ε_t=0.15	$E_\infty = y_0/\varepsilon_t$	$E_1 = A/\varepsilon_t$	$\eta = -E_1/R_0$
model parameters	9.6 N/mm^2	18.76 N/mm^2	951.3 $N/(mm^2 \cdot s)$

Making use of Origin program, the fitting curve of product C2 is shown in Figure 3.37 Fitting curve and test result curve of C2.

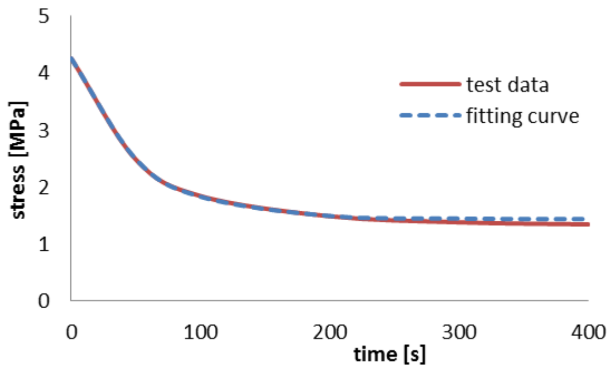

Figure 3.37 Fitting curve and test result curve of C2

4 Experimental results of MAT monotonic tests

4.1 Introduction

In this chapter, experimental results for each membrane tested at different temperature conditions will be presented. The values of strain energy release rate for each membrane interface are compared, as well as the relationship between the membrane debonding force and the piston elevation. Also, the rates of membrane debonding length propagation and the influence of temperature on the strain energy release rate will be discussed.

In the last part of this Chapter, in order to rank various membrane products, comparisons of strain energy release G-values for different membranes under the same test condition will be shown.

4.2 Specimens introduction

As mentioned in Chapter 3, there are four types of specimens for the MAT tests: Steel-Membrane specimen (Steel/M1), Guss Asphalt-Membrane specimen (M1/G-asphalt), Guss Asphalt-Membrane specimen (G-asphalt/M2) and Porous Asphalt-Membrane (M2/P-asphalt). Each membrane layer has two types of interfaces due to connection with different surrounding materials, see Figure 4.1

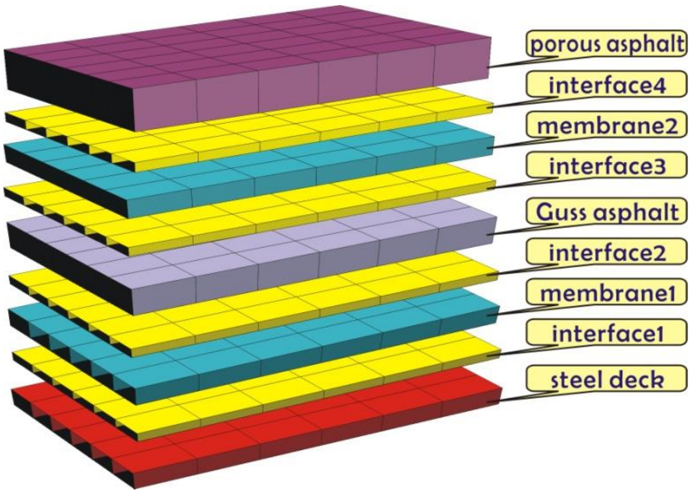

Figure 4.1 Surfacing system layers considering the interfaces

The membrane has been tested with MAT device in order to evaluate the adhesive bonding strength at different substrates under monotonic load until failure. The effect of temperature on membrane bonding strength is also investigated.

The number of specimens is shown in Table 4.1 as below.

Table 4.1 List of MAT testing specimen

Types of membranes	Temperature (^oC)	A		B	C		D	E
		A1	A2	B	C1	C2	D	E
		4mm	4.8mm	5mm	2.4mm	4.7mm	3mm	3mm
Steel/M1	-5	2		2	2	2	2	2
	5	2		2	2	2	2	2
	10	2		2	2	2	2	2
M1/G-asphalt	-5	2		2	2	2	2	2
	5	2		2	2	2	2	2
	10	2		2	2	2	2	2
G-asphalt/M2	-5		2	2		2	2	
	5		2	2		2	2	
	10		2	2		2	2	
M2/P-asphalt	-5		2	2		2	2	
	5		2	2		2	2	
	10		2	2		2	2	

From Table 4.1, it can be seen that, for each interface, six tests have been conducted under three temperature ranges (-5^{o}C, 50^{o}Cand 10^{o}C). Two tests are performed at each temperature range. The second test of each temperature has been conducted for repeatability reasons and in order to prove that the first test results match with the second. In some cases where the first two test results showed great differences additional test will be conducted.

4.3 Experimental results of each membrane under different conditions

4.3.1 Membrane products from Company A

Company A provided two membrane products for MAT tests, which are called membrane A1 and A2. Membrane A1 is used only for the bottom membrane layer in bridge. The membrane A1 specimen adhered to steel deck and Guss Asphalt (GA) are denoted as Steel/A1, and A1/G-asphalt, respectively.

Membrane A2 is used as the top membrane layer in bridge. Membrane A2 specimen adhered to Guss Asphalt (GA) is denoted as G-asphalt/A2; and the membrane A2 specimen connected Porous Asphalt (PA) is called A2/P-asphalt.

The thickness dimension of each membrane type is shown in Table 4.2.

Table 4.2 Dimension for membranes from Company A

Membrane type	Membrane thickness
Steel/A1	4mm
A1/G-asphalt	4mm
G-asphalt/A2	4.8mm
A2/P-asphalt	4.8mm

4.3.1.1 Experimental results for Steel/A1

Figure 4.2 shows the strain energy release rate of Steel/A1 interface at different temperatures. The debonding length versus time relationship of Steel/A1 interface at different temperatures can be seen in Figure 4.3. The Force-Height relationship is shown in Figure 4.4.

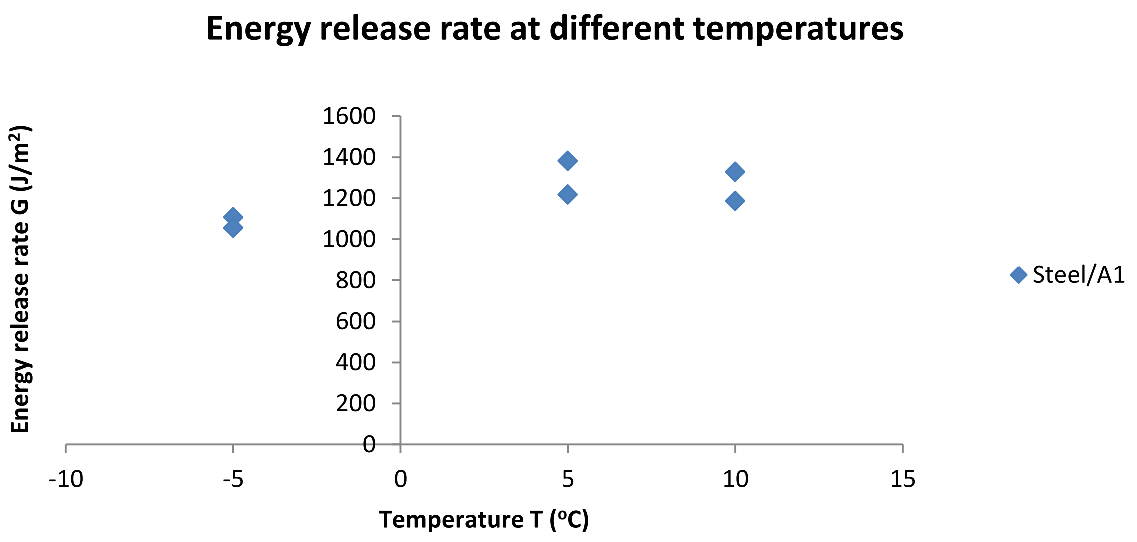

Figure 4.2 Energy release rate of Steel/A1 at different temperatures

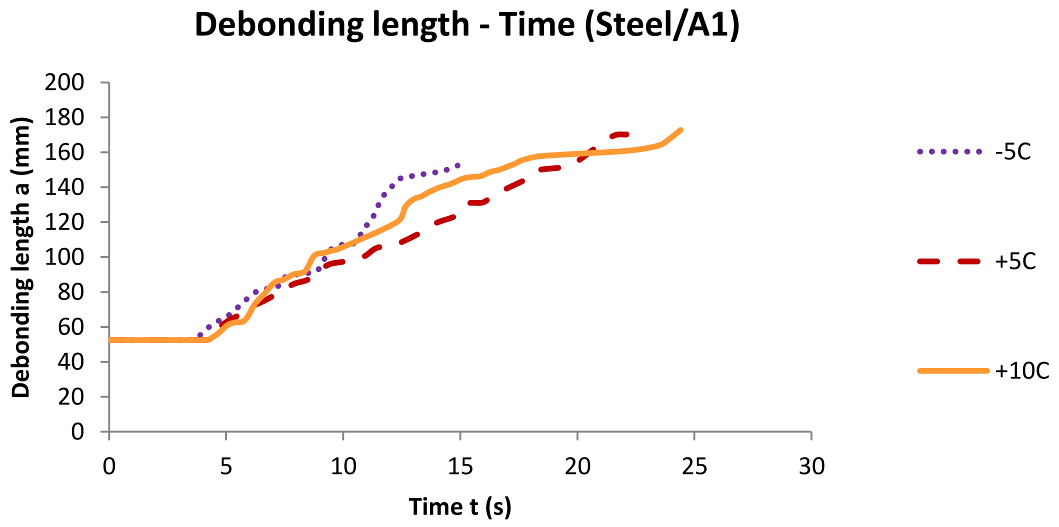

Figure 4.3 Debonding length versus time of Steel/A1 at different temperatures

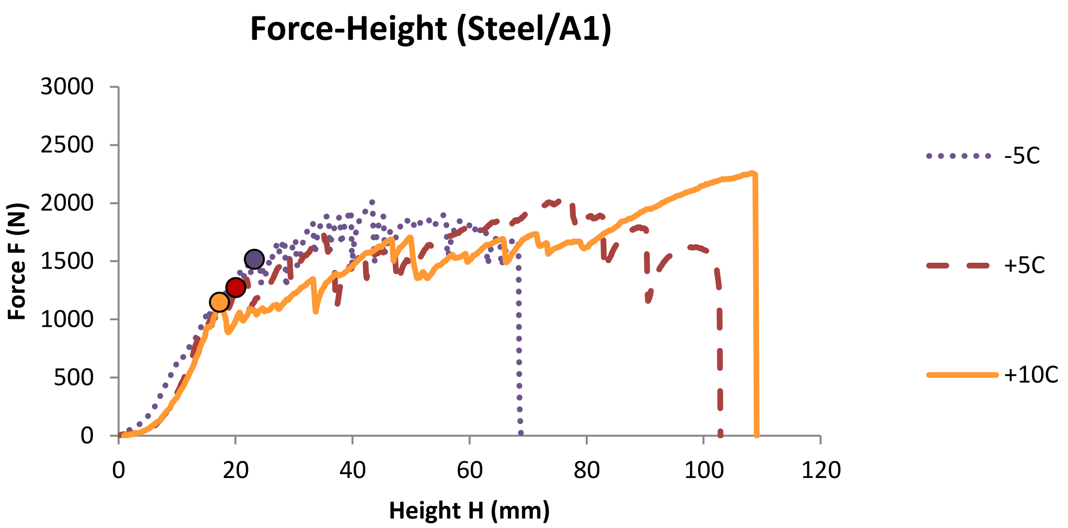

Figure 4.4 Force-Height relationship of Steel/A1 at different temperatures

From Figure 4.2, it can observed that the temperature can affect the strain energy release rate at the membrane interface, and at lower temperature (-5^{o}C), the strain energy release rate of the Steel/A1 membrane interface is the lowest. But above zero degree, the influence of the test temperature is not significant.

Figure 4.3 shows that the membrane debonding length develops similarly at three temperatures. In Figure 4.4, the color points show the moment of the corresponding membrane debonding initiation. The purple, red and golden points correspond to the moments at temperature -5^{o}C, +5^{o}C and +10^{o}C, respectively. It can be observed that, the debonding force at temperature +5^{o}C is the lowest, while that at temperature -5^{o}C is the highest.

4.3.1.2 Experimental results for A1/G-asphalt

Figure 4.5 shows the energy release rate of A1/G-asphalt interface at different temperatures. The debonding length versus time relationship of A1/G-asphalt interface at different temperatures can be seen in Figure 4.6. The Force-Height relationship is shown in Figure 4.7.

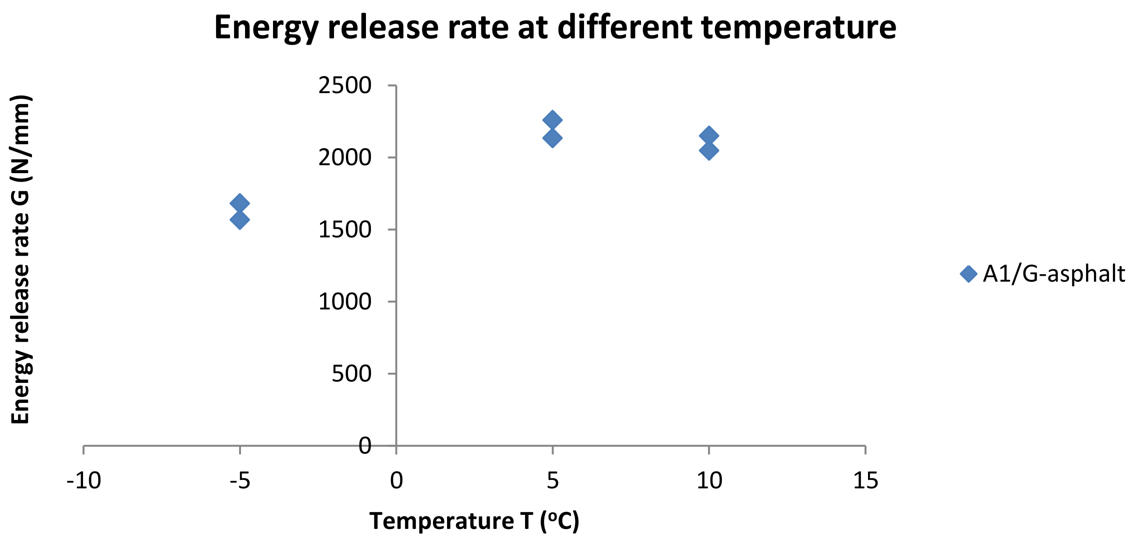

Figure 4.5 Energy release rate of A1/G-asphalt at different temperatures

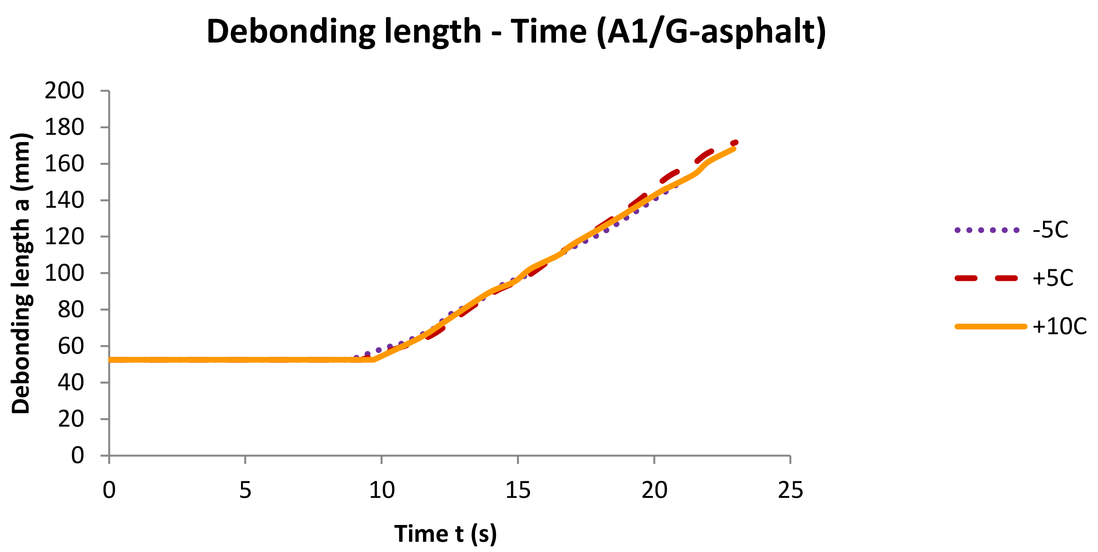

Figure 4.6 Debonding length versus time of A1/G-asphalt at different temperatures

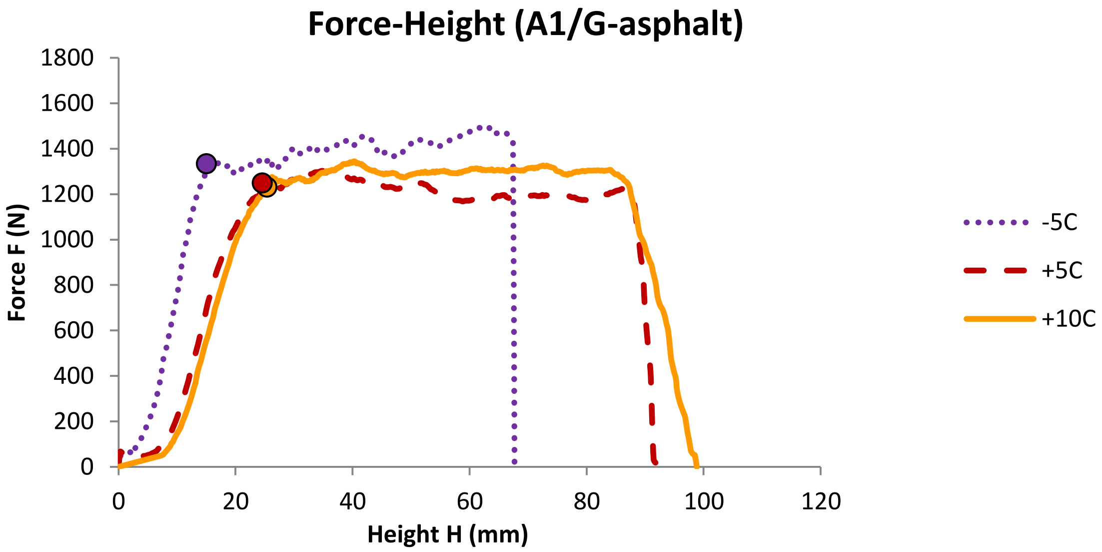

Figure 4.7 Force-Height relationship of A1/G-asphalt at different temperatures

From Figure 4.5, it can be seen that the temperature can affect indeed the starin energy release rate of the membrane interface and at temperature +5^{o}C, the G-value of the membrane interface is the highest, and at temperature -5^{o}C it is the lowest. But the difference between values at +5^{o}C and +10^{o}C is very small. Figure 4.6 shows that the membrane debonding length propagation at three temperatures are about the same.

The color points in Figure 4.7 show the moments of the corresponding membrane debonding initiation. It can be observed that, the debonding forces at three temperatures are about the same But the corresponding piston elevated height at -5^{o}C is lower than the other two.

4.3.1.3 Experimental results for G-asphalt/A2

Figure 4.8 shows the strain energy release rate of G-asphalt/A2 interface at different temperatures. The debonding length versus time relationship of G-asphalt/A2 interface at different temperatures can be seen in Figure 4.9. The Force-Height relationship is shown as Figure 4.10.

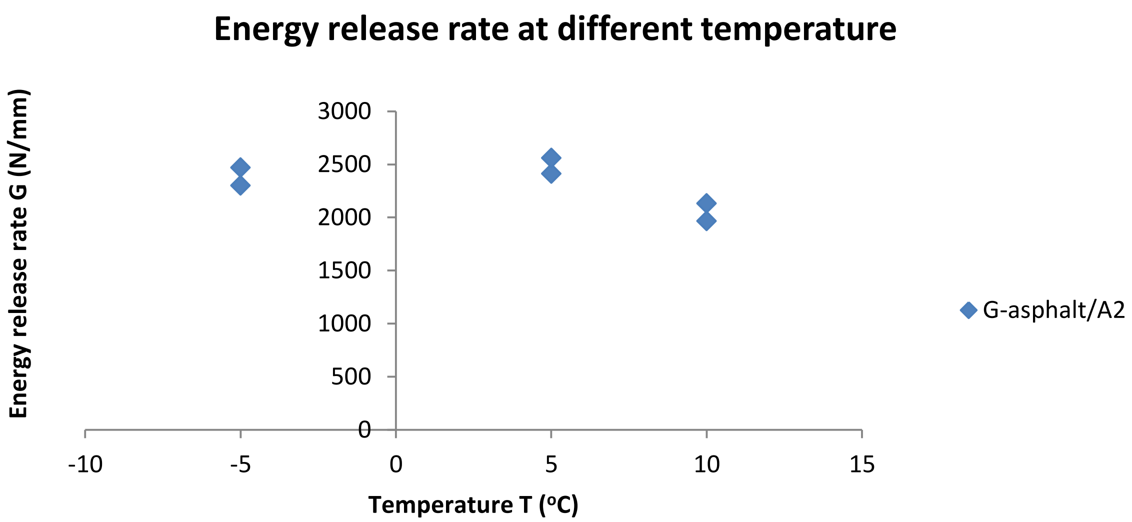

Figure 4.8 Energy release rate of G-asphalt/A2 at different temperatures

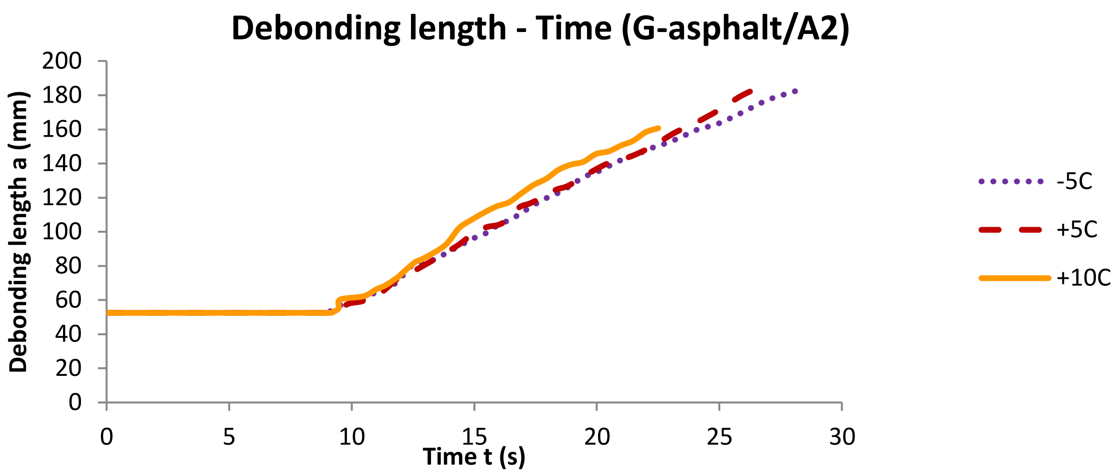

Figure 4.9 Debonding length versus time of G-asphalt/A2 at different temperatures

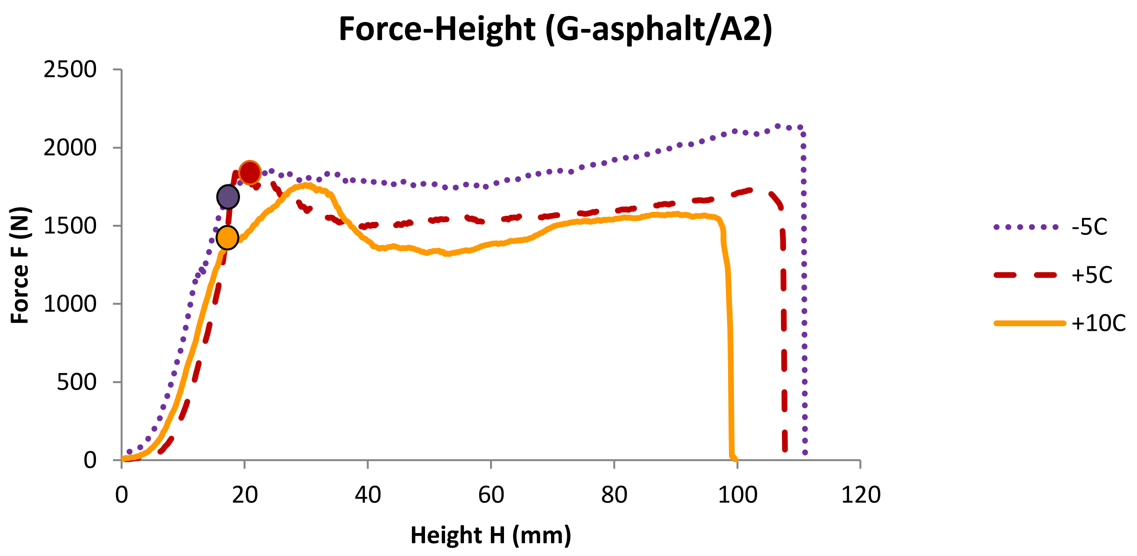

Figure 4.10 Force-Height relationship of G-asphalt/A2 at different temperatures

From Figure 4.8, it can be observed that the temperature can affect the strain energy release rate of this membrane interface and at temperature +5^{o}C, the G-value of the membrane interface is the highest, and at the lower temperature (-5^{o}C) the effect can be ignored. With the increase of temperature, the strain energy release rate of this membrane interface at +10^{o}C becomes lower.

Figure 4.9 shows the membrane debonding length propagation at three temperatures. It can be observed that the membrane debonding length propagation at +10^{o}C is faster than other two cases.

From the force and height relationship in Figure 4.10, it can be seen that, when membrane debonding initiates, values of piston elevated height at three different temperatures are almost the same. But the membrane debonding force at +10^{o}C is lower than that at +5^{o}C and -5^{o}C, which causes the lowest G-value in Figure 4.8. Meanwhile, the membrane debonding force at +5^{o}C is a little greater than that at temperature -5^{o}C.

4.3.1.4 Experimental results for A2/P-asphalt

The following figures show the experimental results of A2/P-asphalt interface. Figure 4.11 shows the strain energy release rate of A2/P-asphalt interface at different temperatures. The debonding length versus time relationship of A2/P-asphalt interface at different temperatures can be seen in Figure 4.12. The Force-Height relationship is shown in Figure 4.13.

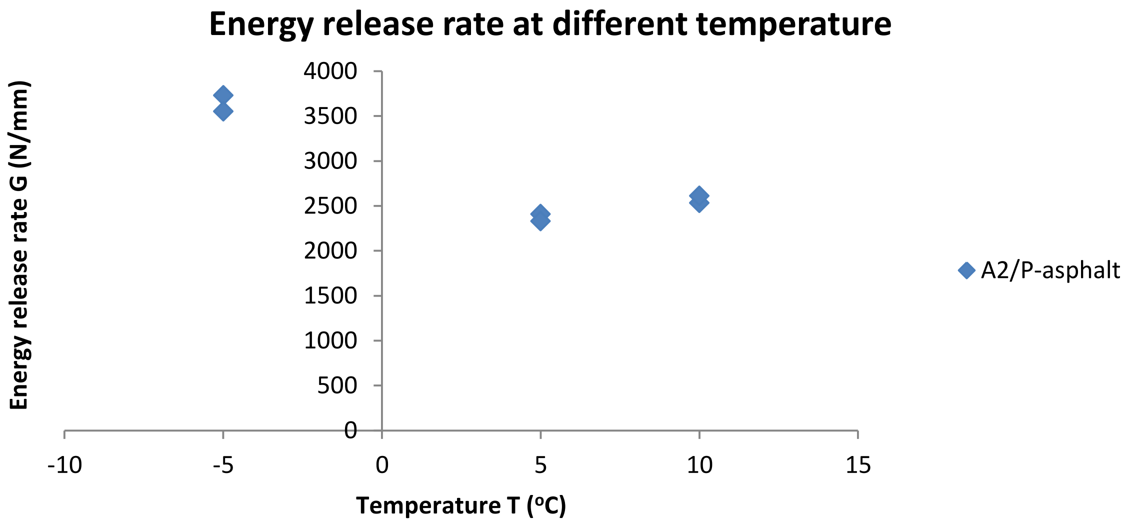

Figure 4.11 Energy release rat of A2/P-asphalt at different temperatures

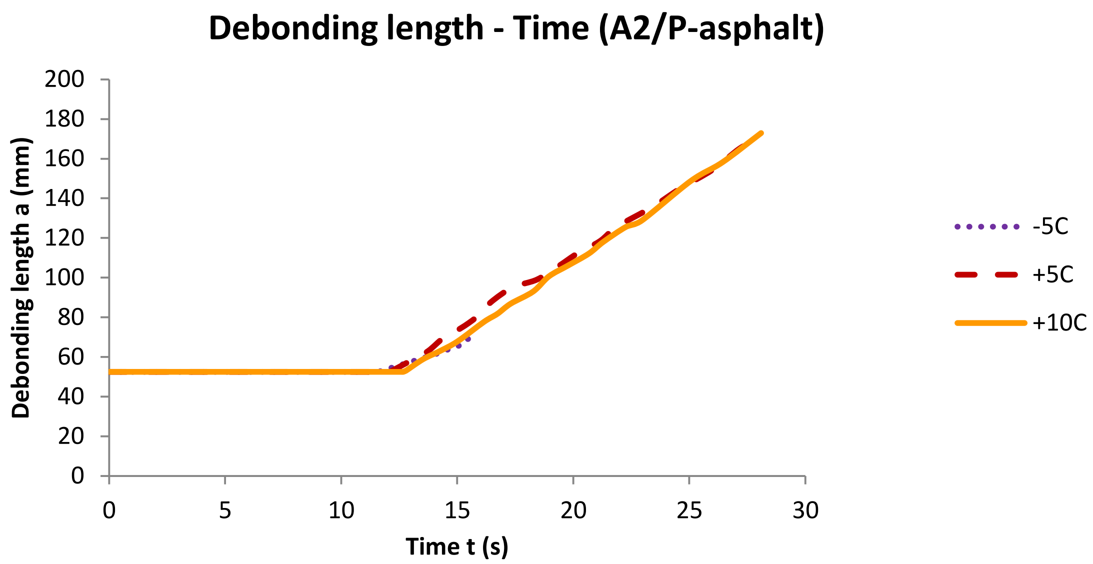

Figure 4.12 Debonding length versus time of A2/P-asphalt at different temperatures

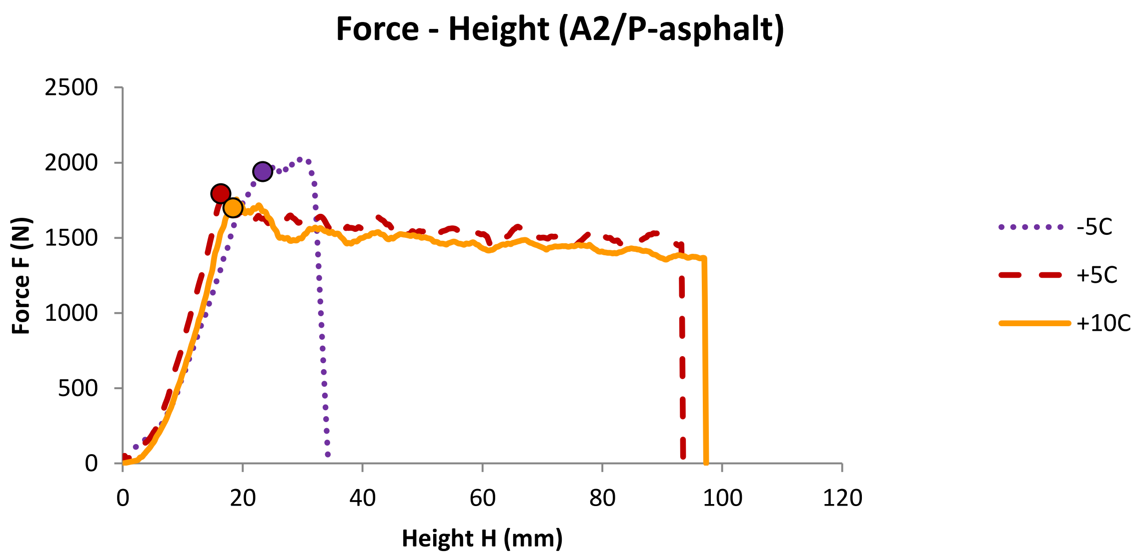

Figure 4.13 Force-Height relationship of A2/P-asphalt at different temperatures

From Figure 4.11, it can be observed that the temperature can affect the strain energy release rate of this membrane interface. At temperature -5^{o}C, the G-value of the membrane interface is the highest, but the difference between +5^{o}C and +10^{o}C is small. By considering the influence above zero degree, the temperature changes will not affect significantly.

Figure 4.12 shows that the membrane debonding length propagation at three temperatures are about the same.

From the force and height relationship in Figure 4.13, it can be seen that the values of force and the piston elevated height at temperature -5^{o}C are higher than those at +5^{o}C and +10^{o}C. Between temperature at +5^{o}C and +10^{o}C, the differences are small.

4.3.2 Membrane products from Company B

Company B provides only one membrane for the MAT test. The bottom membrane connected to steel deck is defined as Steel/B; the bottom membrane adhered to Guss Asphalt (GA) is denoted as B/G-asphalt; the top membrane adhered to GA is denoted as G-asphalt/B; and the top membrane connected Porous Asphalt (PA) is defined as B/P-asphalt.

The thickness of membrane in different samples is listed in Table 4.3.

Table 4.3 Dimension for membrane of Company B

Membrane type	Membrane thickness
Steel/B	5mm
B/G-asphalt	5mm
G-asphalt/B	5mm
B/P-asphalt	5mm

4.3.2.1 *Experimental results for Steel/B*

The following figures show the experimental results of Steel/B interface in MAT test. In Figure 4.14 it shows the strain energy release rate of Steel/B interface at different temperatures. The debonding length versus time relationship of Steel/B interface at different temperatures can be seen in Figure 4.15. The Force-Height relationship is shown in Figure 4.16.

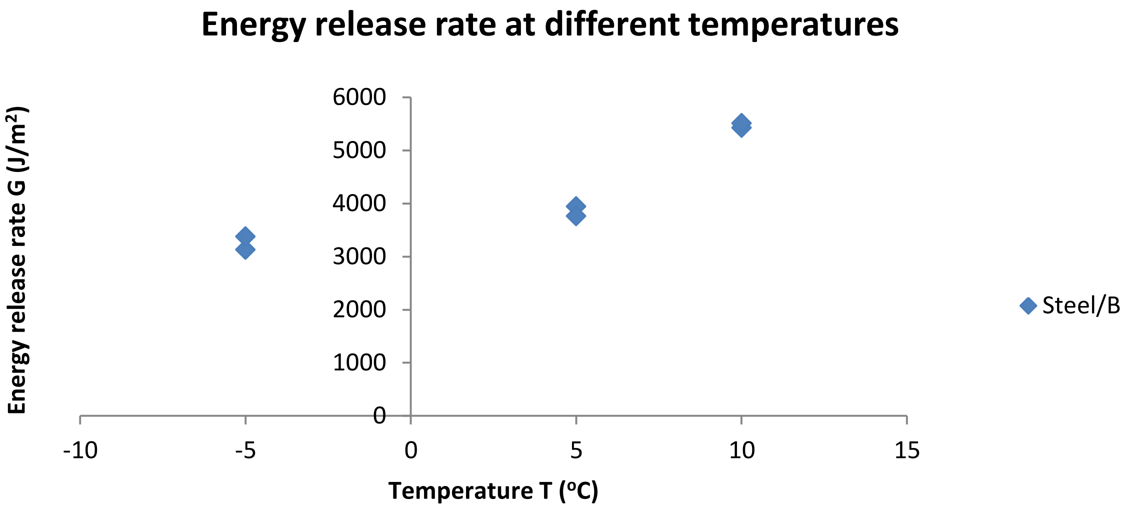

Figure 4.14 Energy release rate of Steel/B at different temperatures

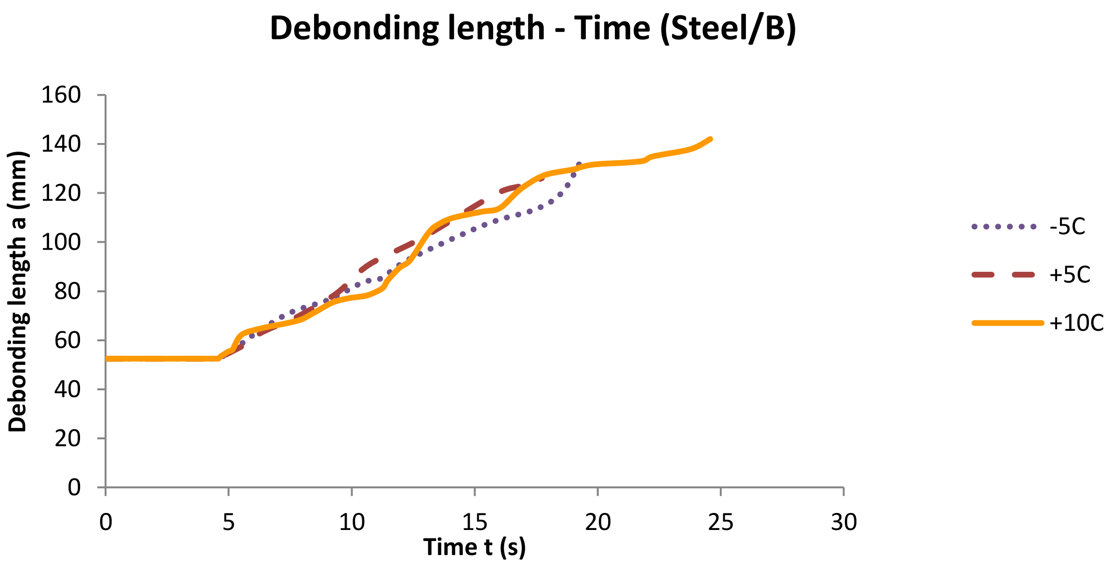

Figure 4.15 Debonding length versus time of Steel/B at different temperatures

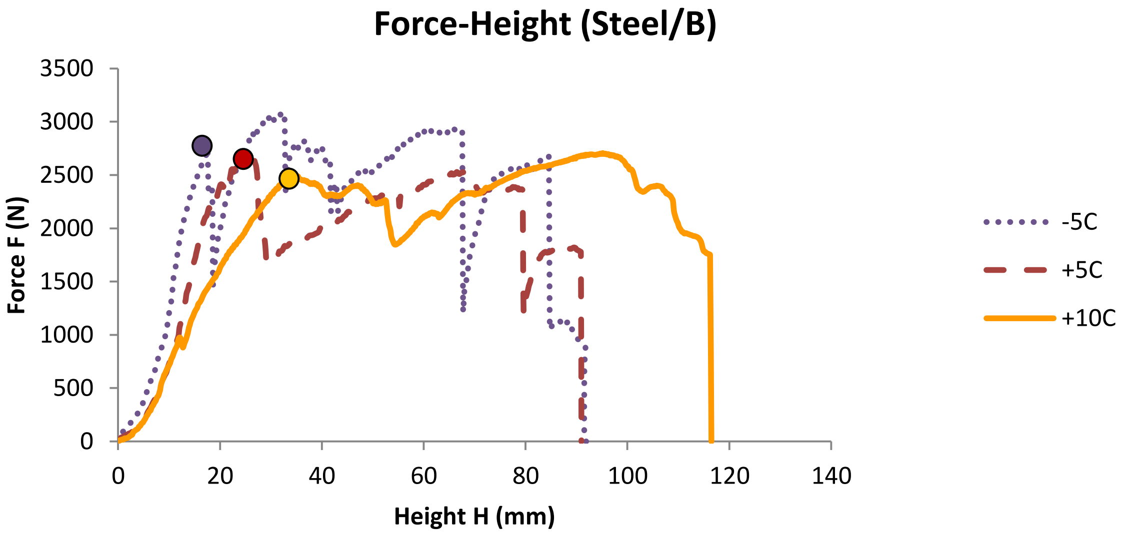

Figure 4.16 Force-Height relationship of Steel/B at different temperatures

It can be seen in Figure 4.14, that the temperature can affect the strain energy release rate of the membrane interface. With the increase of temperature, the strain energy release rate is increased. At temperature +10^{o}C, the G-values of this membrane interface is the higher than other two cases.

Figure 4.15 shows that the membrane debonding length propagation at three temperatures are about the same.

From Figure 4.16, force and height relationship helps us to explain the differences of the strain energy release rate in Figure 4.14. By comparison of these three cases, the forces when debonding are almost the same value, but the piston elevated height are different. At -5^{o}C, the height value is smaller than that at +5^{o}C, and value at +5^{o}C is also smaller than value at +10^{o}C. It means at temperature +10^{o}C, higher total energy is needed to debond the membrane from the substrate.

4.3.2.2 Experimental results for B/G-asphalt (bottom membrane)

The following figures show the experimental results of B/G-asphalt interface in MAT test. Figure 4.17 shows the strain energy release rate of B/G-asphalt interface at different temperatures. The debonding length versus time relationship of B/G-asphalt interface at different temperatures can be seen in Figure 4.18. The Force-Height relationship is shown as Figure 4.19.

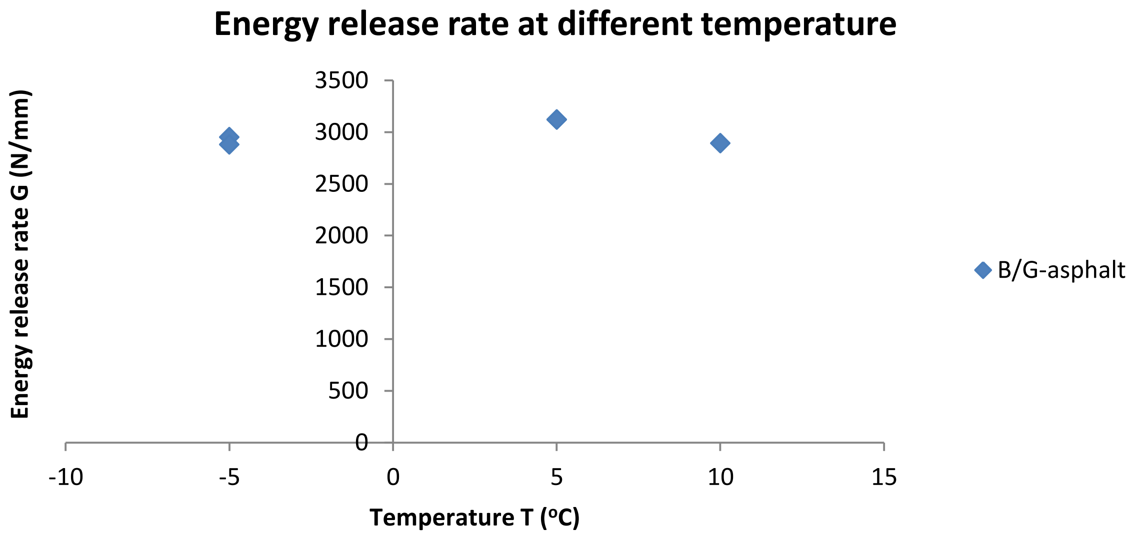

Figure 4.17 Energy release rate of B/G-asphalt at different temperatures

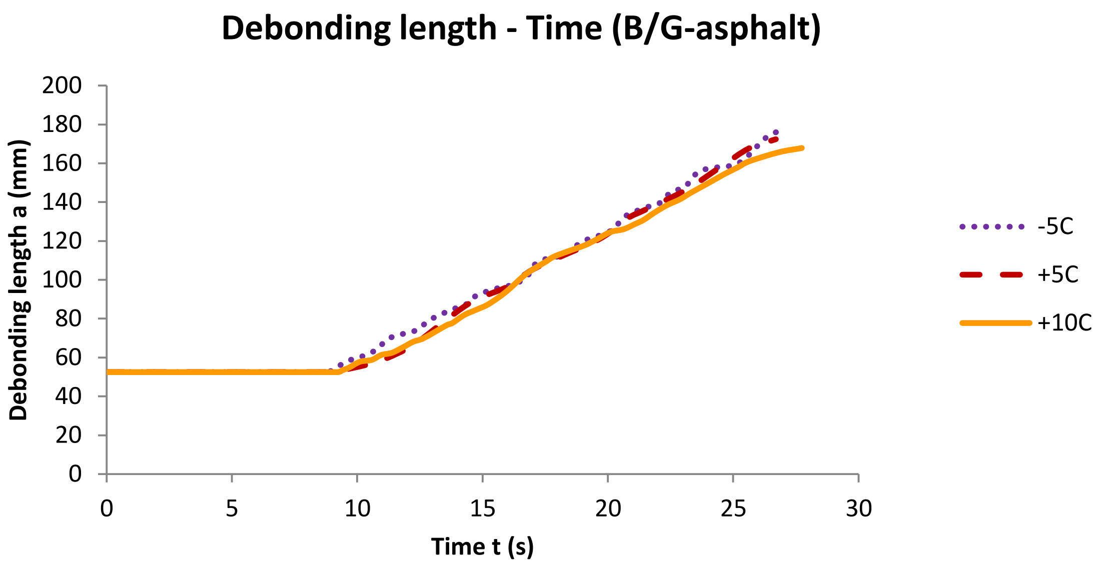

Figure 4.18 Debonding length versus time of B/G-asphalt at different temperatures

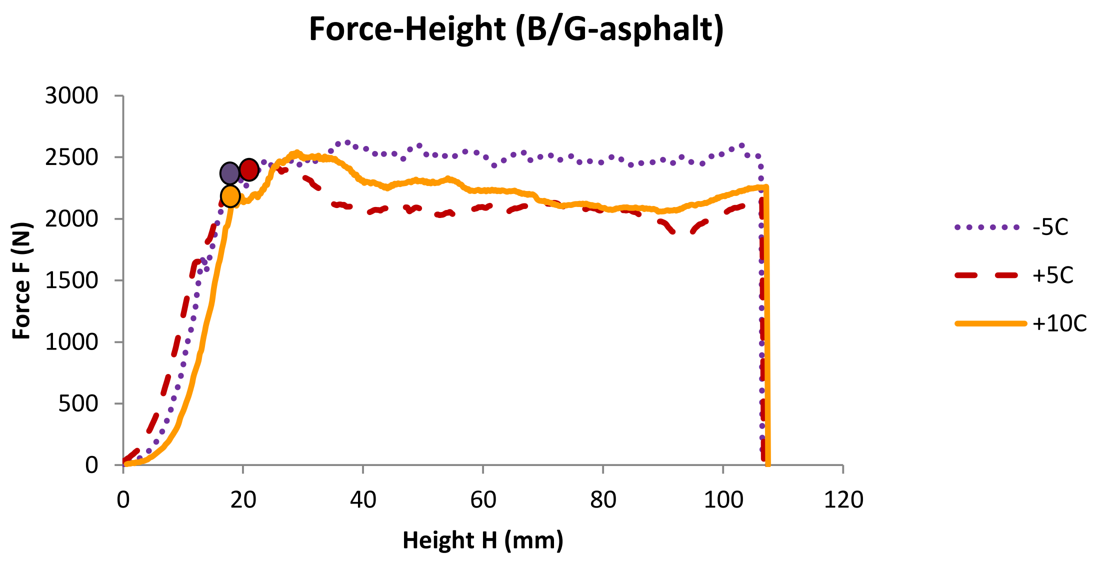

Figure 4.19 Force-Height relationship of B/G-asphalt at different temperatures

It can be seen from Figure 4.17, that the temperature influence on the strain energy release rate of this interface is not significant. Figure 4.18 shows that the membrane debonding length propagation at three temperatures are about the same.

Also from Figure 4.19, force and piston elevated height when debonding at different temperatures have the similar values. Therefore, the temperature influence can be negligible for this membrane interface.

4.3.2.3 Experimental results for G-asphalt/B (top membrane)

The following figures show the experimental results of G-asphalt/B interface in MAT test. In Figure 4.20 it shows the strain energy release rate of G-asphalt/B interface at different temperatures. The debonding length versus time relationship of G-asphalt/B interface at different temperatures can be seen in Figure 4.21. The Force-Height relationship is shown as Figure 4.22.

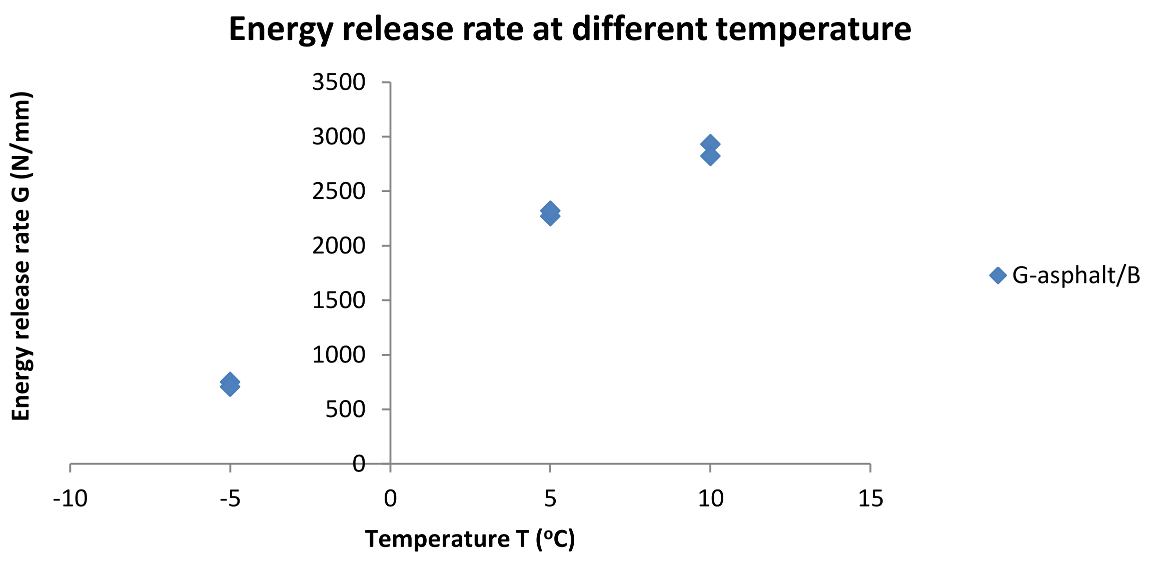

Figure 4.20 Energy release rate of G-asphalt/B at different temperatures

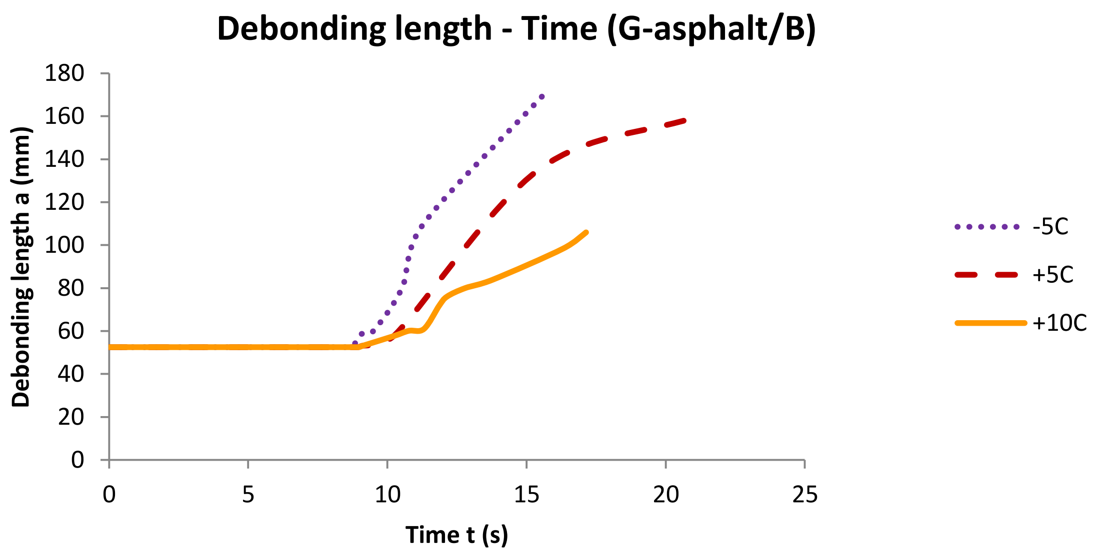

Figure 4.21 Debonding length versus time of G-asphalt/B at different temperatures

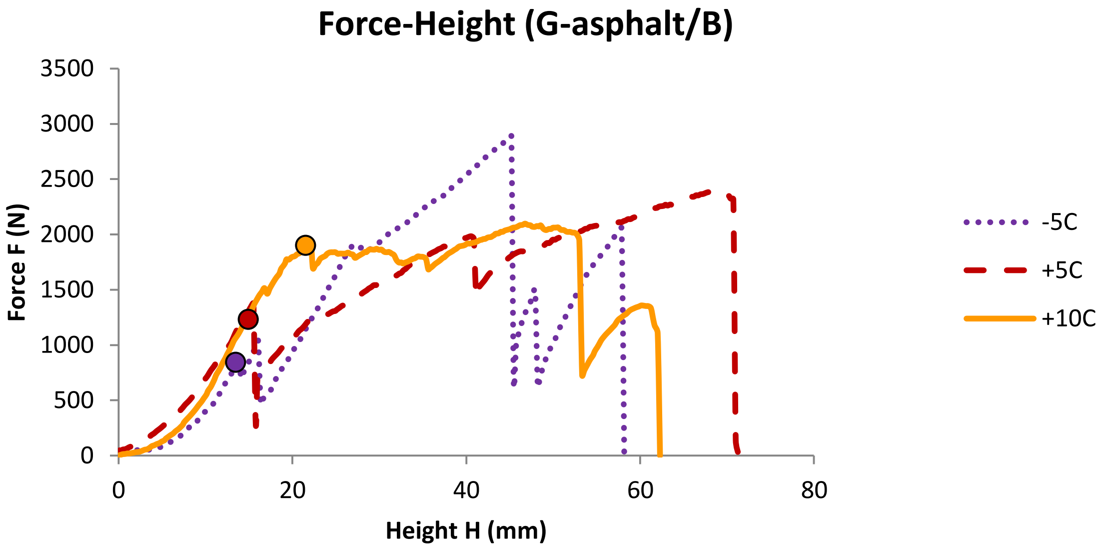

Figure 4.22 Force-Height relationship of G-asphalt/B at different temperatures

As it can be seen in Figure 4.20, there is a clear trend of the results with the strain energy release rate and temperature. With the increase of temperature, the strain energy release rate increases. The temperature influence is significant for this type interface. The highest value of strain energy release rate occurs at temperature +10°C. Meanwhile, in Figure 4.21, the membrane debonding length propagation at temperature -5°C is faster than that at another two higher temperatures. The lower rate of membrane debonding length propagation occurs at temperature +10°C.

From Figure 4.22, it is clear to see that the force when debonding is greatest at temperature +10°C. By comparing the piston elevated height values at -5°C and +5°C, it can be found the height values are nearly the same, but force at +5°C is larger than that at -5°C, which means the strain energy release rate at temperature -5°C is the lowest one.

4.3.2.4 Experimental results for B/P-asphalt

The following figures show the experimental results of B/P-asphalt interface in MAT test. In Figure 4.23 it shows the energy release rate of B/P-asphalt interface at different temperatures. The debonding length versus time relationship of B/P-asphalt interface at different temperatures can be seen in Figure 4.24. The Force-Height relationship is shown in Figure 4.25.

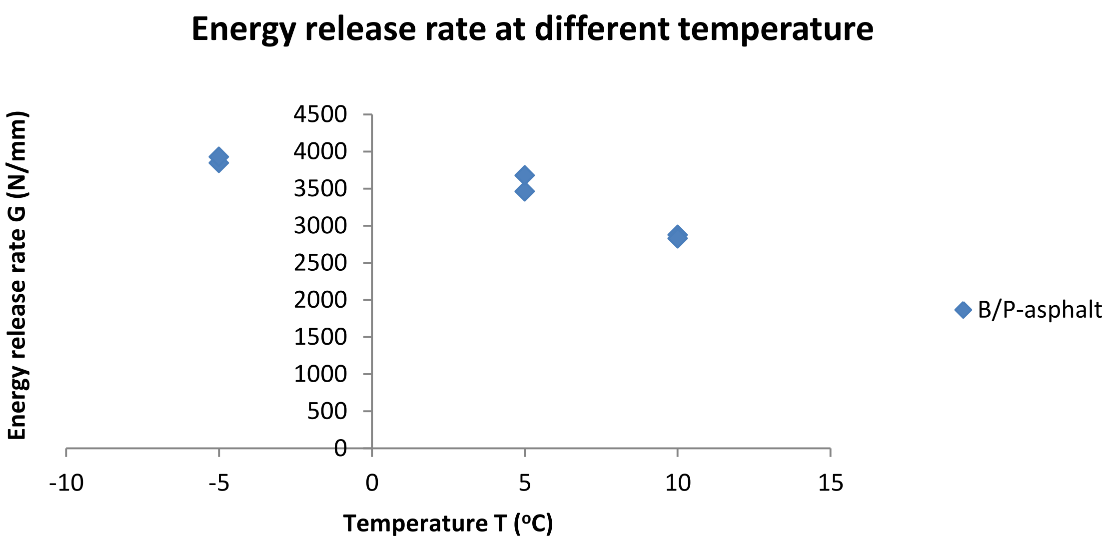

Figure 4.23 Energy release rate of B/P-asphalt at different temperatures

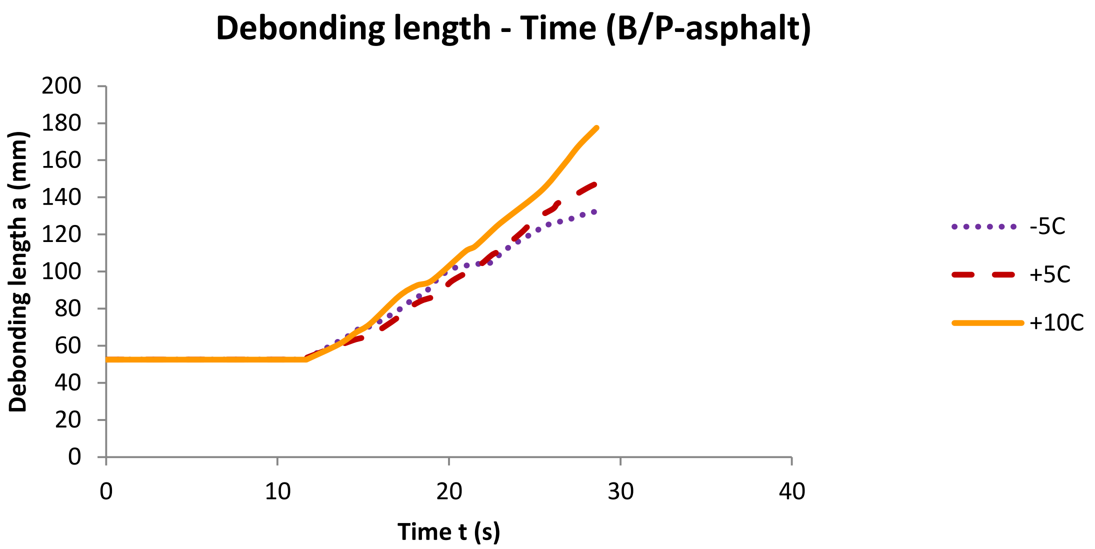

Figure 4.24 Debonding length versus time of B/P-asphalt at different temperatures

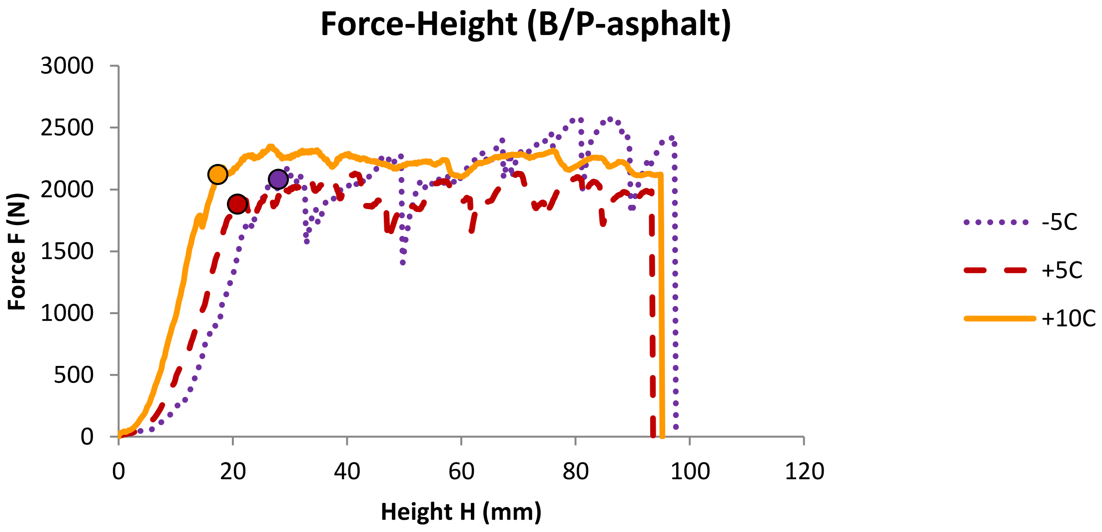

Figure 4.25 Force-Height relationship of B/P-asphalt at different temperatures

The temperature influence can be seen in Figure 4.23. With the increase of temperature, the strain energy release rate of this interface decreases. At temperature -5^{o}C, the strain energy release rate of this interface is the highest. From Figure 4.24, it can be found that the debonding rate at temperature +10^{o}C is the largest.

From the force and height relationship in Figure 4.25, it can be seen that the debonding force at temperature +10^{o}C is the highest among the three cases, but the piston elevated height at temperature +10^{o}C is the lowest, which results the final strain energy release rate is the smallest.

4.3.3 Membrane products from Company C

Company C has provided two membrane products for MAT tests, which are called membrane C1 and C2. Membrane C1 is used only for the bottom membrane. Membrane C1 specimen adhered to steel deck and Guss Asphalt (GA) are denoted as Steel/C1, and C1/G-asphalt, respectively.

Membrane C2 can be used as both bottom and top membrane. The bottom membrane connected to steel deck is denoted as Steel/C2; the bottom membrane adhered to Guss Asphalt (GA) is denoted as C2/G-asphalt; the top membrane adhered to Guss Asphalt (GA) is denoted as G-asphalt/C2; and the top membrane connected Porous Asphalt (PA) is called C2/P-asphalt.The thickness of each membrane type is shown in Table 4.4.

Table 4.4 Dimension for membranes of Company C

Membrane type	Membrane thickness
Steel/C1	2.4mm
C1/G-asphalt	2.4mm
Steel/C2	4.7mm
C2/G-asphalt	4.7mm
G-asphalt/C2	4.7mm
C2/P-asphalt	4.7mm

4.3.3.1 Experimental results for Steel/C1

The following figures show the experimental results of Steel/C1 interface. In Figure 4.26 it shows the energy release rate of Steel/C1 interface at different temperatures. The debonding length versus time relationship of Steel/C1 interface at different temperatures can be seen in Figure 4.27. The Force-Height relationship is shown in Figure 4.28.

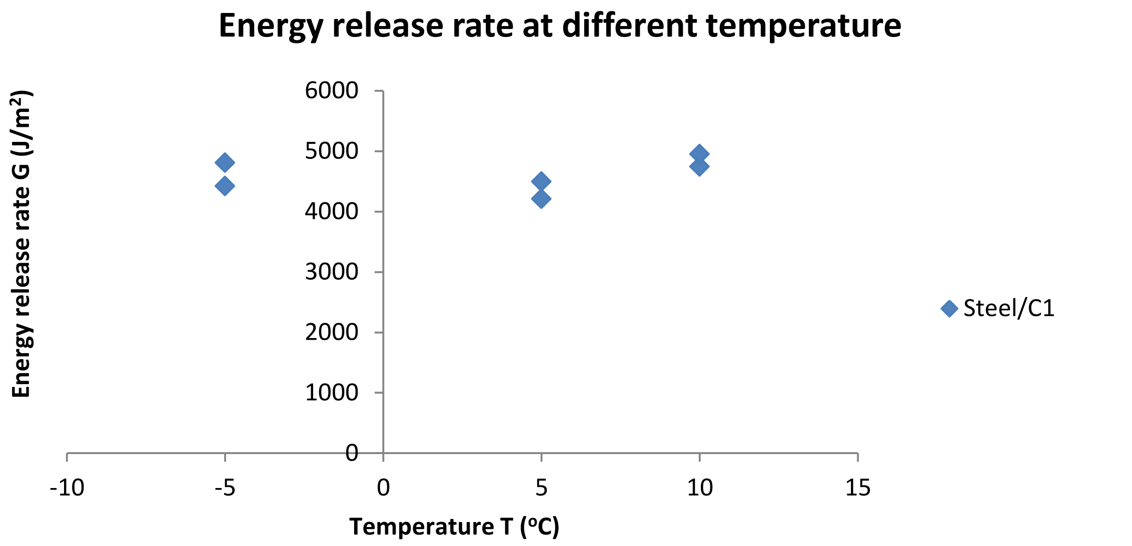

Figure 4.26 Energy release rate of Steel/C1 at different temperatures

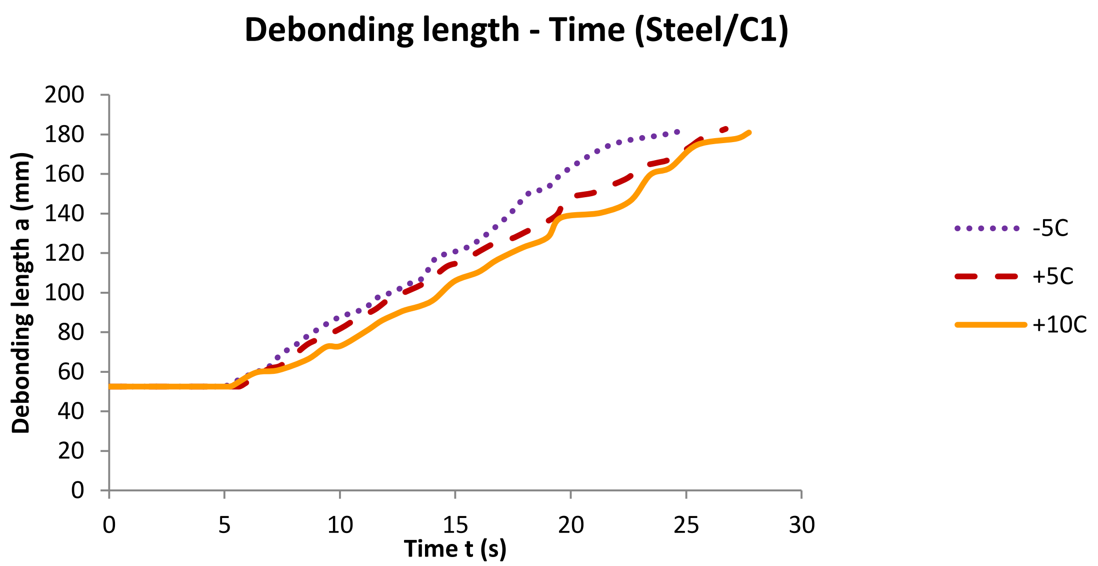

Figure 4.27 Debonding length versus time of Steel/C1 at different temperatures

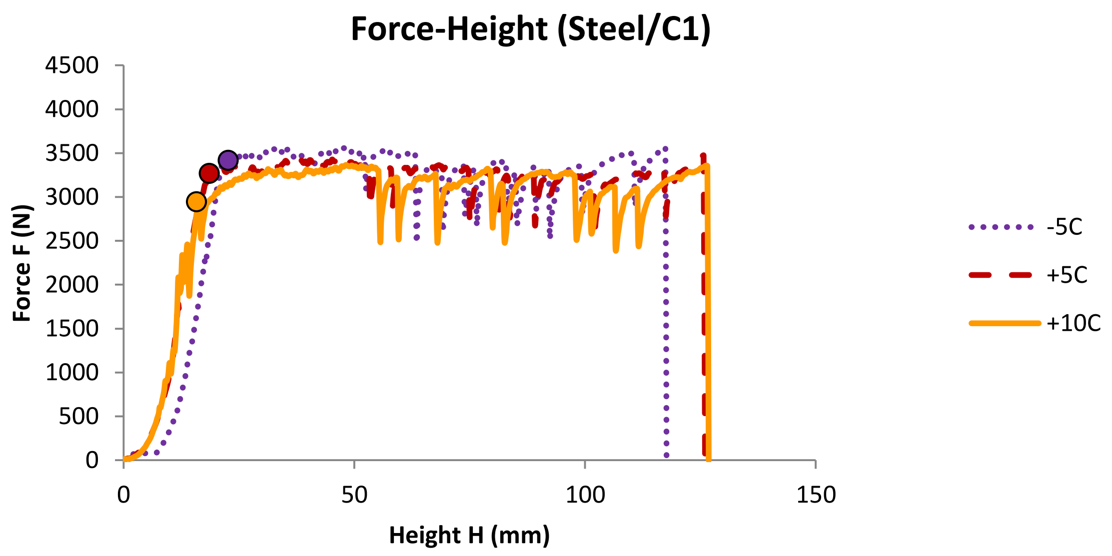

Figure 4.28 Force-Height relationship of Steel/C1 at different temperatures

Figure 4.26 shows the temperature influence on strain energy release rate of Steel/C1 interface is not significant. Figure 4.27 shows the rate of membrane debonding length propagation at lower temperature is higher than that at higher temperatures. When debonding the corresponding force and piston height relationship is showed in Figure 4.28. It can be seen that the values of force and height at different temperatures for three cases are almost the same, which makes the G-values changes little at three temperatures.

4.3.3.2 Experimental results for C1/G-asphalt (bottom membrane)

The following figures show the experimental results of C1/G-asphalt interface in MAT test. In Figure 4.29 it shows the starin energy release rate of C1/G-asphalt interface at different temperatures. The debonding length versus time relationship of C1/G-asphalt at different temperatures can be seen in Figure 4.30. The Force-Height relationship is shown in Figure 4.31.

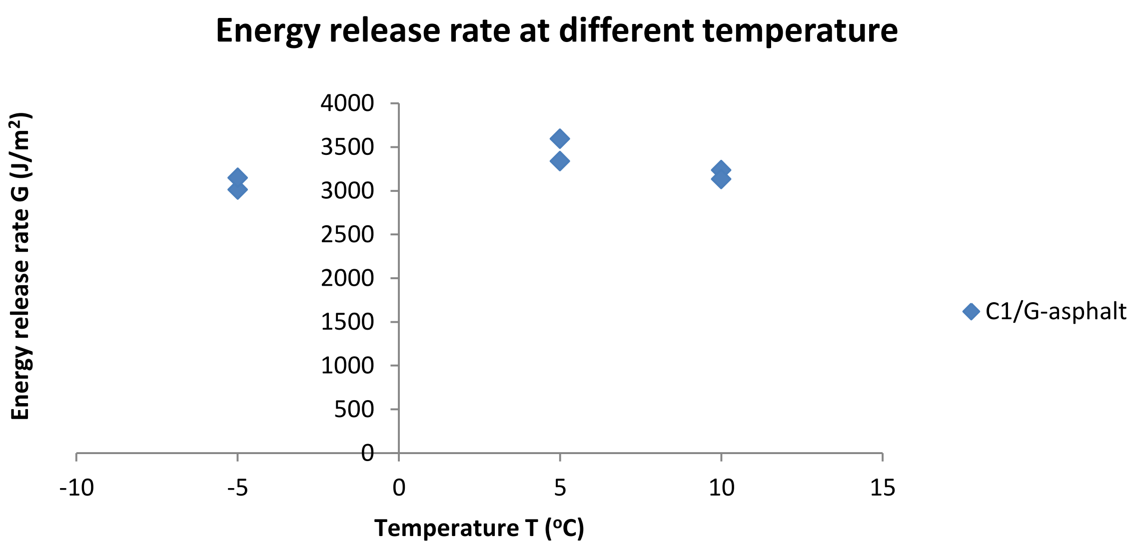

Figure 4.29 Energy release rate of C1/G-asphalt at different temperatures

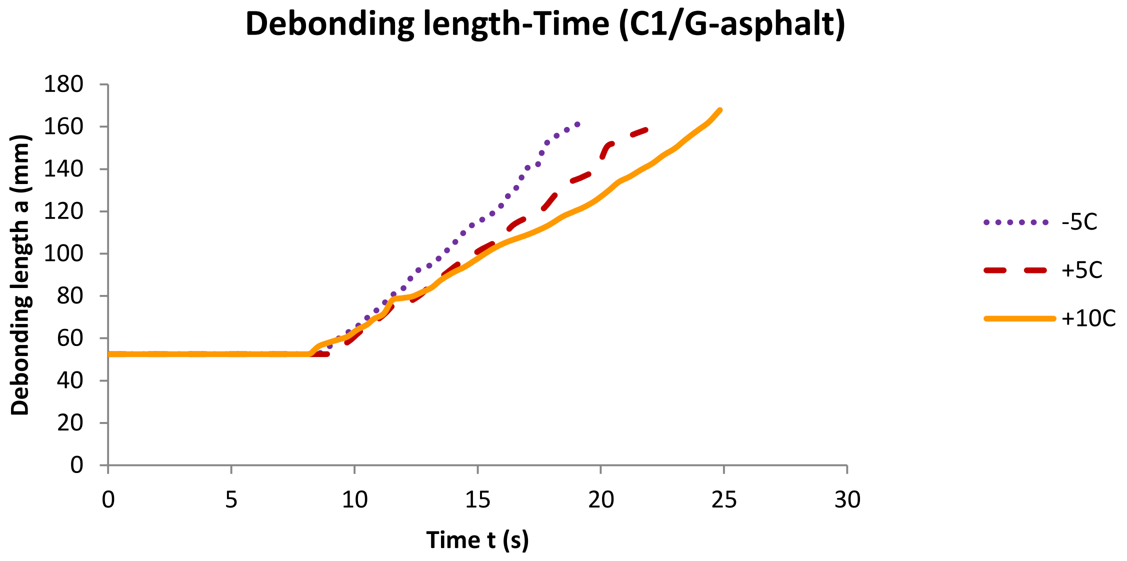

Figure 4.30 Debonding length versus time of C1/G-asphalt at different temperatures

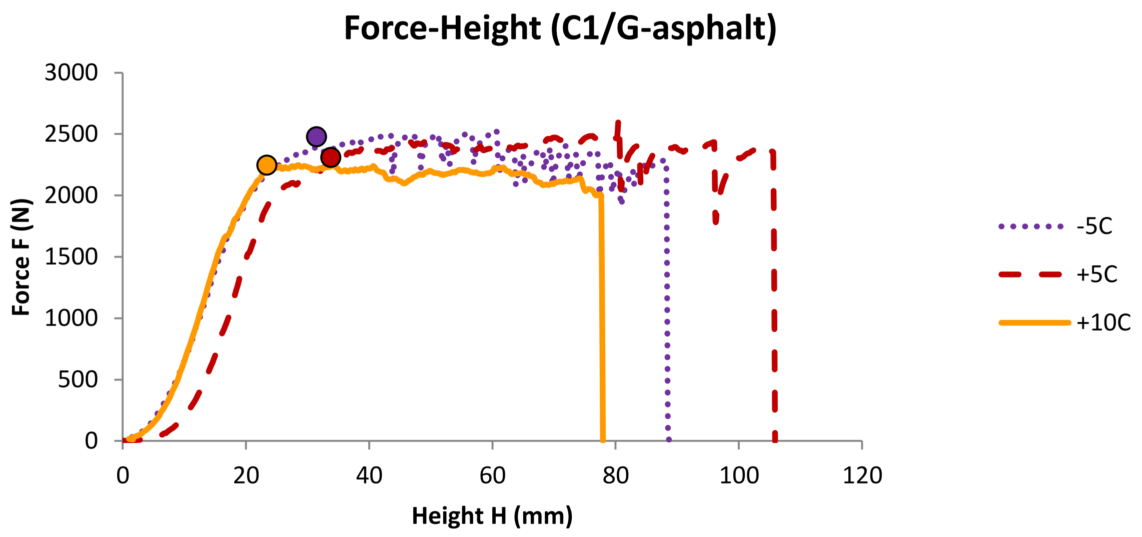

Figure 4.31 Forc-Height relationship of C1/G-asphalt at different temperatures

From Figure 4.29, it can be observed that the temperature has little effects on the strain energy release rate of this type of membrane interface.

Figure 4.30 shows the rate of the membrane debonding length propagates is faster when temperature decreases. Meanwhile, Figure 4.31 shows that the corresponding debonding forces are about the same at different temperatures but the piston elevated height at temperature +5°C is a little higher than the values at temperature -5°C and +10°C. Therefore, the G-value at +5°C is a little higher than the other two cases.

4.3.3.3 Experimental results for Steel/C2

The following figures show the experimental results of Steel/C2 interface in MAT test. In Figure 4.32 it shows the energy release rate of Steel/C2 interface at different temperatures. The debonding length versus time relationship of Steel/C2 interface at different temperatures can be seen in Figure 4.33. The Force-Height relationship is shown in Figure 4.34.

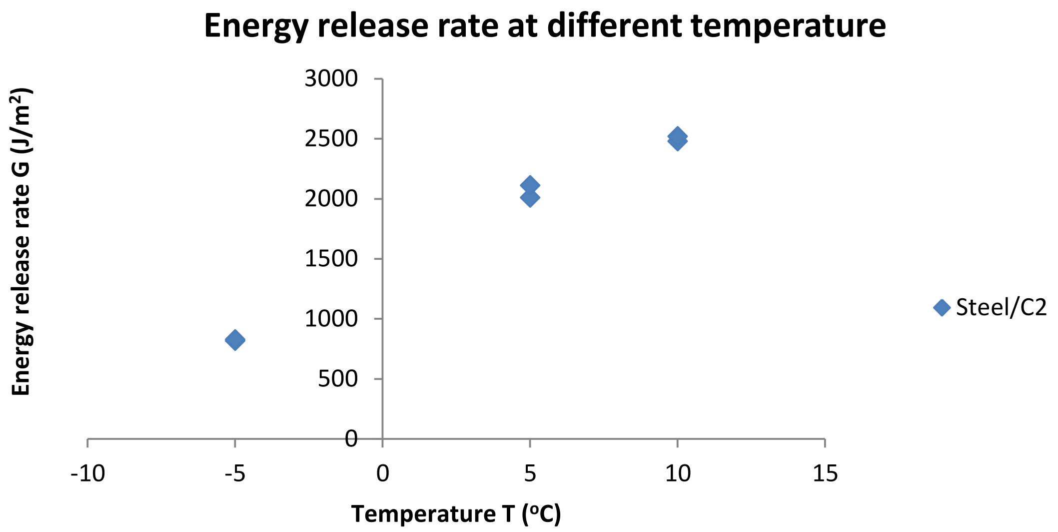

Figure 4.32 Energy release rate of Steel/C2 at different temperatures

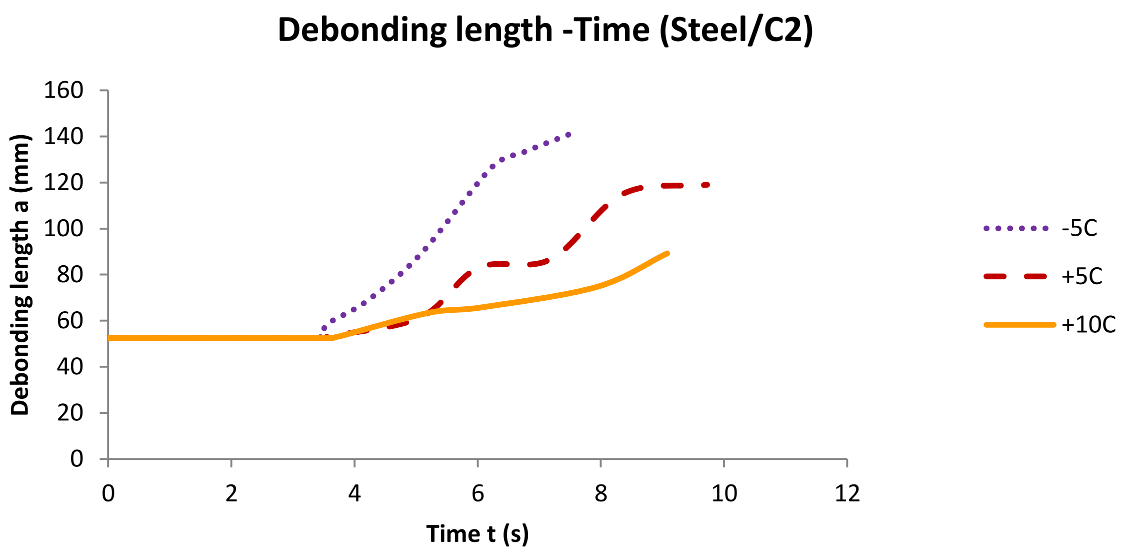

Figure 4.33 Debonding length versus time of Steel/C2 at different temperatures

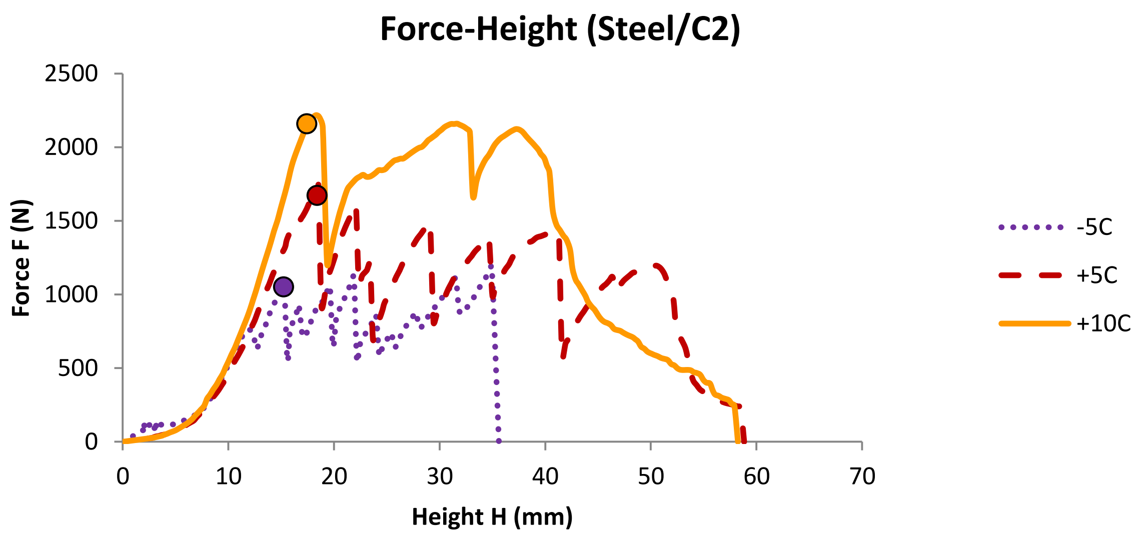

Figure 4.34 Force-Height relationship of Steel/C2 at different temperatures

It can be seen in Figure 4.32, there is a clear trend of the results with the strain energy release rate and temperature for this type interface. With the increase of temperature, the strain energy release rate increases. Apparently the temperature influence is significant for this type interface. The highest value of strain energy release rate of the interface occurs at temperature +10^{o}C. Meanwhile, in Figure 4.33, the rate of membrane debonding length propagation at temperature -5^{o}C is higher than that at another two higher temperatures. The lower rate of membrane debonding length propagation occurs at temperature +10^{o}C.

Figure 4.34 shows the corresponding piston elevated height when debonding at different temperatures are about the same, but the debonding force value at temperature +10^{o}C is the highest and lowest at -5^{o}C.

4.3.3.4 Experimental results for C2/G-asphalt (bottom membrane)

The following figures show the experimental results of C2/G-asphalt interface in MAT test. In Figure 4.35 it shows the energy release rate of C2/G-asphalt interface at different temperatures. The debonding length versus time relationship of C2/G-asphalt at different temperatures can be seen in Figure 4.36. The Force-Height relationship is shown in Figure 4.37.

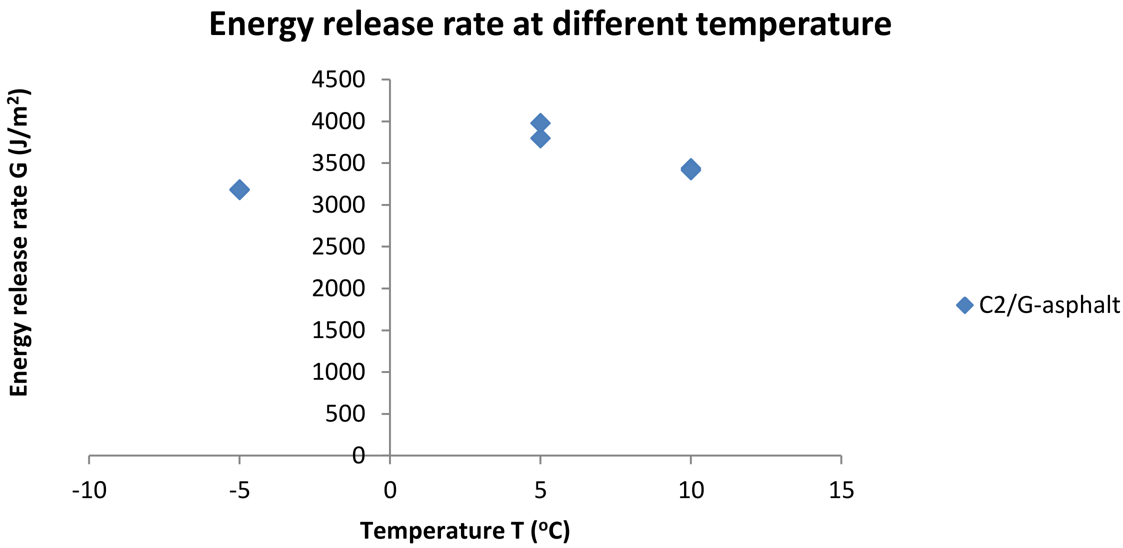

Figure 4.35 Energy release rate of C2/G-asphalt at different temperatures

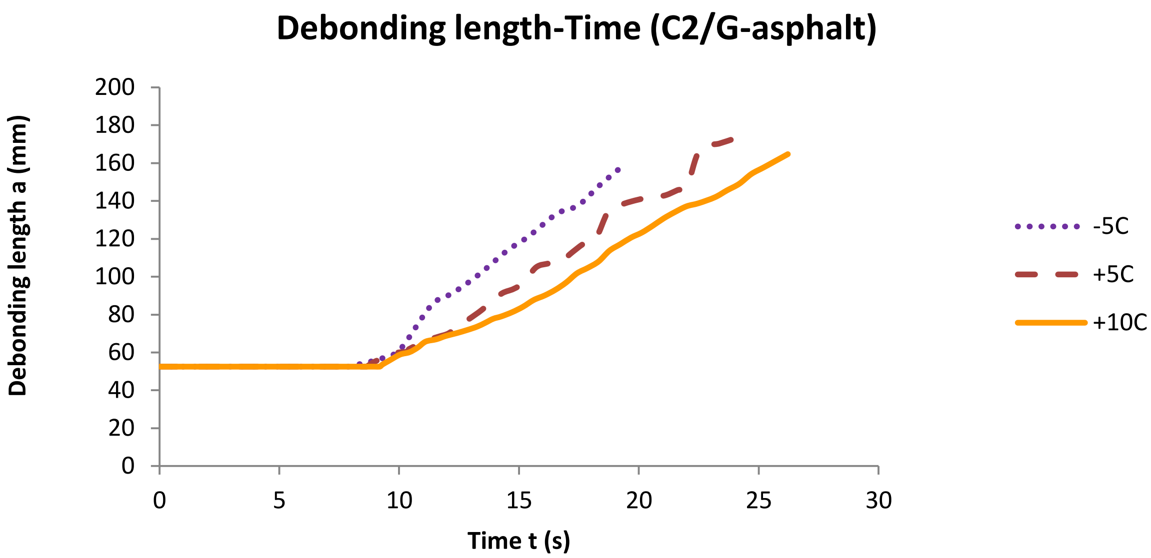

Figure 4.36 Debonding length versus time of C2/G-asphalt at different temperatures

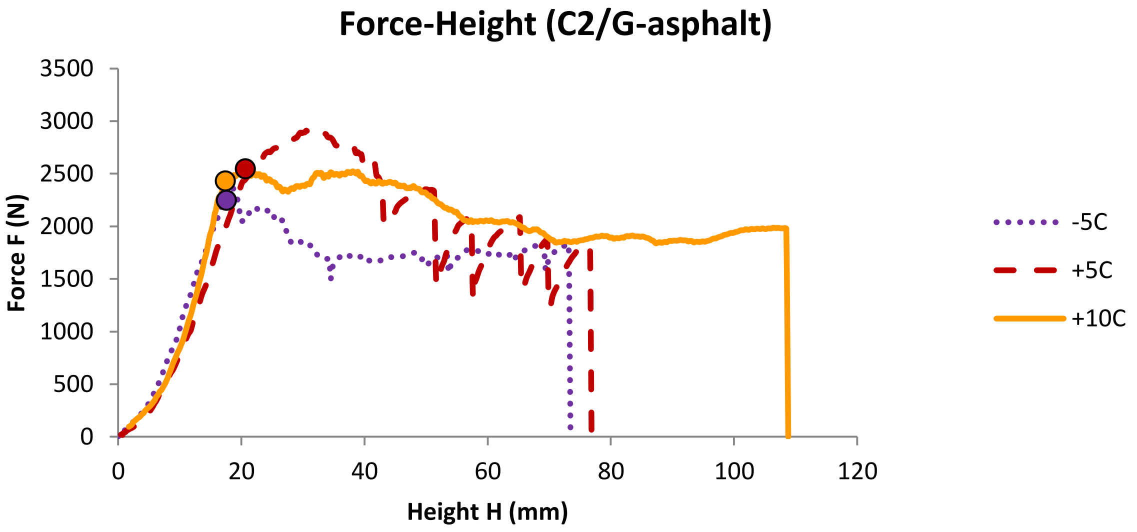

Figure 4.37 Force-Height relationship of C2/G-asphalt at different temperatures

From Figure 4.35, it can be observed that the temperature has little effects on the strain energy release rate of this type of membrane interface. The strain energy release rate at temperature above zero degree is a little higher than that at temperature -5°C.

Figure 4.36 shows the rate of the membrane debonding length propagates is faster at temperature -5°C. Meanwhile, Figure 4.37 shows that the corresponding debonding forces at temperature +5°C are the highest among these three cases.

4.3.3.5 Experimental results for G-asphalt/C2 (top membrane)

The following figures show the experimental results of G-asphalt/C2 interface in MAT test. In Figure 4.38 it shows the energy release rate of G-asphalt/C2 interface at different temperatures. The debonding length versus time relationship of G-asphalt/C2 interface at different temperatures can be seen in Figure 4.39. The Force-Height relationship is shown in Figure 4.40.

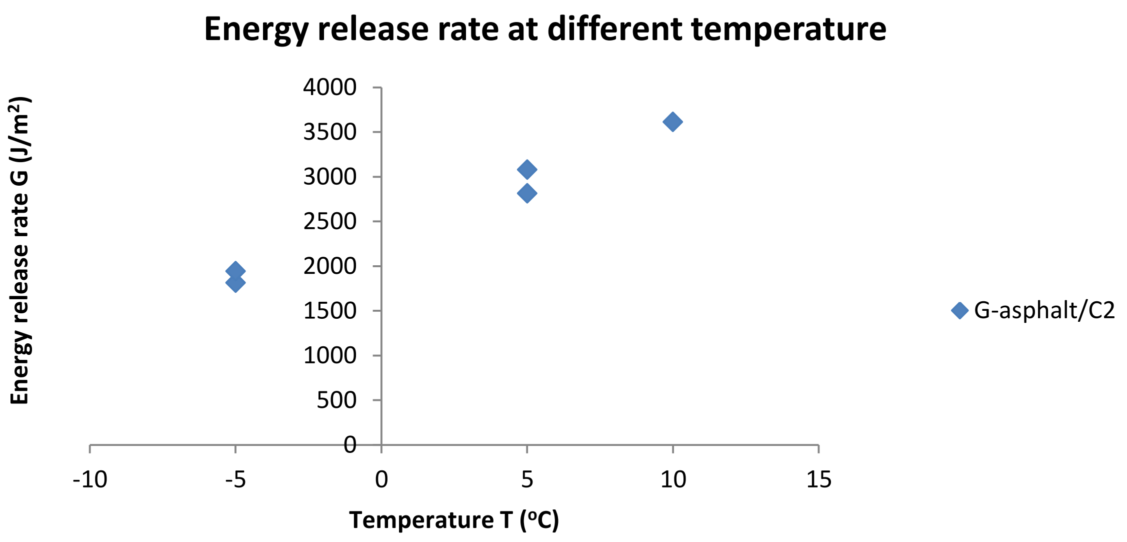

1. Figure 4.38 Energy release rate of G-asphalt/C2 at different temperatures

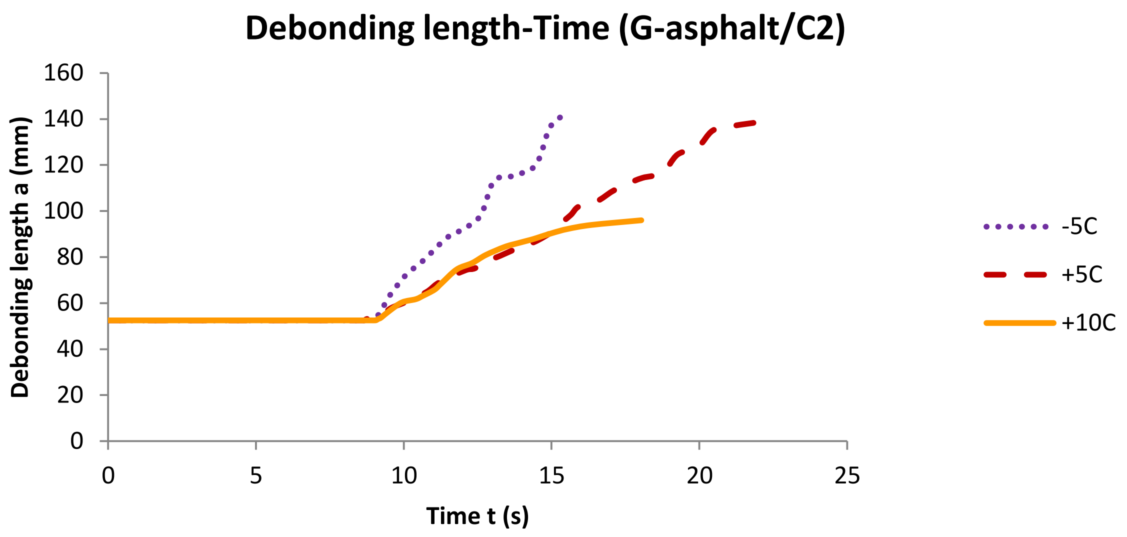

Figure 4.39 Debonding length versus time of G-asphalt/C2 at different temperatures

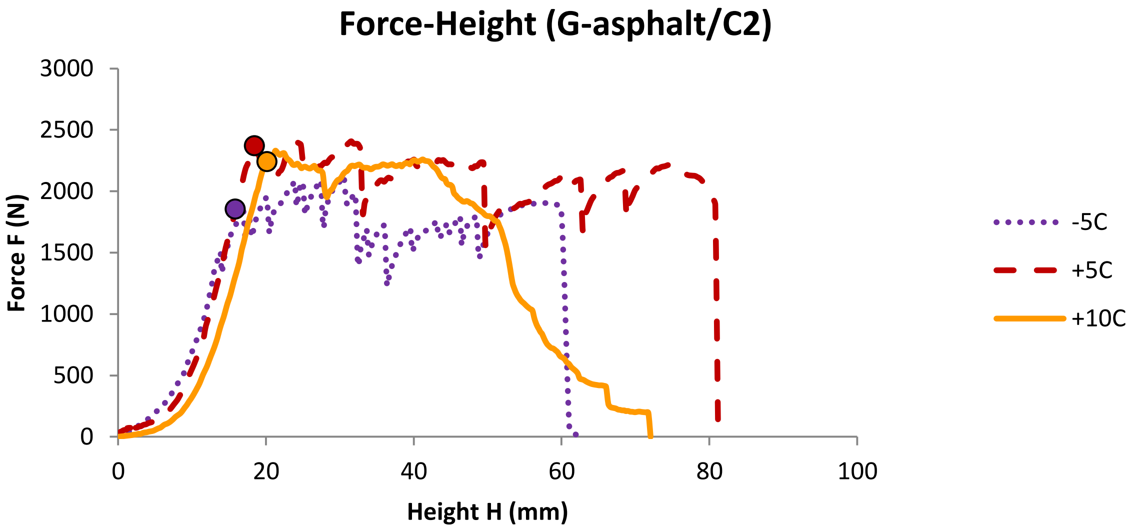

Figure 4.40 Force-Height relationship of G-asphalt/C2 at different temperatures

It can be seen in Figure 4.38, there is a clear trend of the results with the strain energy release rate and temperature. The temperature influence is significant for this type interface. With the increase of temperature, the strain energy release rate of the interface increases. The highest value of strain energy release rate occurs at temperature +10^{o}C. Meanwhile, in Figure 4.33, the debonding rate at lower temperature -5^{o}C is higher than that at another two higher temperatures.

Figure 4.40 shows that the piston elevated height values at different temperatures are about the same, but the debonding force value at temperature +10^{o}C is the highest.

4.3.3.6 Experimental results for C2/P-asphalt

The following figures show the experimental results of C2/P-asphalt interface in MAT test. In Figure 4.41 it shows the energy release rate of C2/P-asphalt interface at different temperatures. The debonding length versus time relationship of C2/P-asphalt interface at different temperatures can be seen in Figure 4.42. The Force-Height relationship is shown as Figure 4.43.

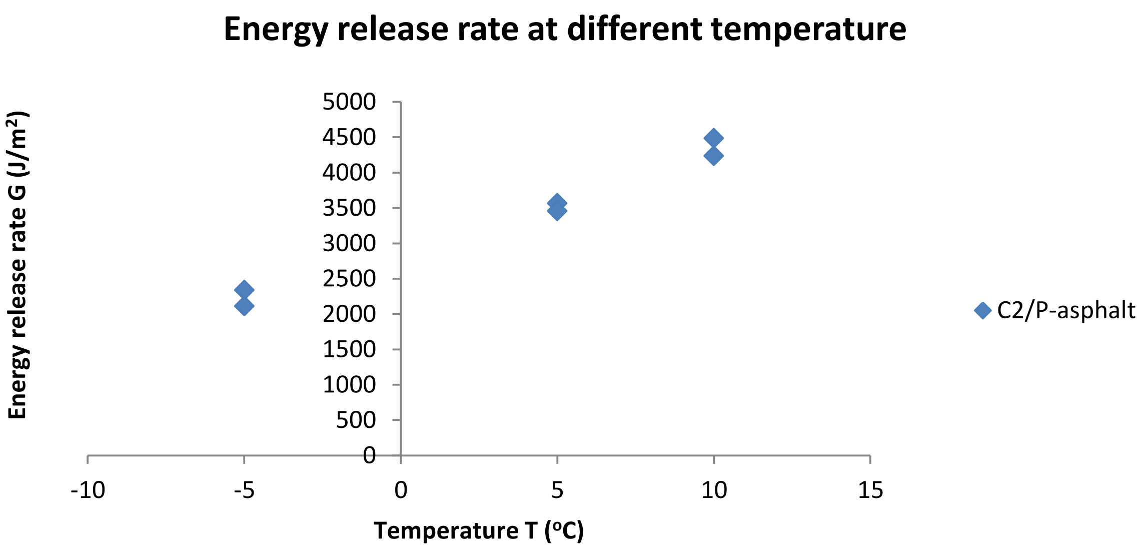

Figure 4.41 Energy release rate of C2/P-asphalt at different temperatures

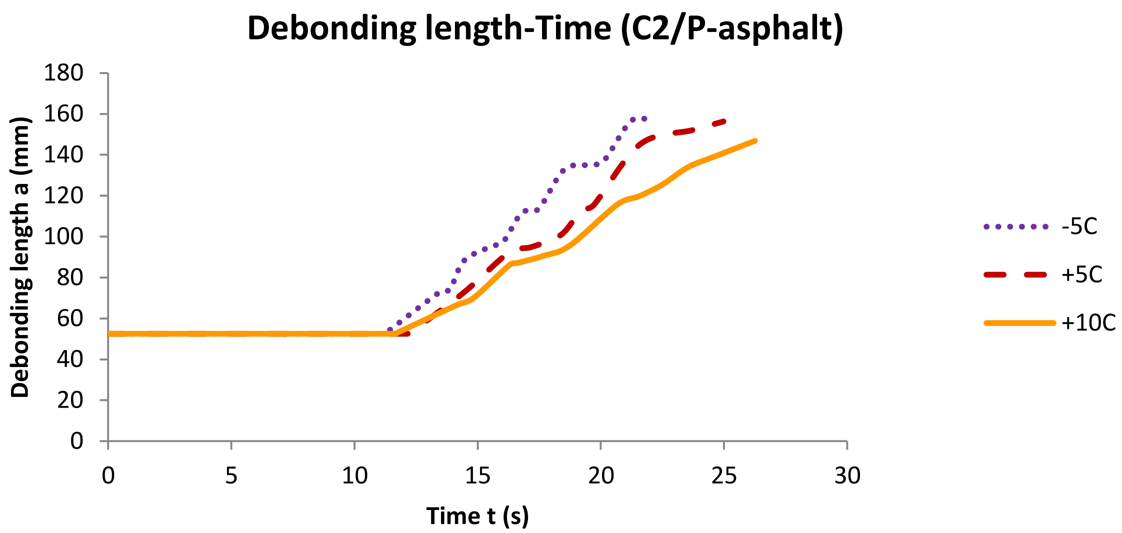

Figure 4.42 Debonding length versus time of C2/P-asphalt at different temperatures

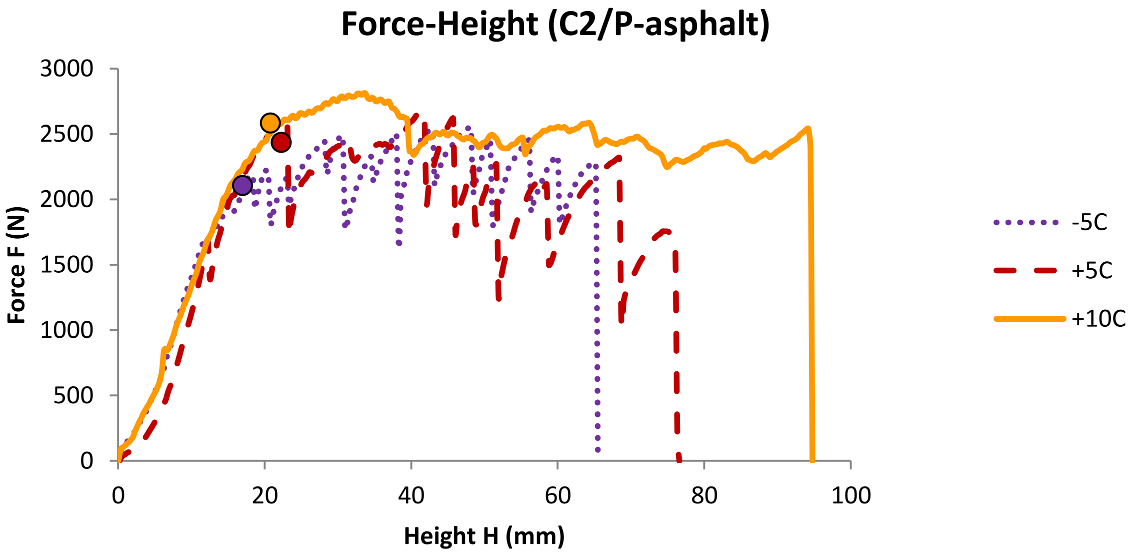

Figure 4.43 Force-Height relationship of C2/P-asphalt at different temperatures

Figure 4.41 shows the strain energy release rate of C2/P-asphalt interface increases with the increase of temperature. Figure 4.42 shows, at lower temperature, the membrane debonding length propagates faster than that at higher temperature.

From Figure 4.43, it can be observed that the corresponding debonding force and piston height at temperature +10^{o}C are the highest, which cause the highest G-value than other two cases as the lower temperature.

4.3.4 Membrane products from company D

Company D has provided one type of membrane product which is utilized both for top and bottom membrane layers in bridge.

The bottom membrane connected to steel deck is defined as Steel/D; the bottom membrane adhered to Guss Asphalt (GA) is denoted as D/G-asphalt; the top membrane adhered to GA is denoted as G-asphalt/D; and the top membrane connected Porous Asphalt (PA) is defined as D/P-asphalt.

The thickness of each membrane type is shown in Table 4.5.

Table 4.5 Dimension for membrane of Company D

Membrane type	Membrane thickness
Steel/D	3mm
D/G-asphalt	3mm
G-asphalt/D	3mm
D/P-asphalt	3mm

Membrane D during MAT test showed the tendency to fail during the debonding propagation, which makes the debonding length development in a short range. Therefore, there is no need to plot the results of debonding length versus time. In this section, only plots of strain energy release rate of the interface at different temperatures and force versus height are included.

4.3.4.1 Experimental results for Steel/D

The following figures show the experimental results of Steel/D interface in MAT test. In Figure 4.44 it shows the strain energy release rate of Steel/D interface at different temperatures. The Force-Height relationship at different temperatures is shown in Figure 4.45.

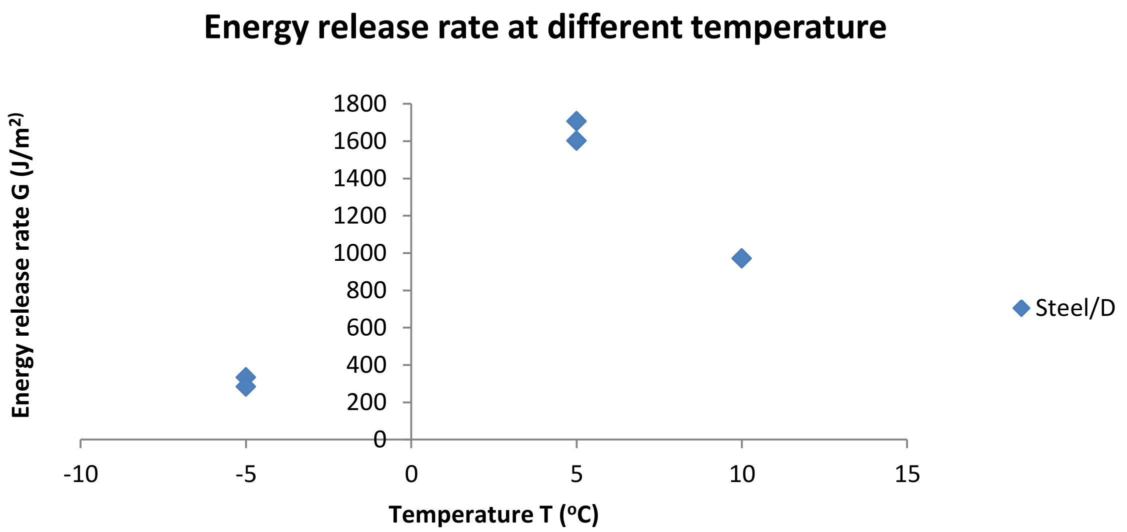

Figure 4.44 Energy release rate of Steel/D at different temperatures

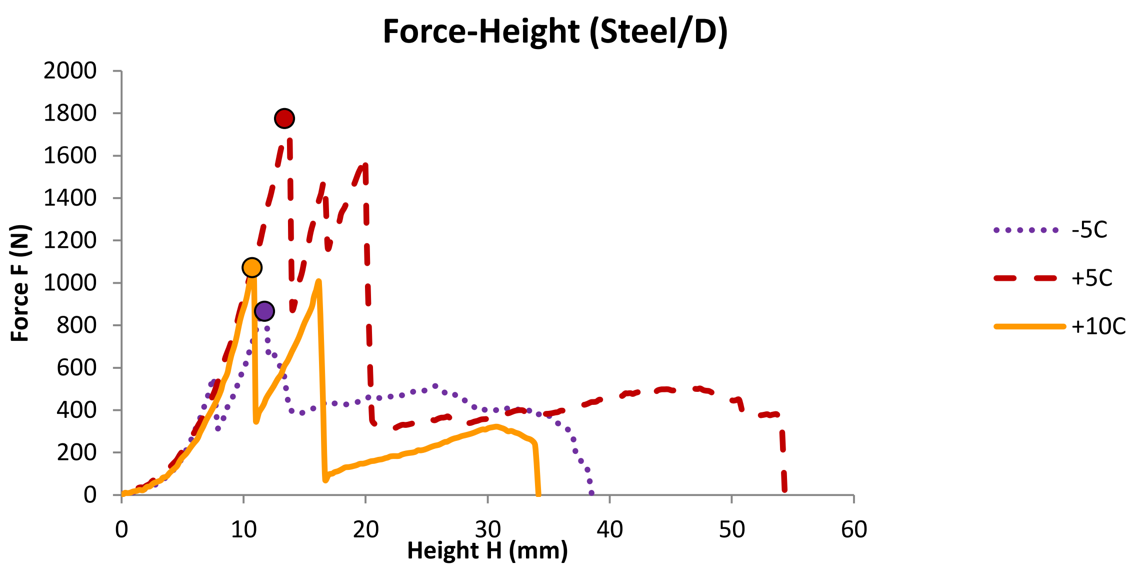

Figure 4.45 Force-Height relationship of Steel/D at different temperatures

In Figure 4.44, it can be observed that the test temperature can influence significantly on the strain energy release rate of this type of membrane interface. At temperature -5^{o}C, the G-value is the lowest, when temperature increases; the G-value also increases. However by comparing the G-value under temperature range of +5^{o}C and +10^{o}C, it is clear that the highest G-value is at temperature +5^{o}C, which can be proved by the fact that the corresponding force when debonding initiates at temperature +5^{o}C is higher than +10^{o}C and -5^{o}C, see Figure 4.45.

4.3.4.2 Experimental results for D/G-asphalt

The following figures show the experimental results of D/G-asphalt interface in MAT test. In Figure 4.46 it shows the strain energy release rate of D/G-asphalt interface at different temperatures. The Force-Height relationship at different temperatures is shown in Figure 4.47.

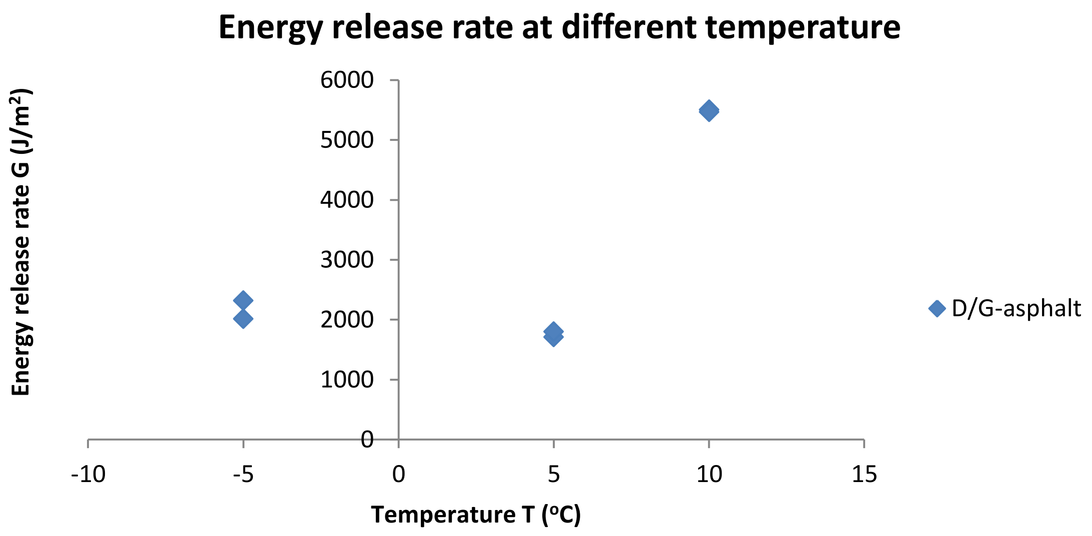

Figure 4.46 Energy release rate of D/G-asphalt at different temperatures

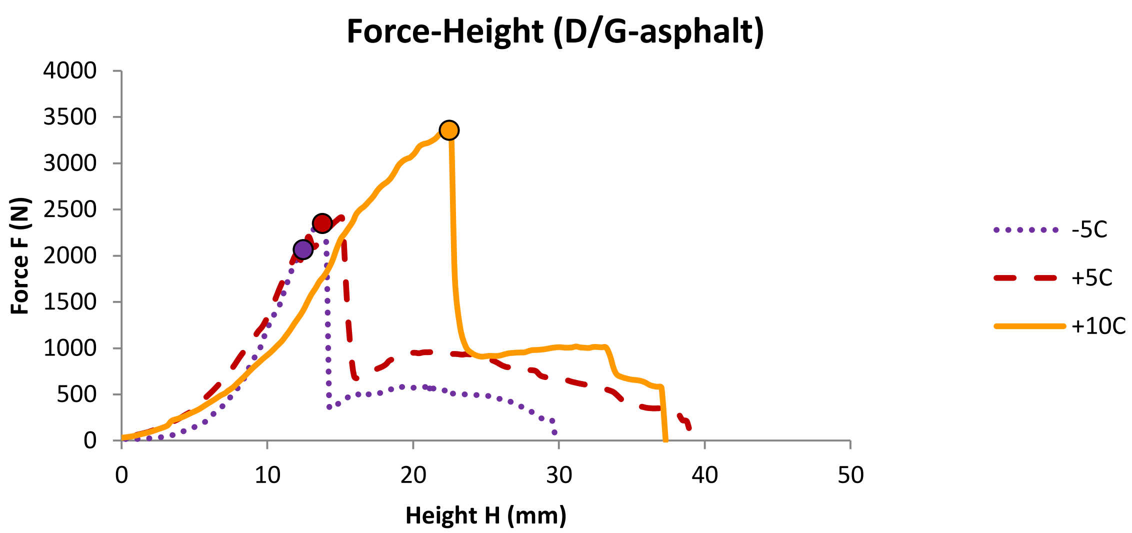

Figure 4.47 Force-Height relationship of D/G-asphalt at different temperatures

It can be observed that the temperature influence is significant on the energy release rate of D/G-asphalt interface. At temperature +10^{o}C, the G-value is much larger than at temperature -5^{o}C and +5^{o}C as it can be seen in Figure 4.46. However, the G-values at temperature -5^{o}C and +5^{o}C are about the same. When debonding the corresponding force and height at temperature -5^{o}C and +5^{o}C the trend lines are close to each other, but the force and height at temperature +10^{o}C are much higher as shown in Figure 4.47.

4.3.4.3 Experimental results for G-asphalt/D

The following figures show the experimental results of G-asphalt/D interface in MAT test. In Figure 4.48 it shows the energy release rate of G-asphalt/D interface at different temperatures. The Force-Height relationship at different temperatures is shown in Figure 4.49.

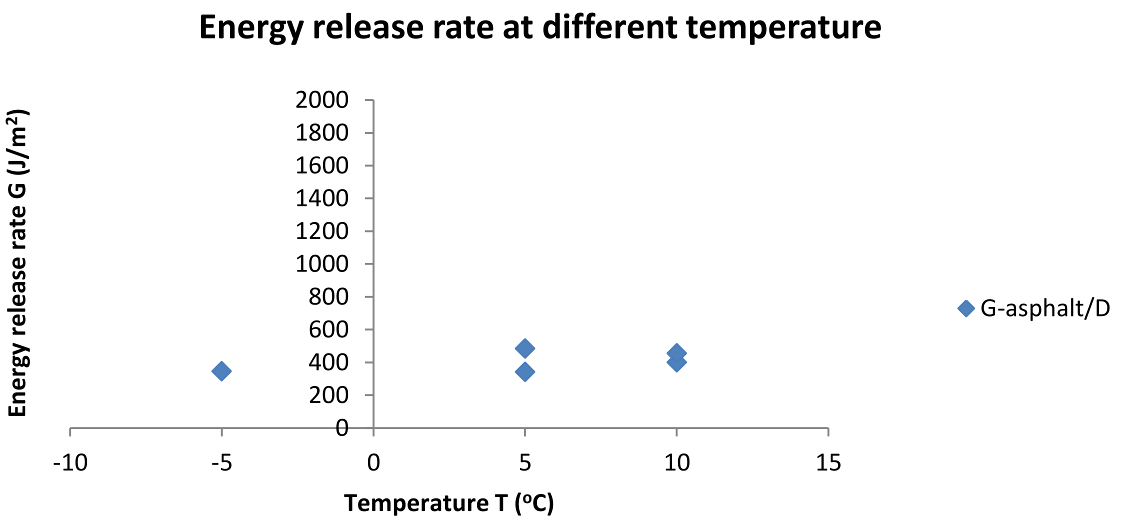

Figure 4.48 Energy release rate of G-asphalt/D at different temperatures

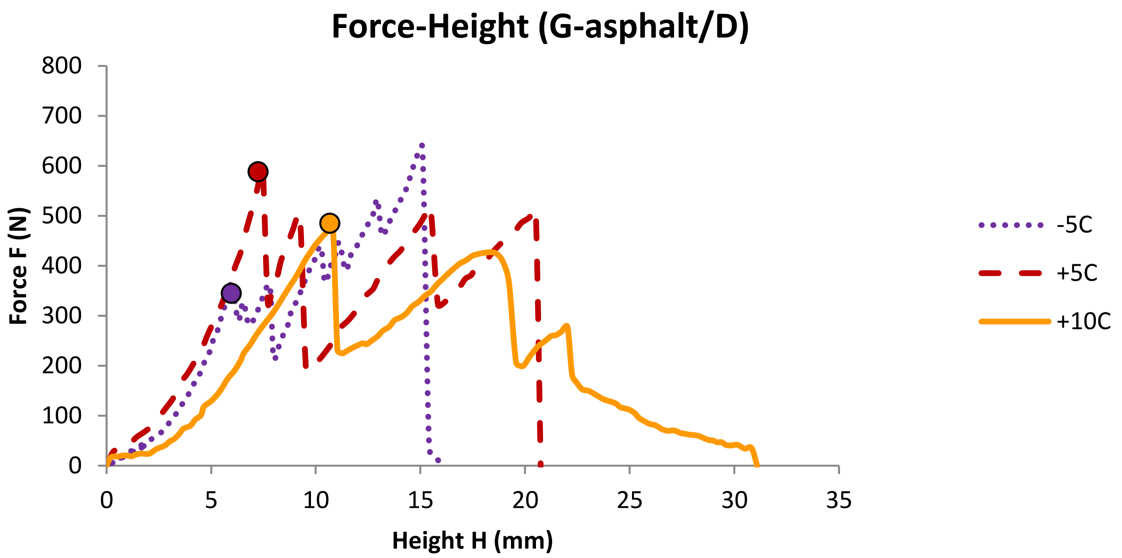

Figure 4.49 Force-Height relationship of G-asphalt/D at different temperatures

From Figure 4.48, the strain energy release rate of G-asphalt/D interface changes insignificant with the increase of temperature. By comparing the G-values at three temperatures(-5°C, 5°C and +10°C), the value at temperature -5°C has founded to be the smallest due to lowest height and force when debonding initiating, Figure 4.49. The corresponding force at temperature +5°C is higher than that at +10°C, but the corresponding height is smaller, which causes the G-values at these two temperatures are about the same.

4.3.4.4 Experimental results for D/P-asphalt

The following figures show the experimental results of D/P-asphalt interface in MAT test. In Figure 4.50 it shows the energy release rate of D/P-asphalt interface at different temperatures. The Force-Height relationship at different temperatures is shown in Figure 4.51.

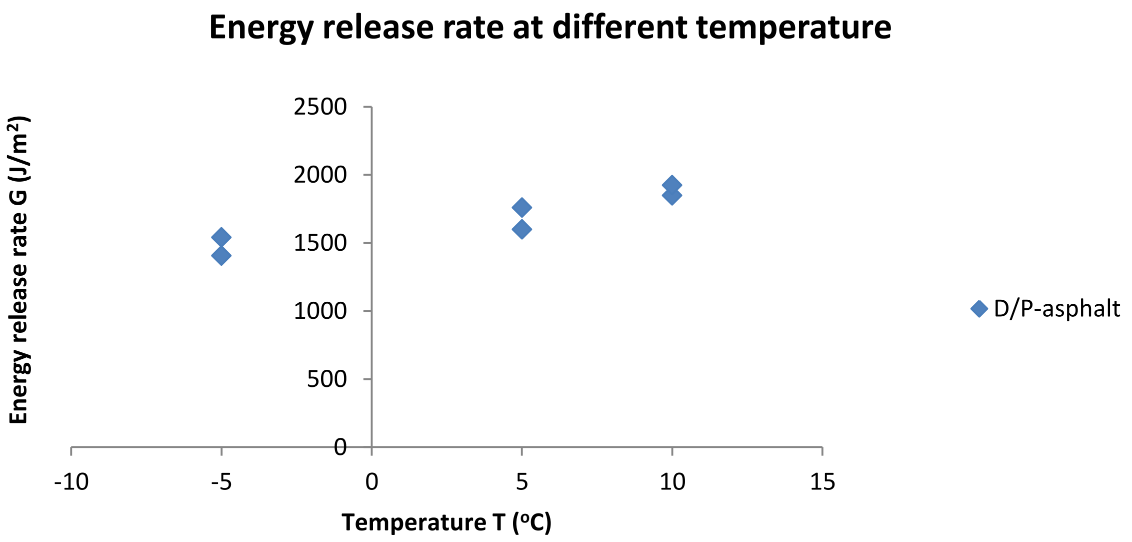

Figure 4.50 Energy release rate of D/P-asphalt at different temperatures

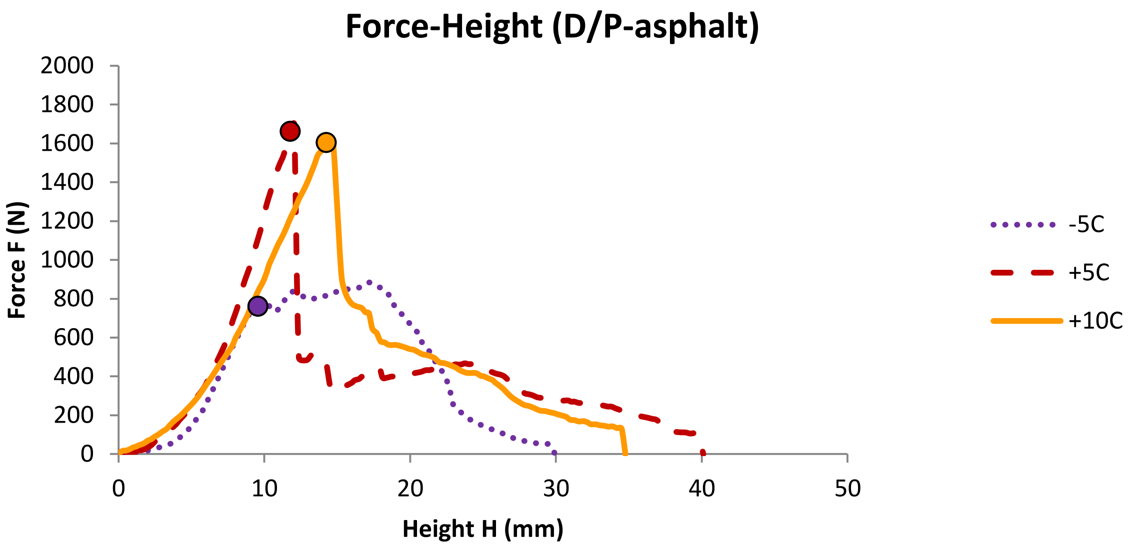

Figure 4.51 Force-Height relationship of D/P-asphalt at different temperatures

The strain energy release rate of this interface increases while the temperature increases, but not significantly. From Figure 4.50, the G-values at three temperatures (-5°C, 5°C and +10°C) do not change a lot. However, the strain energy release rate at temperature +10°C is the highest. Meanwhile, the corresponding force and height when debonding initiated at +5°C and +10°C are quite height than that at -5°C though the stain energy release rate values do not show that difference. Therefore, the final strain energy release rate for this interface increase insignificantly when temperature increases.

4.3.4.5 Experimental results of membrane products from Company E

Company E provided only one membrane product for MAT test. This membrane E is used only as bottom membrane. The membrane specimen connected to steel deck is denoted as Steel/E; the membrane specimen adhered to Guss Asphalt (GA) is denoted as E/G-asphalt.

The thickness of each membrane type is indicated in Table 4.6.

Table 4.6 Dimension for membrane of Company E

Membrane type	Membrane thickness
Steel/E	3mm
E/G-asphalt	3mm

For testing of Steel/E interface, it was observed that, in most cases, membrane E showed the tendency of cohesive failure instead of the adhesive failure in the interface. It means that, in most cases, membrane E were already broken before the membrane debonding initiation in which it makes impossible to calculate strain energy release for this type interface. Therefore, in this section, only the plots of force versus piston height draw the attentions .

4.3.5 Experimental results for Steel/E

The following figures show the experimental results of Steel/E interface in MAT test. It can be observed from Figure 4.52 that the membrane shows brittle response at three temperatures. Instead of the adhesive failure in the interface, the membrane shows cohesive failure. The piston force and elevation height that can break the membrane are higher at temperature +10^{o}C.

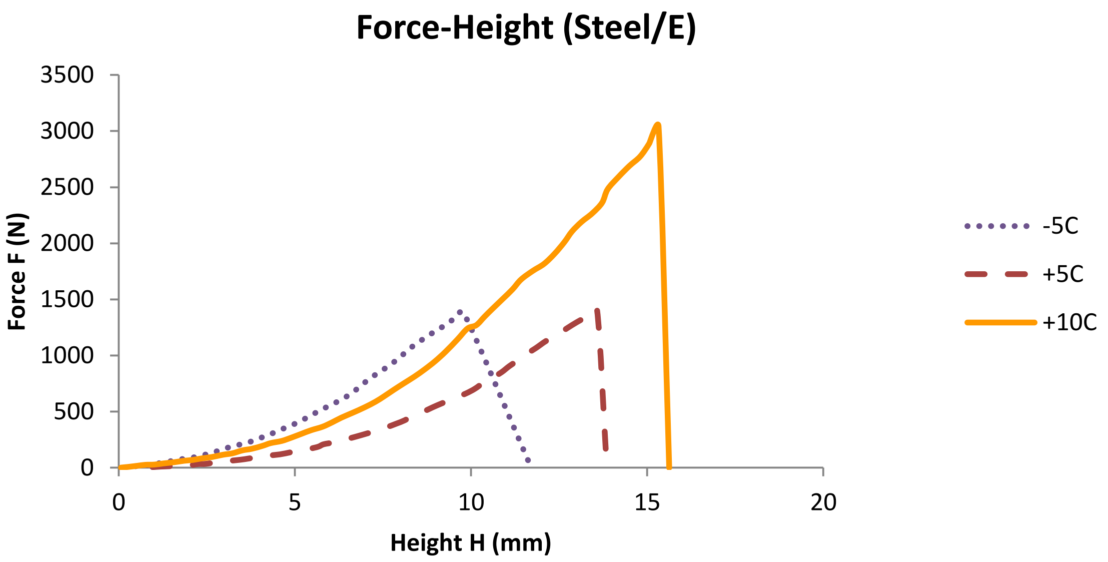

Figure 4.52 Force-Height relationship of Steel/E at different temperatures

4.3.5.1 Experimental results for E/G-asphalt

The following figures show the experimental results of E/G-asphalt interface in MAT test. In Figure 4.53 it shows the strain energy release rate of E/G-asphalt interface at different temperatures. The membrane debonding length versus time relationship of E/G-asphalt interface at different temperatures can be seen in Figure 4.54. The Force-Height relationship is shown in Figure 4.55.

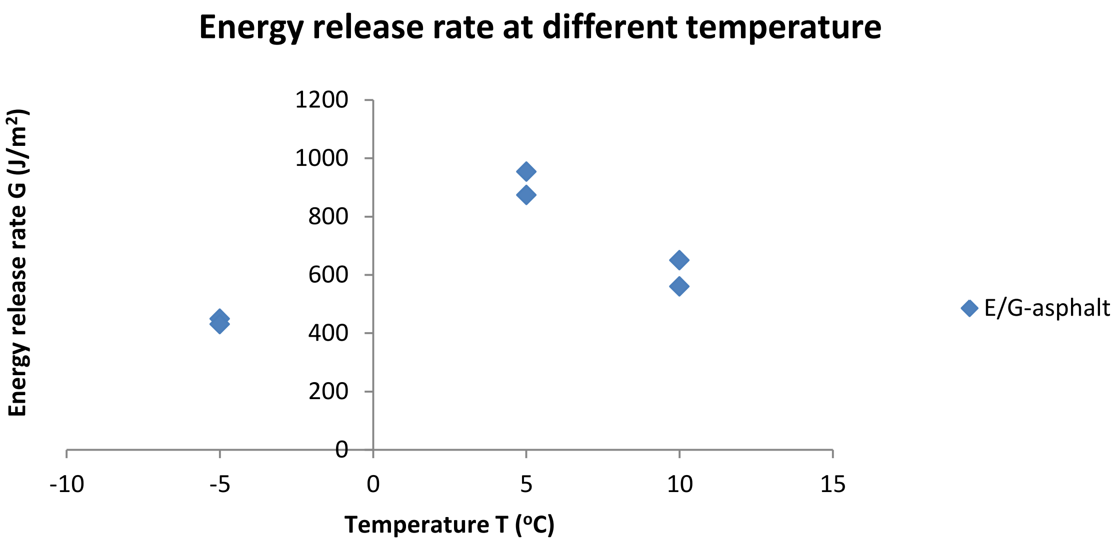

Figure 4.53 Energy release rate of E/G-asphalt at different temperatures

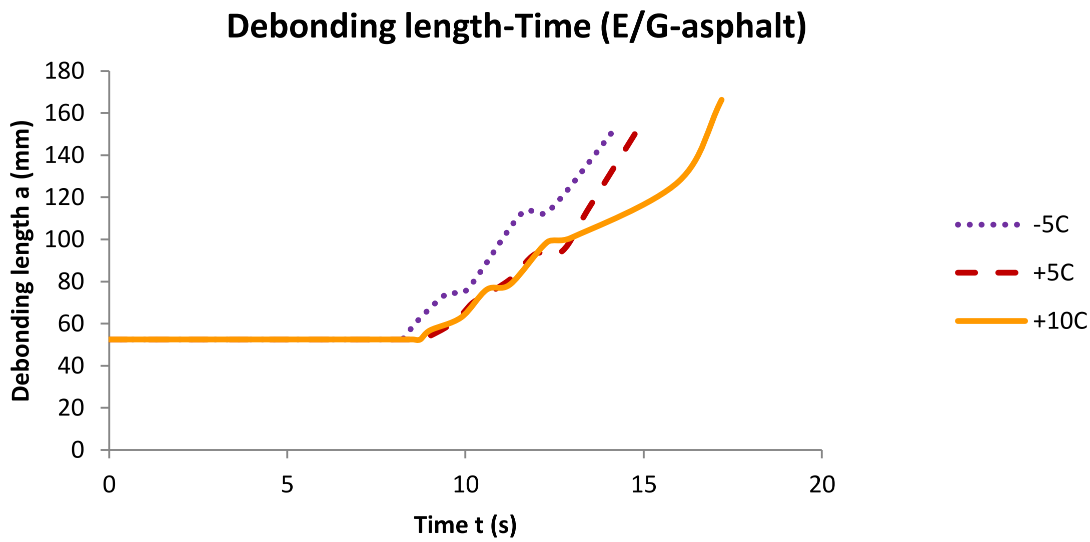

Figure 4.54 Debonding length versus time of E/G-asphalt at different temperatures

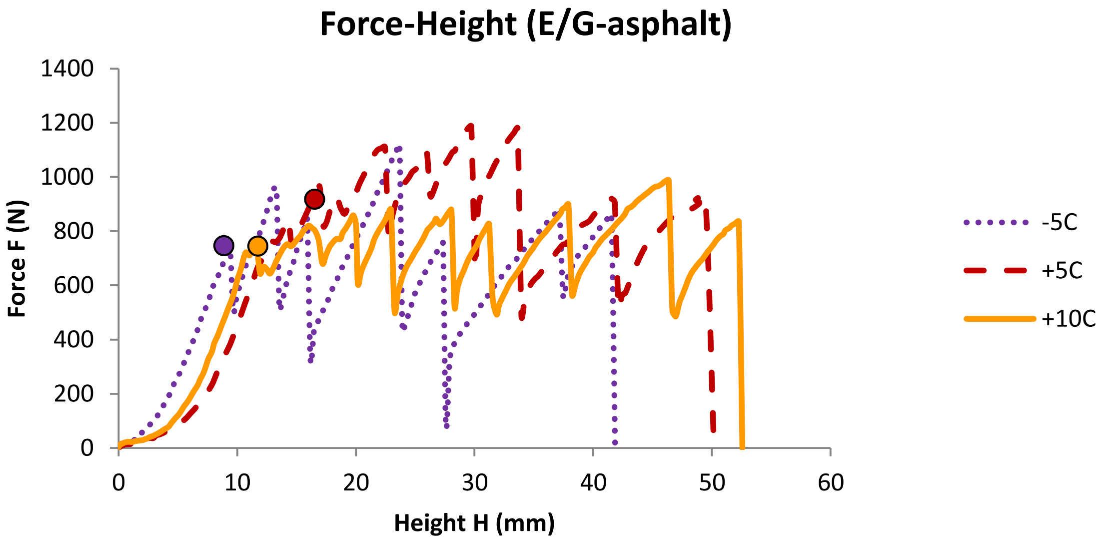

Figure 4.55 Force-Height relationship of E/G-asphalt at different temperatures

In Figure 4.53, it can be observed that the test temperature can influence significantly on the strain energy release rate of this type of membrane interface. At temperature -5^{o}C, the G-value of the interface is the lowest. When temperature is increased, the G-value of the interface is also increased. However by comparing the G-value under temperature range of +5^{o}C to +10^{o}C, it is clear that the highest G-value occurs at temperature +5^{o}C, which can be proved by the fact that the corresponding force when debonding initiates at temperature +5^{o}C is higher than that at +10^{o}C and -5^{o}C, see Figure 4.55.

Figure 4.54 shows, at lower temperature, the membrane debonding length propagates faster than that at higher temperature.

4.4 Comparison of different membranes under the same testing condition

In order to rank the different membrane products, the comparisons for different specimens with the same membrane type under the same temperature condition have been presented. The strain energy release rate G of the membrane interface is utilized as a physical quantity to rank the membrane adhesive bonding strength with different substrates.

4.4.1 Comparison for Steel/M1 (different membranes)

Figure 4.56 to Figure 4.58 show the strain energy release rate of Steel/M1 interface at temperature -5^{o}C, +5^{o}C and +10^{o}C, respectively.

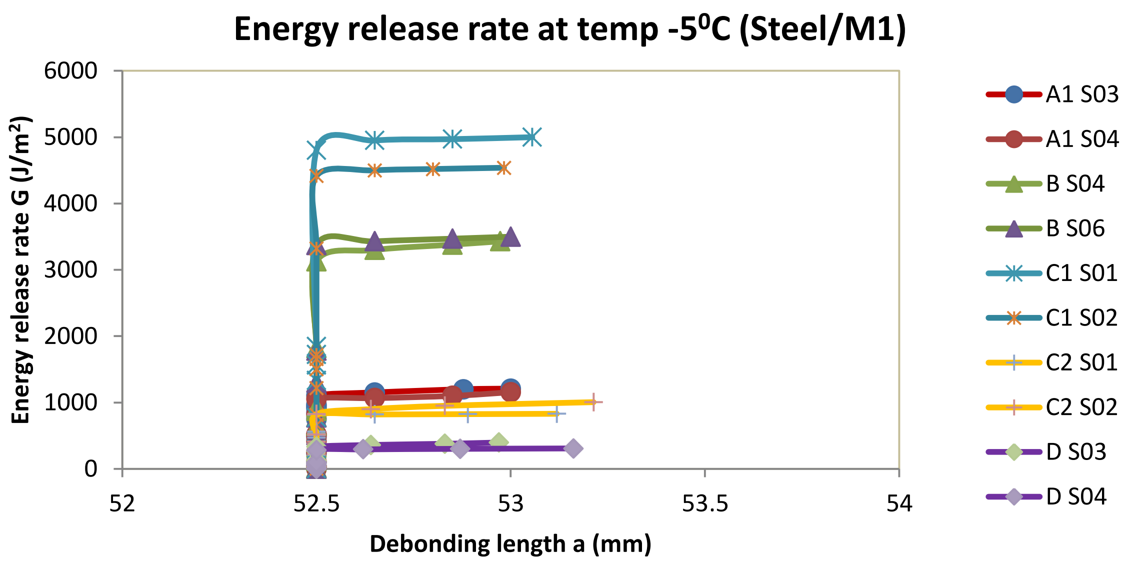

Figure 4.56 Energy release rate of Steel/M1 at temperature -5^{o}C

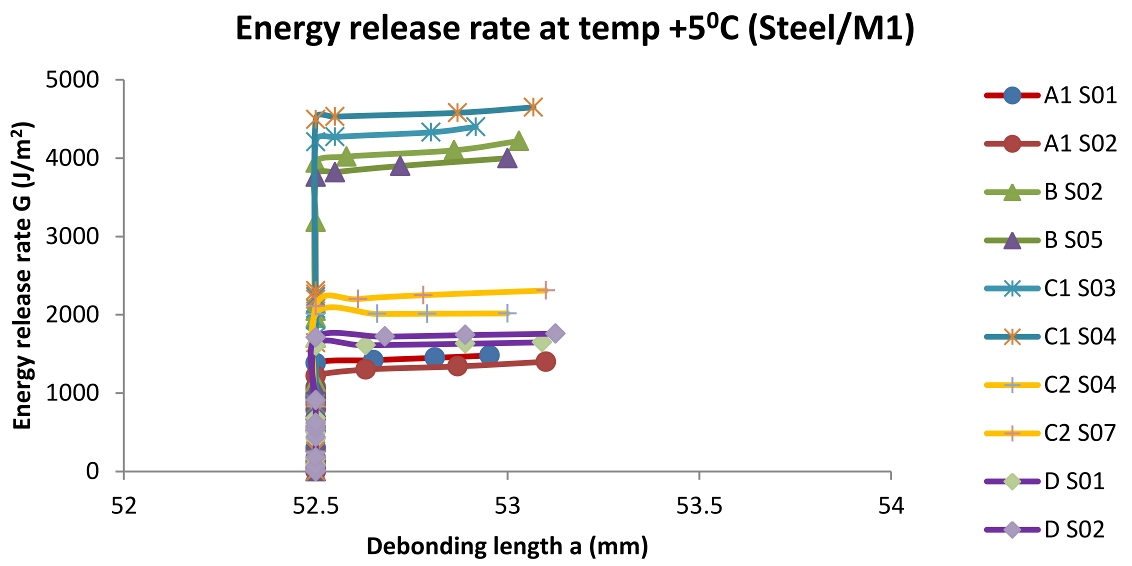

Figure 4.57 Energy release rate of Steel/M1 at temperature +5^{o}C

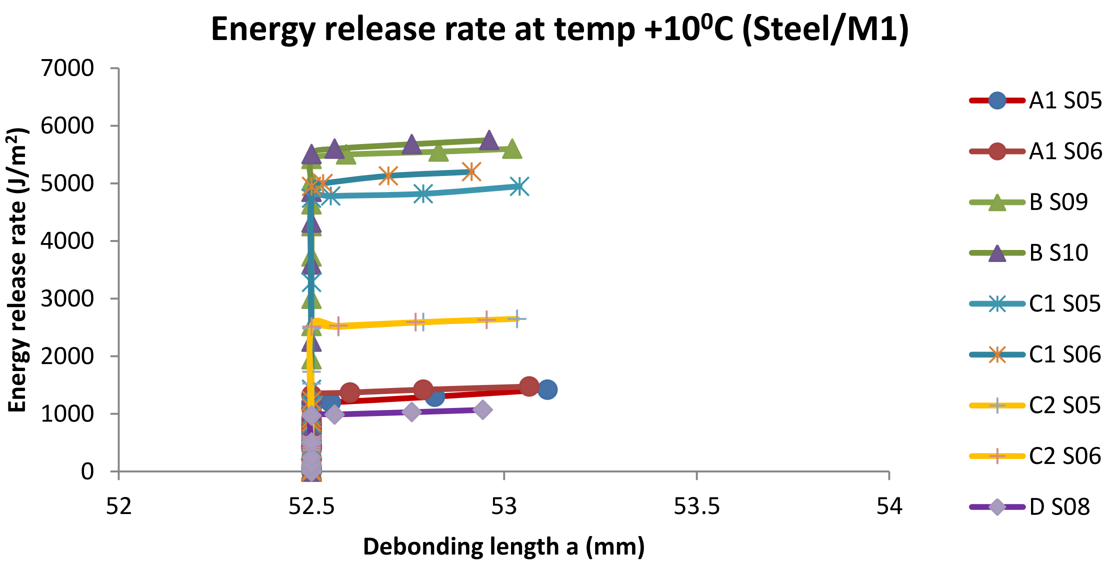

Figure 4.58 Energy release rate of Steel/M1 at temperature +10^{o}C

By comparing of Figure 4.56 to Figure 4.58, it can be observed that the Steel/B and Steel/C1 interface perform better than other membrane types at each temperature, thus Membrane B and C1 can be chosen as the best performed membranes for Steel/M1 type. Here, the strain energy release rate of product E cannot be calculated due to the membrane cohesive failure instead of interface adhesive failure, which means it has good bonding performance. Finally, product B, C1 and E are recommended. The statistics can be found in the Appendix I.

4.4.2 Comparison for M1/G-asphalt (different membranes)

Figure 4.59 to Figure 4.61 show the strain energy release rate of M1/G-asphalt interface at three temperatures (-5^{o}C, +5^{o}C and +10^{o}C), respectively.

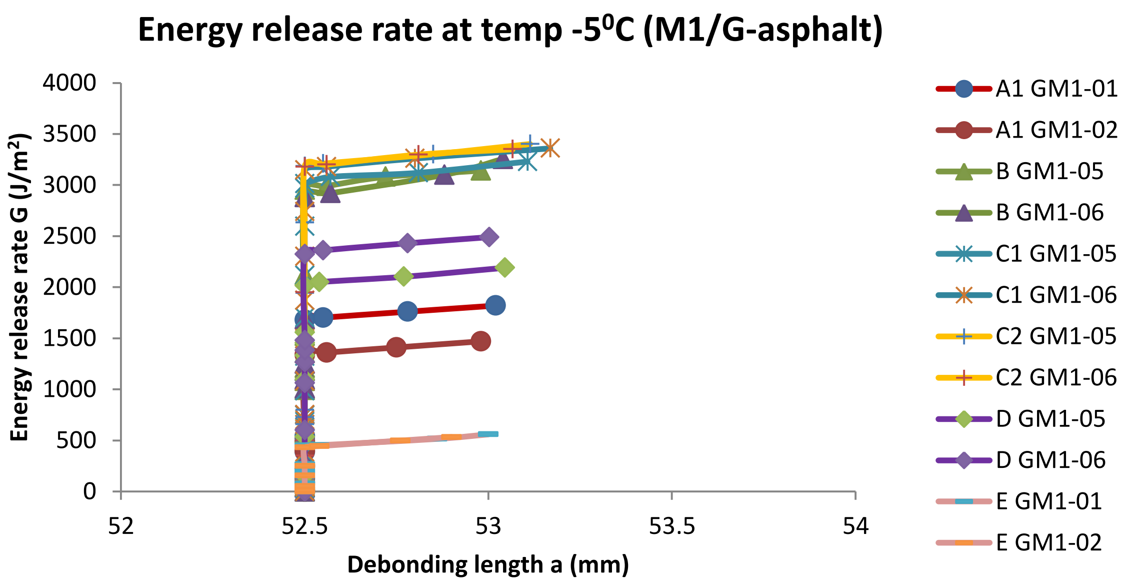

Figure 4.59 Energy release rate of M1/G-asphalt at temperature -5^{o}C

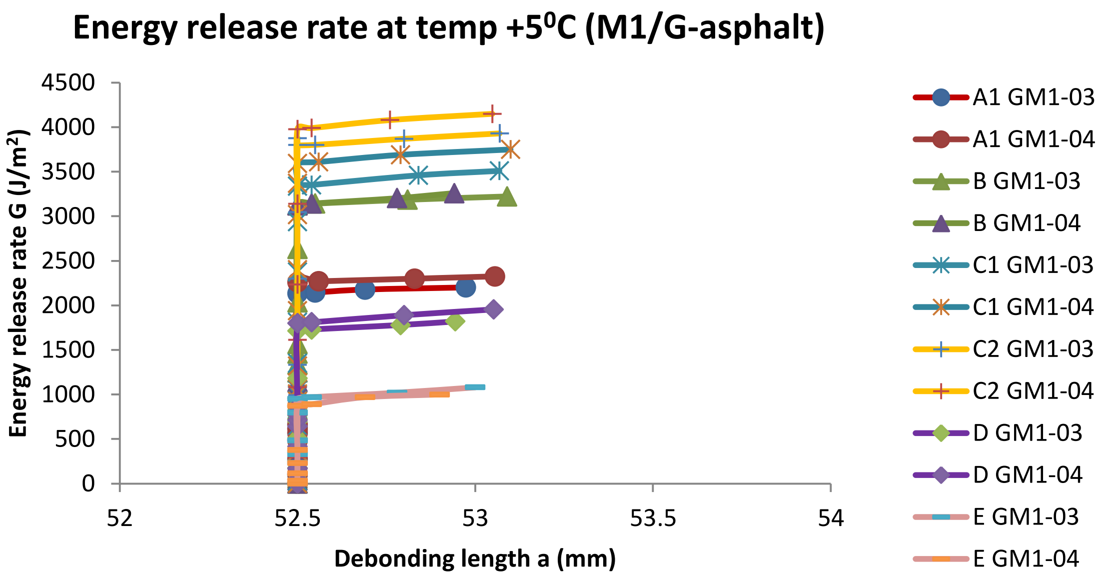

Figure 4.60 Energy release rate of M1/G-asphalt at temperature +5°C

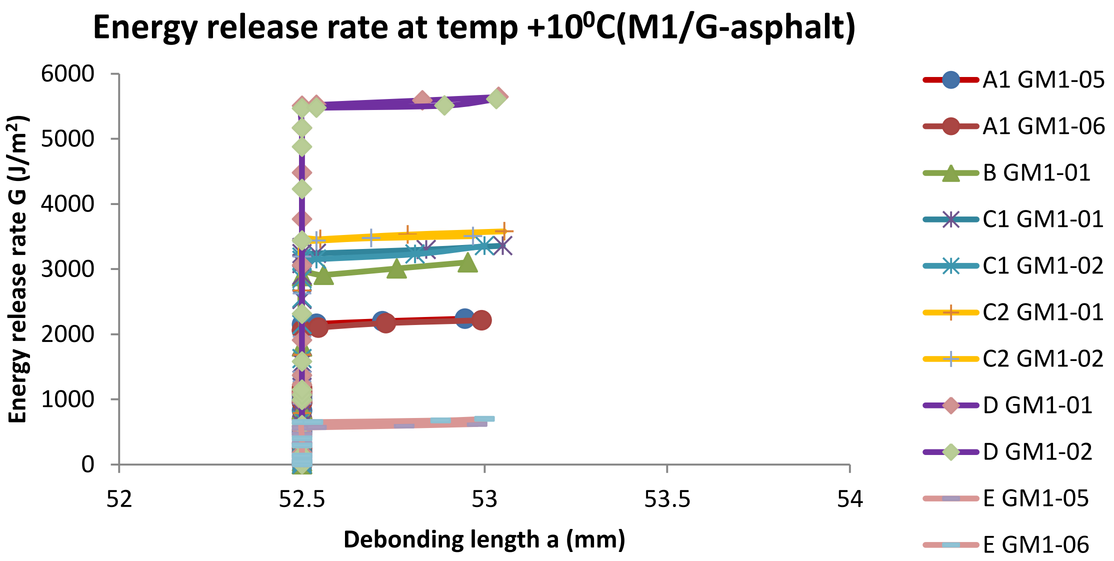

Figure 4.61 Energy release rate of M1/G-asphalt at temperature +10°C

By comparing Figure 4.59 to Figure 4.61, it can be observed that membrane interfaces of B/G-asphalt, C1/G-asphalt and C2/G-asphalt have higher strain energy release rate than the other membrane interfaces at three temperatures (-5°C, +5°C and +10°C),. Although D/G-asphalt performs the best at temperature +10°C, but at other two temperatures (-5°C and +5°C), it performs not as well as other products. Therefore, product B, C1 and C2 are recommended.

4.4.3 Comparison for G-asphalt/M2 (different membranes)

Figure 4.62, Figure 4.60 and Figure 4.64 show the energy release rate of G-asphalt/M2 type at temperature -5°C, +5°C and +10°C, respectively.

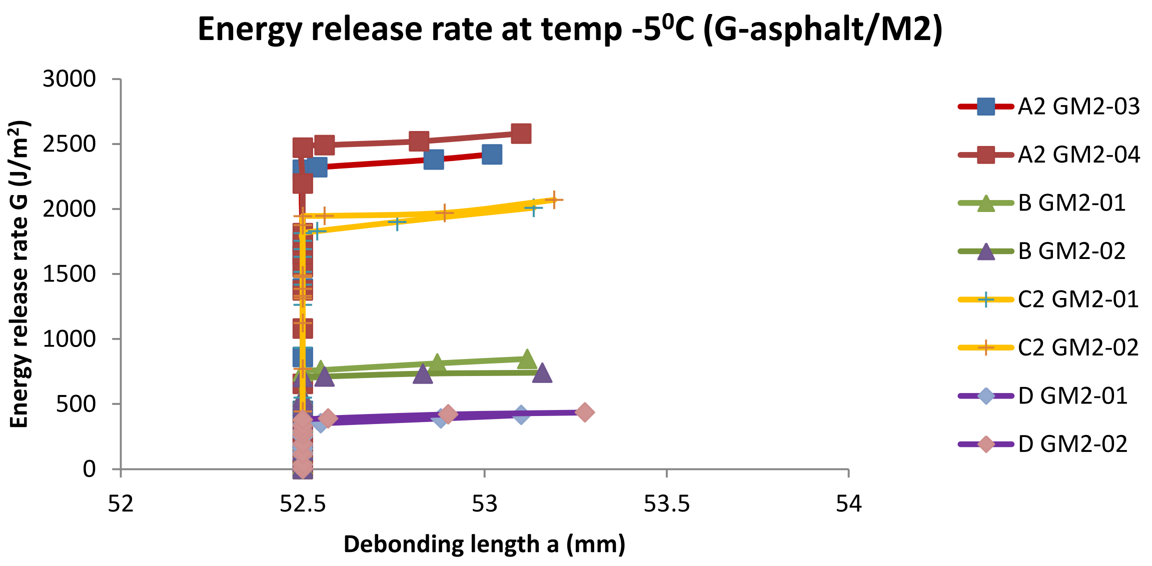

Figure 4.62 Energy release rate of G-asphalt/M2 at temperature -5°C

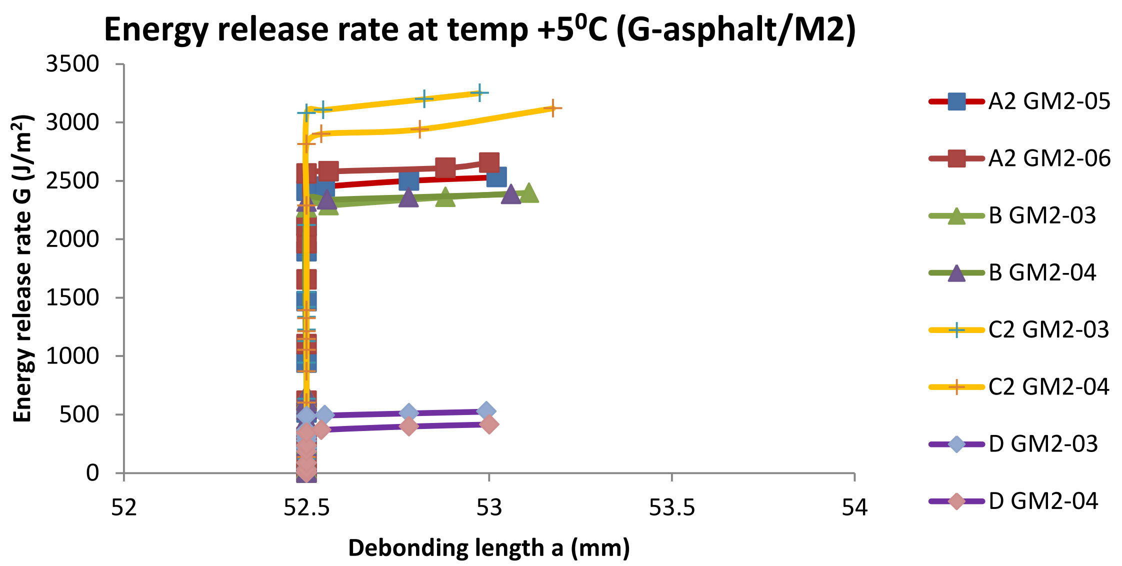

Figure 4.63 Energy release rate of G-asphalt/M2 at temperature +5°C

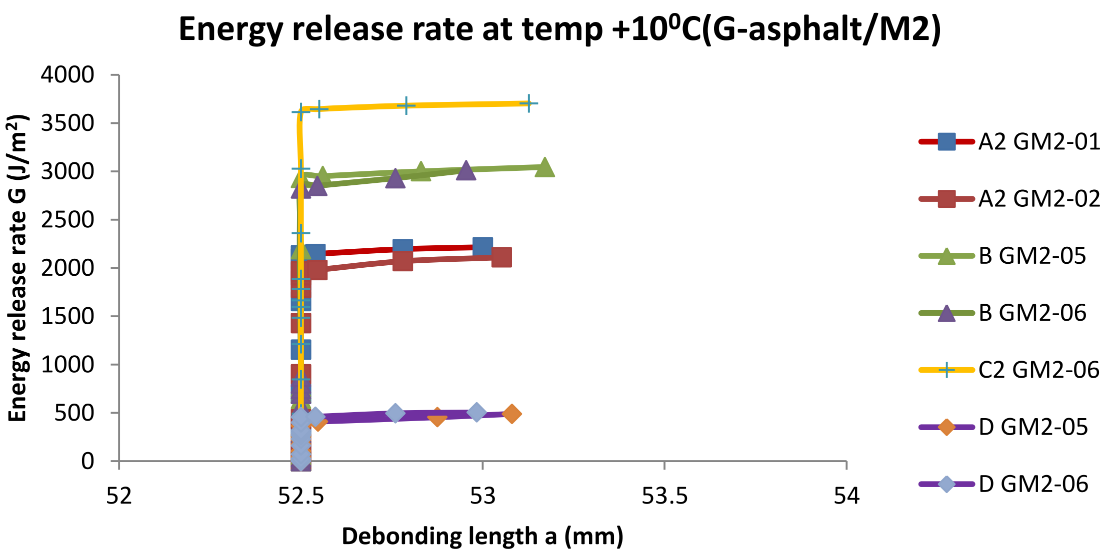

Figure 4.64 Energy release rate of G-asphalt/M2 at temperature +10°C

For membrane type G-asphalt/M2, from comparison among Figure 4.62, Figure 4.63 and Figure 4.64, G-asphalt/C2 and G-asphalt/A2 are the best. From Figure 4.63 and Figure 4.64, it can be seen that membrane type G-asphalt/B performs well at temperature +5°C and +10°C, but due to bad performance at temperature -5°C, it is not chosen for one of the best choices. Therefore, A2 and C2 are recommended as the best two membrane products for this interface.

4.4.4 Comparison for M2/P-asphalt (different membranes)

Figure 4.65 to Figure 4.67 show the energy release rate of M2/P-asphalt interface at temperature -5°C, +5°C and +10°C, respectively.

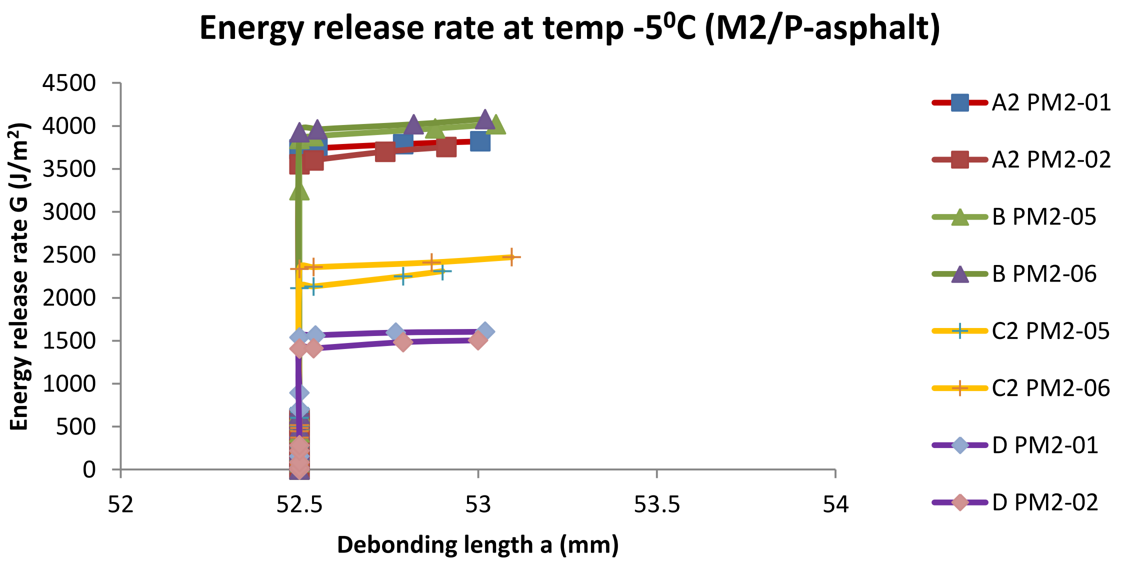

Figure 4.65 Energy release rate of M2/P-asphalt at temperature -5°C

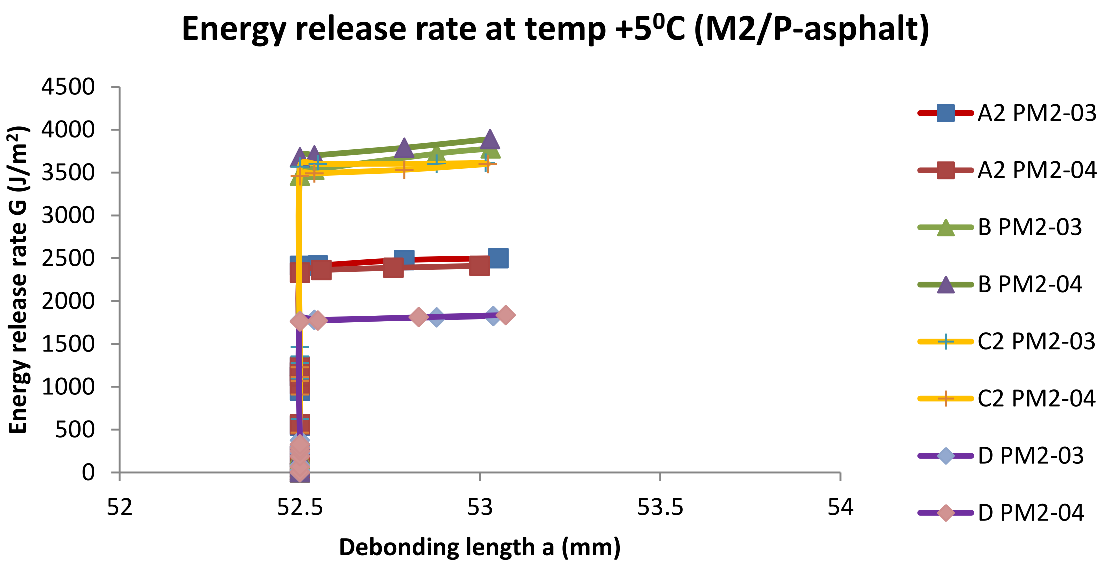

Figure 4.66 Energy release rate of M2/P-asphalt at temperature +5^{o}C

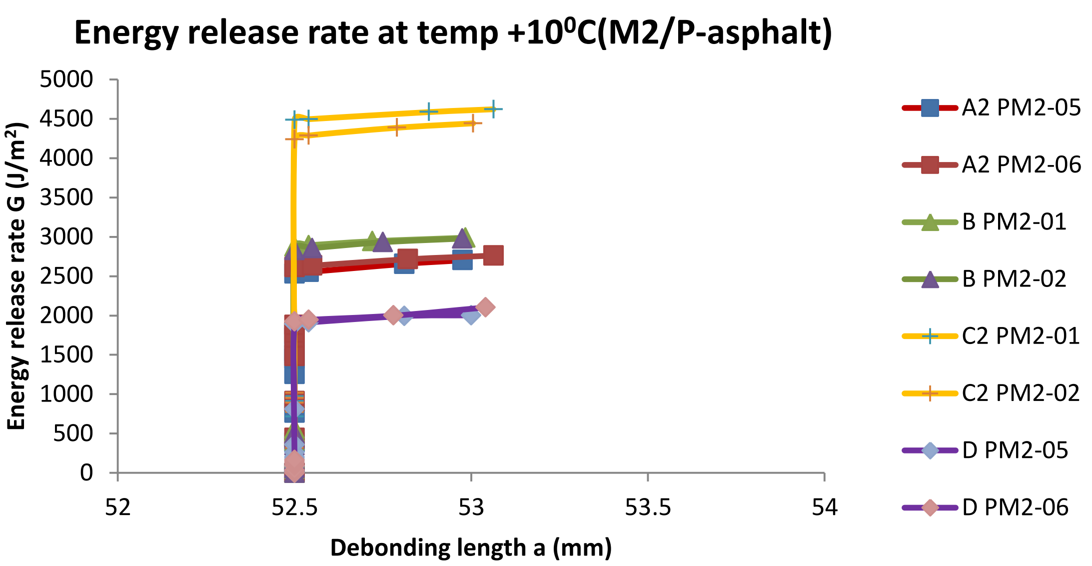

Figure 4.67 Energy release rate of M2/P-asphalt at temperature +10^{o}C

For membrane type M2/P-asphalt interface, from comparison among Figure 4.65, Figure 4.66 and Figure 4.67, A2/P-asphalt interface performs well at temperature -5^{o}C, but at temperature +5^{o}C and +10^{o}C, it performs not as well as C2/P-asphalt and B/P-asphalt interface. By considering the G-value itself, it is still competitive. Therefore, membrane A2 can be taken as one of the best choices. B/P-asphalt interface performs well at each temperature, so membrane B is considered as one of the top membrane products. For membrane interface C2/P-asphalt, the G-value at temperature -5^{o}C is not the highest, but it is still competitive, and at other two temperatures, it shows higher strain energy release rate value. Thus, membrane C2 is also considered as one of the best products for this interface. Finally, product A2, B and C2 are recommended.

4.4.5 Recommended membranes

Table 4.7 shows the recommendations for the best performing interface types according to the previous sections.

As it is mentioned before, in Dutch asphalt surfacing system on an orthotropic steel bridge deck, the asphaltic surfacing structure mostly consists of two membrane layers with four interfaces in total. The characteristics of each interface are different for each side of the membrane. Therefore, in order to rank adequately the adhesive bonding strength of each membrane layer with the surrounding materials, the performance of two interfaces for each membrane should be taken into account.

By considering the performance of two interfaces for each membrane, product B and C1 are recommended as the bottom membrane; C2 performs not well when bonding with steel deck, thus it is not considered as bottom membrane; product E performs good at steel/M1 interface, but it doesn't show good performance at the interface between membrane and GA, thereby it cannot be chosen; A2 performs well when connecting GA and PA, thus A2 is taken as one the best choices for the top membrane; Product B connecting with GA doesn't perform as good as that connecting with PA, so it is not the final choice; Product C2 performs very well when connecting GA and PA, therefore it belongs to best membranes choices.

Table 4.7 The recommended membrane for each membrane type

Membrane type	A		B	C		D	E
	A1	A2	B	C1	C2	D	E
Steel/M1			√	√			√
M1/G-asphalt			√	√	√		
G-asphalt/M2		√			√		
M2/P-asphalt		√	√		√		

For details of the comparisons of strain energy release rate among different membranes interface from different company are listed in Appendix I.

All in all, for bottom membrane (membrane 1), the best suitable membranes are product B and product C1. For top membrane (membrane 2), the best choices are product A2 and product C2.

4.5 Finite element simulation of MAT test

4.5.1 Finite element mesh

The MAT tests with different types of membrane products were selected for the numerical simulations, Liu and Scarpas (2012) and Li (2015). The finite element mesh consists of 20-nodded brick elements, Figure 4.68. The mesh consists of four components: the membrane layer, the substrate, the piston and the contact interface area which represents the interface between membrane and the substrate.

Because of symmetry reason, only half of the MAT device is simulated. The geometric parameters of the specimen are given in Figure 4.68.

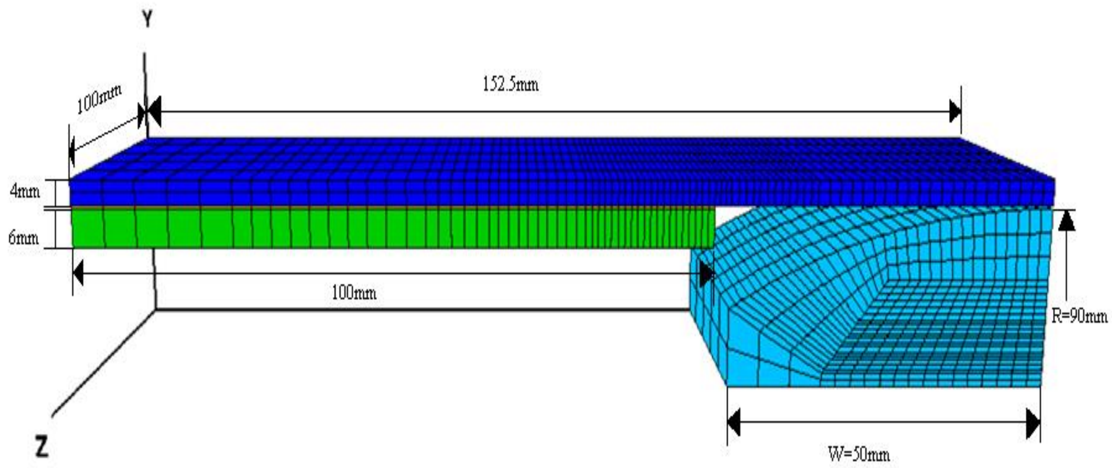

Figure 4.68 FE modeling for MAT simulation

In the numerical simulations performed by Liu and Scarpas (2012) and Li (2015), the membrane A1 and A2 adhered to steel substrate are taken into account. The thickness of the membrane is 4 mm. The thickness of steel plate is 6 mm. The membrane length is taken as 152.5 mm which is shorter than the length of the original structure for reducing the number of FE elements. The substrate is 100 mm in length. The piston radius is 90 mm, and half of the piston width is 50 mm. The boundary conditions are shown in Figure 4.69.

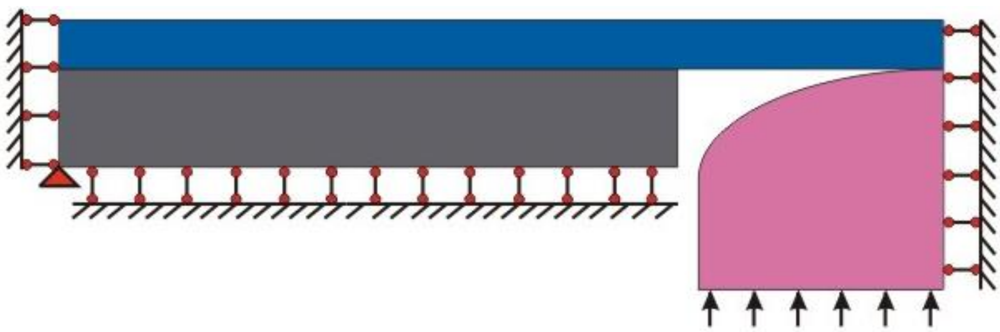

Figure 4.69 Boundary conditions for MAT FE simulation

It can be observed that, at the left side of the boundary (x=0), all nodes are fixed. At the central plane (x=152.5 mm), they can move free vertically. Meanwhile, the bottom surface of the substrate is fixed due to the rigid connection to the MAT setup. A displacement with speed 5mm/s is applied vertically on the bottom plane of the piston.

4.6 Material parameters of substrates and membranes

4.6.1 Substrate parameters

In the numerical investigations of Li (2015), three types of substrates, steel, Guss Asphalt and Porous Asphalt have been chosen for the FE simulations. The basic elastic parameters are shown in Table 4.8.

Table 4.8 Parameters of substrates materials

Substrate	Young's modulus (MPa)	Poisson's ratio
Steel	210000	0.2
Guss Asphalt	3200	0.35
Porous Asphalt	2500	0.35
Piston	210000	0.2

4.6.2 Membrane parameters

The mechanical characteristics of the membrane material are different than the material of substrates and piston. In order to simulate adequately the MAT tests, both the material properties of membrane interface and the properties of membrane itself should be properly determined.

In this research, the membranes products which are utilized for MAT test are mostly made by bitumen-based materials, thereby the mechanical responses of the membrane material are time dependent and temperature sensitive. In order to simulate the membrane response properly, a Visco-Elastic Zener model is utilized for the finite element studies and introduced earlier in chapter 3. For the sake of simplicity, in this thesis simulations of relaxation test via CAPA-3D have been compared with the experiment test results for membrane A1 and A2. For more information about the finite element research can be found in Liu and Scarpas, 2012

4.7 Profiles comparison between MAT tests and FE simulation

In this section, the progressive membrane debonding process in a MAT test is modeled by introducing a traction-relative displacement relationship as a "cohesive traction-separation law" for the contact interface elements in finite element analyses, Liu and Scarpas (2012) and Li (2015).

The area under the traction/relative displacement curves for the contact interface elements is equated to the critical strain energy release rate Gc which can be obtained from the MAT test, see Figure 4.70.

As shown in Figure 4.70, G_c together with δ_{max} govern the shape of the traction-separation function. When interface opening displacement exceeds δ_{max}, the interface loses its bonding strength.

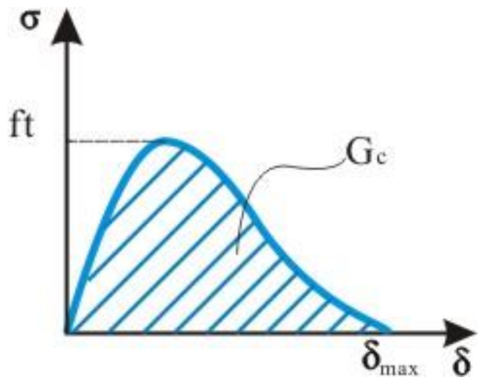

Figure 4.70 Cohesive zone law

As it is discussed before, in this study, the strain energy release rate G_c is used as the objective quantity to characterize the membrane interface bonding strength. Thereby this value will keep as an unchanged parameter during the FE simulation.

The maximum relative displacement, δ_{max}, is also obtained from MAT tests, see Figure 4.70. However, this value is difficult to be precisely measured. Thus during the FE simulation, this parameter can be adjusted by an iterative procedure until the profile of FE simulation fits that of the MAT test. In the meantime, both the force and the height from FE simulation and experimental results should match well at all time, then the simulation is done. This iterative procedure can be drawn in a flow chart, as shown in Figure 4.71.

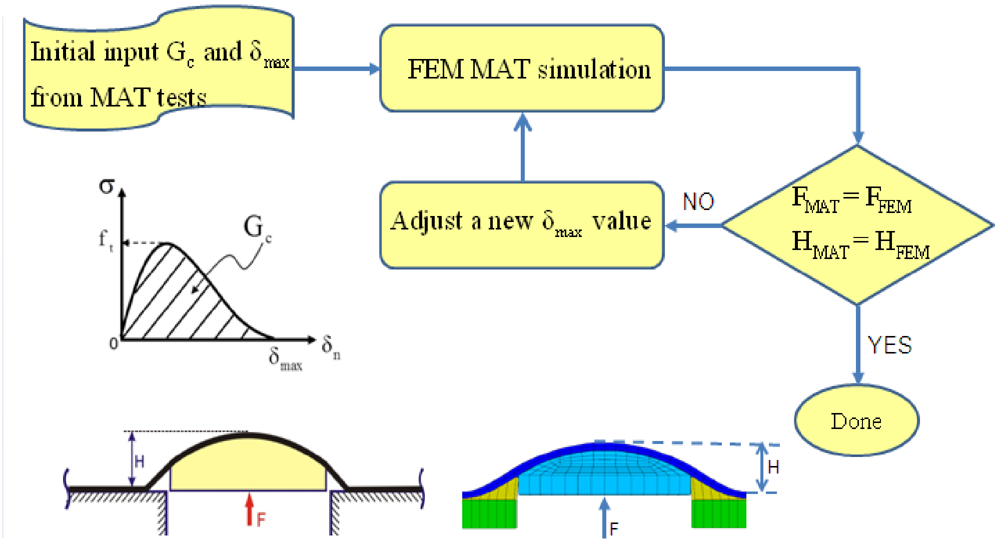

Figure 4.71 Flow chart of validation of δ_c by FE simulation

In this section, membrane A1 and A2 are taken for examples.

The in time contour plots of vertical stress (yy) inside the membrane and the corresponding membrane deformed profiles can be seen as below, see Figure 4.72 through Figure 4.78.

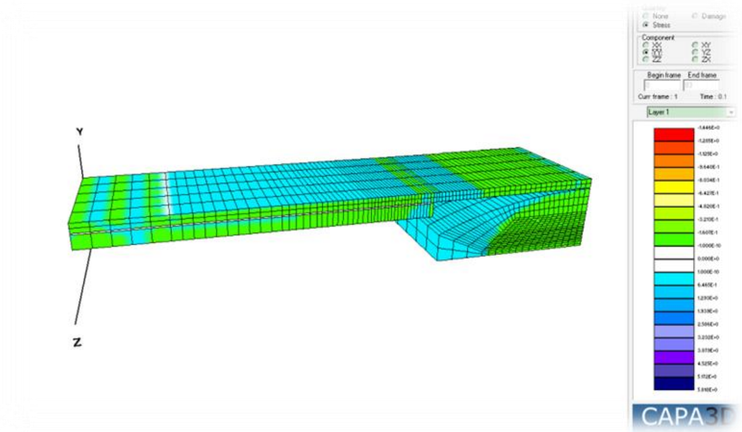

Figure 4.72 Time step =1

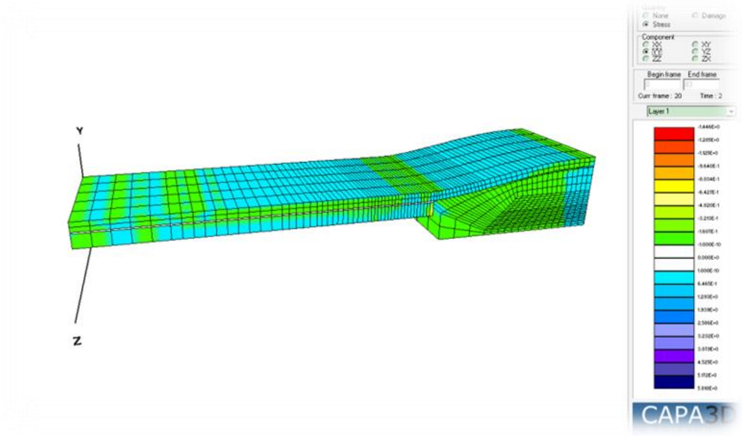

Figure 4.73 Time step =20

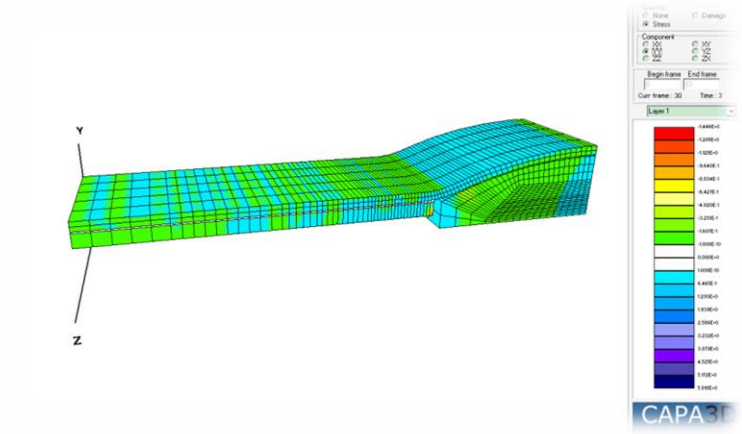

Figure 4.74 Time step =30

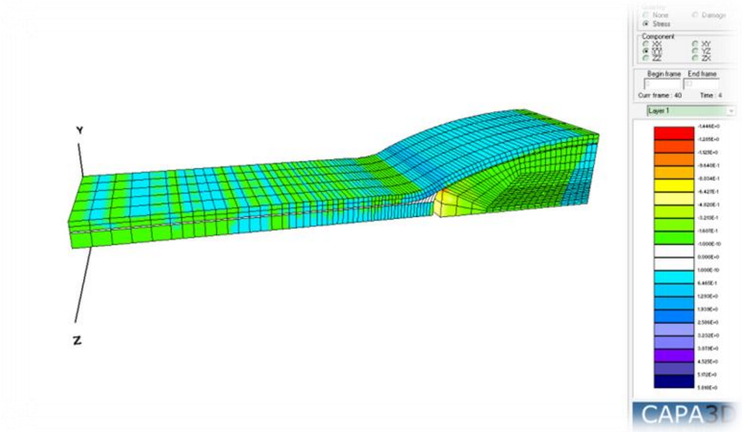

Figure 4.75 Time step =40

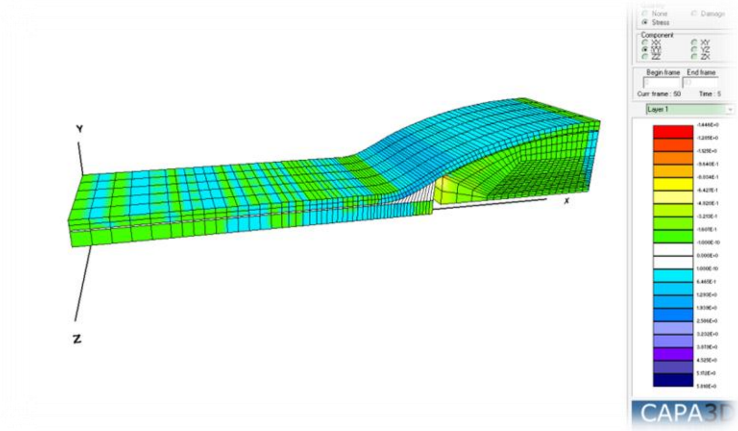

Figure 4.76 Time step =50

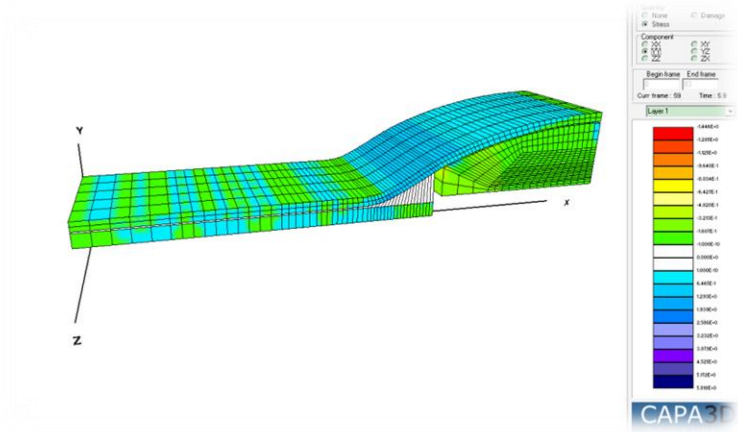

Figure 4.77 Time step =60

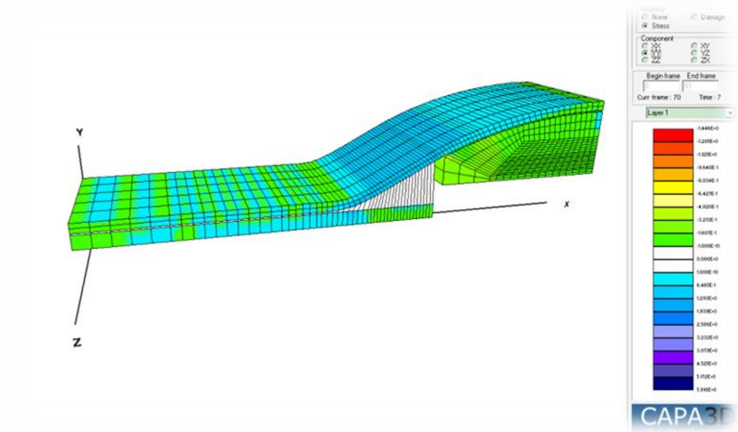

Figure 4.78 Time step =70

The following show the comparisons between FE analyses and experimental results for membrane A1 and A2 with different substrates.

Steel/A1 specimen

The results of Steel/A1 from experiment and FE analysis can be seen in Table 4.9, and the profile comparison is shown in Figure 4.79. It is clear that the force and height of FE analysis and test when debonding initiates are about the same, and the profiles match well.

Table 4.9 Results from FEM and comparison with experimental results for Steel/A1

Steel/A1			
	δ_{max} (mm)	Height (mm)	Force (N)
Experimental result	4.30	16.8	1129
FEM result	4.77	17	1100

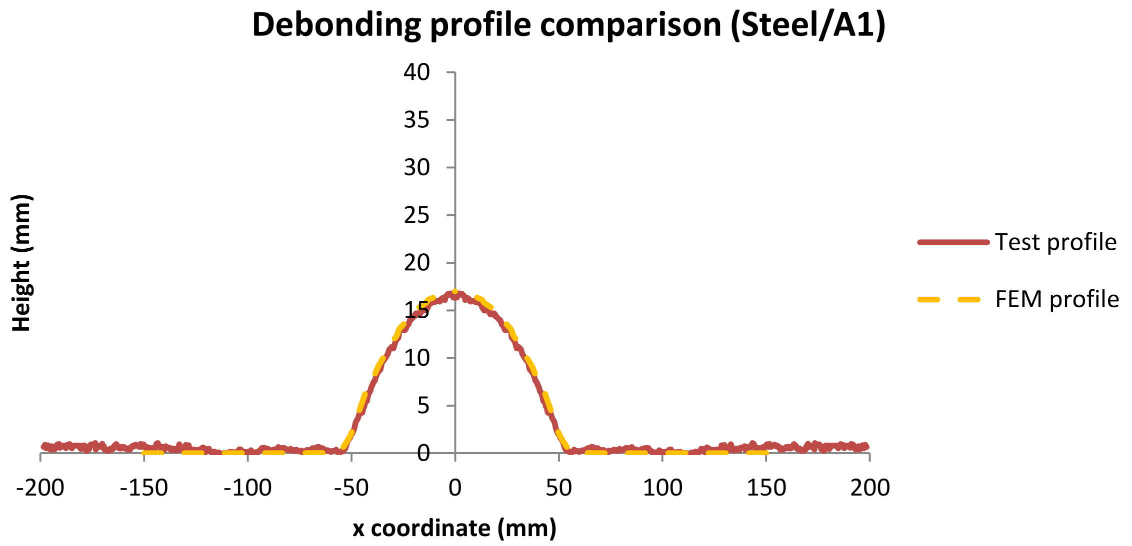

Figure 4.79 Debonding profile comparison between experimental and FEM results

A1/G-asphalt specimen

The results of A1/G-asphalt from experiment and FE analysis can be seen in Table 4.10, and it is observed that the height and force match quite well.

Figure 4.80 shows the profile comparison of experimental result and FE analysis. The profiles when debonding initiates are in agreement.

Table 4.10 Results from FEM and comparison with experimental results for A1/G-asphalt

A1/G-asphalt			
	δ_{max} (mm)	Height (mm)	Force (N)
Experimental result	5.35	22.5	1127
FEM result	5.90	22.5	1120

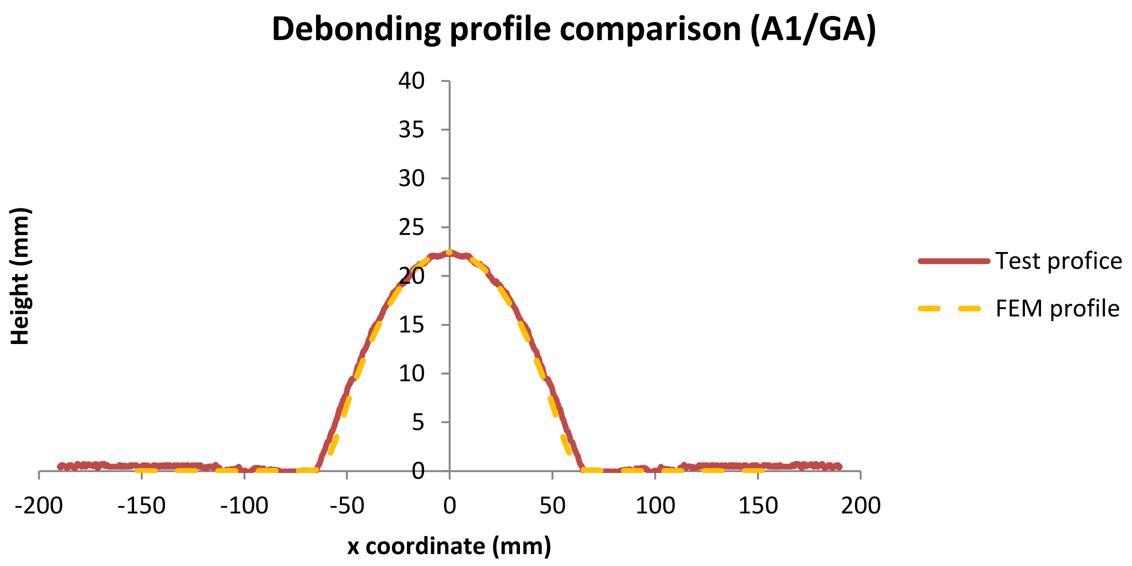

Figure 4.80 Debonding profile comparison between experimental and FEM results

G-asphalt/A2 specimen

The results of G-asphalt/A2 from experiment and FE analysis can be seen in Table 4.11, and through this table, it is clear to see that the height and force for MAT test and FE modeling when debonding initiates, are about the same.

The comparison of profiles when debonding is shown in Figure 4.81. It is considered matching well.

Table 4.11 Results from FEM and comparison with experimental results for G-asphalt/A2

G-asphalt/A2			
	δ_{max} (mm)	Height (mm)	Force (N)
Experimental result	2.27	18.8	1377
FEM result	2.45	19	1350

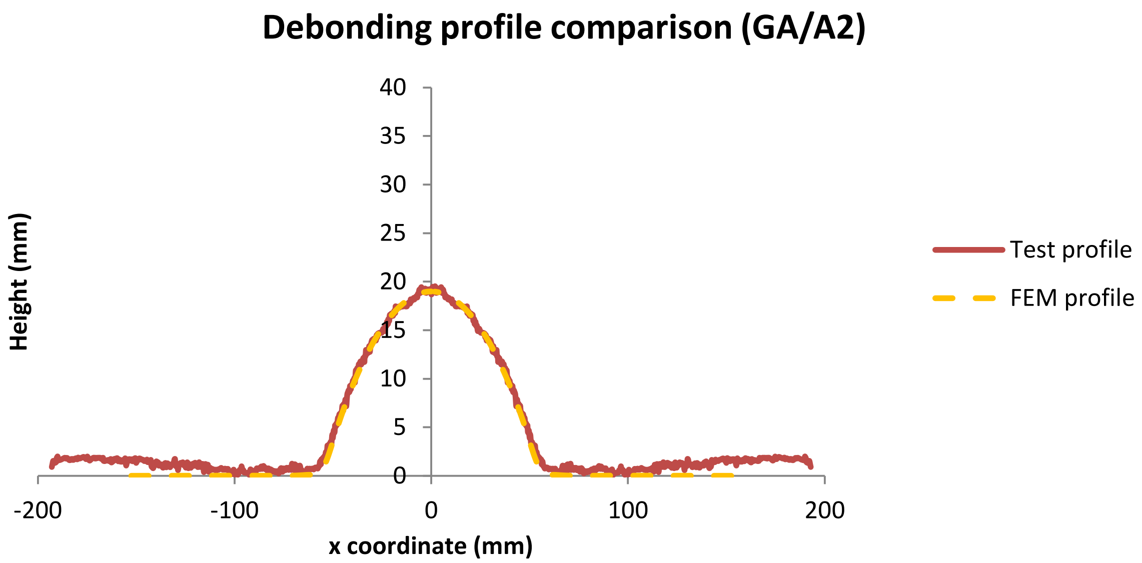

Figure 4.81 Debonding profile comparison between experimental and FEM results

A2/P-asphalt specimen

The force and height of A2/P-asphalt from FE analysis are equal to the results of experiments when debonding initiates, see Table 4.12. The profile of FE analysis matches that of MAT test, as shown in Figure 4.82.

Table 4.12 Results from FEM and comparison with experimental results for A2/P-asphalt

A2/P-asphalt			
	δ_{max} (mm)	Height (mm)	Force (N)
Experimental result	2.10	18.5	1755
FEM result	2.33	18.5	1740

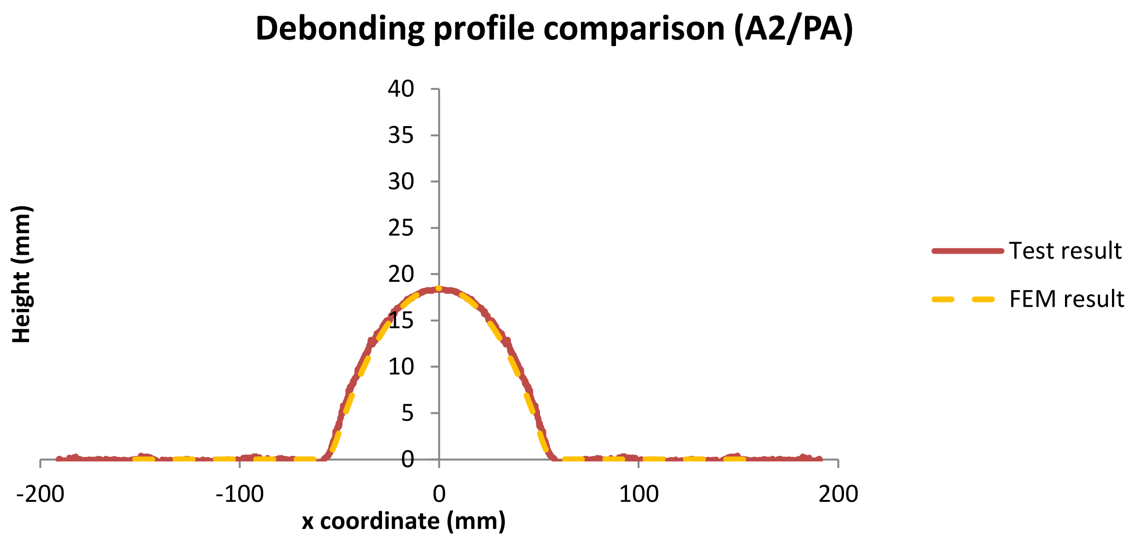

Figure 4.82 Debonding profile comparison between experimental and FEM results

4.8 Conclusions

Based on the results presented, the following conclusions can be made:

- The MAT setup is capable of characterizing the adhesive bonding strength of the various membranes with the surrounding materials. MAT results will allow a better understanding of performance of the membrane on the bridge structure allowing thus optimization of maintenance activities;
- The mechanical response of membrane product is influenced not only by the surrounding substrate but also by the environment temperature;
- Critical energy release rate G_c is a fundamental physical quantity that can be utilized to quantify the membrane adhesive bonding strength with different substrates;
- The material maximum reaction force consists of the combination of both the membrane material response and the membrane bonding response, and it is not an objective measure of the membrane bonding quality. On the other hand G_c is a material physical quality controlling the behavior of only the membrane bonding strength.

- The FE method can be utilized to appropriately model the MAT test.
- The FE simulations show that the strain energy release rate can be indeed chosen as the physical parameter to quantify the membrane bonding characteristics.
- In the further study, parameters used in this MAT test simulation can be utilized for the bridge FE modeling.

5 Experimental results of MAT fatigue loading tests

5.1 Introduction

The monotonic MAT tests provided a fundamentally sound, mechanistic methodology for the expedient ranking of the bonding characteristics of membrane products. In the second phase of this project, the MAT device was modified to enable the investigation of the fatigue response of the three top ranked membrane products from the monotonic MAT tests under cyclic loading conditions at different temperatures

In this chapter, the dissipated energy concept which has been utilized for MAT cyclic loading tests to characterize the fatigue life of membrane products bonded on the different substrates at different temperatures and loading levels. The fatigue damage in the interface between membrane and substrate is related to the amount of dissipated work computed by using the measurement of the actuator load and the membrane deformation during each loading cycle. The MAT laser scanning system determines the shape of the deformed membrane and enables the determination of the debonded length of the membrane during each load cycle. The dissipated work per loading cycle, which is equivalent to the lost part of the total potential energy supplied to the membrane by the actuator per cycle, was used in this study as a measure of the incremental damage in the interface between the membrane and substrate during the testing

The experimental results of the selected membrane products on various substrates tested at two different temperature conditions and three different cyclic loading levels are presented. The values of dissipated work for each membrane interface are compared, as well as the relationship between the membrane debonding length.

The membrane fatigue tests were performed at two temperatures ranges (10^0C and 30^0C). The fatigue tests at 10^0C, were performed with a sinusoidal loading F ranging between $F_{min} = 50N$ and F_{max} =150N at a frequency of 5 Hz for 432 000 cycles. F_{max} was increasing every 432 000 cycles, starting from 150N then 250N and finally 350N, Figure 5.1.

For the fatigue tests at 30^0C, the sinusoidal loading F varied from $F_{min} = 50N$ to F_{max} =100N at a frequency of 5 Hz. The number of applied load cycles was 864 000.

The final part of this chapter In a modified version of the Paris law is used in an attempt to predict the fatigue life of membrane products in adhesively bonded structures based on experimental work conducted using the Membrane Adhesion Tester apparatus (MAT), introduced in earlier chapters. The experimental results from various membrane products bonded to different substrates were validated and compared accordingly.

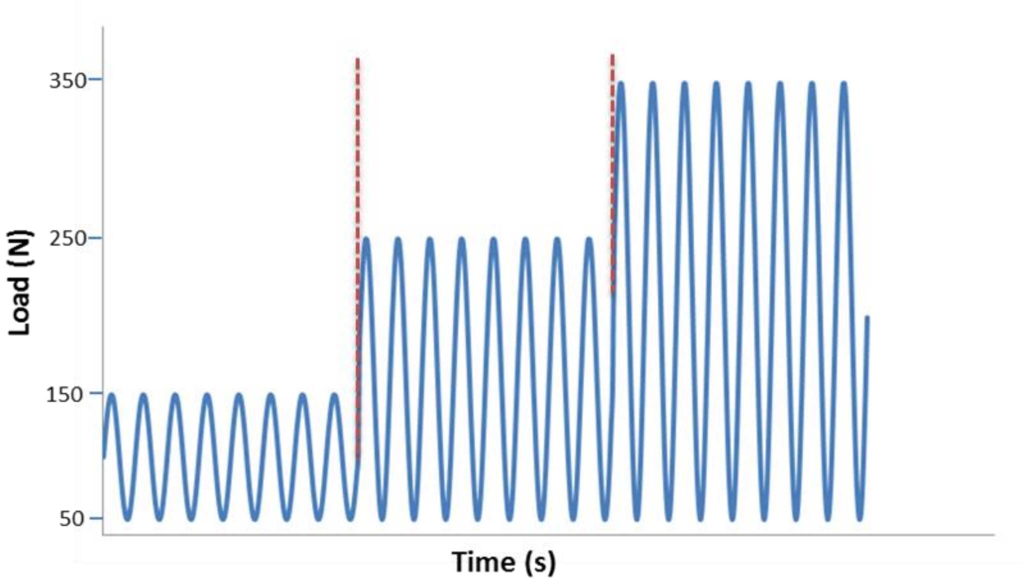

Figure 5.1 Fatigue loading scheme

5.2 Apparatus

In this second phase of the project, the MAT setup that was developed for the monotonic loading tests, was extensively modified to be able to study the fatigue response of the membrane products.

Starting point was that as much of the existing setup had to be reused, including the mounting frame. The current setup was evaluated and the conclusion was that the current actuator and motor drive had to be upgraded to fulfill the specifications necessary for fatigue testing of membrane products. A market survey was initiated to identify alternative actuators and servo drives. After having approached several manufacturers, an actuator and servo-drive from the LinMOT company was chosen. The LinMOT solution offers an embedded force and position control mode.

The new MAT set up is capable of operating in both a monotonic or a cyclic mode. In monotonic mode the actuator and servo drive will be used under displacement control. The user inputs a desired displacement and a desired displacement speed. During this motion (ramp up phase), the applied force to the sample, the position of the piston and the laser profiles are acquired and logged to a file. When the motion is completed the piston retracts to its initial homing position. The sampling frequency of the measured parameters during the ramp up phase is only limited by the rate at which the profiles can be acquired. The sampling frequency will typically be set to 20Hz, so every 50ms, the measured force, piston position and membrane profile will be stored on disk. The maximum time for the ramp up phase is 60 sec. The maximum speed of the displacement is 75mm/sec. The maximum allowed displacement from the bottom position is 150mm. The force constant for this actuator is 60N/A. The motor can thus deliver a maximum of 2040 Newton.

For cyclic testing the actuator and servo drive will be used in force controlled mode. In this mode the user specifies the following parameters in the user interface (UI):

- Maximum value of the applied sinusoidal force. The maximum allowed value is 500N.
- Minimum value of the applied sinusoidal force. The minimum allowed value is 50N.
- The frequency range is : 1 – 5 Hz.
- Snapshot interval time [# cycles]
- Table of processing intervals [# cycles]

A snapshot is defined as a complete acquisition of the measured signals for a limited amount of cycles (periods) of the sine wave. This in order to reduce the size of the data files that otherwise will be generated if all data had to be sampled continuously. The acquisition rate will be 50ms during acquisition of the snapshot.

The following data files are generated during cyclic mode:

- Data file containing: Timestamp @ Fmax, cycle number, minimum force value, maximum force value, displacement value @ Fmax, displacement value @ Fmin, phase angle between force and displacement @ Fmax and the profiles for the left and right laser. This file will have 2570 columns. Excel 2007 and 2010 support up to 16384 columns (AAA - XFD).
- Snapshot file containing cycle number, the sampled data of force value and displacement value.

Additionally the file will contain the phase angle that was calculated for the first cycle of the snapshot. The file will have 2569 columns. The file will be limited in size. When the file size exceeds the file size limitation, a new snapshot file will be generated.

The MAT setup is shown in Figure 5.2. The block schematic overview of the MAT control system is shown in Figure 5.3. The components that are used are listed in Table 5.1.

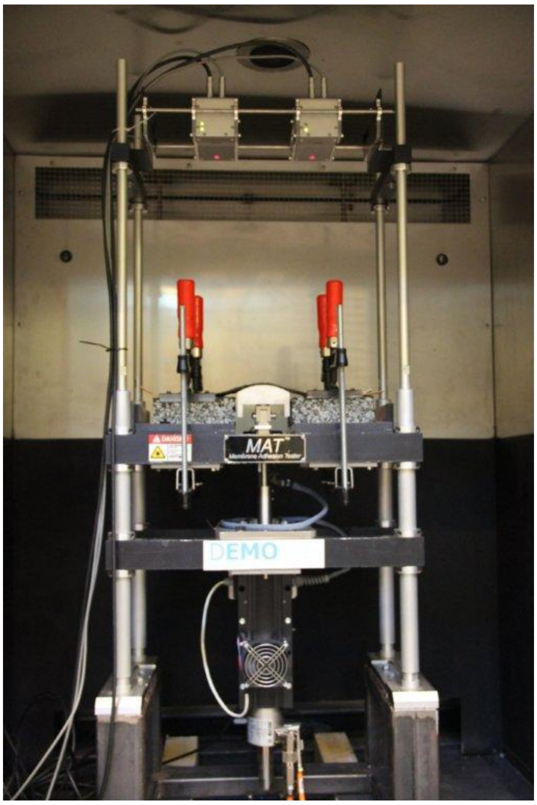

Figure 5.2 MAT set-up

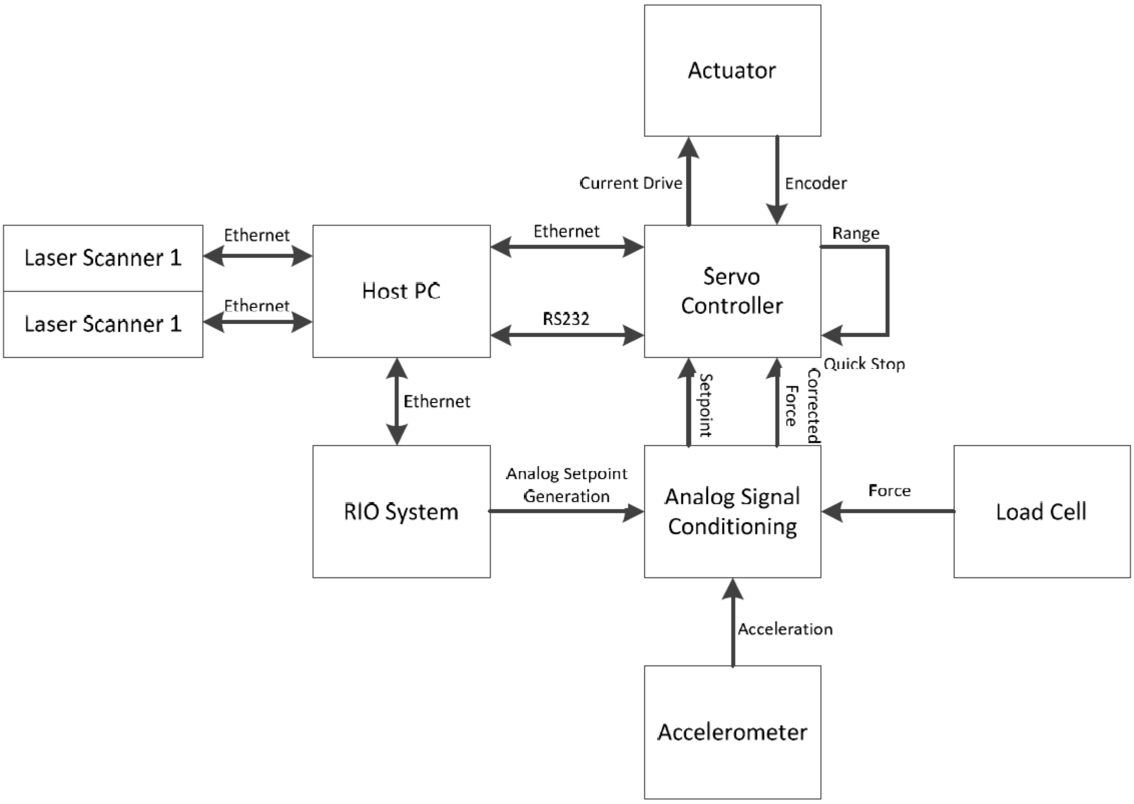

Figure 5.3 Block schematic overview of the MAT control and DAQ system

Component	Type	Manufacturer	Additional
Host PC			
Servo Controller	E1430-DP-QN	LinMOT	
Actuator(stator)	PS01-70x320	LinMOT	
Slider	PL10-28x590/540	LinMOT	
Load cell	2420-1000-B	Interface	1000 lbf
Accelerometer	Model4000A	Measurement Specialities	+/- 100g
Laser scanner 1	LLT2700-100	Micro Epsilon	
Laser scanner 2	LLT2700-100	Micro Epsilon	
Analog signal conditioning		DEMO	

Table 5.1 Used MAT components

5.3 Dissipated Energy Approach for Fatigue Analysis

Fatigue damage/failure in pavements occurs as a result of repeated traffic loading and temperature. In order to study this phenomenon, experimental laboratory testing techniques have been developed by Irwin and Gallaway, (1974) and Porter and Kennedy, (1975), theoretical models by Ramsamooj, (1991, 1999) Baburamani, (1999) Lee et al., (2000) Rodrigues, (2000) Zhang and Raad, (1999, 2001), Lundstrom and Isacsson, (2003) and data analysis methods to predict the fatigue performance of asphalt paving mixtures Pell and Cooper, (1975), Van Dijk, (1975) Hopman et al., (1989) Pronk and Hopman, (1990) Tayebali et al., (1992, 1993) Rowe, (1993)Kim et al., (1997) Ghuzlan and Carpenter, (2000) Rowe and Bouldin, (2000) Al-Khateeb and Shenoy, (2004).

Fatigue failure of a material has been defined in various ways in the asphalt pavement literature, Van Dijk and Vesser, (1977) Pronk and Hopman, (1990) Tayebali et al., (1992, 1993), developed fatigue failure criteria based on the mode of loading. Hopman et al., (1989) Rowe, (1993) Kim et al., (1997), Rowe and Bouldin, (2000) Ghuzlan and Carpenter, (2000). Used energy methods to define fatigue failure,

Fatigue testing can be conducted using the constant stress mode and the constant strain mode of testing. In the constant stress mode of testing, Pell and Cooper, (1975) and Tayebali et al., (1992), defined fatigue failure as the complete fracture of the specimen due to tensile strains. Other researchers such as Rowe (1993) defined fatigue failure when the initial complex modulus has been reduced by 90%. Van Dijk (1975) defined fatigue failure as occurring when the initial strain doubled.

In the constant strain mode of testing, since the stress decreases during the fatigue test while strain stays constant, defining fatigue failure is more difficult. The most common and widely used definition for fatigue failure in the constant strain mode is the 50% reduction in the initial stiffness as defined by Pronk and Hopman (1990) and Tayebali et al. (1992, 1993). A 50% reduction in the initial modulus was also defined as fatigue failure by Van Dijk and Vesser (1977). Subsequently, the 50% reduction in stiffness was adopted to define the fatigue failure point by the AASHTO as a provisional standard TP8-94 (2002).

When a material is subjected to cyclic loading will accumulate damage. The material will fail when it becomes damaged to the point at which it cannot carry any more loads. Therefore, damage can be defined as the deterioration that occurs in the material prior to failure (reduction in the structure integrity of the material under repeated loading).

Miner (1945) is one of the first researchers to relate failure of the material to damage. Several methods are being used to study damage in asphalt concrete pavement (Kim and Little 1990, Lee and Kim 1998). Dissipated energy was used as an indicator of damage in the asphalt layer (Van Dijk 1975; Van Dijk and Visser 1977, Pronk and Hopman (1990). These studies assumed that the fatigue life depends on the accumulation of dissipated energy from each load cycle. In later studies, damage was related to the rate of change in dissipated energy from one cycle to the next Carpenter and Jansen (1997).

Extensive effort was directed towards using dissipated energy in the study of fatigue behaviour of asphalt concrete because of its potential to overcome many of the problem with current approaches. The dissipated energy approach has many advantages. For example, it is simple in principle and easy to use, requiring only the dissipated energy in each load cycle.

The dissipated energy concept has been widely utilized for four-point bending beam (4PB) test to characterize the fatigue life of asphalt concrete mixture. In most cases, the four-point bending beam consists of only one layer of same mixture. The advantage of 4PB test has the advantage of providing a constant bending moment and zero-shear over the length of the beam. Assuming that the deflection due to the shear is neglected, this produces uniform bending in the central third of the beam and simplifies the analysis.

5.3.1 Dissipated Energy Concept

When a constant load is applied to a viscoelastic material, the area under the stress-strain curve represents the energy being input into the material. During the loading-unloading process, the unloading curves coincide with the loading curves if all the energy is totally recovered, see Figure 5.4. If the two curves do not coincide but trace different paths, an energy loss is happened within the material. Part of the energy is transported, or say dissipated, out of the material system due to the external work, in the form of mechanical work, heat generation, or damage. This phenomenon is called "Hysteresis" and the energy change within one load cycle is the dissipated energy which equals to the area within the hysteresis loop. A plot of the stress–strain hysteresis loop has been shown in Figure 5.5.

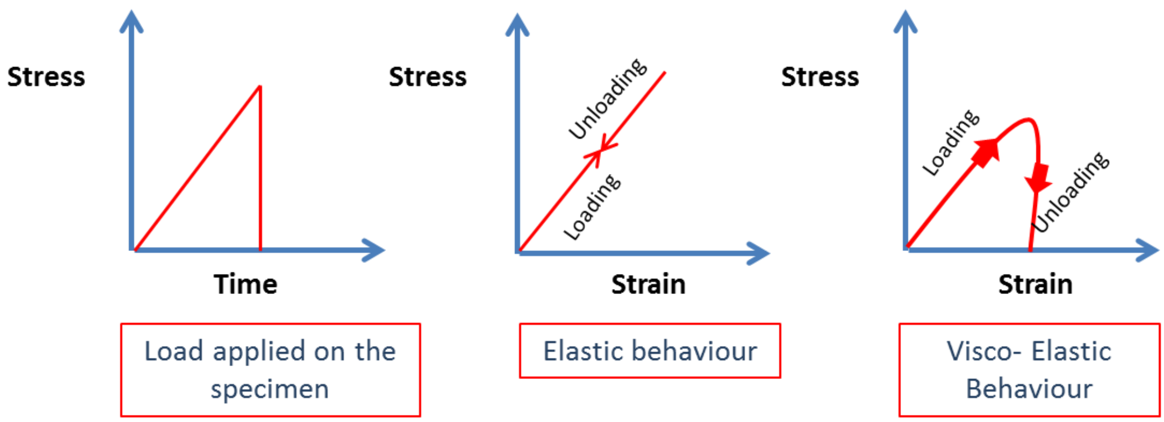

Figure 5.4 Elastic and Visco-Elastic behavior

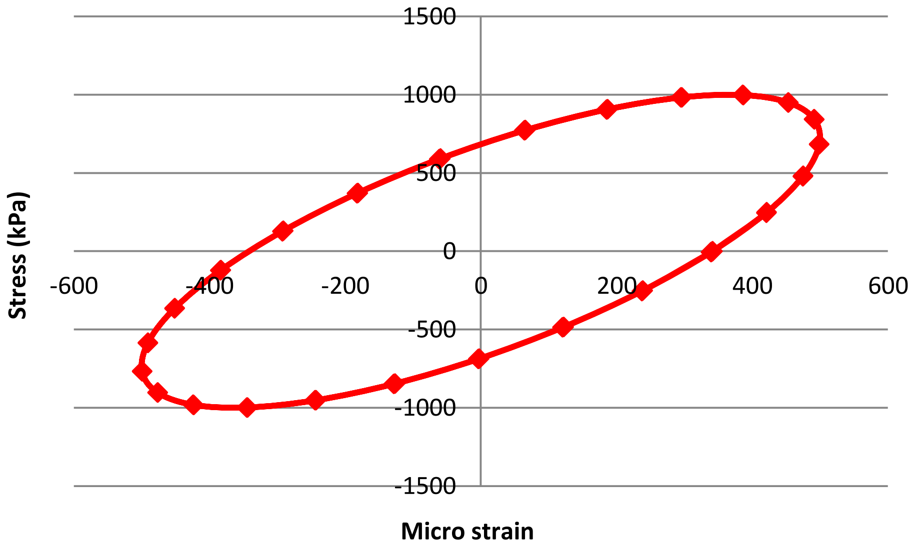

Figure 5.5 A stress-strain hysteresis loop (one load cycle)

The dissipated energy from cycle loading can be determined by calculating the energy losses associated with the phase angle, see Figure 5.6. The area of the hysteresis loop represents the dissipated energy and the following equation can be used to calculate its value in a linear viscoelastic material:

$$DE_i = \pi \sigma_i \varepsilon_i \sin \phi_i \tag{5.1}$$

where:

DE_i = Dissipated energy in cycle i;

σ_i = Stress level in cycle i;

ε_i = Strain level in cycle i;

ϕ_i = Phase angle between σ and δ in cycle i;

For certain case, if stress σ is not a directly measurable quantity, the above equation can be expressed also in term of dissipated work and the similar equation can be used:

$$DW_i = \pi F_i \delta_i \sin \phi_i \tag{5.2}$$

where:

DW_i = Dissipated work in cycle i;

F_i = Force level in cycle i;

δ_i = Displacement level in cycle i;

ϕ_i = Phase angle between F and δ in cycle i;

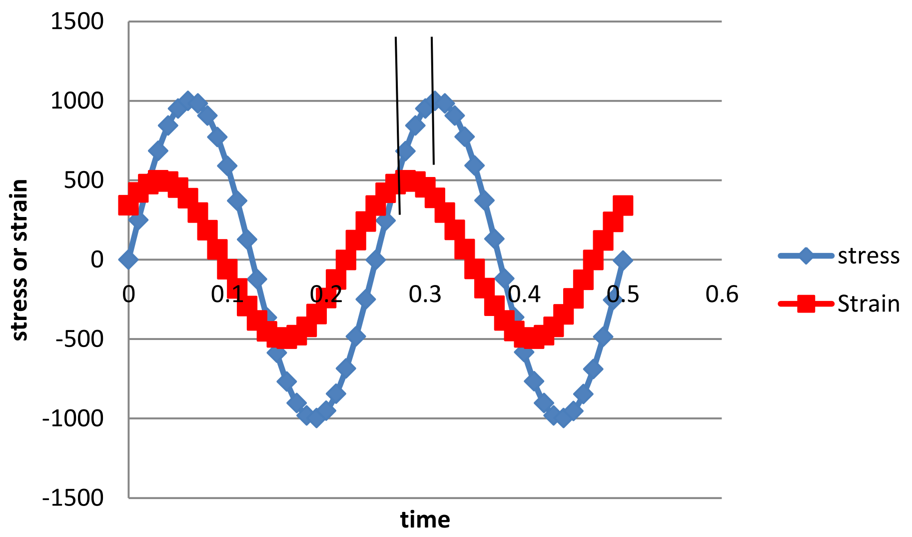

Figure 5.6 Oscillating stress, strain and phase angle

During a fatigue test, where repeated stresses are applied to a sample below the failure stress, the stiffness reduces and microcracks are induced to the material, therefore the dissipated work DW, varies per loading cycle.

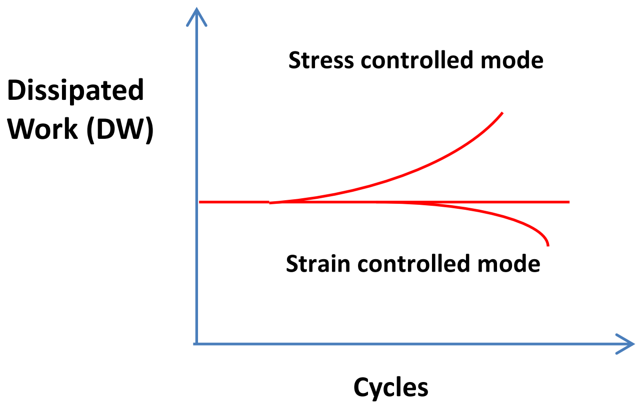

Figure 5.7 Dissipated energy versus Load cycle for different loading modes

The energy dissipated during each loading cycle captures effects not only of the imposed strain but also of the mixture properties. In fatigue testing, the amount of energy dissipated per loading cycle changes throughout the fatigue test in different manners for different loading modes. It increases in a controlled stress test while decreases in a controlled strain test Figure 5.7. One simple dissipated energy parameter cannot describe the two modes of fatigue tests consistently, thus the fatigue results are treated differently depending on different loading modes in the traditional analysis.

5.3.2 Ratio of Dissipated Energy Change (RDEC) Approach

A few researchers have considered using the dissipated energy concept to relate fatigue damage Carpenter, Ghuzlan and Shen (2003), Rowe,(1993), Tayebali, Deacon, Coplantz, and Monismith,(1993), Van Dijk,(1975), Van Dijk and Vesser,(1977), Baburamani and Porter,(1996). Some used the initial dissipated energy, others the total dissipated energy, or simply the dissipated energy vs. load cycle. Van Dijk (1975,1977) found that there is a solid relationship between the total amount of energy dissipation and the number of loading cycles to failure. This relationship is highly material dependent, however the loading mode, the effect of frequency and temperature do not influence significantly. Pronk and Hopman, (1991) suggested the dissipated energy per cycle/period is responsible for the fatigue damage. Tayebali et al. (1992) introduced two terms: the stiffness ratio which is the ratio of the stiffness at load cycle (i) to the initial stiffness; and the dissipated energy ratio which is defined as the ratio of cumulative dissipated energy up to load cycle (i) to the cumulative dissipated energy up to fatigue life. His work suggested there is a unique relationship between the stiffness ratio and the dissipated energy ratio, but not necessarily between cumulative dissipated energy and fatigue life.This relation was found to be mixture and temperature dependent.

Unfortunately all the approaches introduced above tend to be inadequate. They are either material or loading mode dependent, or both. Rowe, (1993) obtained good results using the rate of change in dissipated energy to indicate fatigue failure. Carpenter and Jansen (1997) also showed that the change in dissipated energy can be more directly related to damage accumulation and fatigue life. This work was refined and expanded by Ghuzlan,(2001) and

Ghuzlan and Carpenter (2000), and a detailed dissipated energy ratio analysis was further developed by Carpenter, Ghuzlan, and Shen (2003).

According to these studies, the rate of change in dissipated energy by itself does not provide for a single unified method to examine failure in different test modes. That is, the precise same variable or procedure is not used in each mode to define failure. Thus, failure is still determined differently for the different fatigue modes. To overcome this difficulty, Ghuzlan and Carpenter (2000) examined a ratio of the change in dissipated energy between two cycles divided by the dissipated energy of the first cycle.

In general, energy dissipated in a cycle depends on the energy dissipated in the previous cycles, or in other words, it is history (path) dependent Erberik and Sucuoglu, (2002). As shown in Figure 5.8, during a cyclic fatigue test, the stress-strain hysteresis loop of later load cycles do not overlap with the previous ones and the area of the loops has been changed, indicating some damage has been done to the material. For a sample material, in order to have damage there must be a change in dissipated energy (Ghuzlan, 2001). In every cycle, only a part of the dissipated energy contributes to damage. The rest is dissipated by means of viscous deformations, heat generation etc.

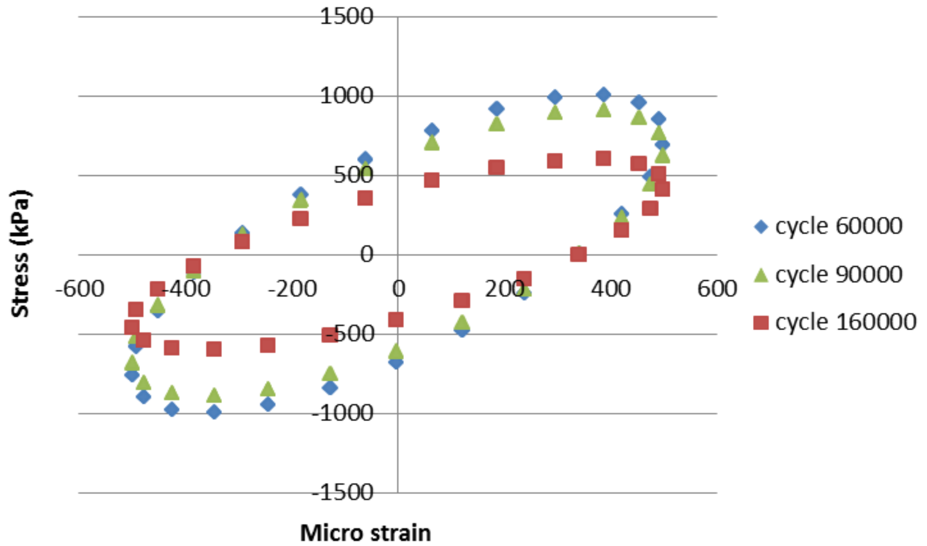

Figure 5.8 Different stress-strain hysteresis loop, controlled strain testing

The relative change value of dissipated energy has a direct relation to damage accumulation. A low amount of relative change in energy dissipation can be found either in high fatigue resistance materials, low external loading amplitudes, or both. Such relative change in dissipated energy represents the total effect of fatigue damage without the necessity of considering material type, loading modes and severity separately.

This concept was first initiated by Carpenter and Jansen (1997) who suggested using the change in dissipated energy to relate damage accumulation and fatigue life. The work was refined and expanded by Ghuzlan and Carpenter (2000), and then well applied and verified by Carpenter et al. (2003) which uses the ratio of dissipated energy change (RDEC) as an energy parameter to describe HMA fatigue damage. This ratio can be represented as:

$$RDEC_a = \frac{DE_a - DE_b}{DE_a\left(b-a\right)} \tag{5.3}$$

where:

$RDEC_a$ = the average ratio of dissipated energy change at load cycle a, comparing to next cycle b;
a, b = load cycle a and b, respectively. The typical cycle count between cycle a and b for RDEC calculation is 100, i.e., b-a=100;
DE_a, DE_b = the dissipated energy produced in load cycle a, and b, respectively;

Similar as Eq. (5.2), Eq. (5.3) can be expressed by using the ratio of dissipated work change (RDWC) as:

$$RDWC_a = \frac{DW_a - DW_b}{DW_a\left(b-a\right)} \tag{5.4}$$

where:

$RDWC_a$ = the average ratio of dissipated work change at load cycle a, comparing to next cycle b;
a, b = load cycle a and b, respectively. The typical cycle count between cycle a and b for RDWC calculation is 100, i.e., b-a=100;
DW_a, DW_b = the dissipated work produced in load cycle a, and b, respectively;

RDEC or RDWC eliminates the energy that dissipates in other forms without producing damage. This provides a true indication of the damage being done to the mixture from one cycle to another by comparing the previous cycle's energy level and determining how much of it caused damage.

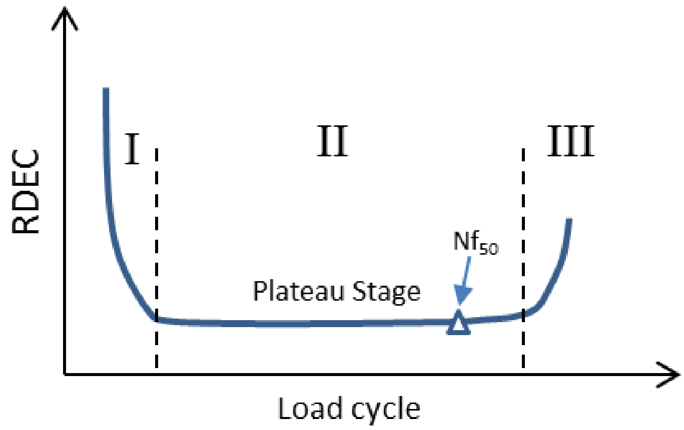

Figure 5.9 Typical RDEC plot with three behaviour zones (Carpenter et al. 2003)

As introduced by (Ghuzlan 2001) and Carpenter et al. (2000, 2003, 2005), the damage curve represented by RDEC vs. loading cycles can be distinctively divided into three stages. The schematic chart is given in Figure 5.9. Such damage curve develops a plateau after the initial period. This plateau stage (stage II), an indication of a period where there is a relatively constant percentage of input energy being turned into damage, will extend throughout the main service life until a dramatic increase in RDEC, which gives a sign of true fatigue failure (stage III). The RDEC curve is representative for fatigue behavior. RDEC curves with similar trend: a rapid decrease, followed by a plateau region for the majority of the fatigue cycles, have also been noticed in Portland Cement Concrete material fatigue testing (Daniel and Bissirri, 2005) and bitumen binder fatigue testing (Shen et al., 2006). In the plateau stage (stage II), the RDEC value is almost constant, characterizing a period where there is a constant percentage of input energy being turned into damage. Also the stiffness follows a three stage evolution process see Figure 5.10 after a rapid evolution of stiffness (phase I), stiffness decrease seems more regular (phase II); fracture occurs in the final stage (phase III) and it is characterised by an acceleration stiffness drop Therefore another good point is a correlation between the three stage evaluation of stiffness with the tree stage evaluation of dissipated energy.

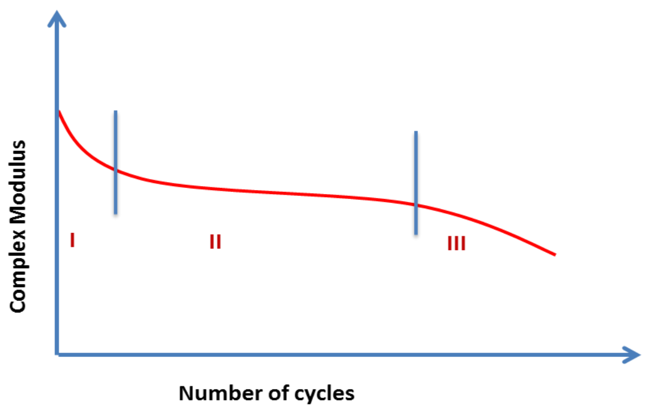

Figure 5.10 Variation of stiffness as a function of load cycles

In the plateau stage (stage II), the RDEC value is almost constant, characterizing a period where there is a constant percentage of input energy being turned in to damage. A plateau value is defined as the RDEC value corresponding to the 50% stiffness reduction load cycle (Nf50). This typical value was selected because at this load cycle (Nf50), the RDEC is always in the plateau stage and the Nf50 is the defined failure point. The plateau value is a comprehensive damage index that contains the effect of both material property and loading effect, hence can be fundamental energy parameter to represent fatigue behaviour. A low plateau value can be found either in high fatigue resistant materials, low external loading amplitude or both. In this research, fatigue failure (Nf) refers to the 50% initial structure stiffness reduction.

5.4 Fatigue tests conducted at 10^0C

Product A1

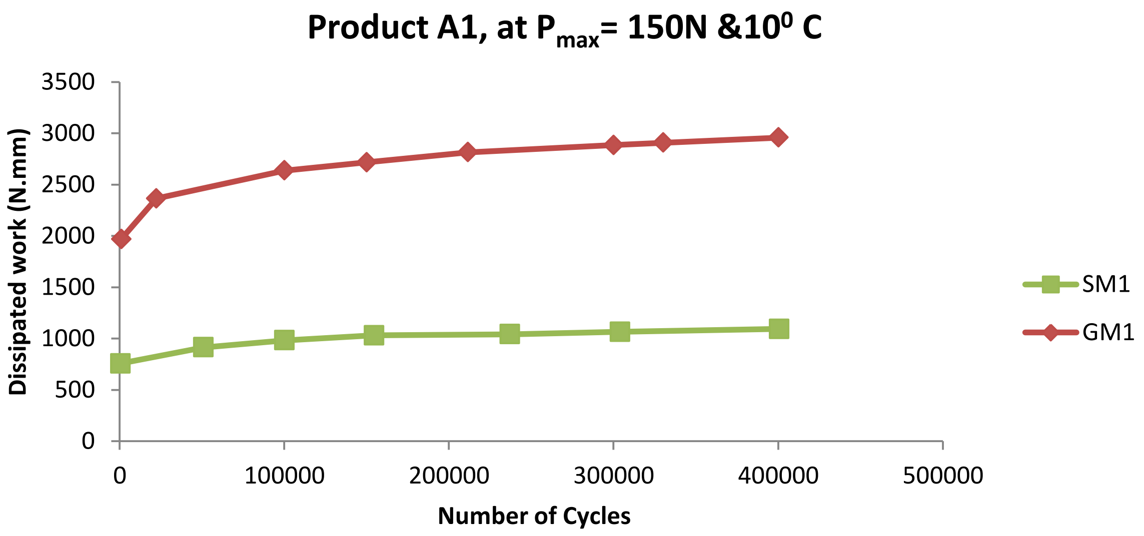

Figure 5.11 Dissipated work vs number of cycles P_{max}=150N

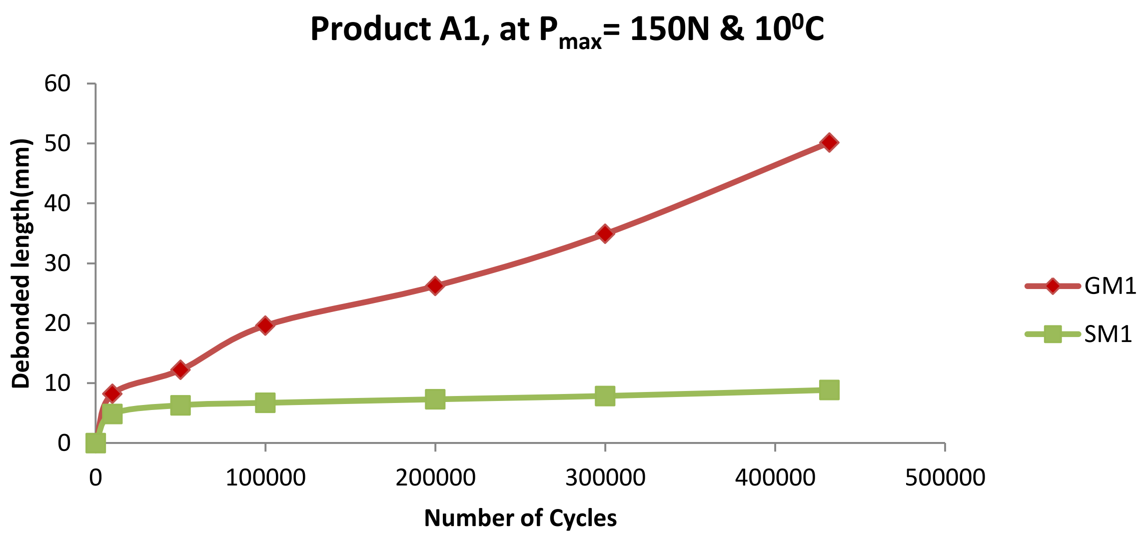

Figure 5.12 Debonded length vs Number of cycles P_{max}=150N

In Figure 5.11 and Figure 5.12 the results for product A1 at P_{max}=150N & 10^{o}C are presented. It can be observed for product A1, higher dissipated work was spent on debonding the GM1 interface than SM1. It can also be seen that debonding of the SM1 stops to develop after 2000 load cycles. However the larger and faster development of the debonding length of the GM1 interface can be observed in Figure 5.12

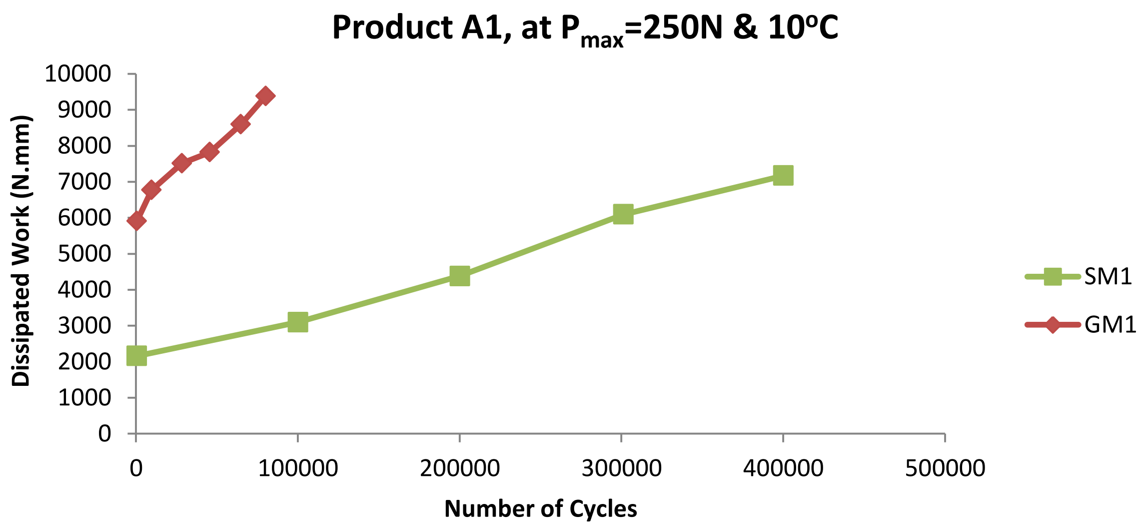

Figure 5.13 Dissipated work vs number of cycles at P_{max}=250N

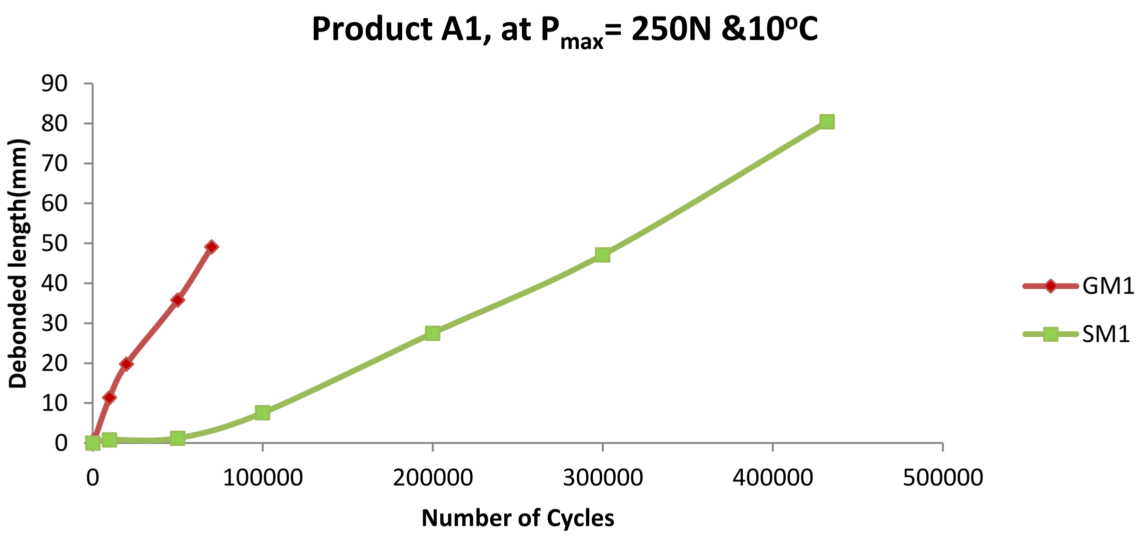

Figure 5.14 Debonded length Vs Number of cycles P_{max}=250N

When the load applied on the membrane was increased to 250N, higher work has dissipated in the GM1 interface indicating faster damage (debonding) development, Figure 5.13 and Figure 5.14. The GM1 interface failed at 100,000 load cycles while the SM1 interface showed a stable debonding length propagation until the end of the test.

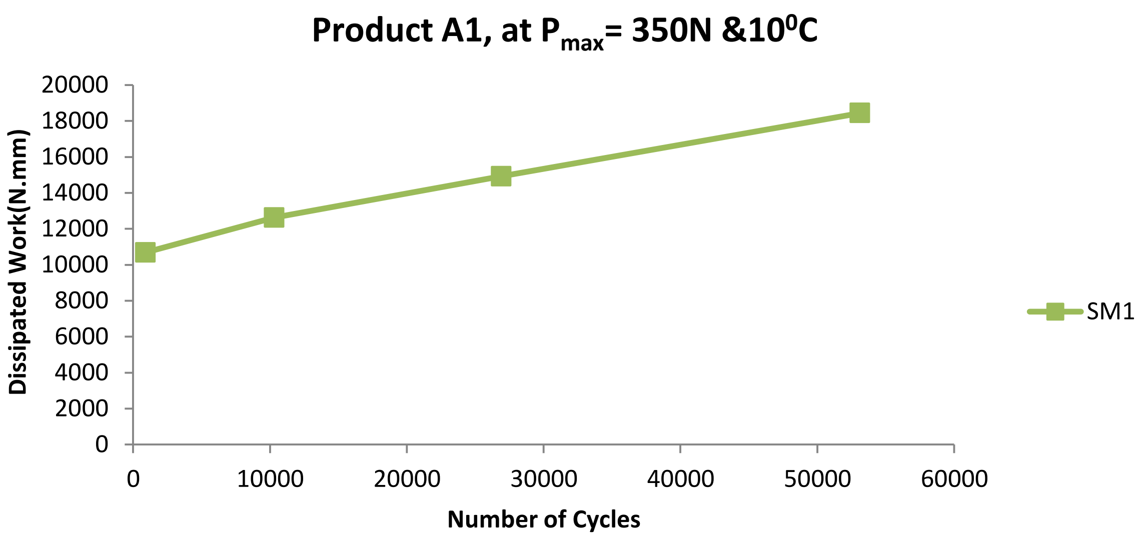

Figure 5.15 Dissipated work vs number of cycles P_{max}= 350N

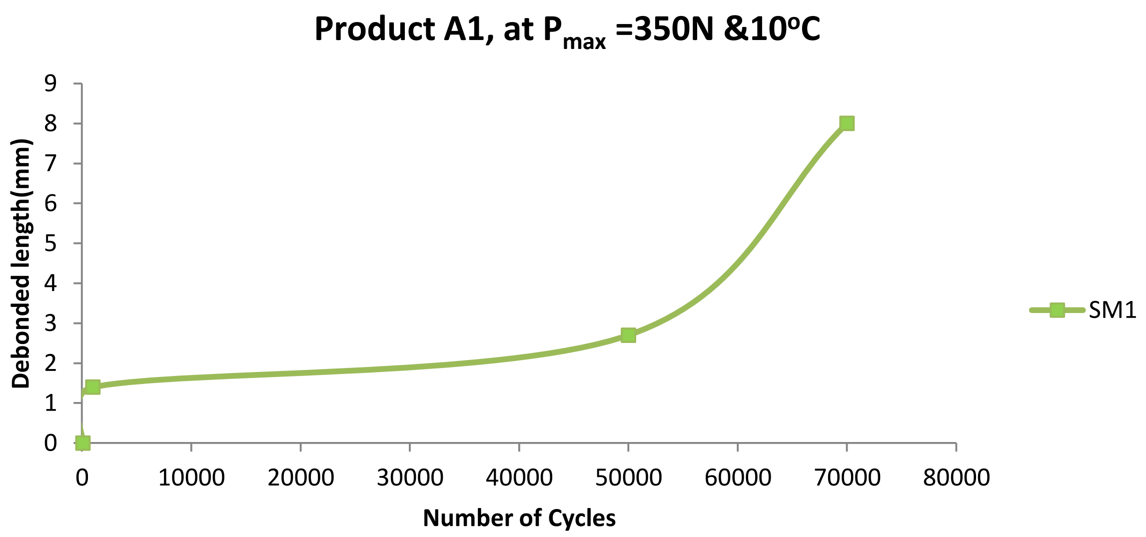

Figure 5.16 Debonded length Vs Number of cycles P_{max}=350N

In Figure 5.15 the results from product A1 at 350N load level are presented. At this load level only the SM1 interface has been tested due to the fact that the product A1 was already fully debonded from previous load level of 250N. Figure 5.16 presents the debonded length versus load cycles showing a steady development during the first 50,000 cycles and then a sudden increase causing full failure on this sample.

Product A2

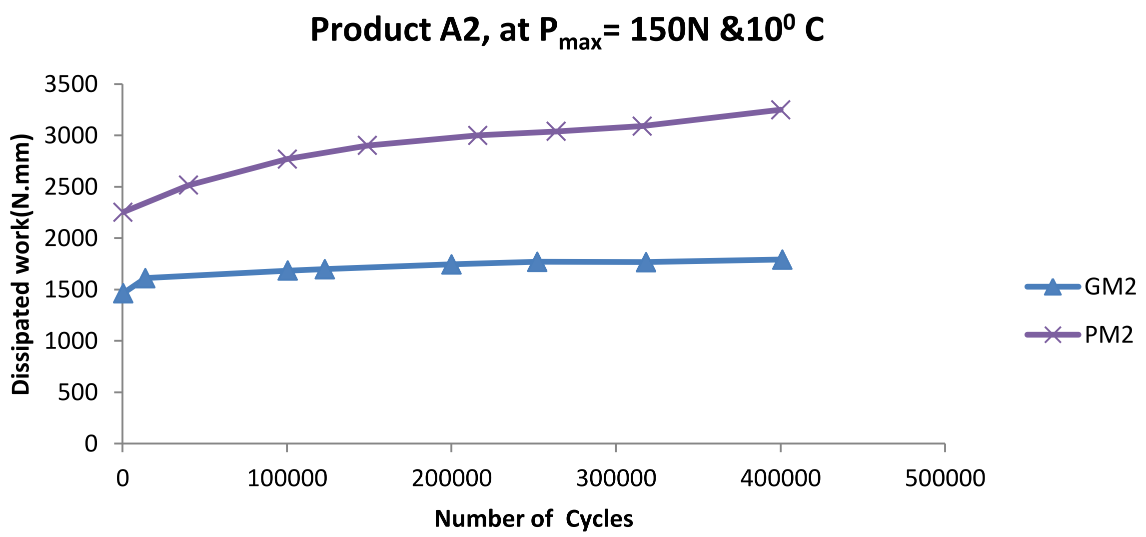

Figure 5.17 Dissipated work vs number of cycles at Pmax= 150N

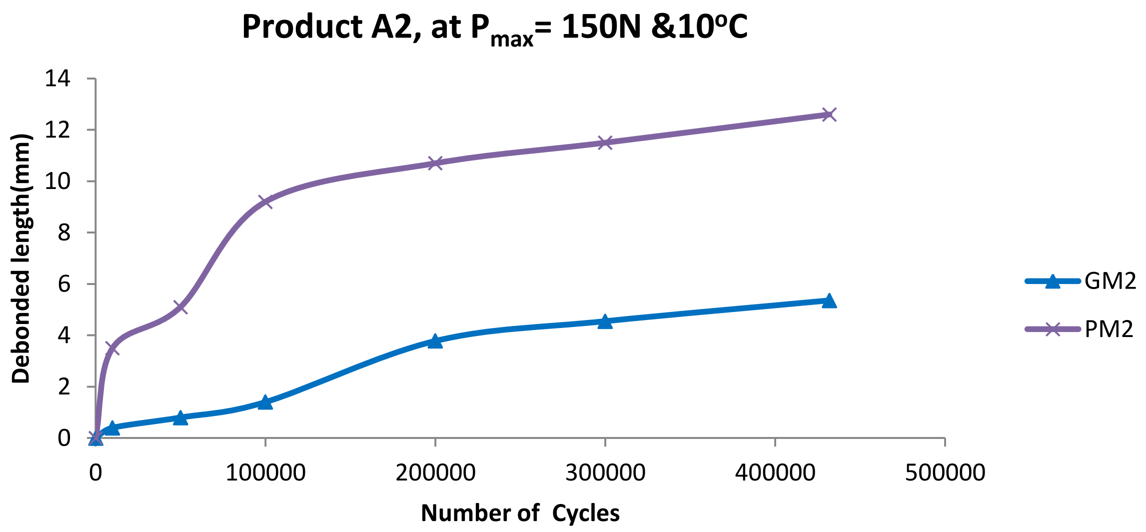

Figure 5.18 Debonded length vs number of cycles at P_{max}= 150N

In Figure 5.17 and Figure 5.18 the results from GM2 and PM2 interfaces are presented for product A2. At the load level of 150N, the best interface is the GM2 with lower values in terms of dissipated work but also in terms of debonded length. From Figure 5.18 it can be observed that product A2 at the PM2 interface debonded faster than the GM2 interface reaching higher values at the end of the fatigue test.

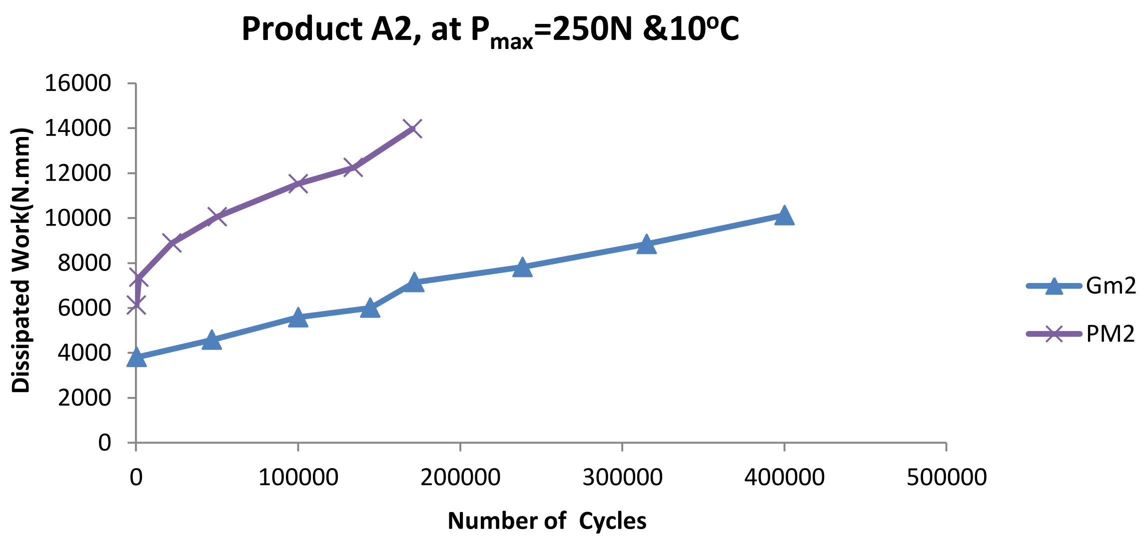

Figure 5.19 Dissipated work vs number of cycles at P_{max}= 250N

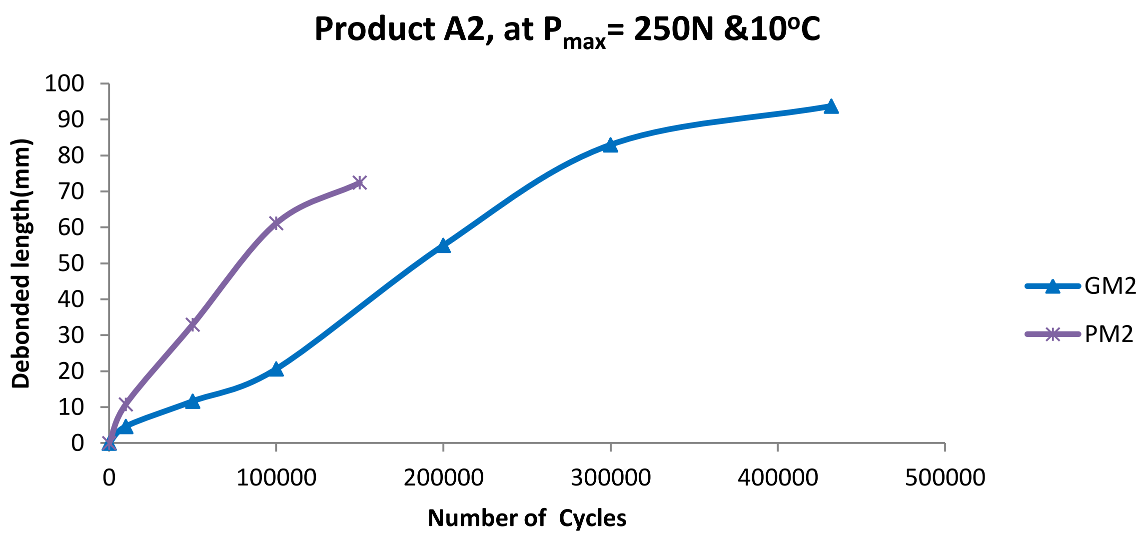

Figure 5.20 Debonded length vs number of cycles at P_{max}= 250N

Figure 5.19 and Figure 5.20 present the results for product A2 for GM2 and PM2 interfaces at 250N load level. Both figures show that the interface with the lower values in terms of dissipated work and debonded length is the GM2 interface. From Figure 5.20 it can be seen that the debonding process started immediately after loading, reaching maximum values after 120,000 load cycles.

The change of dissipated work as a function of the applied load is summarized and presented for all interfaces for product A1 and A2 in Figure 5.21,Figure 5.22,Figure 5.23 and Figure 5.24

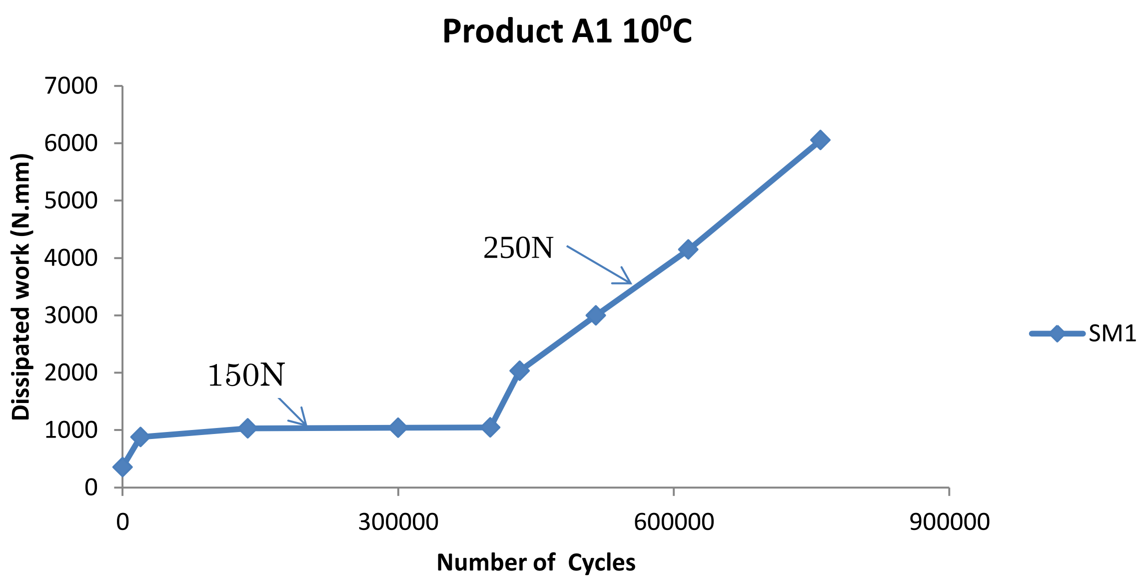

Figure 5.21 Dissipated work Vs number of cycles for product A1 at SM1 interface

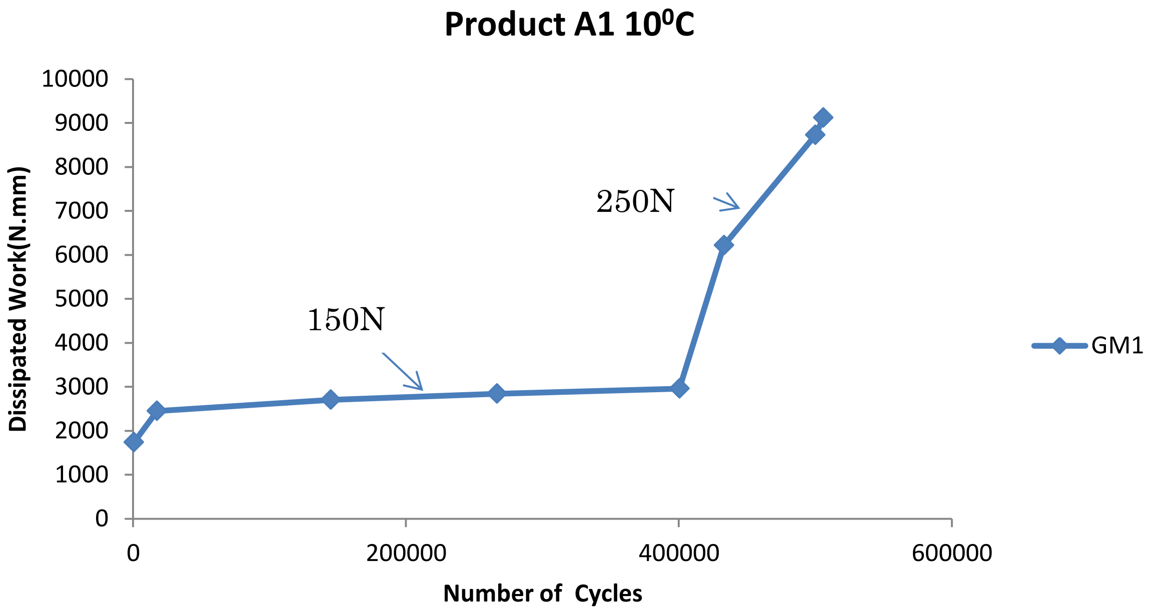

Figure 5.22 Dissipated work Vs number of cycles for product A1 at GM1 interface

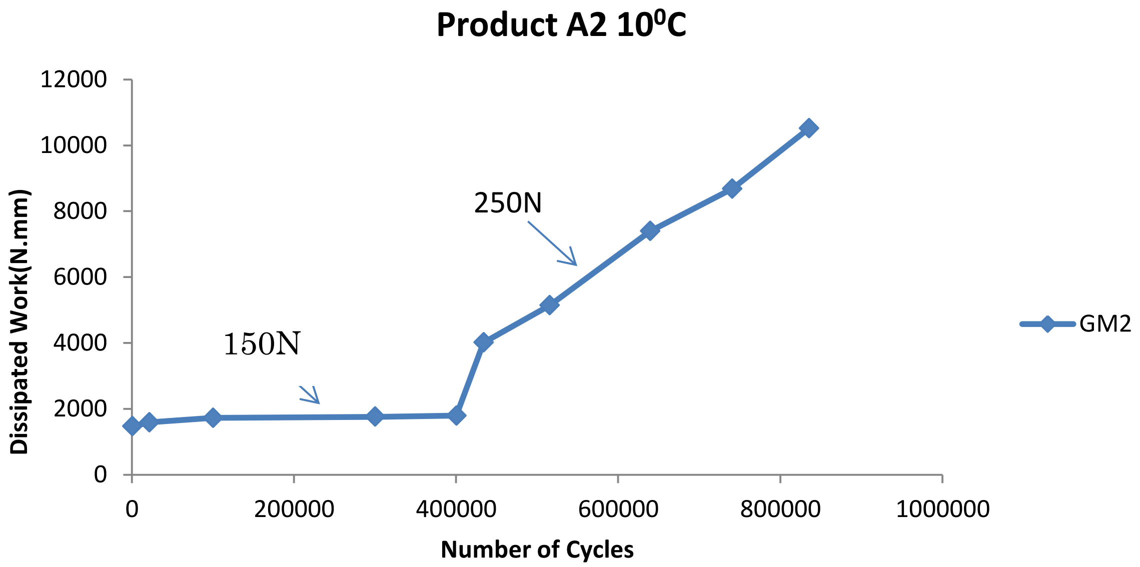

Figure 5.23 Dissipated work Vs number of cycles for product A1 at GM2 interface

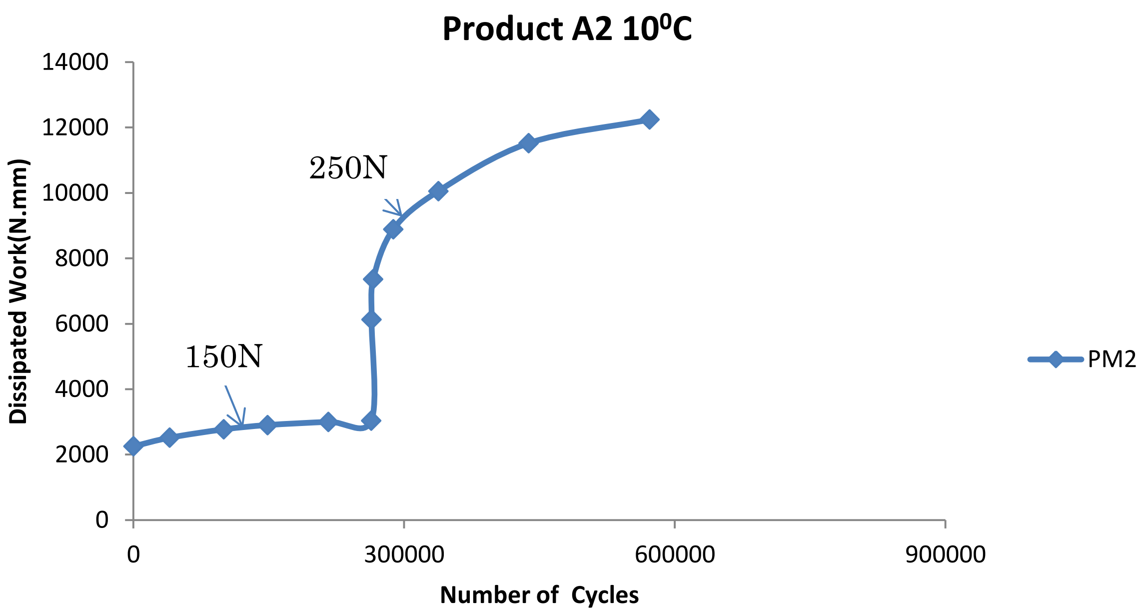

Figure 5.24 Dissipated work vs number of cycles for product A2 at PM2 interface

Product C1

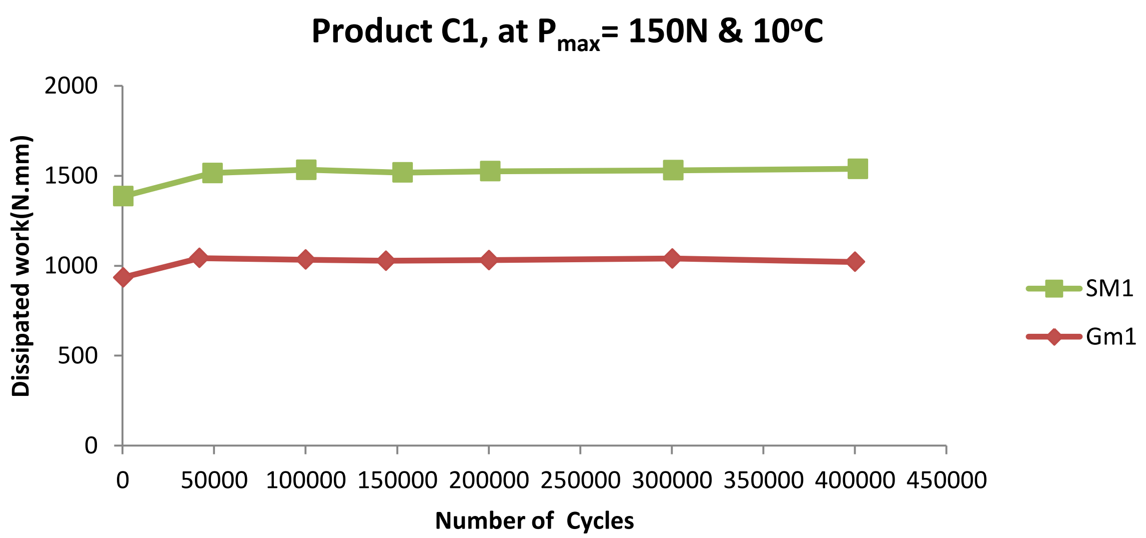

Figure 5.25 Dissipated work vs number of cycles at P_{max}= 150N

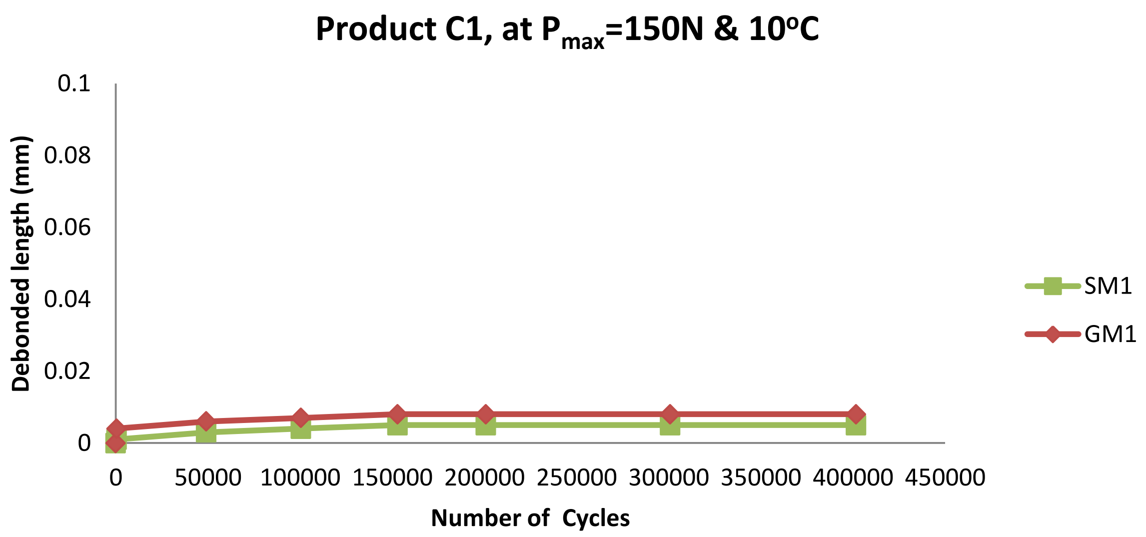

Figure 5.26 Debonded length vs number of cycles at P_{max}= 150N

As it can be observed from Figure 5.25, at load level of 150N, both interfaces of SM1 and GM1 with product C1 shared constant dissipated work during the completion of the fatigue test. Higher values were observed at the SM1 interface however from Figure 5.26 it can be seen that for both interfaces there is no change in the debonded length, proving the fact that there is no actual debonding at this level.

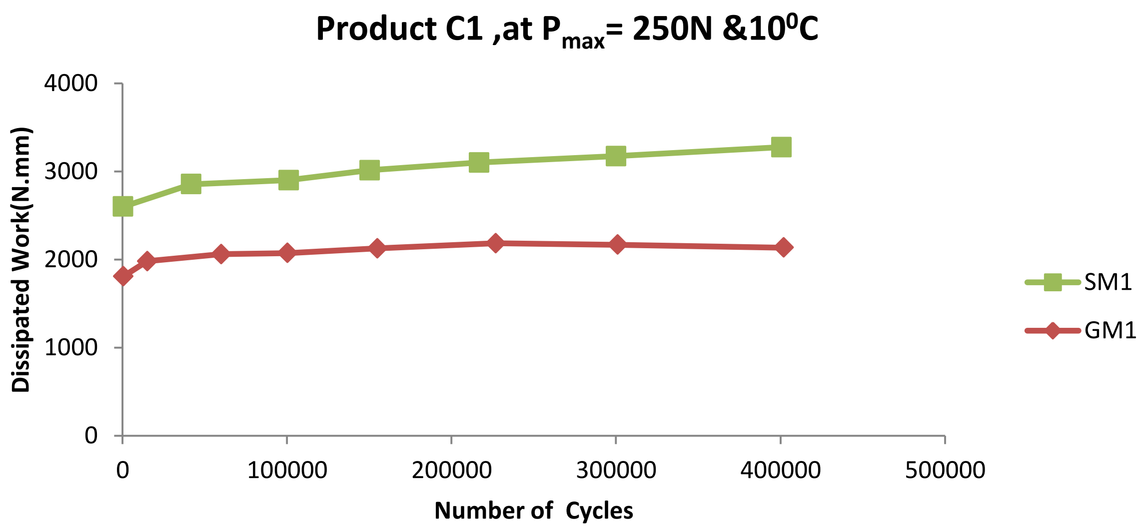

Figure 5.27 Dissipated work vs number of cycles at P_{max}= 250N

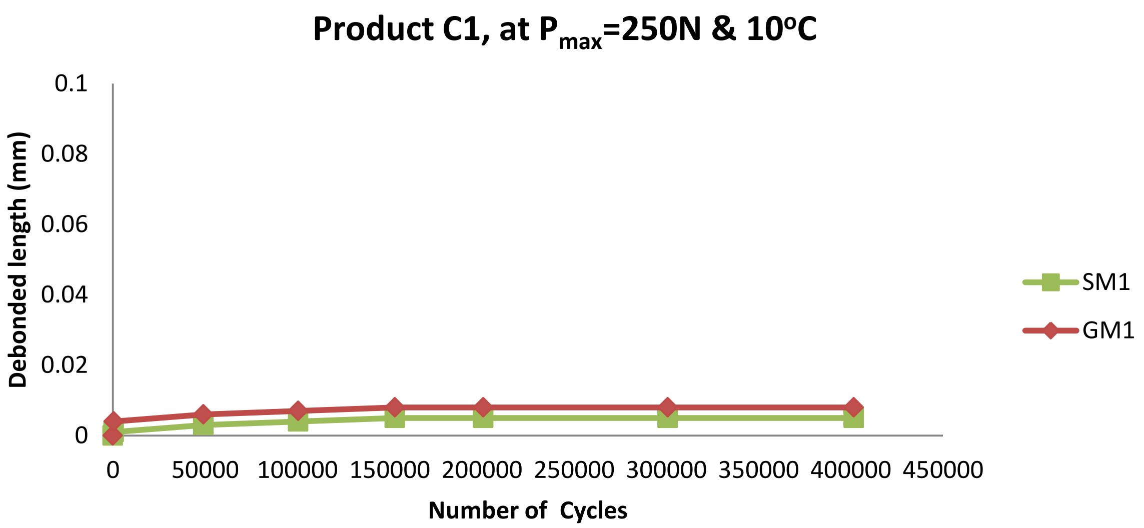

Figure 5.28 Debonded length vs number of cycles P_{max}= 250N

At load level of 250N, similar observations as the previous cases can be made for GM1 and SM1 interfaces of product C1, Figure 5.25 . The interface with the higer values is still the SM1 interface, Figure 5.27, however no change at the debonded length was observed Figure 5.28

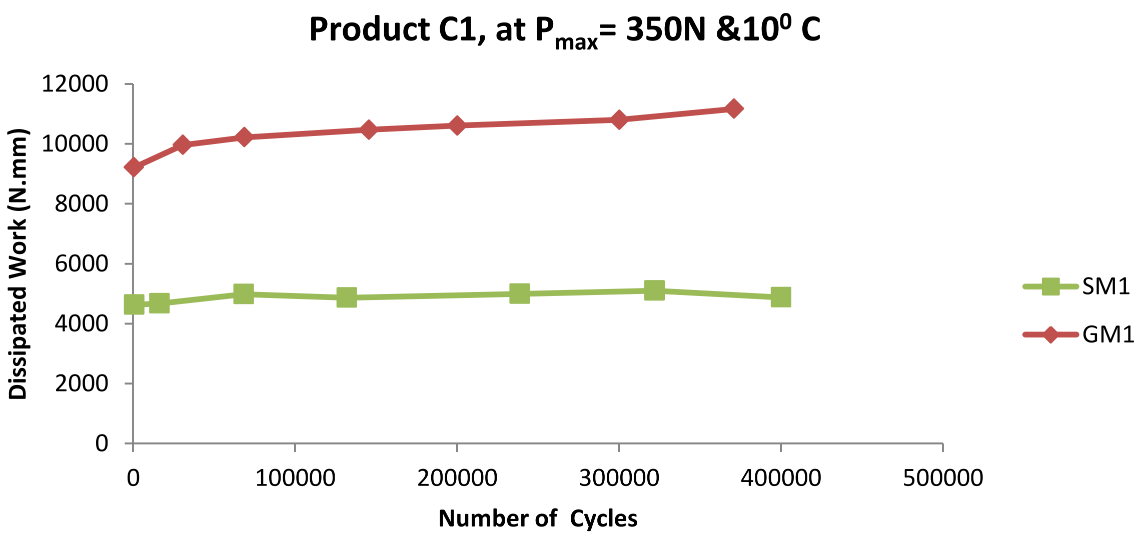

Figure 5.29 Dissipated work vs number of cycles at P_{max}=350N

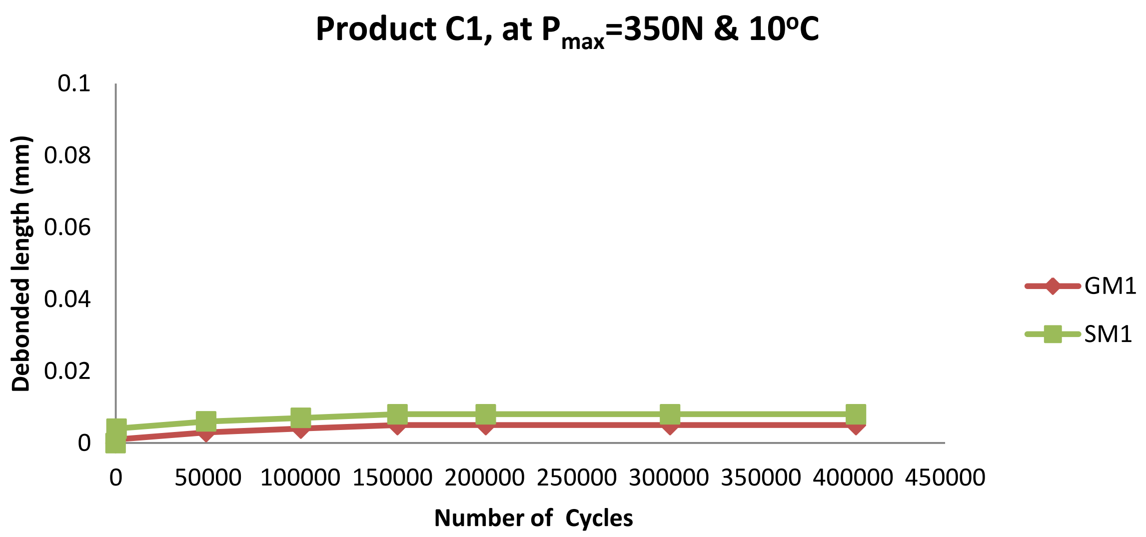

Figure 5.30 Debonded length vs number of cycles P_{max}=350N

Finally at a load level of 350N although the GM1 interface was found to be the one with the highest values in terms of dissipated work, no change observed at the debonded length for both interfaces, Figure 5.26. This means that debonding was no significant for product C1 at all predefined loading levels. The change in dissipated work due to change of the applied load levels is summarized and presented for all interfaces for product C1, in Figure 5.31 and Figure 5.32.

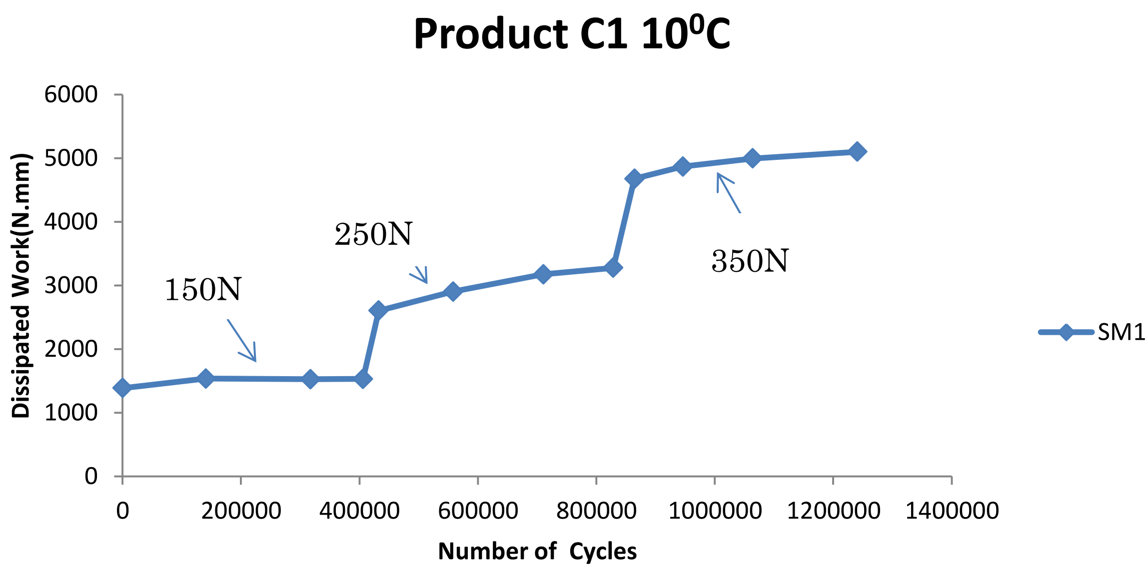

Figure 5.31 Dissipated work vs number of cycles for product C1 at SM1 interface

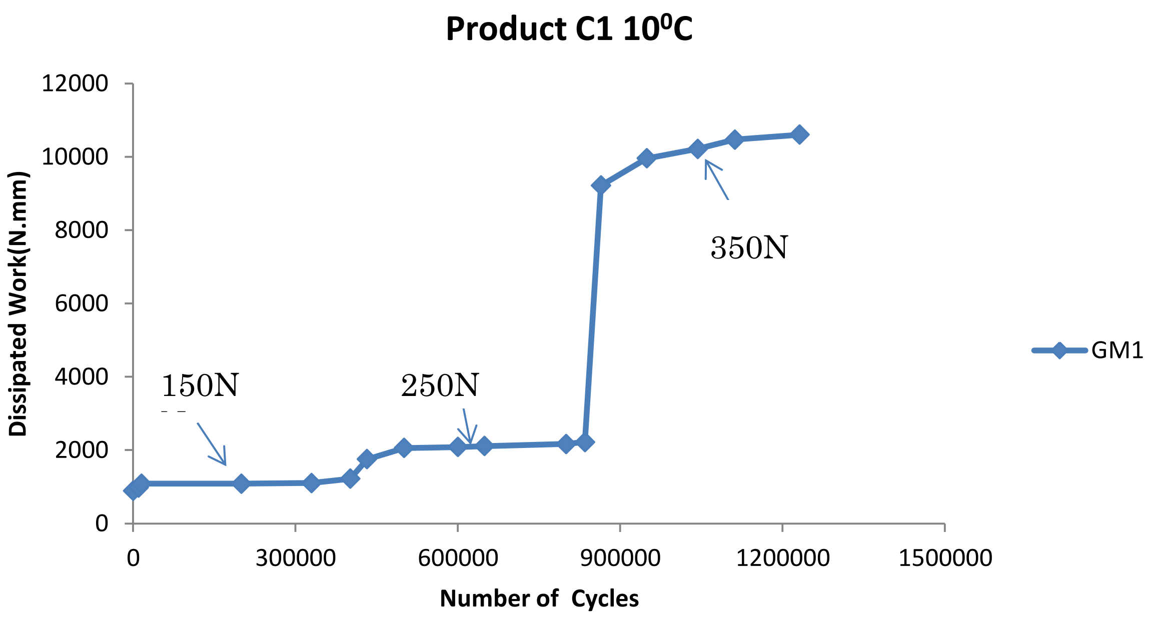

Figure 5.32 Dissipated work vs number of cycles for product C1 at GM1 interface

Product C2

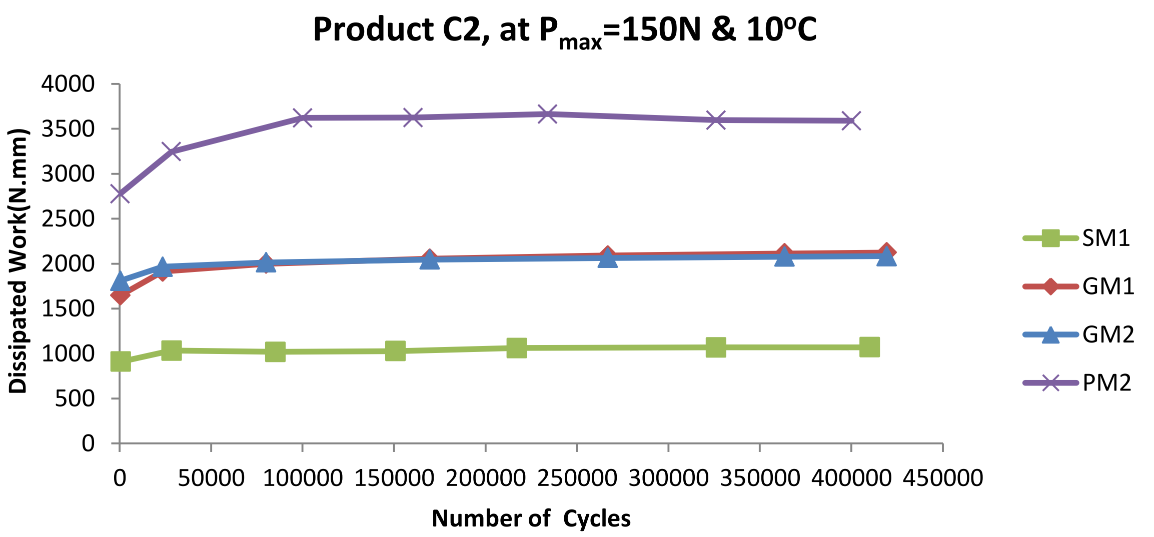

Figure 5.33 Dissipated work vs number of cycles at P_{max}=150N

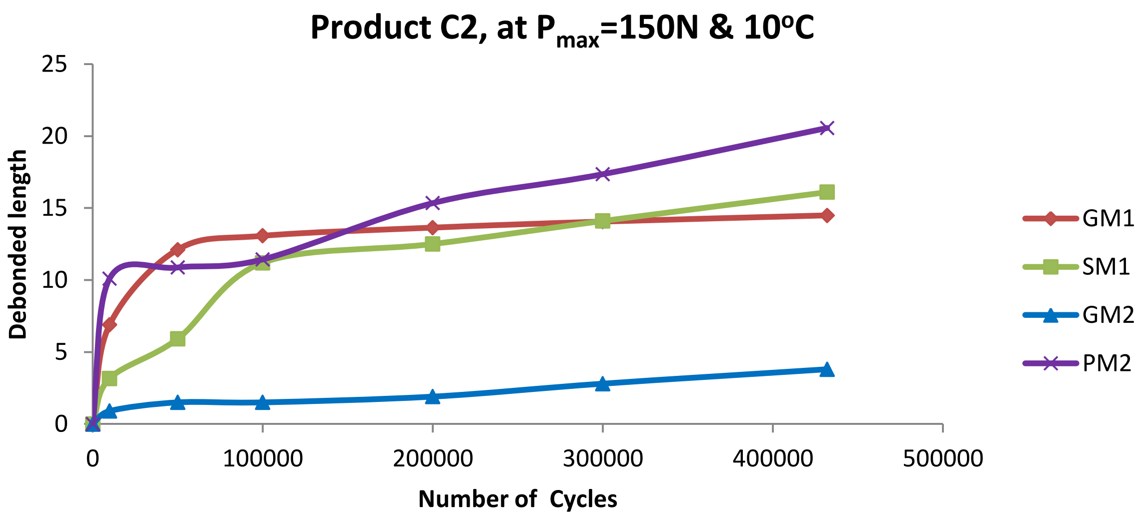

Figure 5.34 Debonded length vs number of cycles at P_{max}=150N

In Figure 5.33 the results from product C2 at 150N load level are presented. At this load level the SM1 interface has performed better than the others having the lower values in terms of dissipated work. GM1 and GM2 interfaces have identical response at this load level, however from Figure 5.34 it can be seen that GM1 debonds faster than the GM2 interface producing longer debonded length at the end of the fatigue test. The PM2 interface was found to be the worst one in terms of dissipated work and debonding length and debonding speed.

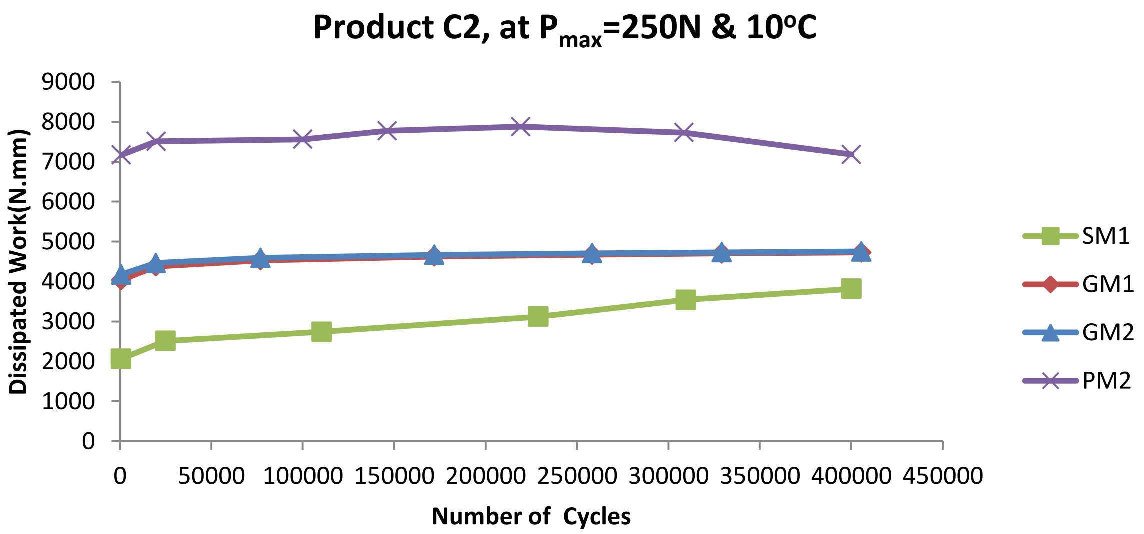

Figure 5.35 Dissipated work vs number of cycles at P_{max}= 250N

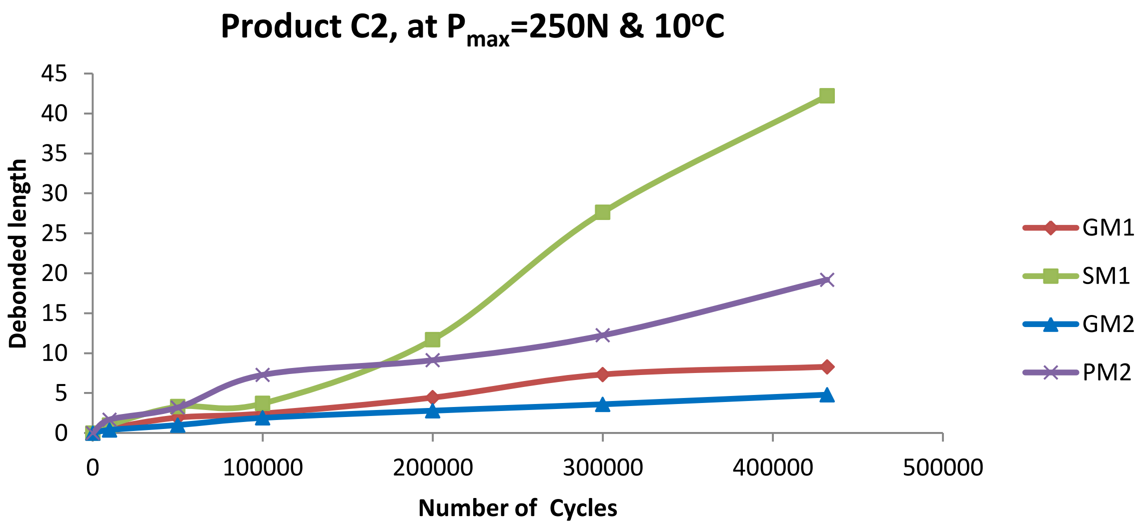

Figure 5.36 Debonded length vs number of cycles at P_{max}= 250N

Similar observations can be made for product C2 of a load level of 250N Figure 5.35. The SM1 interface performed better the other interfaces having the lower values in terms of dissipated work. However SM1 debonded faster after load cycle 100000. The GM1 and GM2 interfaces have identical response as the cases in the previous load level. From Figure 5.36 it can be seen that debonding in the GM1influence develops faster than at the GM2 interface producing higher values at the completion of the test. The PM2 interface was found to be the worst one in terms of dissipated work and debonding length.

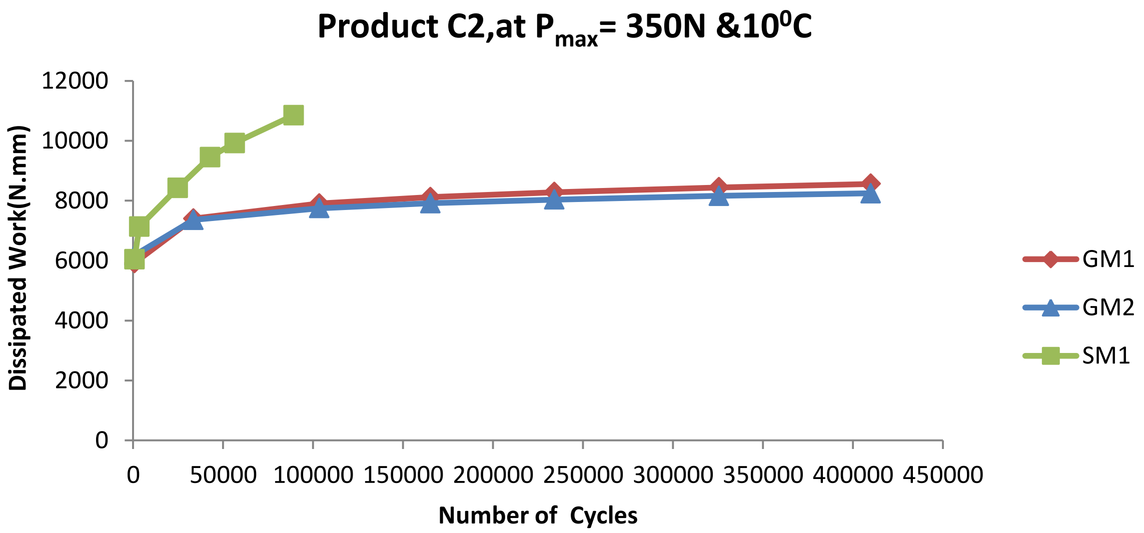

Figure 5.37 Dissipated work vs number of cycles at P_{max}= 350N

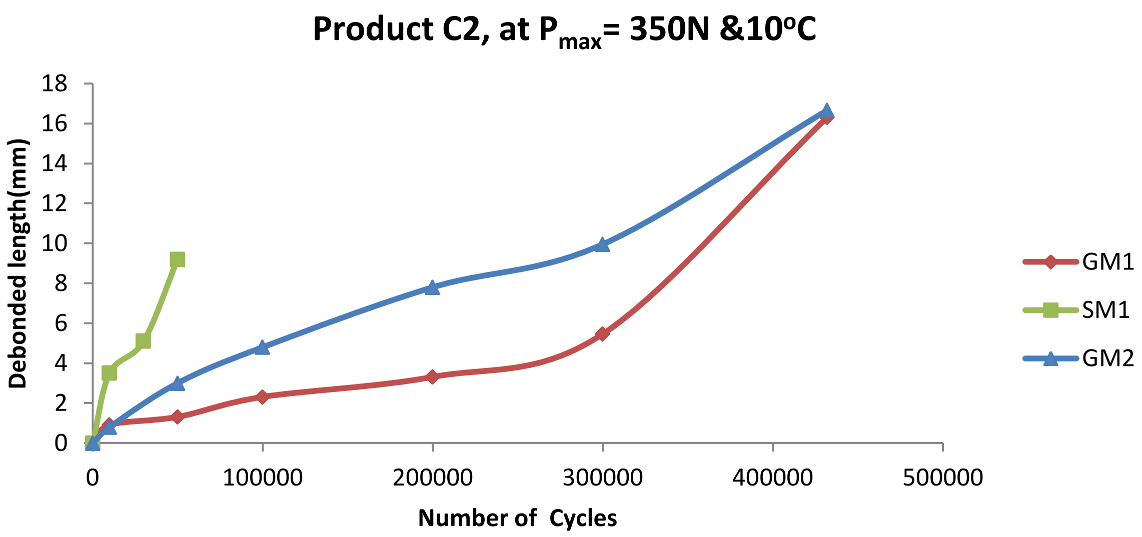

Figure 5.38 Debonded length vs number of cycles at P_{max}= 350N

Finally at the load level of 350N, the SM1, GM1 and GM2 imterfaces have been tested with product C2,Figure 5.37 and Figure 5.38. The test results of the PM2 interface were not shown in the above figures because the PM2 specimen was fully debonded after completion of the tests at 250N load level. It can be observed that GM1 and GM2 show to have similar response in terms of dissipated work. The SM1 interface was found to be the worst one and debonded before the completion of the first at 100,000 cycles.

The change in dissipated work as a function of the applied load level is summarized and presented for all interfaces for product C2, in Figure 5.39, Figure 5.40,Figure 5.41 and Figure 5.42.

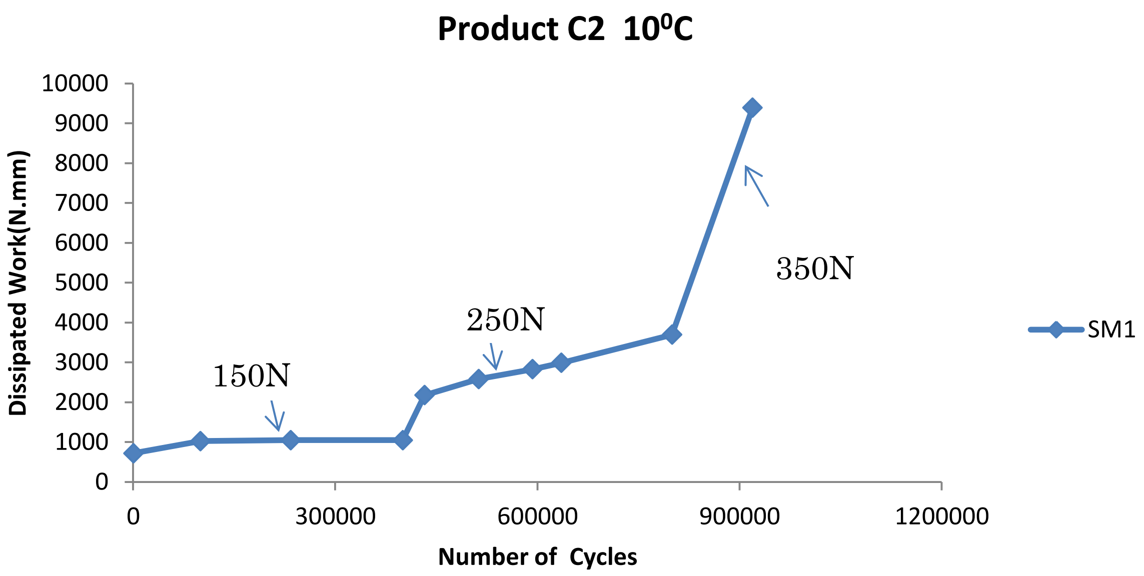

Figure 5.39 Dissipated work vs number of cycles for product C2 at SM1 interface

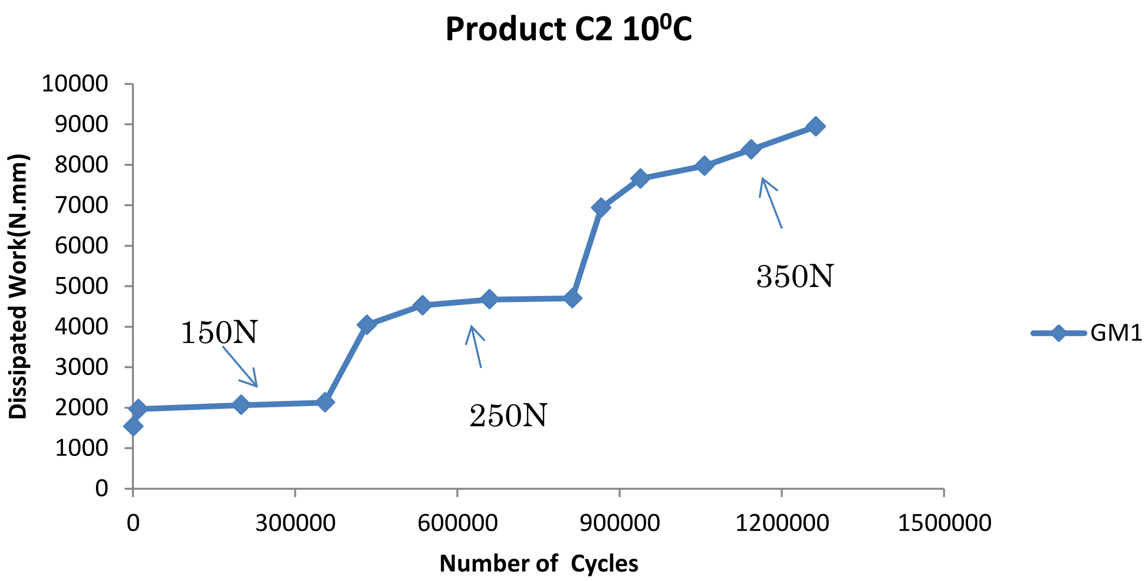

Figure 5.40 Dissipated work vs number of cycles for product C2 at GM1 interface

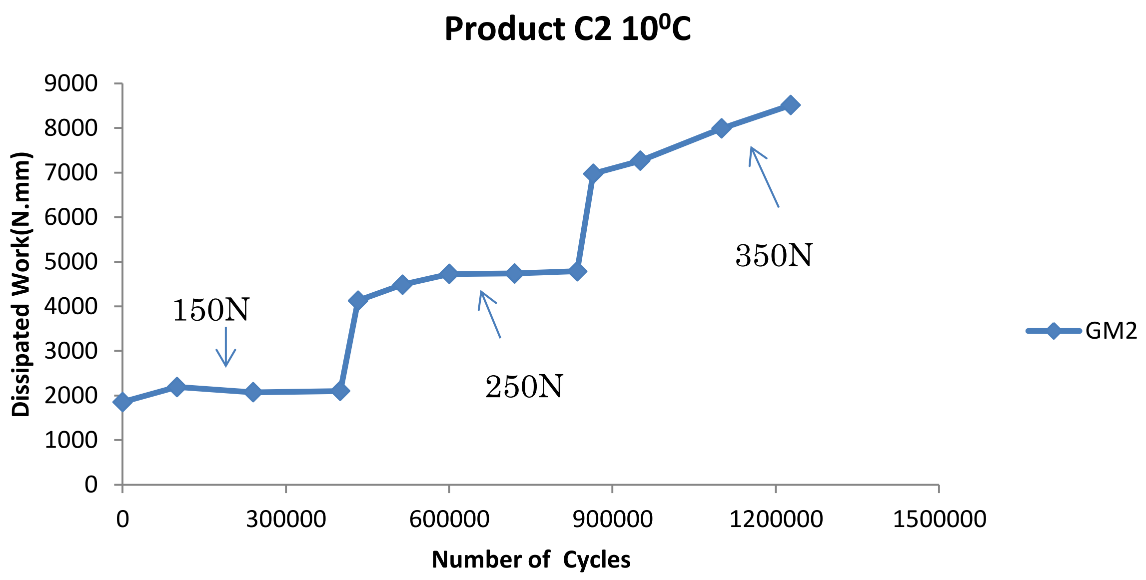

Figure 5.41Dissipated work vs number of cycles for product C2 at GM2 interface

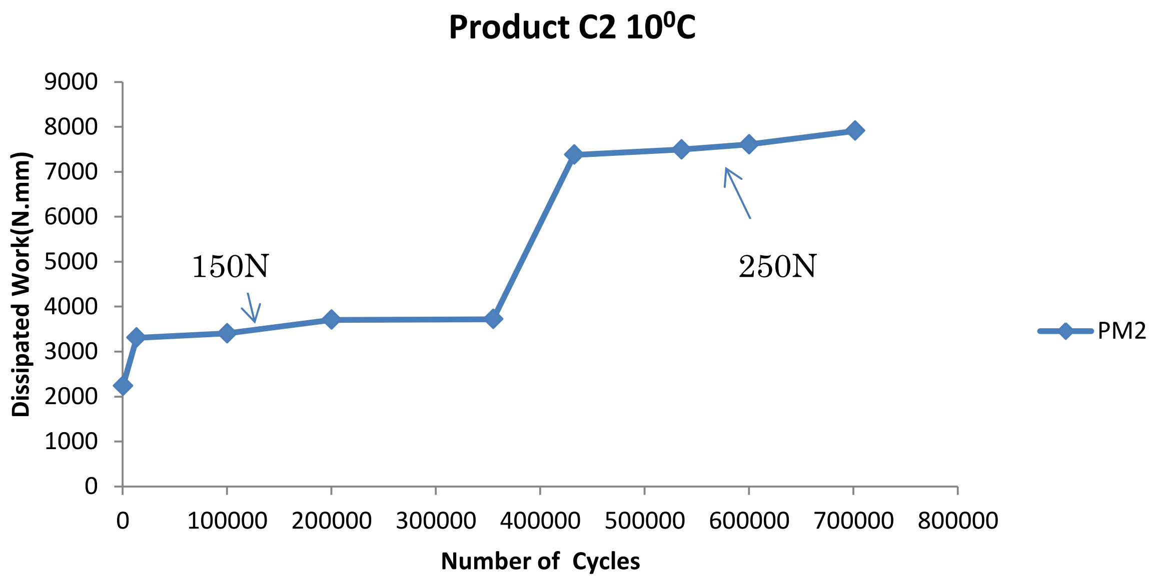

Figure 5.42 Dissipated work vs number of cycles for product C2 at PM2 interface

5.5 Comparison based on Ratio of dissipated work change at $10^{0}C$

The Figures below show the ratio of dissipated work change (RDWC) curves for three different products at three different load levels (150N,250N and 350N) at $10^{0}C$. The comparisons of ratio of dissipated work change has been conducted for all products and all tested interfaces.

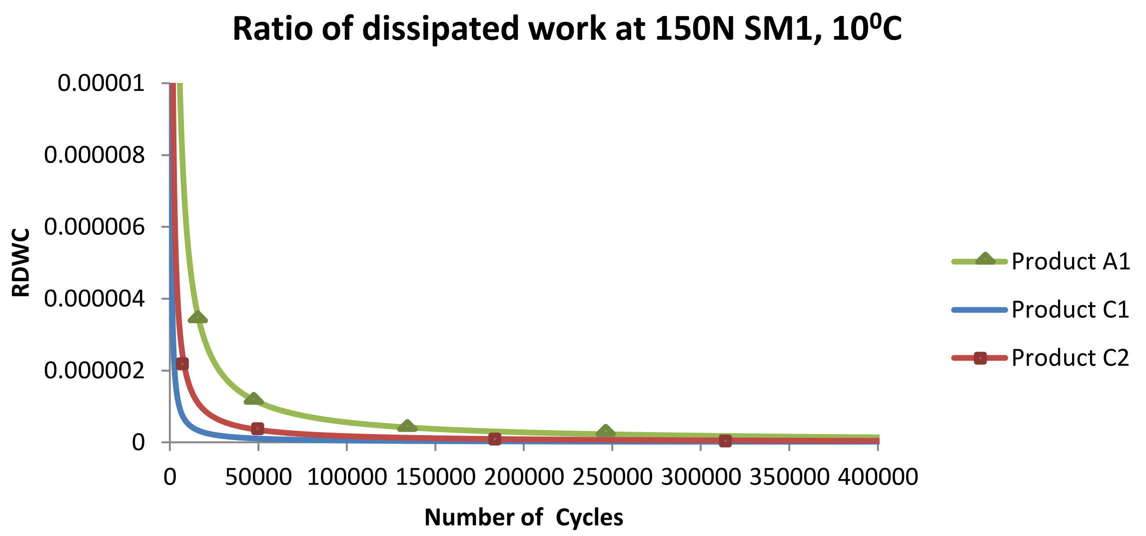

Figure 5.43 RDWC vs number of cycles at SM interface, at P_{max}=150N

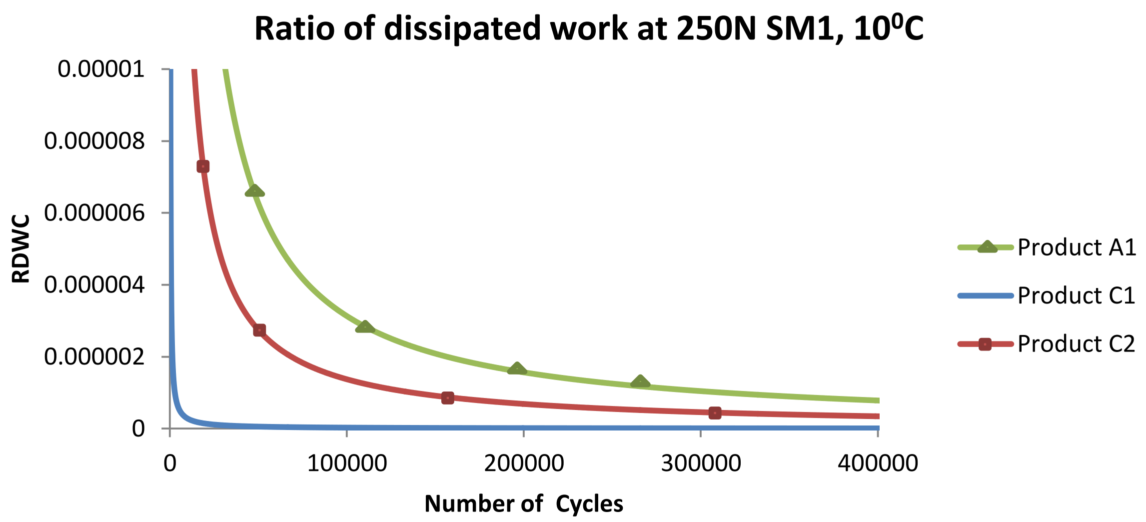

Figure 5.44 RDWC vs number of cycles at SM interface, at P_{max}= 250N

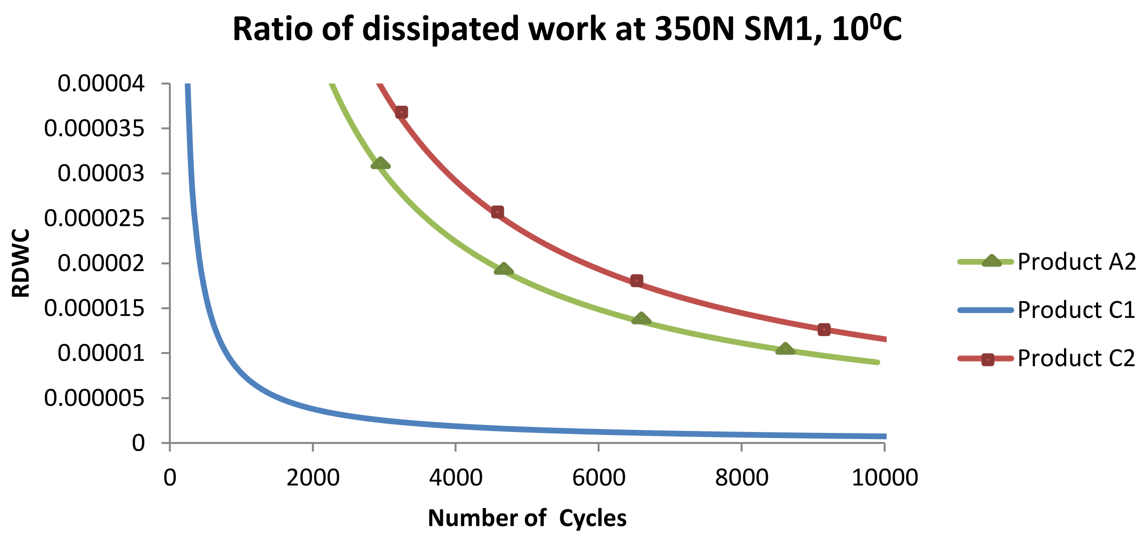

Figure 5.45 RDWC vs number of cycles at SM interface, at P_{max}=350N

It can be observed from Figure 5.43, Figure 5.44 and Figure 5.45 that, after the initial loading period, the plateau stage was reached. This plateau stage indicates a period where there is a relatively constant percentage of input energy turned into damage. At the SM1 interface, the plateau values of product C1 were always lower than the other two products indicating that less input energy turned into SM1 interface damage. Particularly, at 150N and 250N load levels, Figure 5.43 and Figure 5.44, C1 product showed almost no energy being turned into fatigue damage.

Product C2 was found to have better fatigue resistance than product A1 at 150N and 250N load levels. However at 350N load level product A1 was found to have lower RDWC values than product C2. That can explain why at 350N load level, the C2 membrane was debonded earlier than the A2 product, see Figure 5.16 and Figure 5.38.

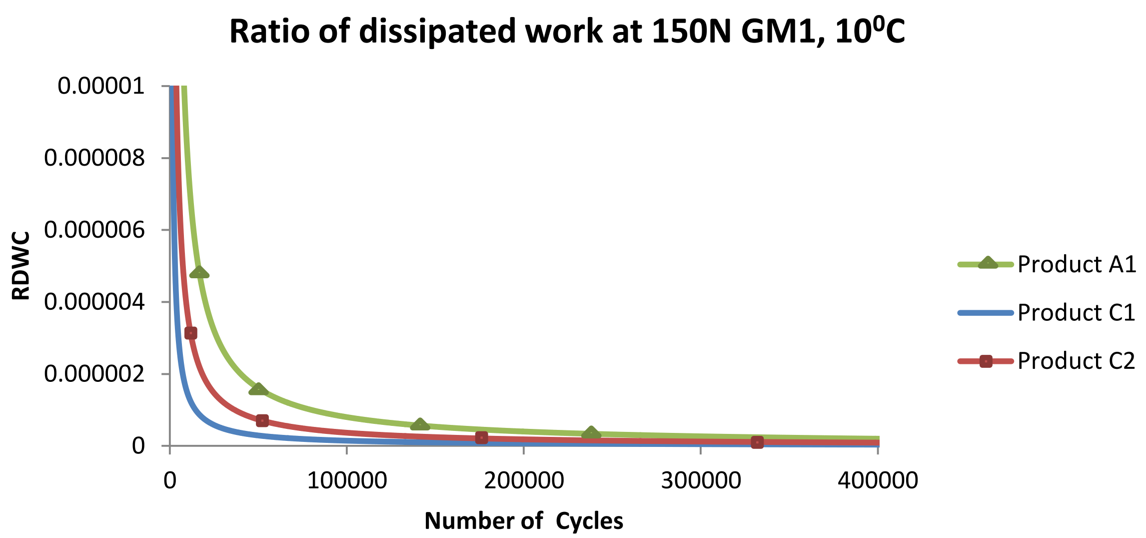

Figure 5.46 RDWC vs number of cycles at GM1 interface, at P_{max}=150N

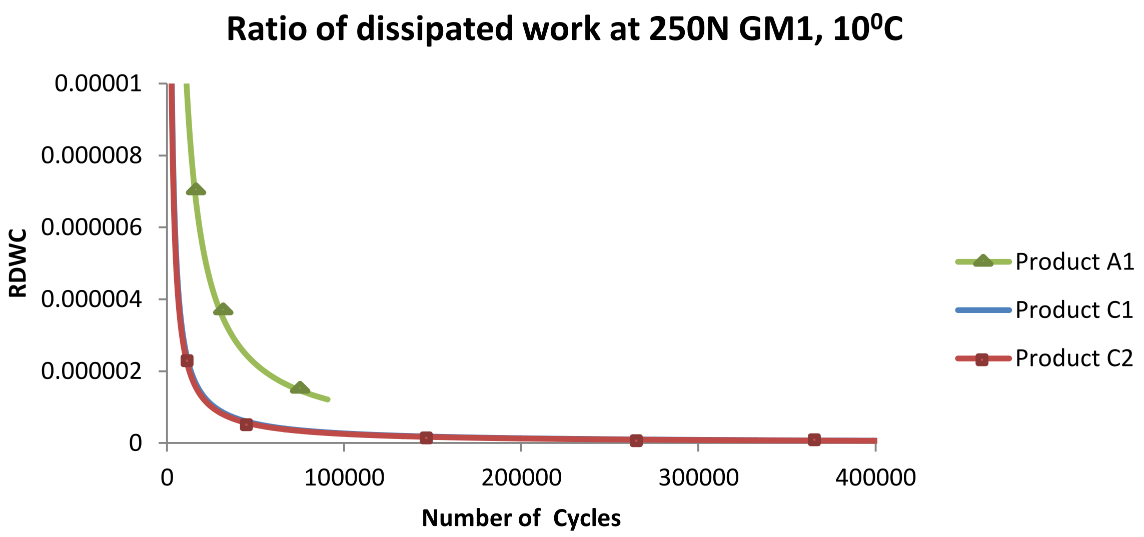

Figure 5.47 RDWC vs number of cycles at GM1 interface, at P_{max}=250N

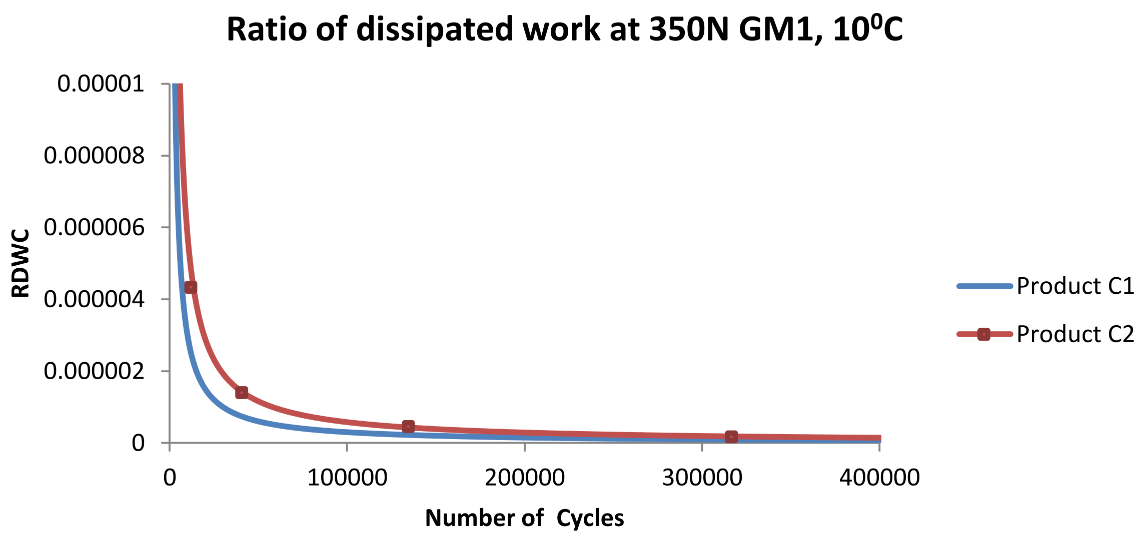

Figure 5.48 RDWC vs number of cycles at GM1 interface, at P_{max}=350N

In Figure 5.46, Figure 5.47 and Figure 5.48, the results for product A1, C1 and C2 at GM1 interface are presented. Similarly as in SM1 interface, product C1 was found to have the lower RDWC vales followed by product C2 and A1 respectively. At 250N load level, the RDWC curves for product C2 and C1 were overlapped showing a similar response at this interface at this load level, Figure 5.47. Product A1 could not be tested at 350N load level because it was fully debonded during the first 100,000 cycles at the previous load level (250N), Figure 5.47.

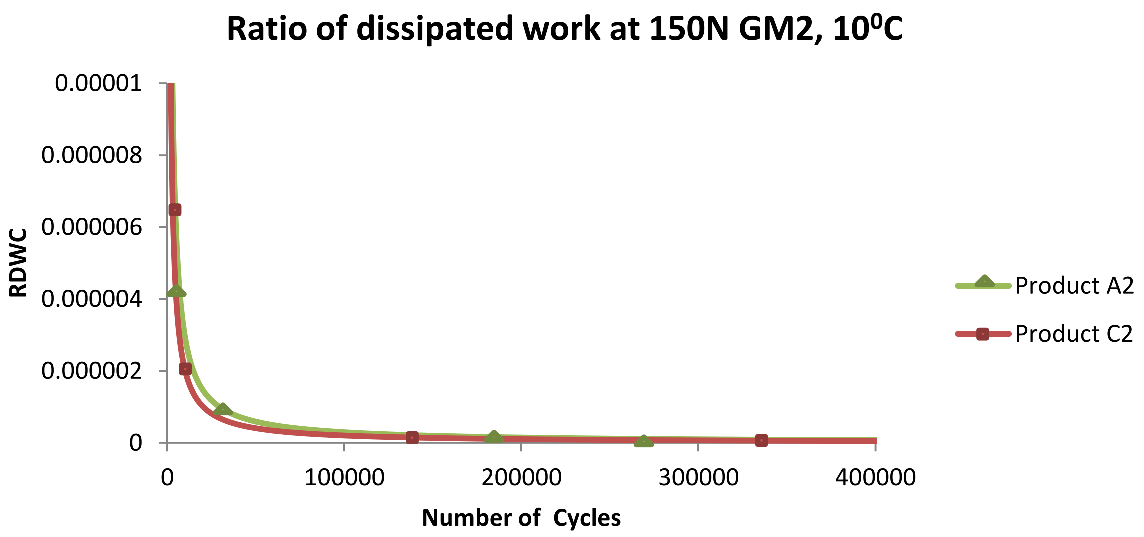

Figure 5.49 RDWC vs number of cycles at GM2 interface, at P_{max}= 150N

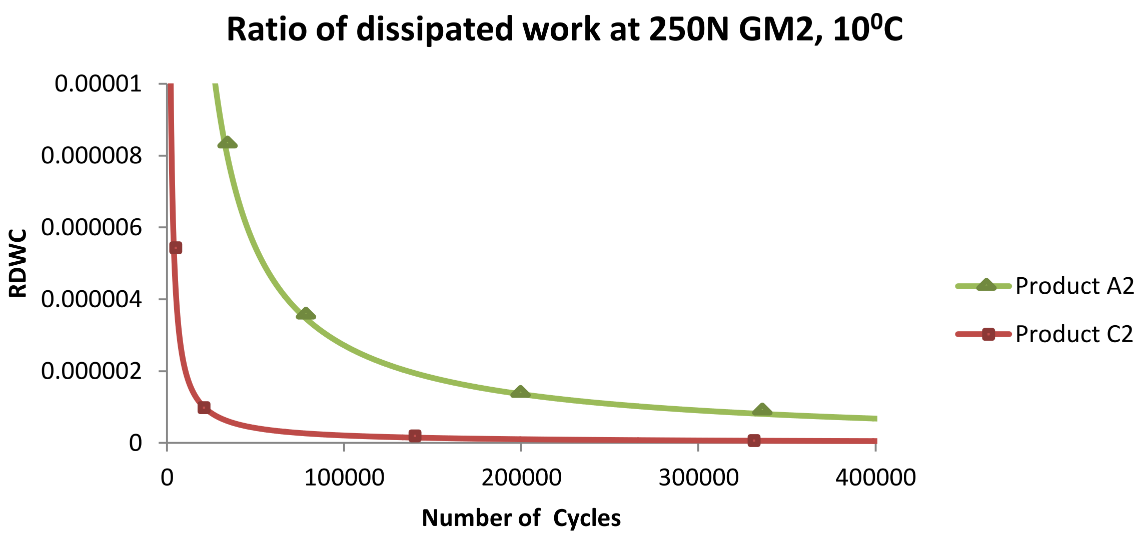

Figure 5.50 RDWC vs number of cycles at GM2 interface, at P_{max}= 250N

At the GM2 interface, only Product A2 and C2 were tested. None of these products were able to be tested at 350N load level hence only the RDWC curves from 150N and 250N are presented in Figure 5.49 and Figure 5.50 It can be observed that the two RDWC curves at 150N load level showed similar response for both products but with slightly lower RDWC values for product C2, Figure 5.49 However, at the 250N load level, product A2 showed higher value of RDWC than the product C2 which indicates that the product C2 had better fatigue resistance at GM2 interface than the product A2 during the completion of the test.

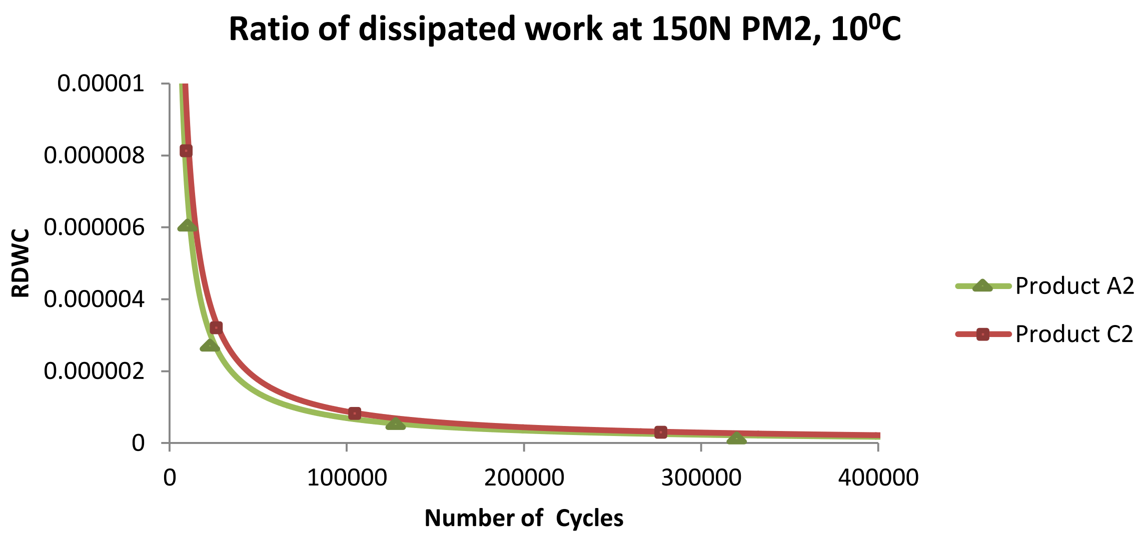

Figure 5.51RDWC vs number of cycles at PM2 interface, at P_{max}=150N

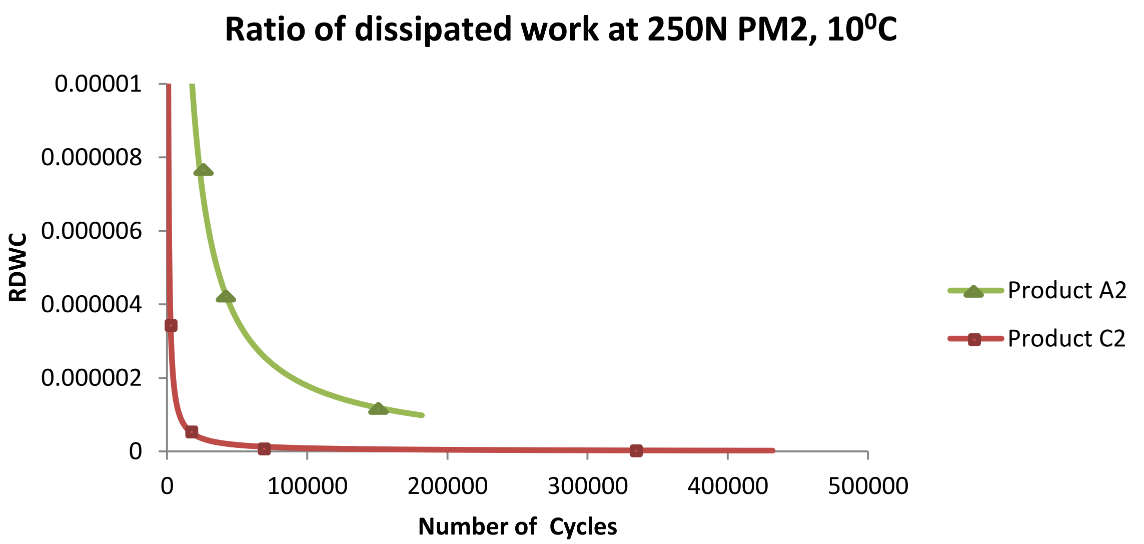

Figure 5.52 RDWC vs number of cycles at PM2 interface, at P_{max}=250N

At the PM2 interface, product C2 was found to have slightly lower values of RDWC at 150N load level, Figure 5.51. However, a significant difference of RDWC between those two products can be observed at 250N load level in Figure 5.52. It can also be seen that the RDWC curve of product A2 stopped to develop after 20,000 load cycles because it was fully debonded.

5.6 Fatigue tests conducted at 30⁰C

The results from the tests conducted at 30^0C are presented below. These tests were performed at one load level, 100N for 864 000 cycles for all tested products and all interfaces. Nevertheless, at some interfaces the tests were completed before the maximum of 864000 load cycles due to large deformation of the samples.

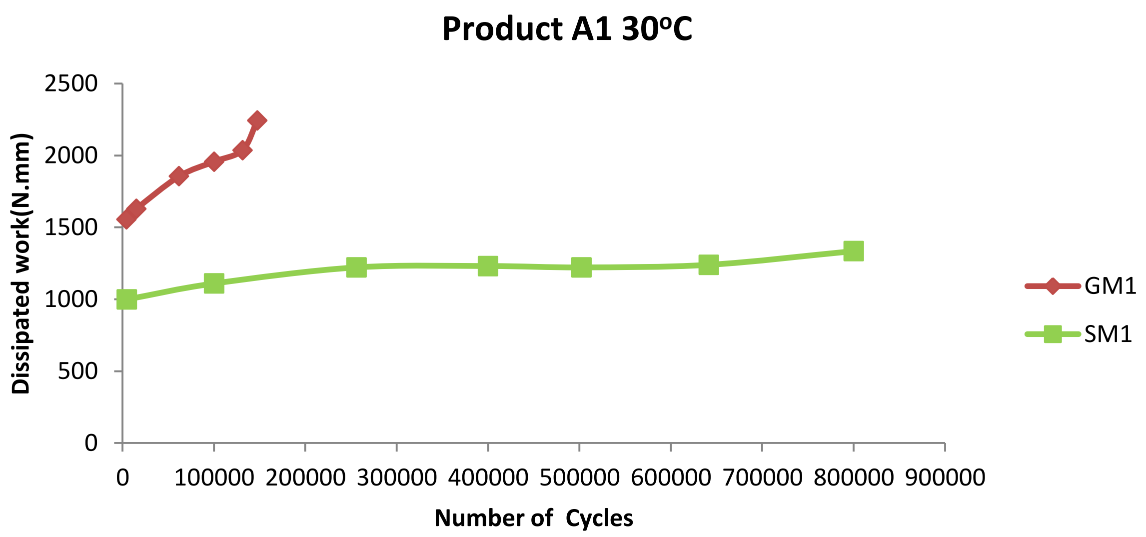

Figure 5.53 Dissipated work vs number of cycles for product A1

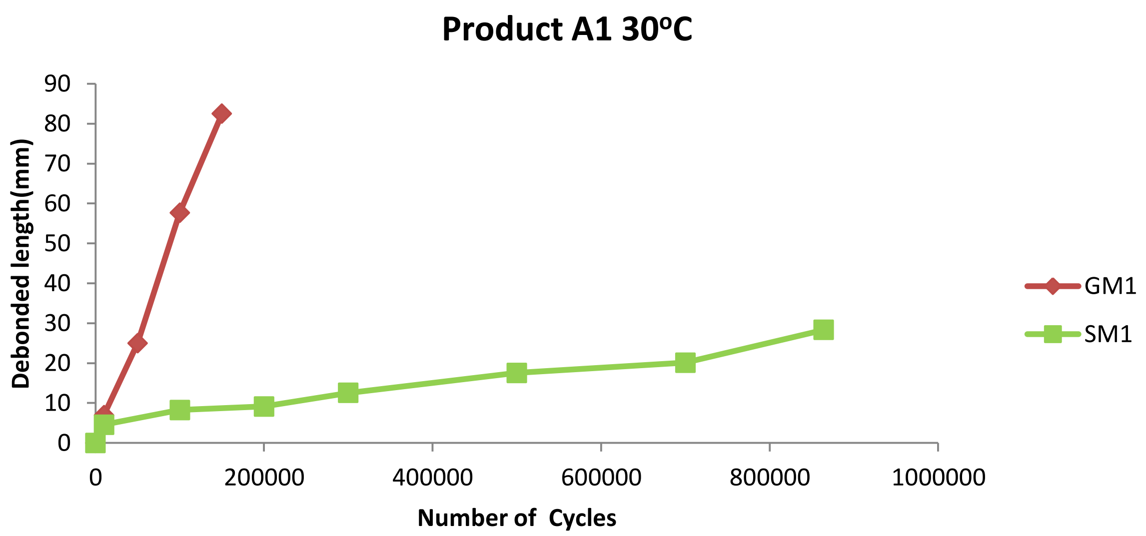

Figure 5.54 Debonded length vs number of cycles for product A1.

Figure 5.53 and Figure 5.54 present the results for product A1 at the GM1 and the PM1 interfaces. The SM1 interface was found to be the one with the lower values in terms of dissipated work producing a steady response during the completion of the fatigue test. For the GM1 interface for product A1, the dissipated work value was found to increase since the begging of the test. From Figure 5.54 it can be seen that the GM1 interface is the worst one compared with the SM1. The debonding process started since the beginning resulting to full debonding after the first 100,000 load cycles.

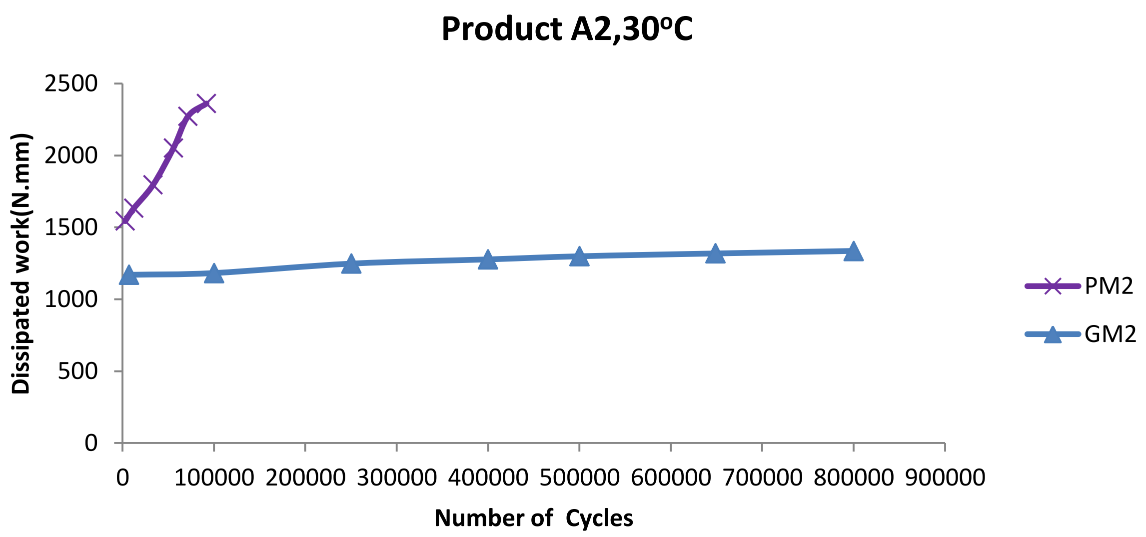

Figure 5.55 Dissipated work vs number of cycles for product A2

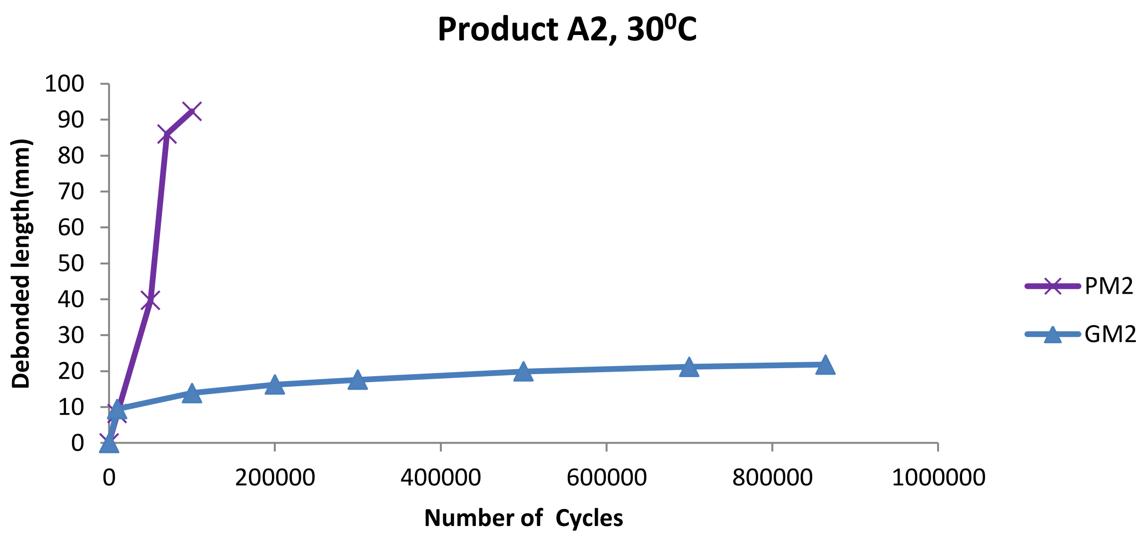

Figure 5.56 Debonded length vs number of cycles for product A2.

In Figure 5.55 and Figure 5.56 the results from the GM2 and PM2 interfaces for product A2 are presented. For this case, the PM2 interface was found to be the worst one in terms of dissipated work. It can be concluded that A1 performs better at SM1 than GM1 and A2 performs better at GM2 than PM2. High rates of debonding were observed as early as 10,000 cycles and the membrane debonded fully.

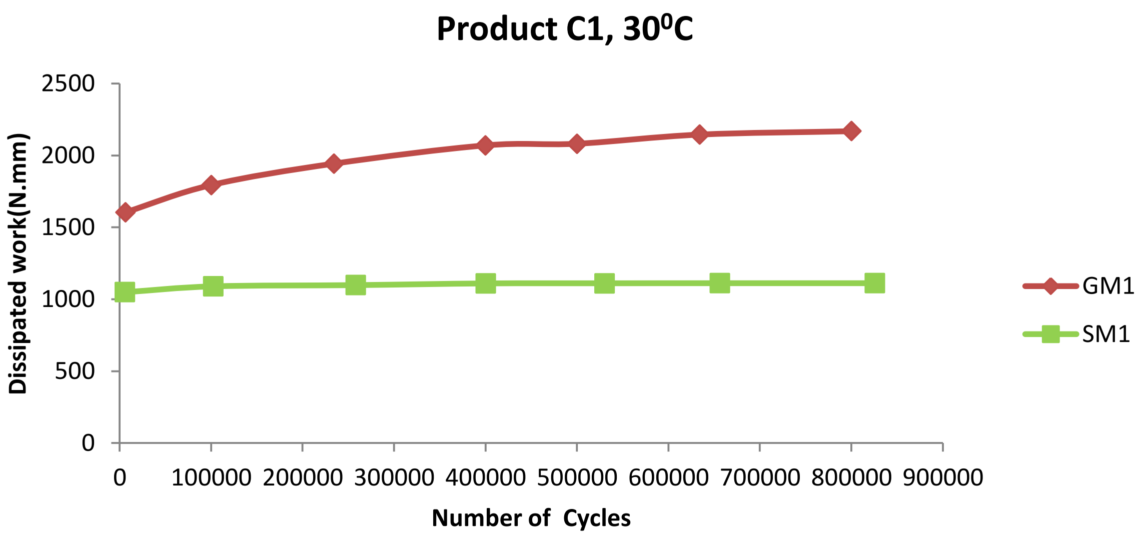

Figure 5.57 Dissipated work vs number of cycles for product C1

In Figure 5.57 and Figure 5.58 the results from product C1 are presented. This product is used only as a bottom membrane which means that is only applicable on steel and Guss interfaces. SM1 interface was found to be the one with the lower values in terms of dissipated energy which produces a steady response during the completion of the fatigue test, Figure 5.57.

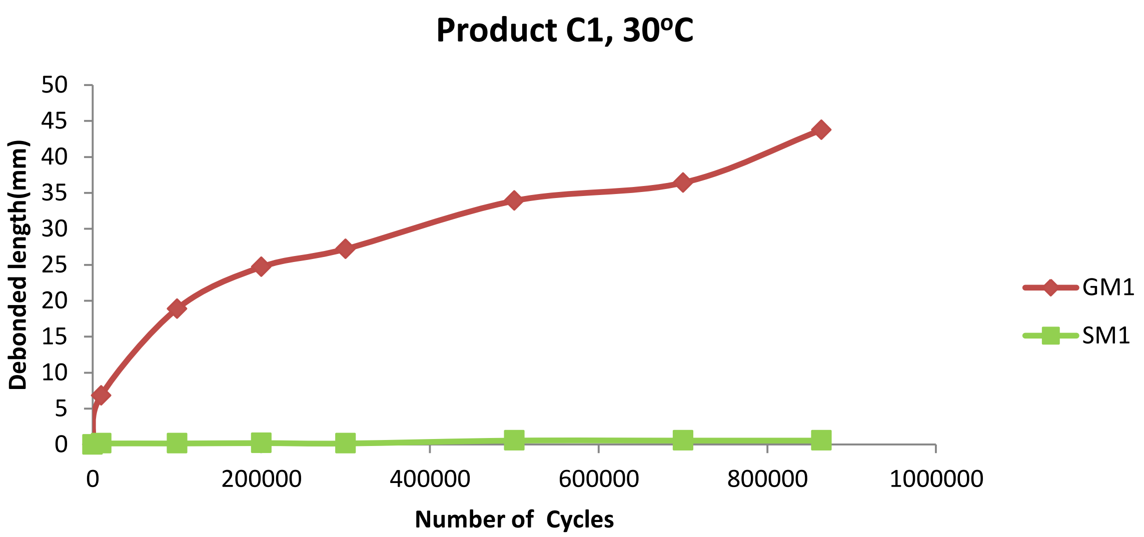

Figure 5.58 Debonded length vs number of cycles for product C1

In Figure 5.58 the debonded length versus number of cycles is presented for product C1 at interface GM1 and SM1. As it can be noticed the SM1 interface produces a steady response during the fatigue tests with zero debonding. On the other hand GM1 was found to have 45mm of debonding length at the end of the test. This could also explain the higher values of dissipated work of GM1 than the one of SM1 in Figure 5.57

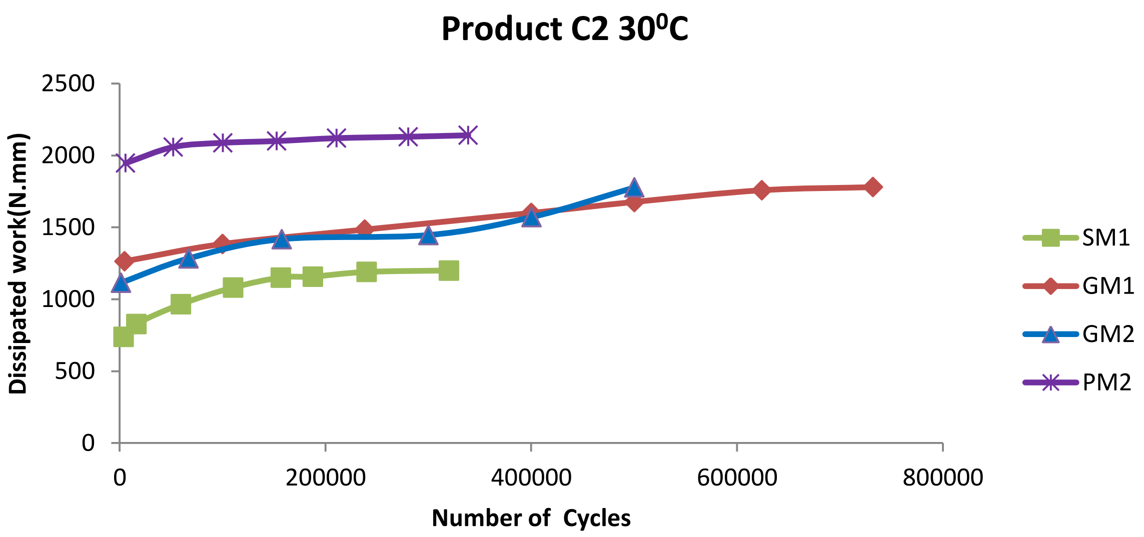

Figure 5.59 Dissipated work vs number of cycles for product C2

In Figure 5.59 the dissipated work versus number of cycles is presented for all interfaces for product C2. As it can be noticed the PM2 is the worst interface in accordance with the values of dissipated work. The SM1 interface shows lower values of dissipated work than the other interfaces. The GM1 and GM2 interfaces show almost the same response.

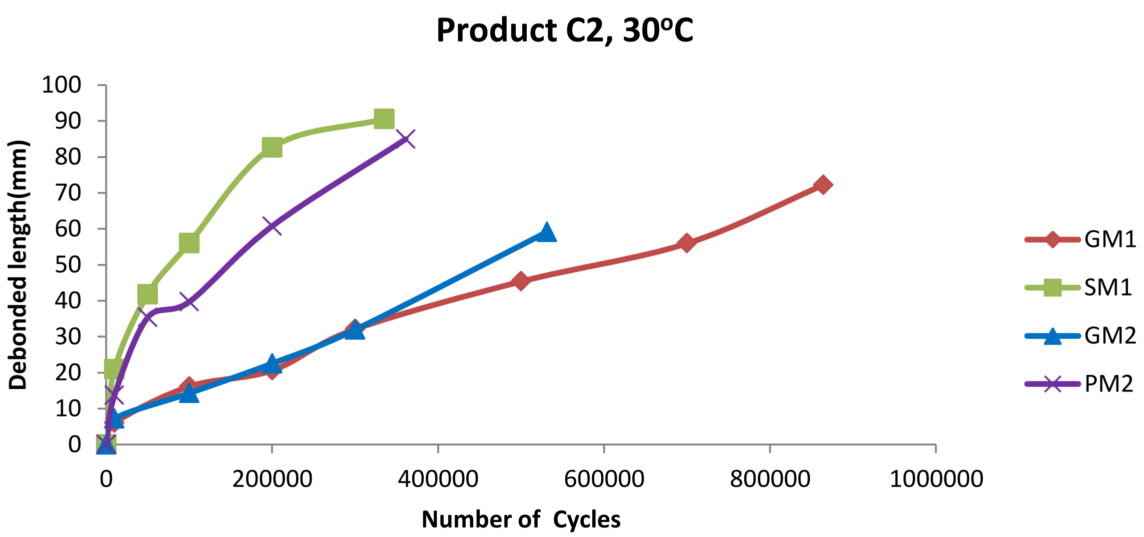

Figure 5.60 Debonded length vs number of cycles for product C2

In Figure 5.60 the results of debonded length versus number of cycles at 30^{o}C are presented for product C2. As it can be noticed the SM1 interface produced higher debonding during the fatigue tests and the debonding speed is faster than the other interfaces. The GM1 and GM2 interfaces produced almost the same results although GM1 last for longer loading cycles. For the PM2 interface the debonding process started at the beginning of the test and developed faster.

5.6.1 Comparison based on Ratio of dissipated work change at T=30⁰C

The Figures below show the RDWC plots for three different products conducted at temperature T=30^{0}C and load level P_{max}=100N. A comparison in terms of ratio of dissipated work change (RDWC) has been conducted for all products and all tested interfaces .

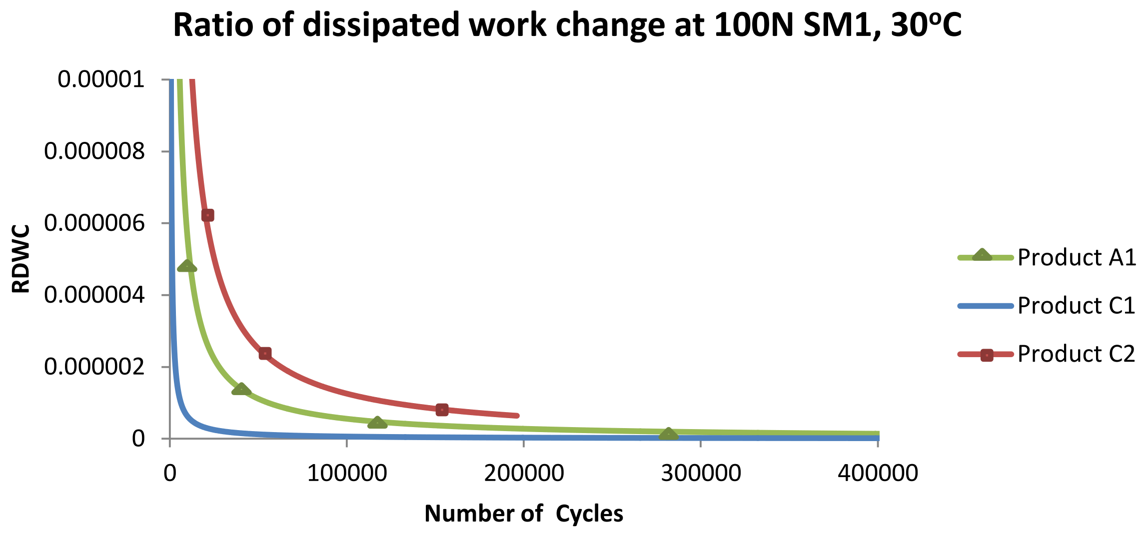

Figure 5.61 RDWC vs number of cycles at SM interface at P_{max}=100N

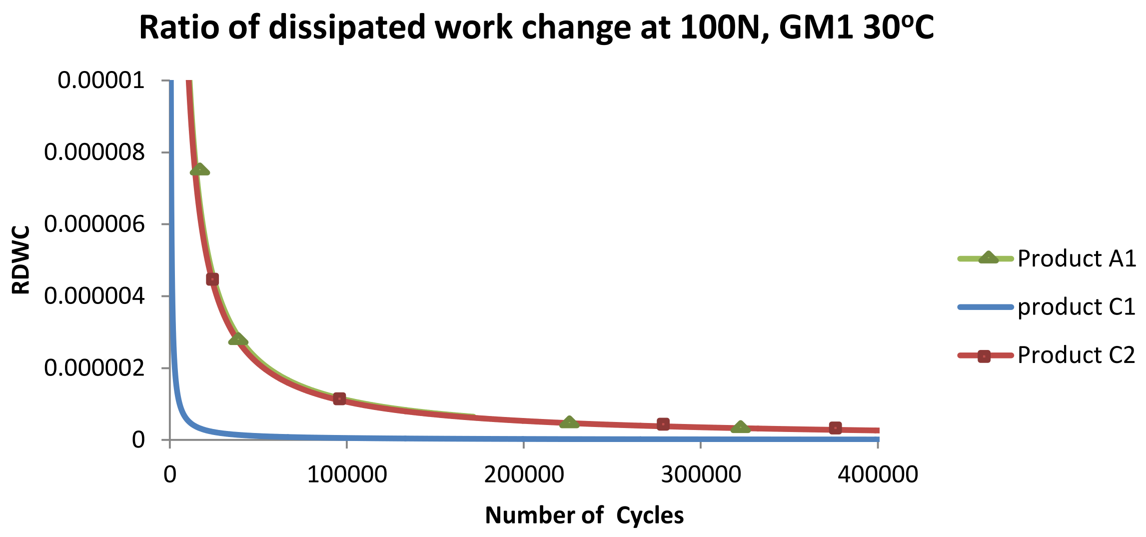

Figure 5.62 RDWC vs number of cycles at SM interface at P_{max}= 100N

For both interfaces SM1 and GM1 at 30^{0}C, product C1 was found to have the lower RDWC values than product A1 and C2, see Figure 5.61 and Figure 5.62. At GM1 interface, product C2 and A1 were found to have similar response with the overlapped RDWC curves, Figure 5.62. However, significant difference can be observed at the SM1 interface between product C2 and A1. Higher RDWC values occurred at the SM1 interface with product A1, Figure 5.61

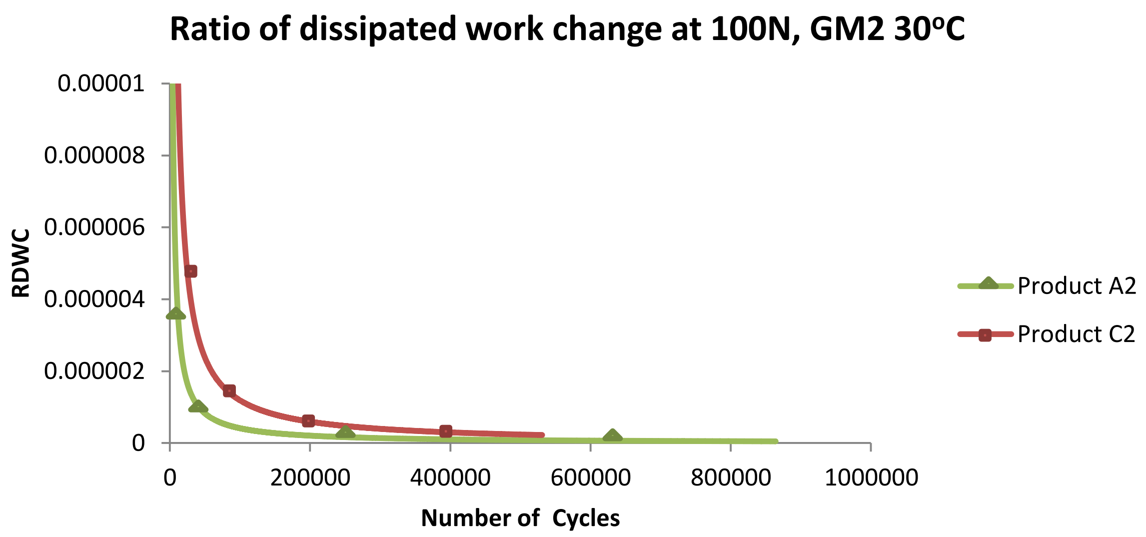

Figure 5.63 RDWC vs number of cycles at SM interface at P_{max}= 100N

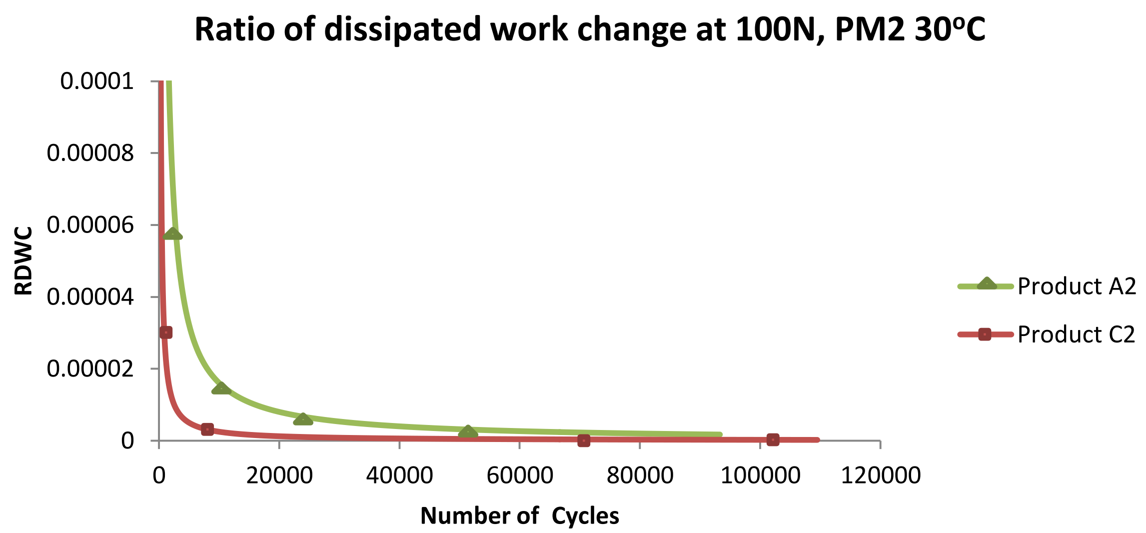

Figure 5.64 RDWC vs number of cycles at SM interface at P_{max}= 100N

At GM2 interface, product A2 was found to have lower RDWC values, Figure 5.63. However, at PM2 interface, product C2 was found to have lower RDWC values, Figure 5.64. It can also be seen that product C2 at PM2 interface reached its plateau stage earlier than the product A2. This, results faster debonding at PM2 interface for product A2 at 30°C than for product C2, see Figure 5.56 and Figure 5.60.

5.7 Service Life Prediction of Membrane Products by MAT apparatus

Paris' law is a well-known and widely used method for predicting fatigue crack growth in engineering materials. In this research a modified version of the Paris law is used in an attempt to predict the fatigue life of membrane products in adhesively bonded structures. The research is based on experimental work conducted using the Membrane Adhesion Tester apparatus (MAT), introduced in earlier chapters. The experimental results from various membrane products bonded to different substrates were validated and compared accordingly. A numerical method based on real traffic data obtained from Merwede bridge, located at A27 in the Netherlands, is introduced in order to predict the fatigue life of membrane materials used in a multilayer system for orthotropic steel deck bridges. The number of cycles to failure is calculated by integrated the fatigue crack growth law between initial and final crack length. The crack growth law is formulated in terms of the energy release rate which is determined at any crack length.

5.7.1 Background theory

Most of the engineering components operate under cyclic loading. The result of these cyclic loads is the appearance of crack initiation, crack propagation and a fatigue life,. Fatigue loading is assimilated to sinusoidal stress or strain cycles of constant amplitude and often characterised by frequency, mean stress and the stress ratio R which defined as the ratio of minimum to maximum stress during a loading cycle. A typical stress versus time for fatigue loading is shown in Figure 5.65

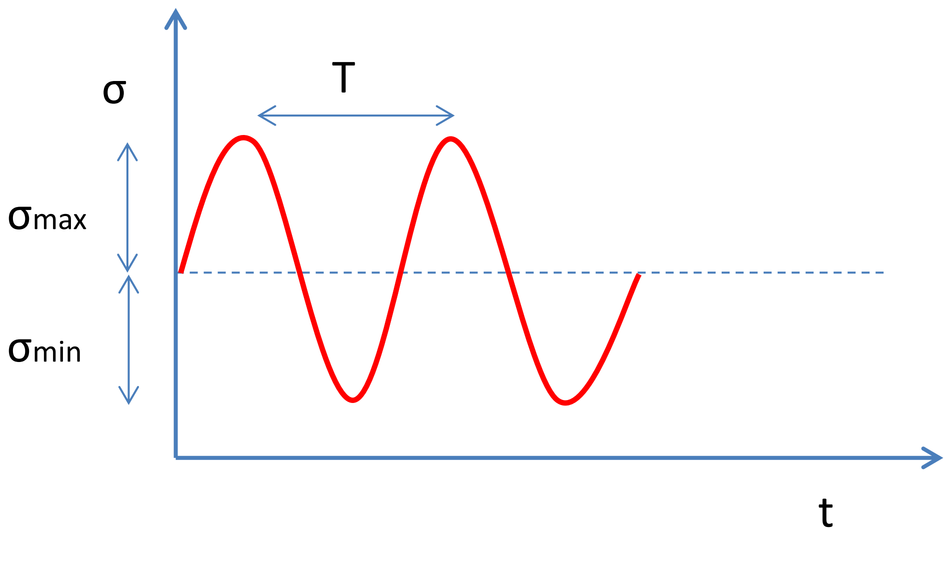

Figure 5.65 Typical Stress level variation versus time

The stress intensity factor and the energy release rate defined as,

$$\Delta K = K_{max} - K_{min} \tag{5.5}$$

$$\text{or} \qquad \Delta G = G_{max} - G_{min}, \tag{5.6}$$

where K_{max} or G_{max} are related to the maximum stress values of a loading cycle and K_{min} or G_{min} the minimum. The crack propagation is defined as the crack extension per number of cycles and is denoted as da/dN. Ewalds and Wanhill (1984) found that the correlation between ΔK or ΔG is independent of the stress range and the crack length. This observation is commonly plotted in a log-log diagram and shows a sigmoidal trend.

According to Barsom (1999) "all structural members or test specimens can be loaded to various levels of K''. This is analogous to the situation where unflawed structural members can be loaded to various levels of stress, σ. The stress field near crack tips can be categorized as Mode I, opening mode, Mode II, sliding and Mode III tearing, which each of them is characterized by a "local mode of deformation" as illustrated in Figure 5.66. The opening mode, I, is related to local displacement in which the crack surfaces move directly apart. The sliding mode, II, is related with local displacement in which the crack surfaces slide over one another perpendicular to the leading edge of the crack. The tearing mode, III, is related with local displacement in which the crack surfaces slide with respect to one another parallel to the leading edge. These three modes can be used to "describe the most general case of crack tip deformation and stress fields" Paris and Sin (1965).

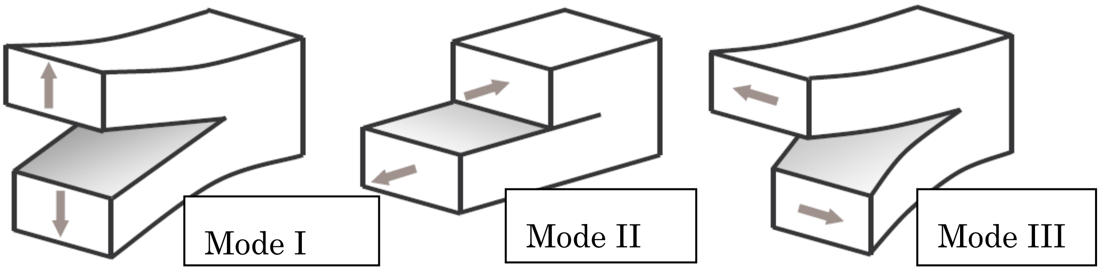

Figure 5.66 The three basic modes of crack surface displacements

Pagano and Schoeppner (2000) found that the use of G for composite materials is certainly more consistent with the analytical models in use than K, even though Kmin can be defined rigorously in contrast to G. Hence, the majority of the studies about delamination or debonding for this research, use the energy release rate, G instead of the stress intensity factor K to predict the initiation of the crack.

5.7.2 Methodology of service life prediction

There have been many attempts to describe the crack growth rate curve by 'crack growth laws', which are usual semi or wholly empirical formulae fitted to a set of data. The most widely known is the Paris equation, Paris, Gomez and Anderson, (1961)

$$\frac{da}{dn} = C(\Delta K)^m \tag{5.12}$$

In which C is a material constant depending on the material property, temperature, stress ratio and environment. The exponent m descripes the slope of the fatigue crack propagation curve in the logo-log plot. The Paris law that relates the crack growth rate(da/dN) to G is given by:

`

$$\frac{da}{dn} = DG^n \tag{5.13}$$

For the need of this research a modified Paris law that relates the crack growth rate/ delamination growth rate (d*a*/d*N*) to the maximum strain energy release rate *G*, is given by Martin and Murri, (1990):

$$\frac{da}{dN} = DG^{n}\left(\frac{1-\left(G_{th}/G\ \right)^{n_1}}{1-\left(G\ /G_c\right)^{n_2}}\right) \tag{5.14}$$

In wich D, G, GC, Gth, n, n1, n2 are fitting parameteres.
The difference between the above expression and the classical Paris law is that Eq.5.14 describes the full da/dN versus G curve; i.e., including the threshold and accelerating crack growth regions. The sigmoidal shape of da/dN – G fatigue crack or delamination growth rate curve is defined by Eq.(5.14) see Figure 5.67.

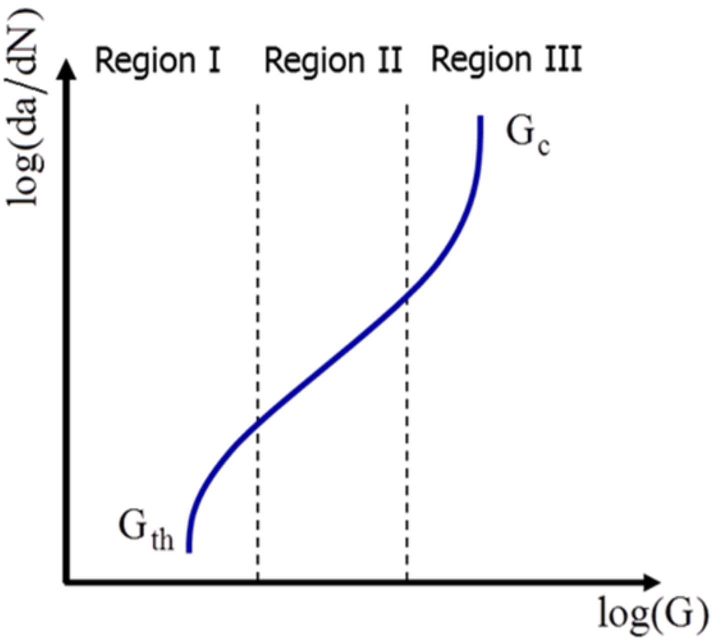

Figure 5.67 Fatigue crack growth rate curve da/dN -G

The da/dN – G fatigue crack curve divides the curve into three different regions according to the curve shape and the mechanism of crack extension.
In region I there is the fatigue threshold G_{th}, below which cracks either propagate at an extremely low rate or do not propagate at all. Figure 5.68 Knowledge of G_{th} permits the calculation of permissible crack lengths or applied stress in order to avoid fatigue crack growth. This region is highly influenced of microstructure, mean stress and environmental conditions.

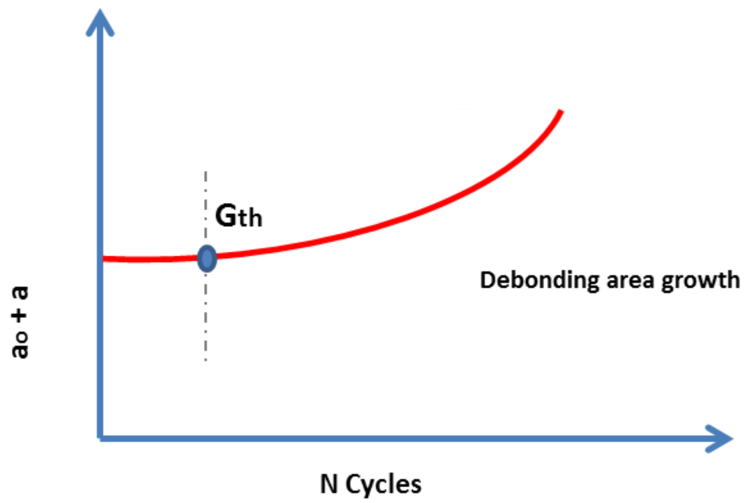

Figure 5.68 Graphical observation of Gth

In region II the crack growth rate da/dN increases relatively rapidly with increasing the G, is often some power function of G leading to linear relationship between log(da/dN) and log(G) see Figure 5.67. This region is highly influenced by certain combinations of environment, mean stress and frequency. Finally, in region III the crack growth rate curve rises to an asymptote where the max G becomes equal to the critical energy release rate, obtained experimentally from the monotonic tests conducted with MAT apparatus. Graphically, the Gc value is the kink point on the gamma curve, Figure 5.69.

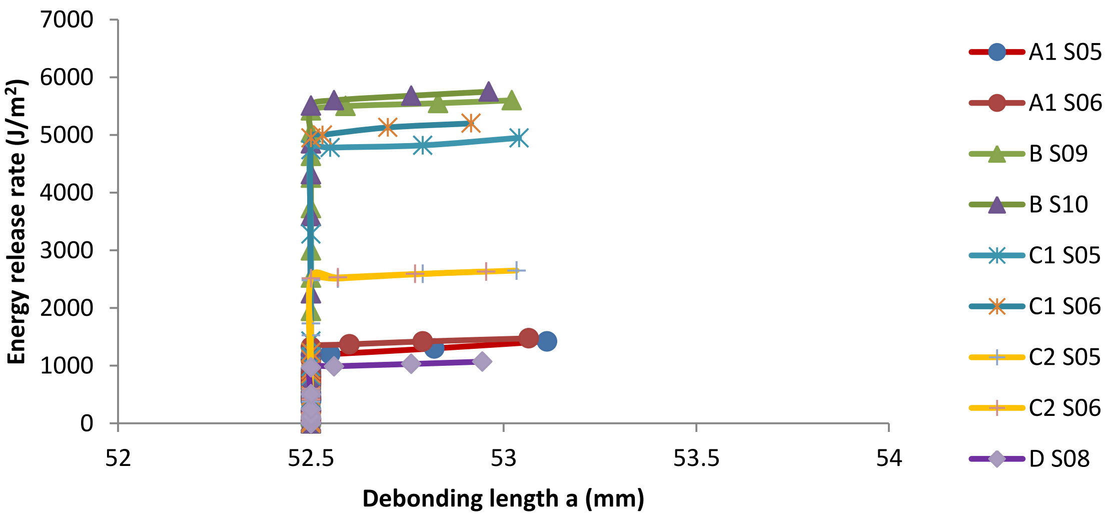

Figure 5.69 Energy release rate at 10^0C

In order to find the location of the critical tensile stresses on Merwede bridge, FEA illustrations have been conducted by Li (2015). The critical higher tensile stress is found where the bridge deck is supported by stiffeners or cross beams, around the wheel load. The higher tensile stress concentration is mainly due to the higher stiffness difference between the asphalt layer, above the membrane and the steel stiffener below.

At this location, close to the bottom membrane, the distributions of the stress perpendicular to the membrane surface for three different temperatures is presented in Figure 5.70. The critical tensile stress at the location close to the bottom membrane is σ_R= 0.4MPa.

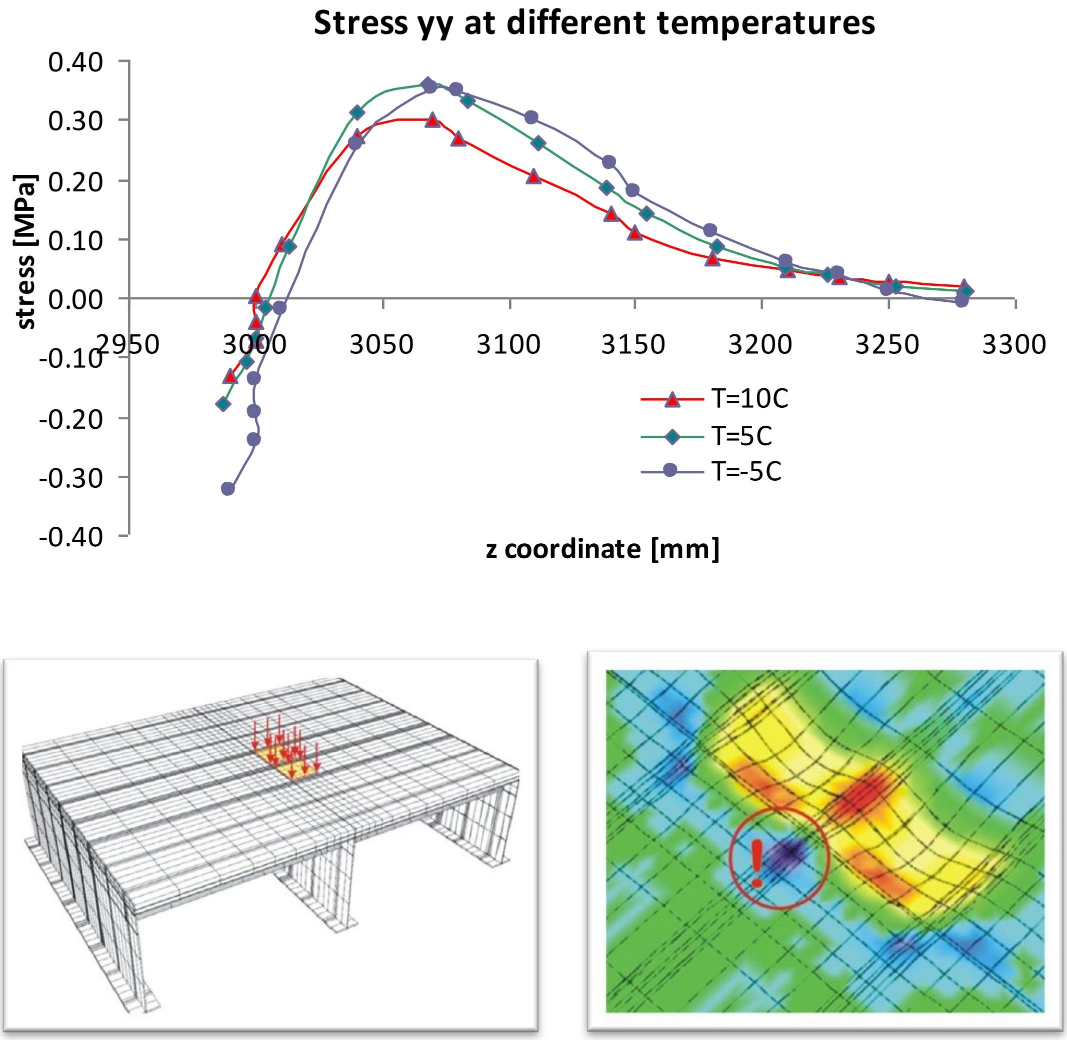

Figure 5.70 Maximum tensile stress yy at the bottom membrane

In MAT test, by using the constative relations of Eq.3.5 and Eg.3.9 in section 3.5 , the same critical stress occurred in the membrane can be related to the piston height and the corresponding piston force level, see Figure 5.71. once the piston force corresponding to the membrane critical stress at bridge is known, the service life of membrane can be predicted by using the relationship derived in the next section. It should be noted that the membrane response shown in Figure 5.71 depends on the membrane material type, loading rate and testing temperature.

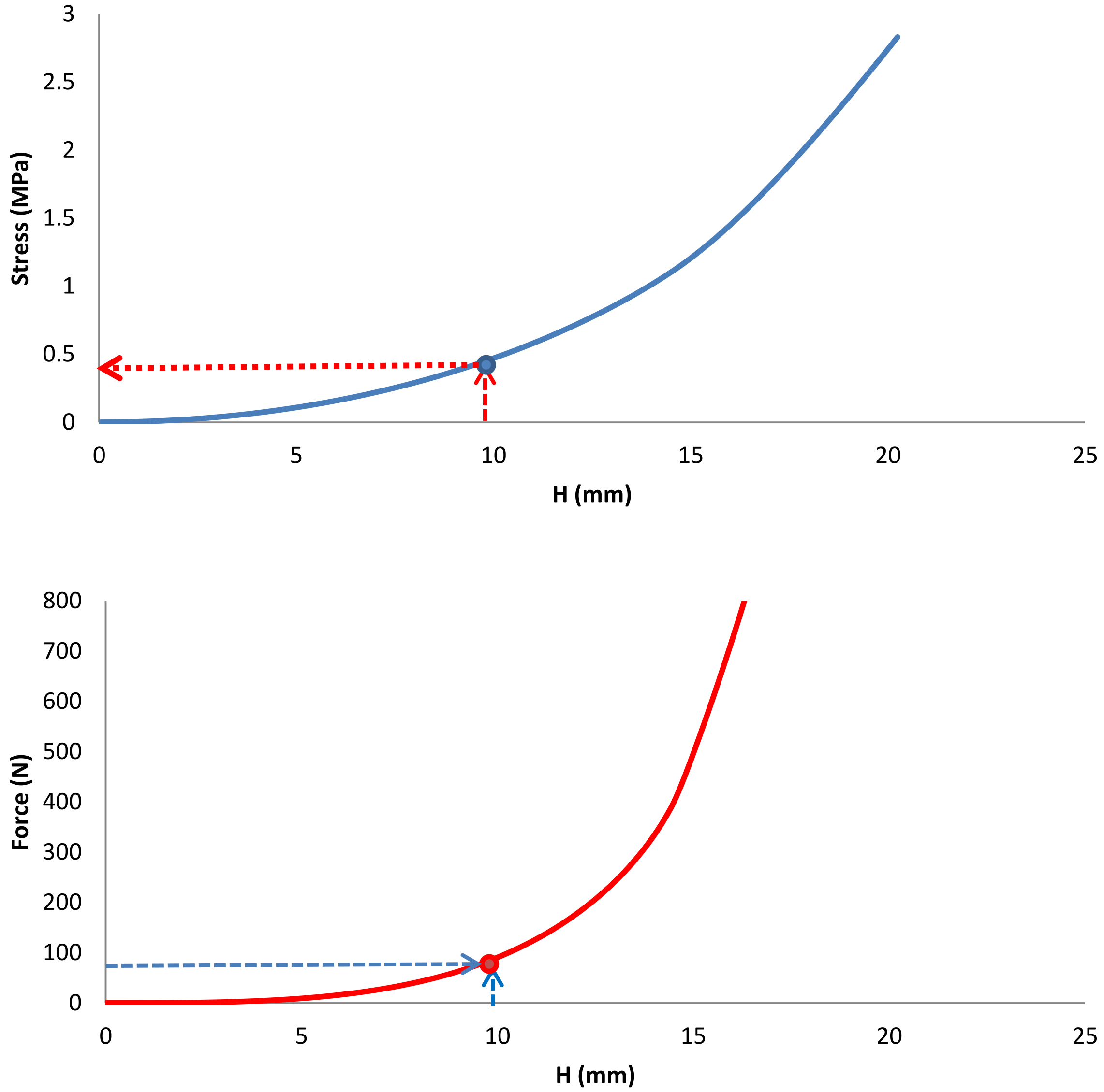

Figure 5.71 Critical stress and corresponding piston force level in MAT

One of the main requirements of the membrane products is to be able to withstand 18.8 million cycles, which is the maximum number of truck load in 8 years determined by traffic data obtained from real measurements on Merwede bridge. Therefore, in this study 18.8 million repetition is considered as the N_f which is the minimum requirement of fatigue life of membrane products. For illustration, some typical experimental curve fittings for product A1 and C2 at SM1 and PM2 interfaces at 150N load level at 10^0C using the modified Paris law are presented in Figure 5.73Figure 5.72 and Figure 5.73.

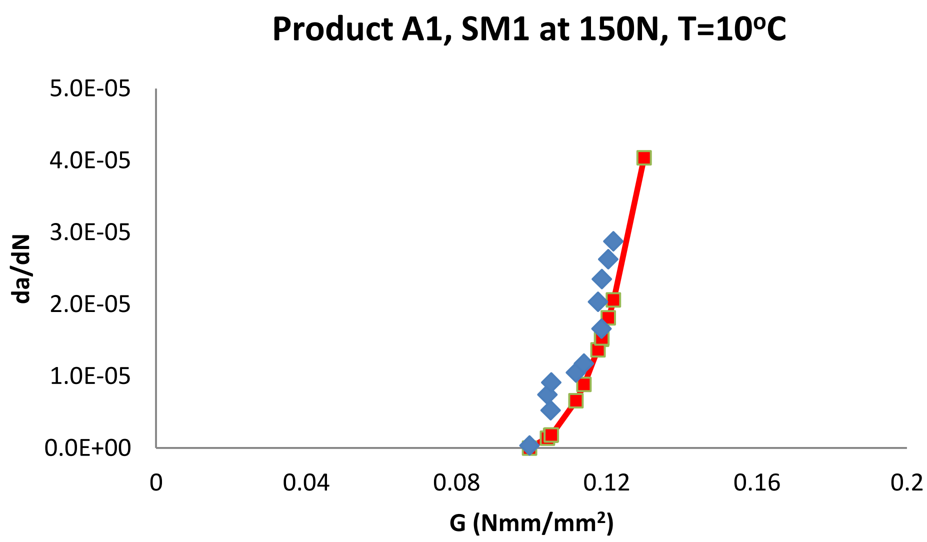

Figure 5.72 Experimental curve fitting for product A1

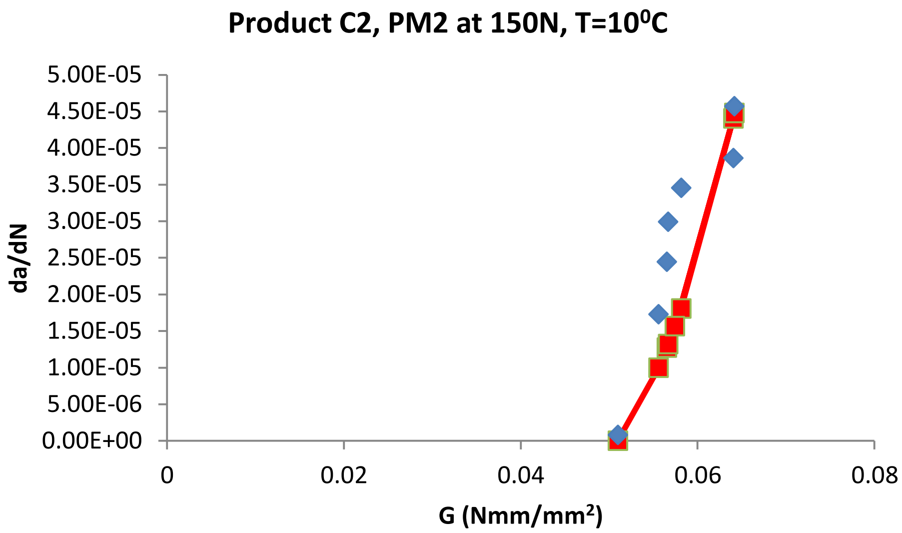

Figure 5.73 Experimental curve fitting for product C2

The number of cycles to failure (N_f) can be obtained by integrating Eq. (5.14) from an initial crack length (a_0) to a final crack length (a_f) as:

$$N_f = \int_{a_0}^{a_f} \frac{1}{da/dN} da = \int_{a_0}^{a_f} \left(\frac{1-\left(G\ /G_c\right)^{n_2}}{DG^n\left[1-\left(G_{th}/G\ \right)^{n_1}\right]} \right) da \qquad (5.15)$$

The final crack length (a_f) can be also considered as a critical debonding length, In order to find the critical debondedd length for the calculations of the fatigue life of the associated membrane products, Li (2015) has modeled the fatigue damage in the membrane interface based on 5PB laboratory tests and also based on Merwede bridge conditions.

For the 5PB finite element mesh six combinations of non-bonded membrane interfaces simulation performed.

Figure 5.74 illustrates the development of the tensile strain in the asphalt surfacing layers at the locations near to the debonded membrane interfaces when the debonding length is increased from 0, 26, 52, 78,104, 130 and 188mm.

It can be seen that the length of the debonded membrane interfaces can influence significantly the tensile strain development in the PA layer, see Set 1, 2 & 6 in Figure 5.74. The larger the number of debonded membrane interface elements in the 5PB beam, the more tensile strains are developed in the PA layer, see Set 6 in Figure 5.74.

It can be observed that all the curves show a clear turning point at a debonding length of approximate 25 to 30 mm. This implies that a debonding length of 25 to 30 mm is an important geometric parameter for the membrane to structurally affect the surfacing system response. For a membrane layer debonded less than 25 mm, it may not harm a surfacing structure in the short term, however its long term effect stays vague and needs further investigation. The critical debonding length of 25 mm could be also utilized in evaluating the fatigue life of the membrane bonded on the specific surfacing material.

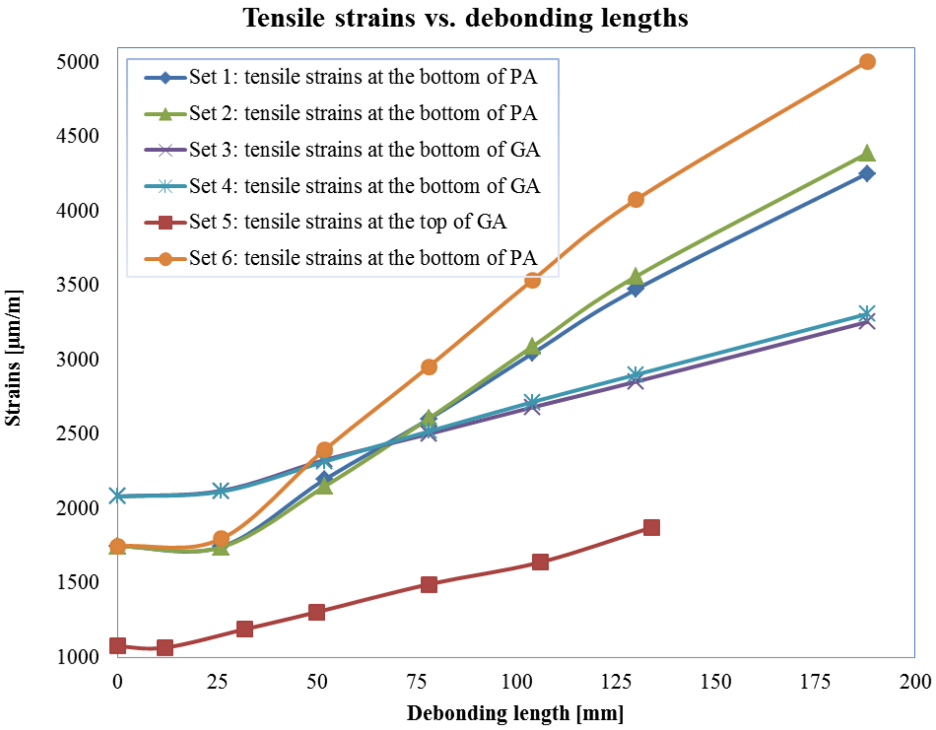

Figure 5.74 The maximum tensile strains of simulation cases with various cracking lengths in interface layers

The same observation can be seen in Figure 5.75 where FE study is based on real scale orthotropic steel deck bridge (OSDB).

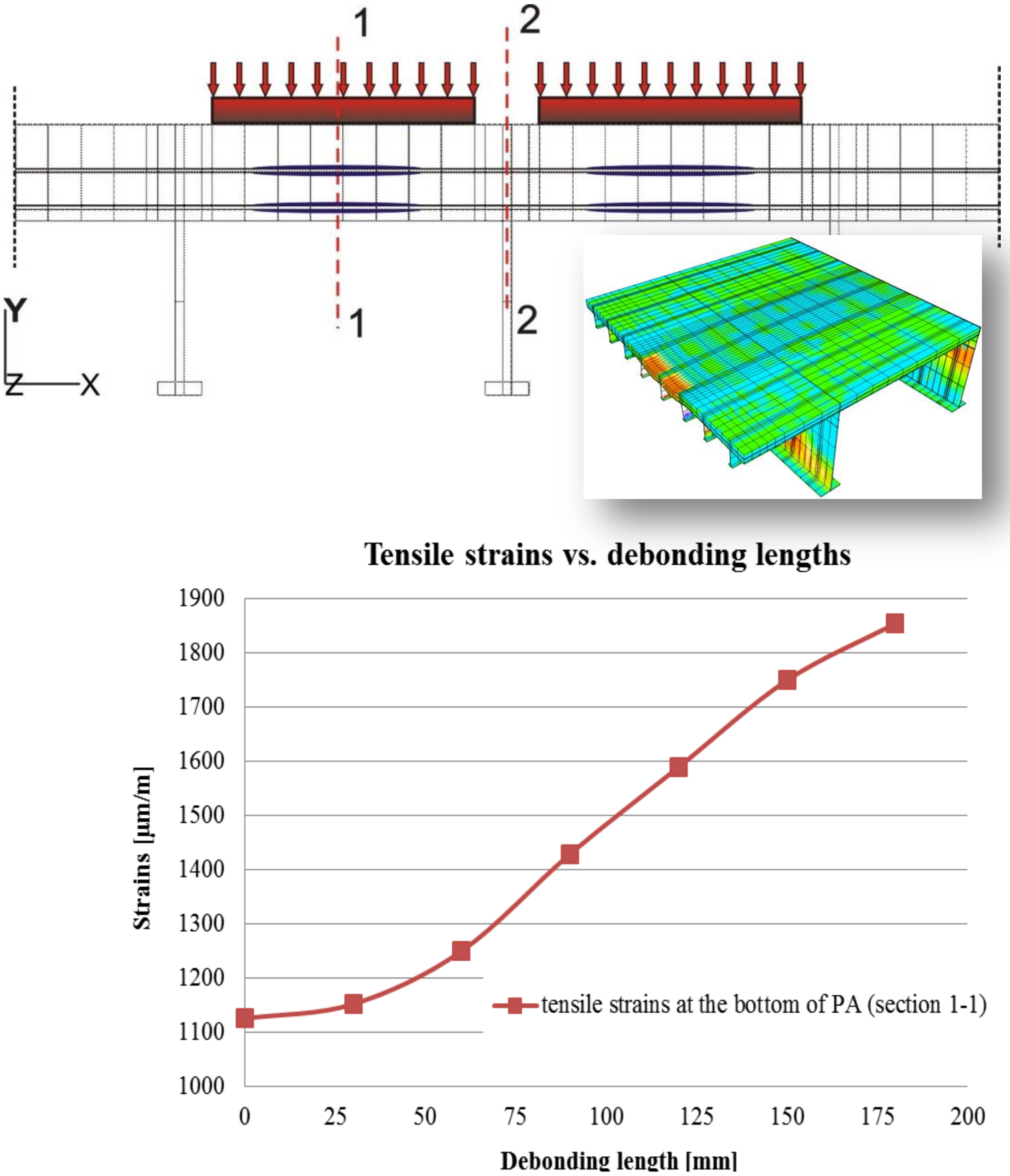

Figure 5.75 The maximum tensile strain on OSDB at various cracking

The parameters D, n, n_1 and n_2 of Equation (5.15) can be obtained by fitting to experimental data. The influence of these parameters to the fatigue crack growth curve is shown in Figure 5.76. It can be observed that D and n are mainly influencing the curve in region II where there is a linear relationship between da/dN and G, n_1 effects region I where the G_c exists and finally, region III is sensitive to n_2 constant where the G_{th} can be obtained. A full list of the fitting parameters used for all test products is summarised in Table 5.2.

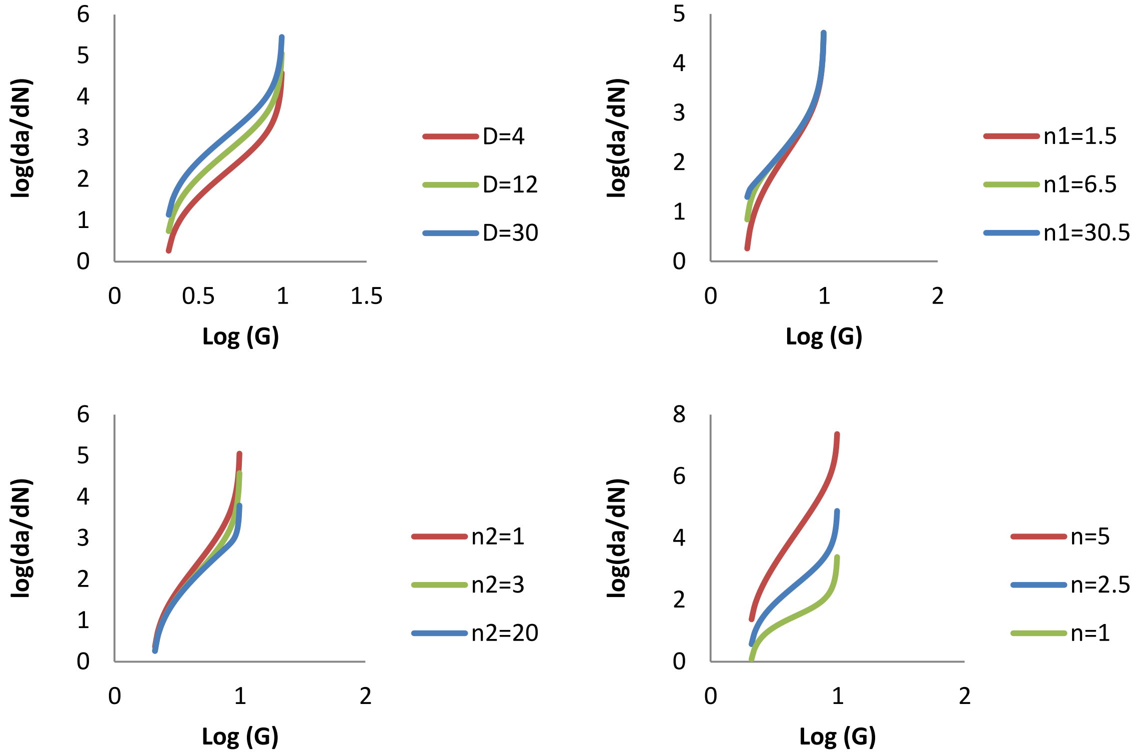

Figure 5.76 Parameter sensitivity

Table 5.2 below show a list of the various parameters used in the modified Paris law function for the experimental prediction of the fatigue life of the test products. The experimental predictions at 150N, 250N and 350N load are also stated here.

Table 5.2 NF calculations and fitting curve parameters at 10^0C

Product	Interface	^0C	Load level	D	n	n_1	n_2	G_c	G_{th}	a_0 (mm)	a_f (mm)	N_f
A1	SM01	10^0C	150N	8	5	1.4	1.5	1.25	0.092	57.02	82.02	1,248,559
			250N	1.8	4.0	1.7	1.5	1.25	0.175	63.94	88.94	181,177
			350N	3.7	6.7	1.3	1.5	1.25	0.310	141.39	166.39	96,646
	GM01	10^0C	150N	8	3.2	1.4	1.5	2.1	0.089	63.68	88.68	173,988
			250N	2	2.5	1.2	1.5	2.1	0.158	97.3	122.3	40,413
			350N	2	2.5	1.2	1.5	2.1	0.25	66.29	91.29	7,212
A2	GM02	10^0C	150N	7	4.2	1.1	1.5	2.05	0.062	54.7	79.7	1,488,423
			250N	1.6	3.4	1.8	1.5	2.05	0.128	59.4	84.4	125,349
			350N	1.7	4.5	2.4	1.5	2.05	0.20	53.23	78.23	43.292
	PM02	10^0C	150N	4	4.7	0.8	1.5	2.6	0.071	60.4	85.4	1,245,084
			250N	2.2	3.4	2.1	1.5	2.6	0.137	77.22	102.22	47.845
			350N	2.1	3.6	2.3	1.5	2.6	0.15	64.95	89.95	7,174
C2	SM01	10^0C	150N	6	3.4	0.9	1.5	2.5	0.0732	61.9	86.9	554,700
			250N	2.6	3.2	1.6	1.5	2.5	0.135	69.3	94.3	257,136
			350N	1.1	5.1	4.8	1.5	2.5	0.22	110.03	135.13	117,965
	GM01	10^0C	150N	8	4.8	1.1	0.4	3.4	0.091	58.52	83.52	1,277,137
			250N	1.6	4.8	1.2	1.5	3.4	0.176	64.55	89.55	1,160,409
			350N	1.5	7.9	5.0	1.5	3.4	0.25	69.9	94.9	538,430
	GM02	10^0C	150N	1.5	4.1	0.8	1.5	3.6	0.070	62.4	87.4	1,567,392
			250N	2.1	5.5	0.9	1.5	3.6	0.178	60.3	85.3	1,121,030
			350N	1.3	7	1.5	1.5	3.6	0.31	61.12	86.12	634,184
	PM02	10^0C	150N	7	3.5	1.1	1.5	4.3	0.048	62.67	87.67	486,066
			250N	2.3	4.3	2.1	1.5	4.3	0.123	75.74	100.74	450,586
			350N	5	4	2.3	1.5	4.3	0.182	82.32	107.32	410,100

5.7.3 Experimental results

As it was stated earlier all membrane products should withstand at least 18.8 million repetitions at the service load condition, hence, in order to derive the fatigue life of the products at different loading conditions, several trials with all the various fitting functions such as power function, algebraic curve, exponential curve or logarithmic were carried out. Figure 5.77 to Figure 5.80 presents a quick comparison of the experimental tests conducted at these load levels.

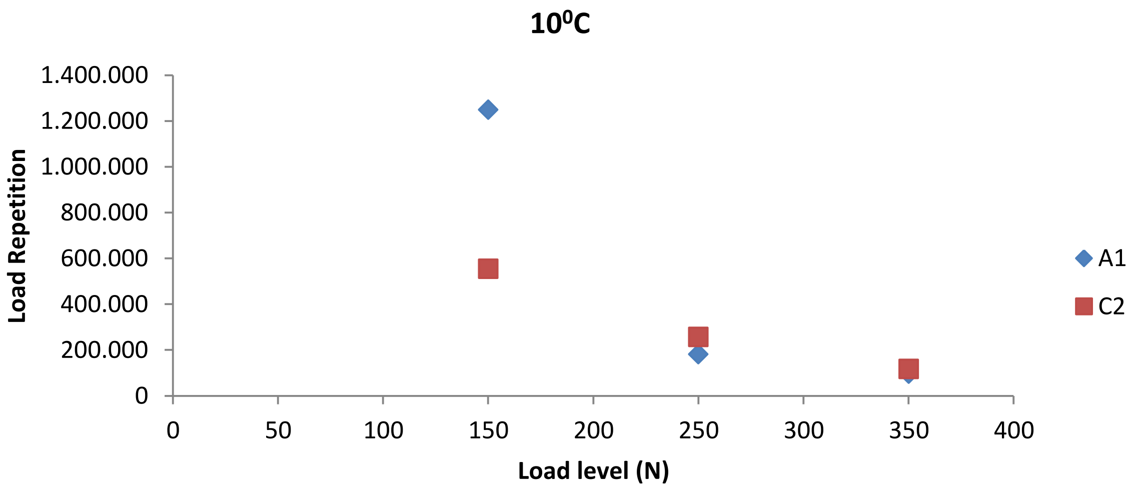

Figure 5.77 Experimental comparison of products at SM interface

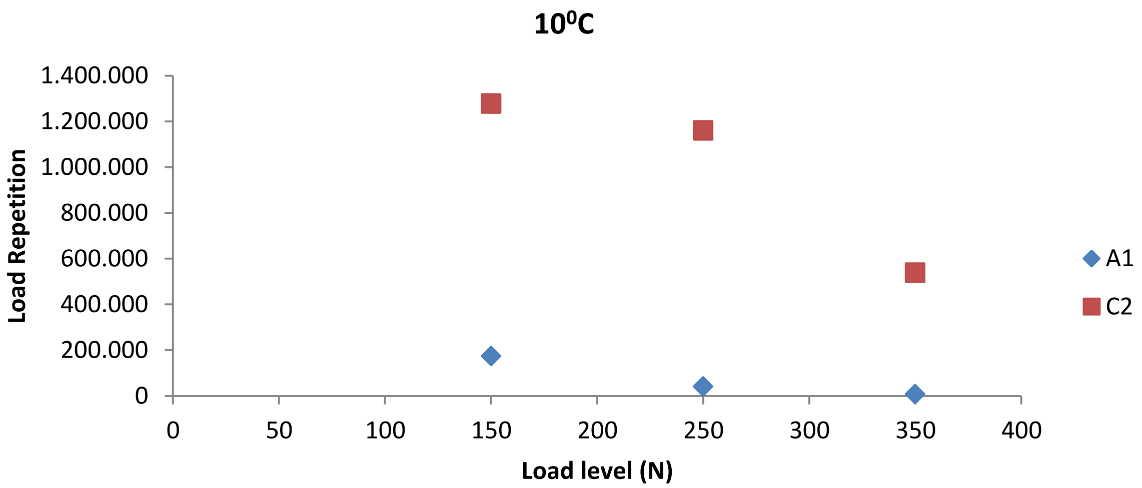

Figure 5.78 Experimental comparison of products at GM1 interface

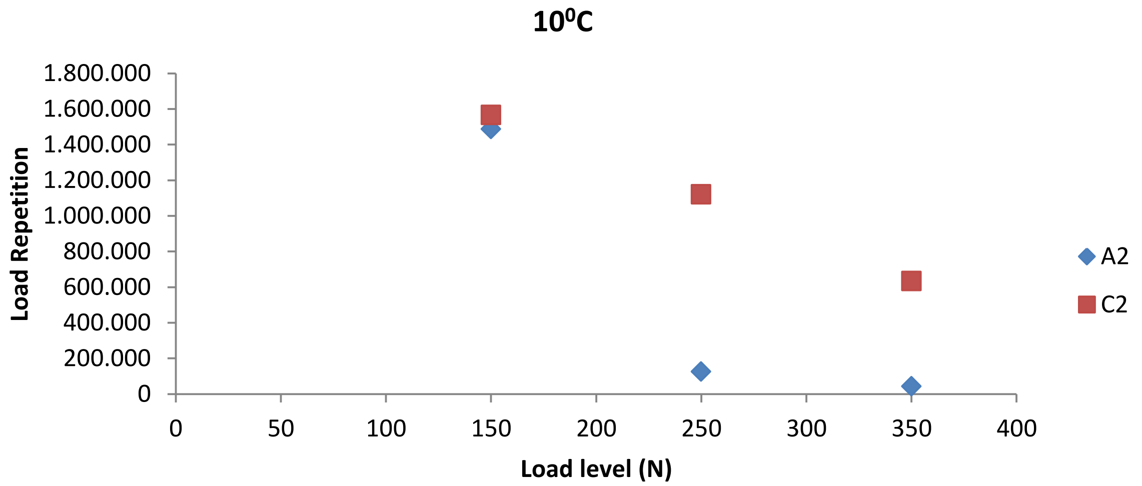

Figure 5.79 Experimental comparison of products at GM2 interface

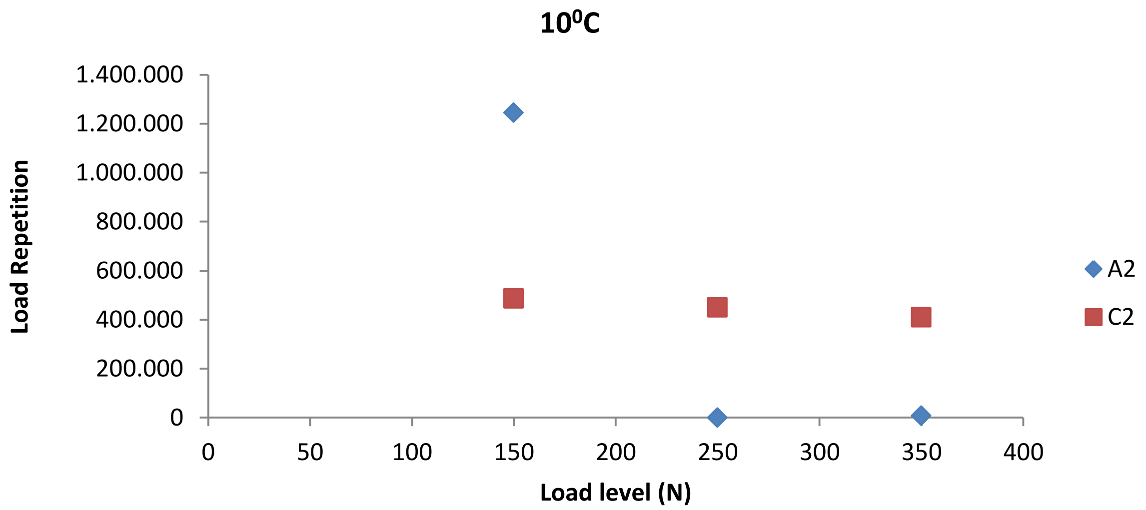

Figure 5.80 Experimental comparison of products at PM2 interface

Figure 5.81 shows a typical curve fitting attempt to obtain the fatigue life of membrane N_f at load level 150N, 250N and 350N of MAT tests. It was observed that, an asymptotic model with hyperbolic function can very well represent the force- load repetition prediction model.

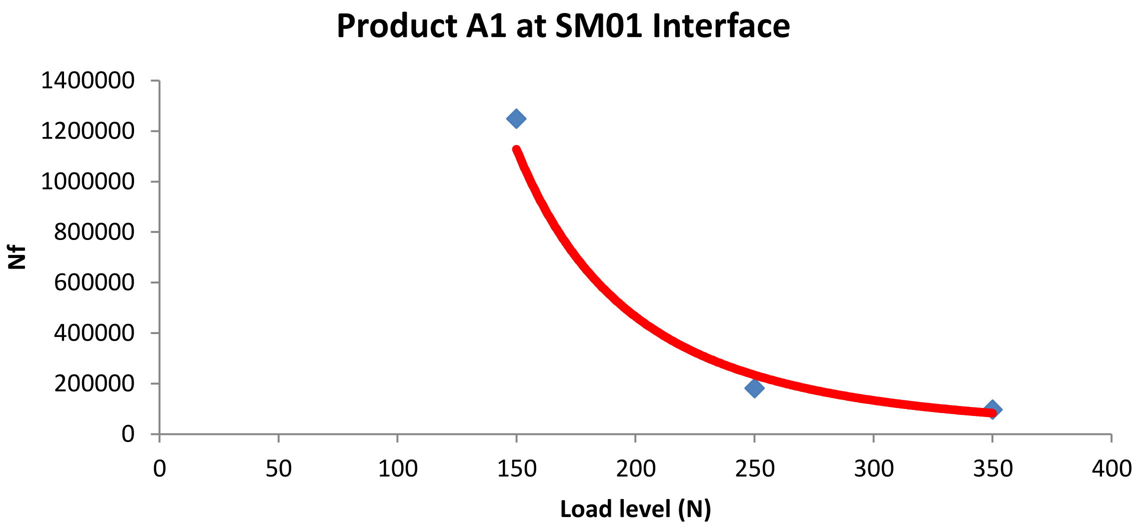

Figure 5.81 Curve Fitting experimental data

The function used for the prediction of the fatigue life is :

$$N_f = A_0 + \frac{B}{(Z - C_0)^2} \qquad \text{For all } Z \geq C_0 \qquad (5.16)$$

Where A_0 C_0 and B are fitting parameters , Z is the applied piston load level from MAT. As it can be seen in Figure 5.82, all tested membrane products have different force level where the prediction calculations are made. Once the piston load level corresponding to the membrane critical stress at bridge is known from Figure 5.82, the service life of the membrane can be predicted using the Eg (5.16)

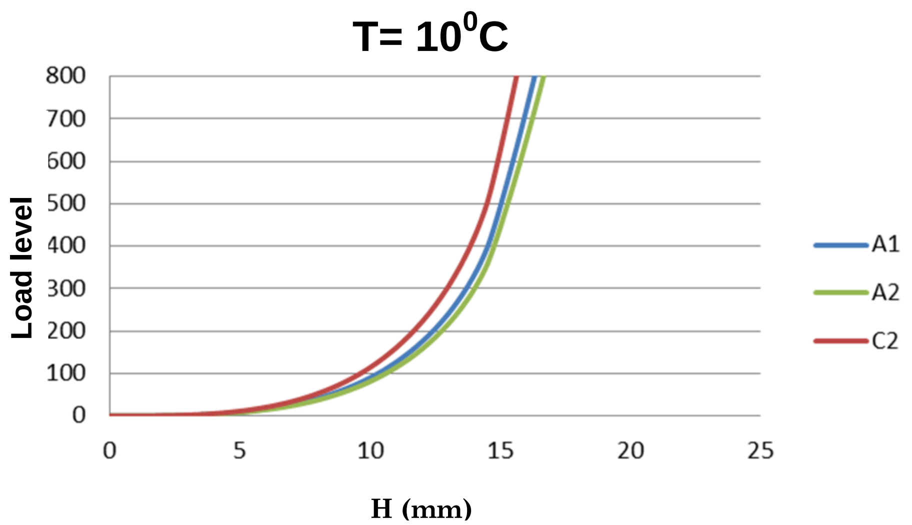

Figure 5.82 Identification of piston load in MAT for different membrane products

In Figure 5.83 the connection between the MAT device and the real bridge is graphically represented

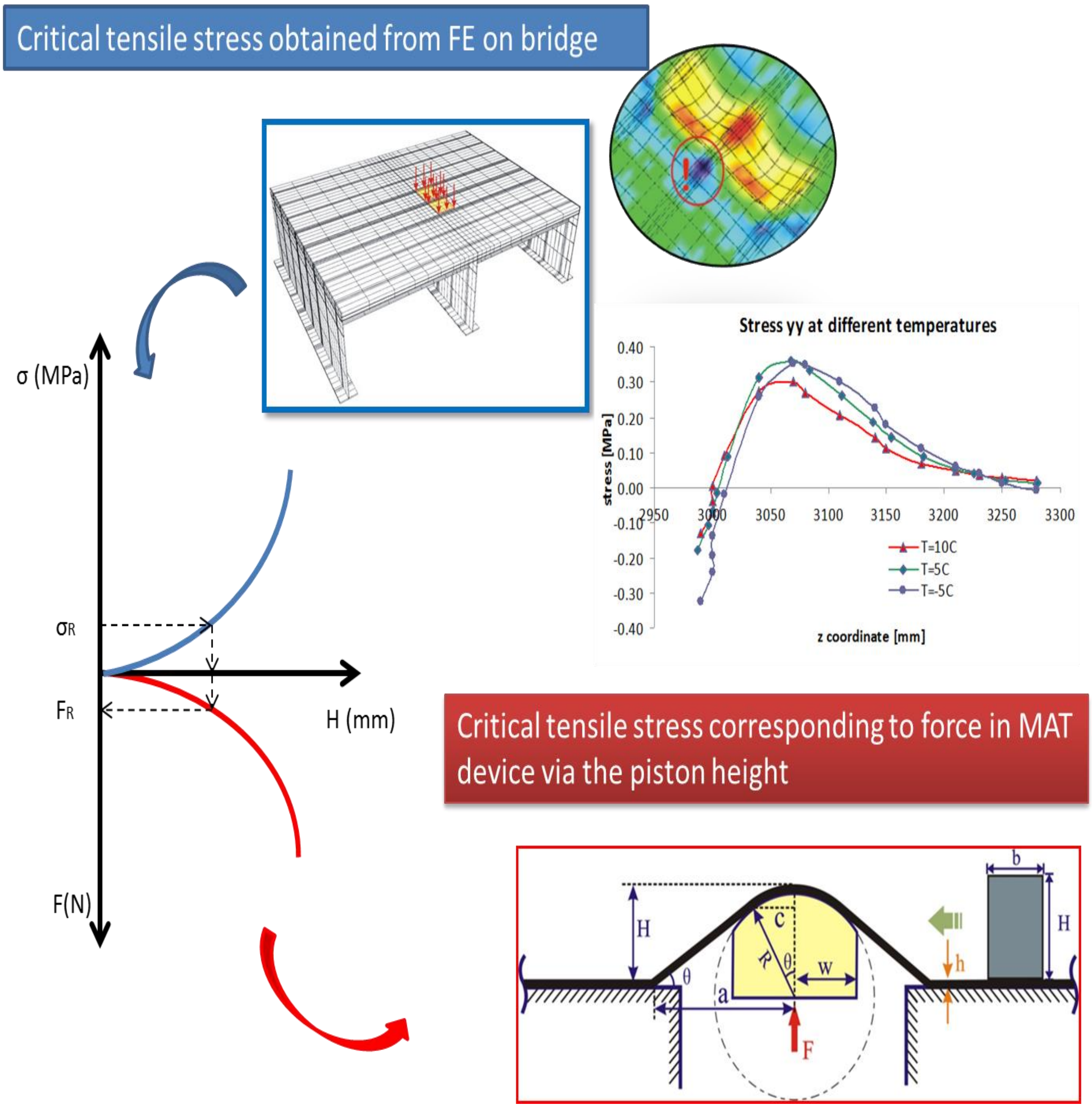

Figure 5.83 Graphical representation of the methodology

In Table 5.3 the fatigue life of the membrane products is summarised. As it can be observed all the selected membrane products A1, A2 and C2 fulfil the 18 million requirement at all interfaces SM01, GM01, GM02 and PM02. C1 product is not listed here due to the fact that there is no debonding at these load levels on the corresponding interfaces at 10^0C.

Table 5.3 fatigue life predictions at 10^0C

Product name	Interface	Predicted load F(N)	N_f
A_1	SM01	75	27 millions
A_1	GM01	75	19 millions
A_2	GM02	75	20 millions
A_2	PM02	75	20 millions
C_2	SM01	50	20 millions
C_2	GM01	50	30 millions
C_2	GM02	50	25 millions
C_2	PM02	50	18 millions

5.8 Conclusion

Based on the results presented in this chapter, the following conclusions can be made.

- The fatigue response of a membrane product is influenced not only by the surrounding substrate but also by the environmental temperature and loading level applied on the membrane;
- The concept of dissipated energy/work provides a fundamental and expedient means to evaluate the fatigue life of membrane products on different substrates;
- As damage accumulates in a specimen, the dissipated work varies depending on the rate of membrane debonding.
- Product C1 performs quite well as the bottom membrane, both at 10^0C and 30^0C, in term of values of dissipated work and debonding length.
- Product C2 and A2 are considered as the best choices for the top membranes.
- The observations from the MAT cyclic loading tests are coincident to the observations from MAT monotonic static loading tests. It means that the findings of this research is a further proof that the methodology utilized in this research project is adequate for ranking the bonding characteristics of various membrane products on different substrates for OSDB construction.
- The methodology developed in this research project is adequate not only for ranking the bonding characteristics of various membrane products on different substrates but also for predicting the actual fatigue life of membrane products on OSDB construction.
- The fatigue response of a membrane product is influenced both by the load level and the environmental conditions
- The asymptotic model can be utilised to predict the membrane fatigue life, however more sophisticated models might give more accurate results.
- Accuracy of results can be improved if tests are conducted at lower load levels. Restrictions of the set up limited the minimum applied load to 150N in this research.

6 Experimental results of 5PB Beam Tests on Orthotropic Steel Deck Bridges

Orthotropic steel bridges consist of a 10-14 mm steel deck plate supported in two perpendicular directions, by U-shaped stiffeners and crossbeams in the longitudinal and transverse direction respectively. Due to lightweight and flexibility become popular in the last decades but several problems were reported in relation to asphalt surfacing materials such as rutting, cracking, loss of bond between the surfacing system and steel deck Mangus and Sun (1999).

The five point bending (5PB) beam test is a laboratory scale test that allows studying the fatigue resistance of surfacing layers on orthotropic bridge decks Mangus and Sun (1999). Hameau et al. (1981) report the most severe load case for surfacing layers of orthotropic bridge decks is when they are subjected to negative moments. The 5PB beam test has become a French standard test method (NF-P98-286, 2006), Mangus and Sun (1999).

In this report, the multi-surfacing layers together with the steel plate in 5PB beam are treated as a whole, the fatigue damage in 5PB beam is related to the amount of dissipated work computed by using the measurement of actuator load and loading platen deformation during the loading cycle. The dissipated work, which is equivalent to the lost part of the total potential energy of the beam, can be used to explain the incremental damage during the testing. The concept of dissipated work is explained in earlier chapters.

For the purposes of this research 5PB beam test was performed in order to understand if this type of test can be directly used to evaluate the performance of the multilayer system on steel deck and also to perform a laboratory scale test that would allow studying the fatigue resistance of surfacing layers on orthotropic bridge decks.

In the first part of this chapter the experimental device of the 5PB, test conditions and the instrumentation are described. In the second part, the results of the 5PB specimens with four different membrane products as bonding layers at two temperatures $-5\circ$C and $+10\circ$C are exposed. The results show that the in time deformation measurements are allowable to evaluate the fatigue response of the entire structure. The stiffness and the bonding characteristics of the intermediate membrane sheet as well as the wearing course behaviour seem to have great influence on the mechanical response of multilayer bridge surfacing system.

6.1 Description of the five-point bending test

In order to assess the fatigue resistance of the steel bridge multi-layer surfacing system, the French five-point bending beam test has been used. It was developed by the“Laboratoire Central des Ponts et Chausse´es”(LCPC) in the 70s, and its main advantage is the ability to safely represent the conditions on a real steel deck applying negative moments Mangus and Sun (1999). This occur at the alignment of the stiffener web when each of the wheel of a double tyre is positioned at each side of the web, Figure 6.1.

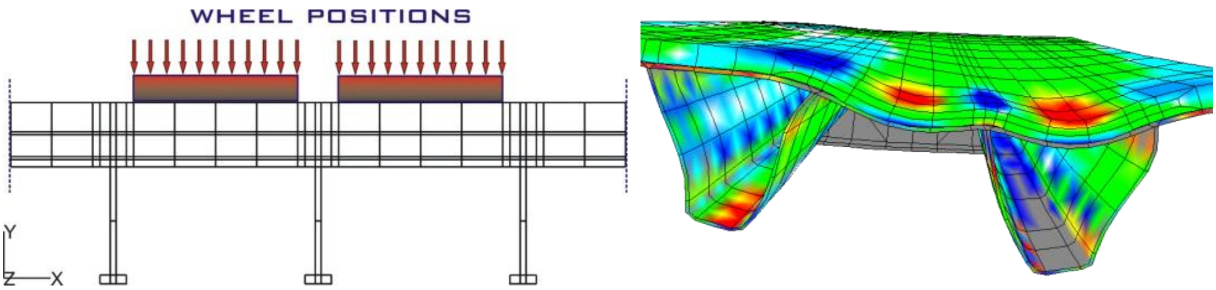

Figure 6.1 Schematic representation of the area of concern

In the Netherlands an asphaltic surfacing structure for orthotropic steel deck bridge mostly consists of two structural layers, Figure 6.3. The upper layer consists of Porous Asphalt (PA) because of reasons related to noise hindrance. For the lower layer a choice between Mastic Asphalt (MA) or Guss Asphalt (GA), can be made Mangus and Sun (1999). Therefore, in order to study the fatigue response of the typical Dutch steel deck bridge, 5PB specimen with the two wearing course, top layer with PA and bottom layer with GA bonded by two membrane sheets are investigated.

6.2 Sample preparation

The sample preparation took place at BAS research and technology company in The Netherlands. For the preparation, a wooden mould with dimensions 65 x 580 x 90 has been utilized in order to be able to produce six samples, Figure 6.2. The steel plates placed at the bottom of the mould then the bottom membrane was bonded and finally the GA was applied. After cooling of the GA, the second membrane was applied according to the manufacturer specification and then the PA was compacted on the top. Lastly a hydraulic saw has been used in order to cut and separate the six samples from the mould. The properties of the asphalt layers can be found in chapter 3.

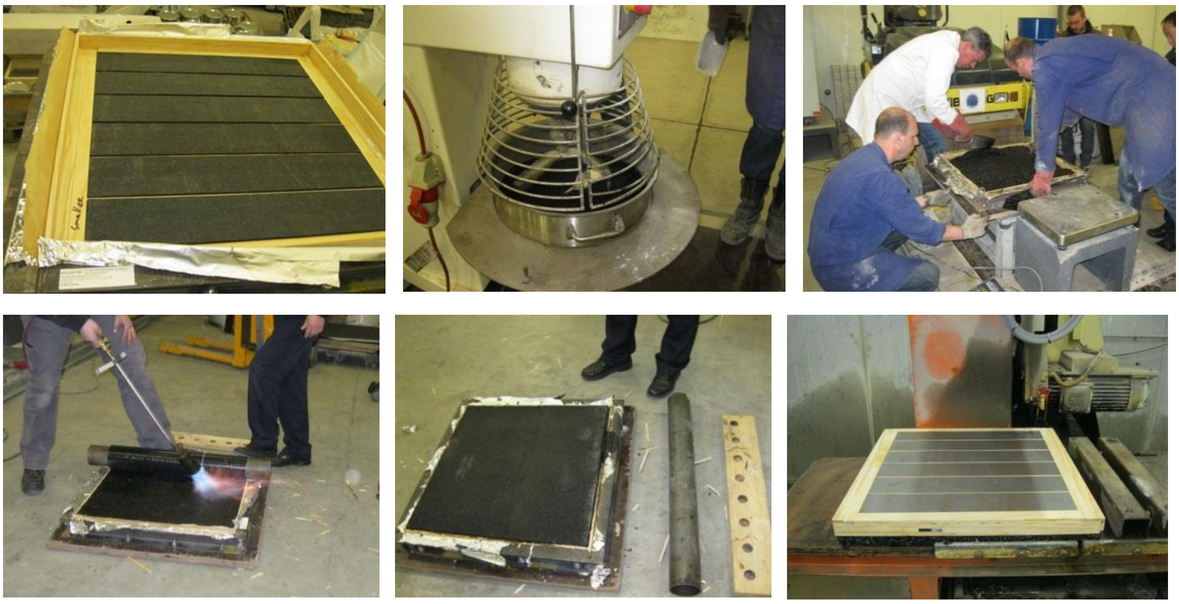

Figure 6.2 Specimen preparation

The final specimen is consisted of 10 mm-thick steel plate, 2 to 4mm-thick bottom membrane, 30mm Guss asphalt layer, 4.7-4.8mm-thick top membrane and 40mm of porous asphalt layer, see Figure 6.3.

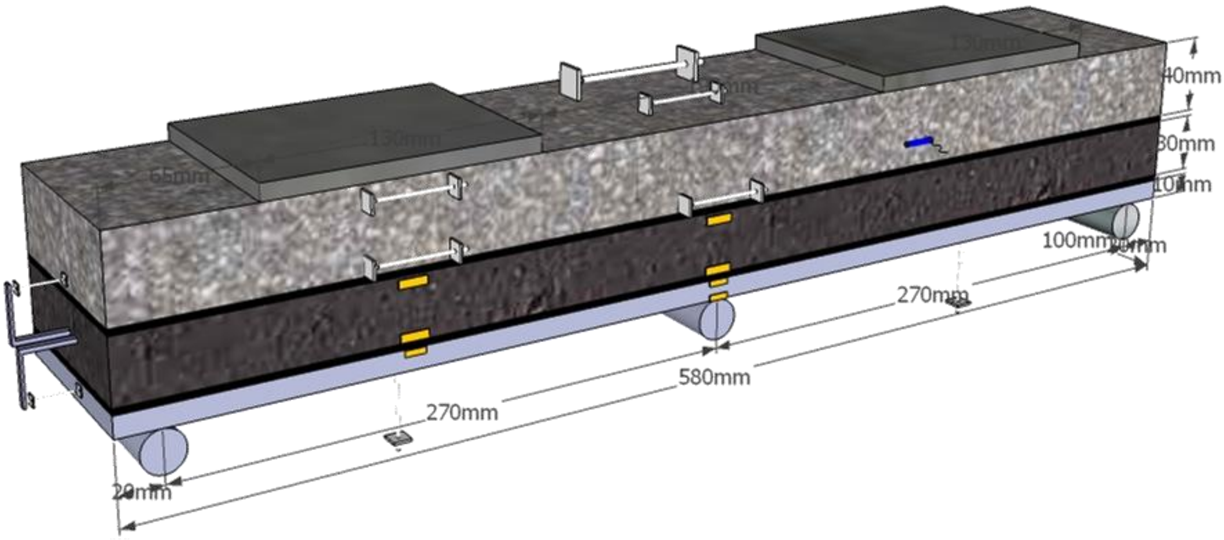

Figure 6.3 Specimen geometry and composition

For the specimen preparation a steel plate with 580 mm x 100mm x 10mm was used. Four different types of samples have been prepared, named as beam 1 bonded with membrane products A1 and A2 from company A, beam 2 bonded with membrane products B from company B, beam 3 bonded with membranes product C1 and C2 from company C and beam 4 bonded by membrane C2 from company C, see Figure 6.4.

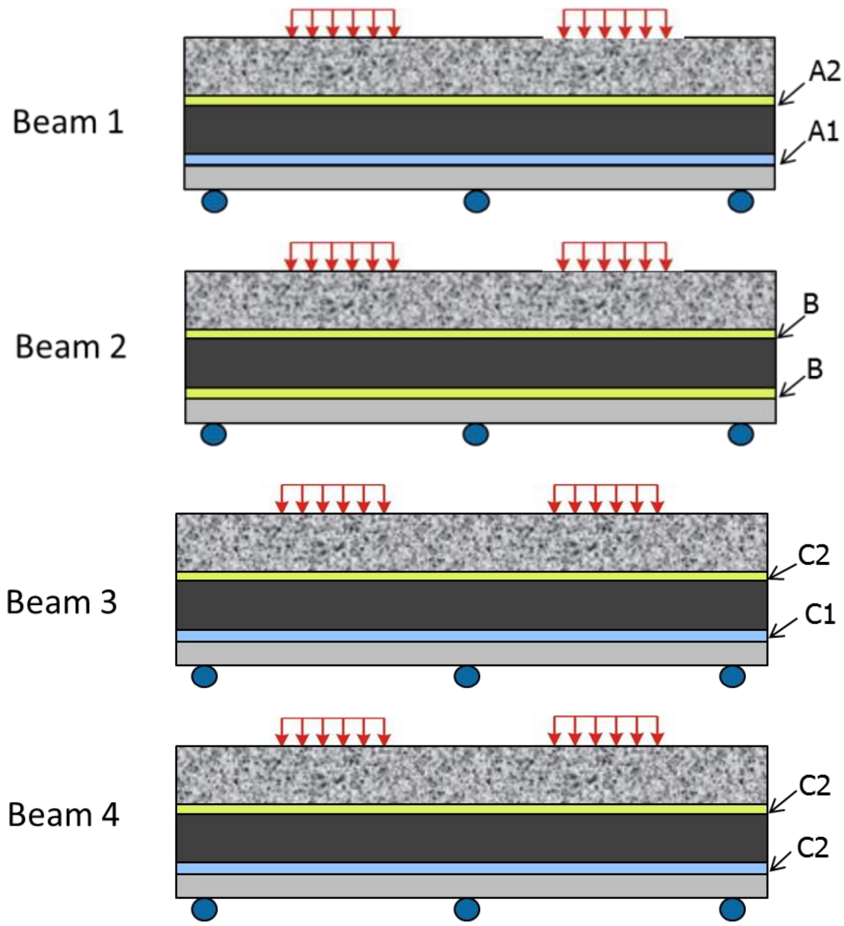

Figure 6.4 Four different types of samples

6.3 Experimental set up

Both static and fatigue tests were performed under two temperatures ranges (-5^{0}C and +10^{0}C),Figure 6.5. The Static tests were performed prior to the fatigue testsusing ramping force. The maximum force is 18.4 kN and the ramp time to maximum force is 40 sec. For the fatigue tests, sinusoidal compression loading P ranging between F_{max} and 0.1xF_{max} at a frequency of 4Hz was applied for two million cycles. In order to perform the tests under controlled temperature conditions the set up was properly insulated and enclosed within a climate chamber. Figure 6.6.

For the purpose of this report the specimens were 100mm wide and therefore each shoe print was 130mm long and 100mm wide. The pressure load applied on each shoe was 0.707 MPa. This load pressure corresponds with 9.2 kN on each shoe (0.707MPa x 130mm x 100mm), which means a total of 18.4kN. If the same pressure load of 0.707MPa is applied on a wheel print type B (double tyre 220mm by 320mm), it corresponds with 100kN wheel load which is typical truck load utilized in the Netherland. (Mangus and Sun 1999).

.

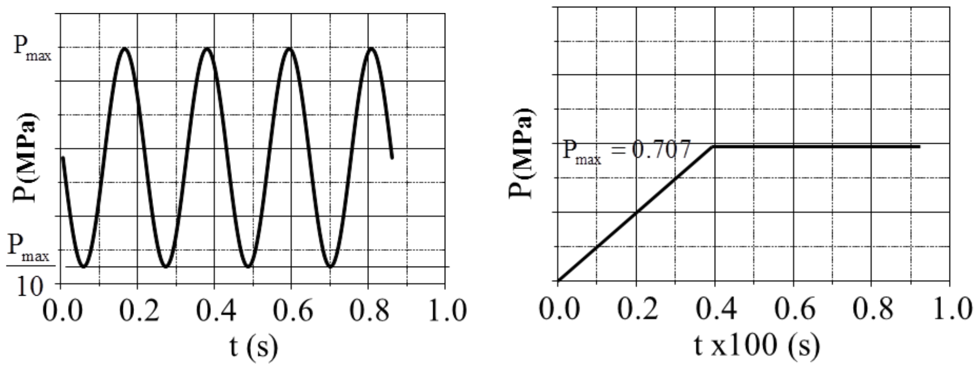

Figure 6.5 Fatigue and static response

The climate chamber and the specimen temperature were measured by two temperature sensors. One is in the chamber to measure the chamber room temperature and another one is on the upper face of the porous asphalt to measure the specimen temperature.

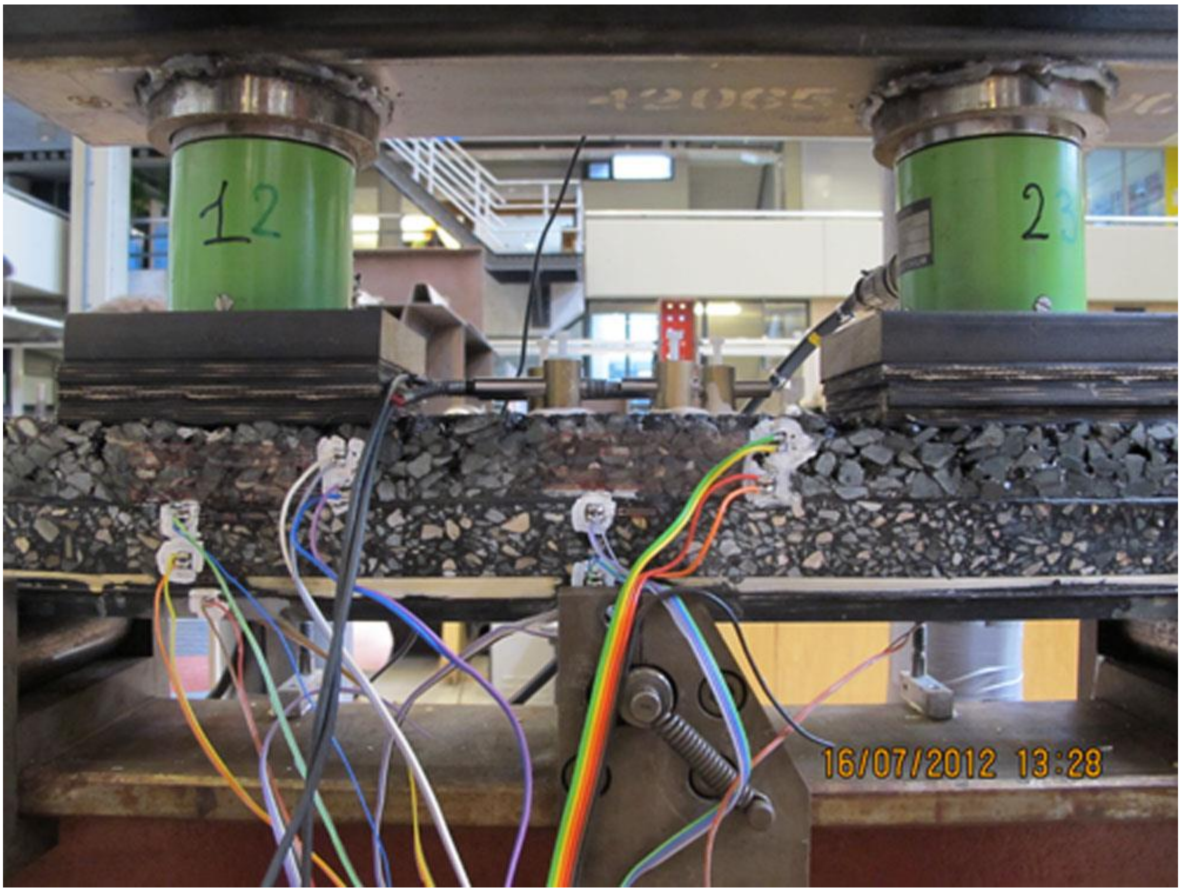

Figure 6.6 The five-point bending beam test set up

6.4 Instrumentation

Fourteen strain gauges have been adhered on the front side of the sample in order to monitor the evolving strains of the asphalt layers, where cracks are likely to appear. The back side of the sample has been paint white with coloured vertical lines covering the whole width of the sample in order to easily identify cracks and shear movements. The most vulnerable area is at the middle of the sample above the central support where high strain development is expected, see Figure 6.7. For this reason seven strain gauges have been placed at the middle area, see Figure 6.8.

- Three strain gauges are on the PA, the first one close to top surface (RK0013), the secon one close to the top membrane (RK0015) and the third one is on the upper face of the sample between the loading shoes (RK016).
- Two strain gauges are on the GA , one close to top membrane (RK001) and another one close to bottom membrane (RK002)
- and two strain gauges are glued on the steel plate, one close to bottom membrane (RK005) and one close to the bottom surface (RK006).

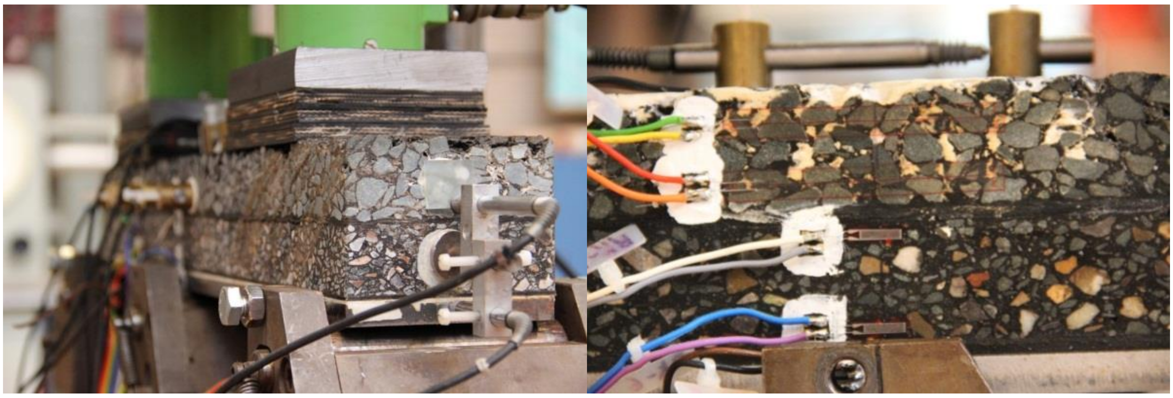

Figure 6.7 Instrumentation of strain gauges and LVTDs on the specimen

Another vulnerable area is below the load cells where five strain gauges have been glued, see Figure 6.8.

- Two strain gauges are on PA, one close to top surface and one close to top membrane named RK0011 and RK0012.
- Two strain gauges are on the GA, named RK007 and Rk008.
- One strain gauges is glued on the steel plate close to the bottom membrane(RK009).

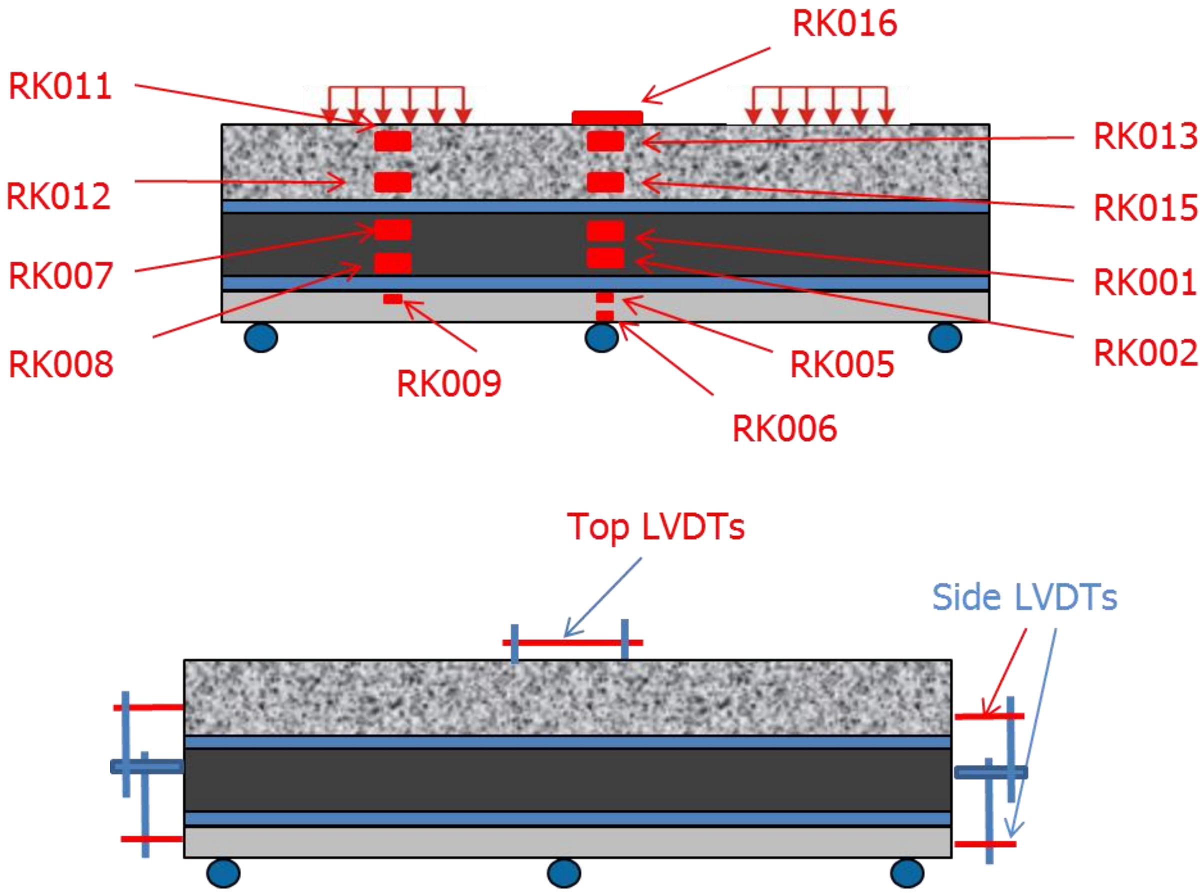

Figure 6.8 Position of strain gauges and LVDTs

Two different types of displacement sensors, LVDT (Linear Variable Differential Transformer) were positioned on the upper face of the sample at the center, but also at the both sides of the sample see Figure 6.7 and Figure 6.8. Both accuracy and a large detection area are ensured: the first sensor (LVDT 1: ±2.5mm and l=60 mm) is certain to have a measurement zone where cracks are likely to appear, and the second (LVDT 2: ±1.0 mm) and l=30 mm) senses the displacements more precisely. Finally another set of LVDTs has been placed at both sides of the sample in order to monitor the shear deformation between the asphalt layers and also between the GA and steel.

6.5 Discussion and results

6.5.1 Static tests

The static tests were performed before the fatigue tests until a maximum total load of 18.1 kN which results to load pressure 0.707MPa on each shoe The ramp time to maximum load is 40 sec. The strains recorded by the strain gauges during the static tests can be compared with the strain predictions from the FE simulations but also can give an indication about the integral response of the beam layers.

Based on the work done by Muraya (2007) and Medani (2006), a set of primary parameters for porous asphalt and guss asphalt at 10^{0}C and -5^{0}C were decided, Table 6-1.

Table 6-1 Parameters of porous asphalt and guss asphalt

temperature(°C)	material layer	E1(MPa)	E_∞ (MPa)	Poisson's ratio	η (MPa.s)
10	Porous asphalt	200	1	0.3	15750
	Guss asphalt	450	3	0.3	15750
-5	Porous asphalt	2000	10	0.3	22500
	Guss asphalt	4500	30	0.3	22500

By using the theory of Zener model that is described in the previous section, the model parameters of E_∞ and E_1 as well as parameter η can be deductive through fitting curve by Origin program. The Zener model parameters for the five membrane products are listed in Table 6-2.

Table 6-2 Properties of the five membrane products at +10 °C and -5 °C

Temperature(°C)	Property	A1	A2	B	C1	C2
10	E1	6.19	5.7	4.59	9.24	9.38
	Poisson's ratio	0.15	0.15	0.15	0.15	0.15
	Eta η	1876	1911	192	336.65	475.65
	E∞	5.045	4.38	2.962	16.215	4.8
-5	E1	61.9	57	45.9	92.4	93.8
	Poisson's ratio	1.5	1.5	1.5	1.5	1.5
	Eta η	18760	19110	1920	3366.5	4756.5
	E∞	50.45	43.8	29.62	162.15	48

The FE simulations of the 5PBT specimen that is manufactured by membrane product B is presented here to verify the FE model. Figure 6.9 and Figure 6.10 show the comparisons of transversal strains recorded during the static tests along the thickness of the tested beam. It can be observed that the numerical predictions show good agreement with the experimental results. It can be seen that all tested beams produce higher strain values at 10 °C rather than at -5 °C. The influence of the temperature on the strain of the steel deck plate is not significant. The maximum tensile strain at section 2-2 is generated at the top face of PA and the maximum compressive strain at section 1-1 is generated also on the top face of PA but it is closer to the loading plate.

It can be concluded that the material models that were verified by the MAT test, is capable to characterize the integral response of the multilayer surfacing system in the 5PB beam test. The numerical results indicate that, once the appropriate material parameters are available, the FE model shows good comparison with the observed behaviour of the tests.

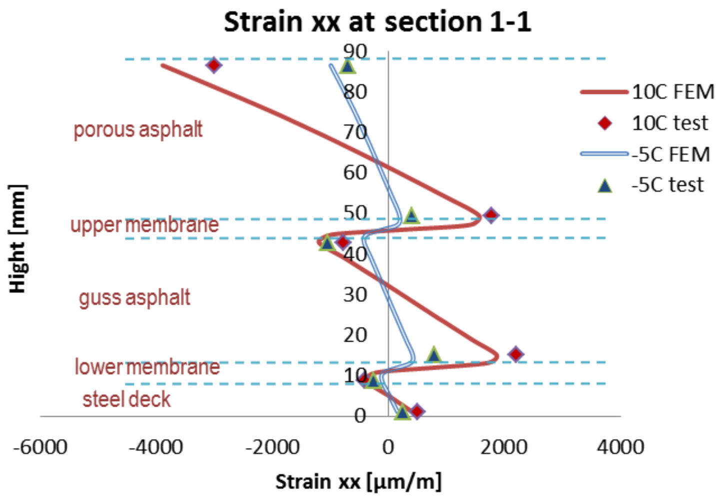

Figure 6.9 Transversal strains at section 1-1 (membrane B, 10 °C and -5 °C)

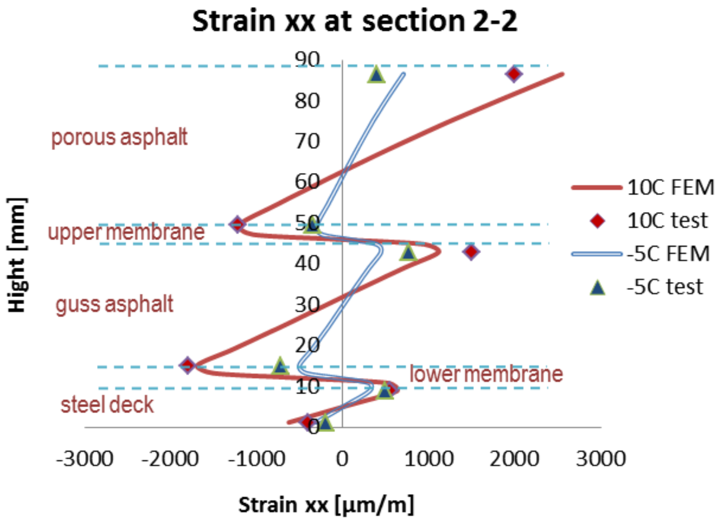

Figure 6.10 Transversal strains at section 2-2 (membrane B, 10 °C and -5 °C)

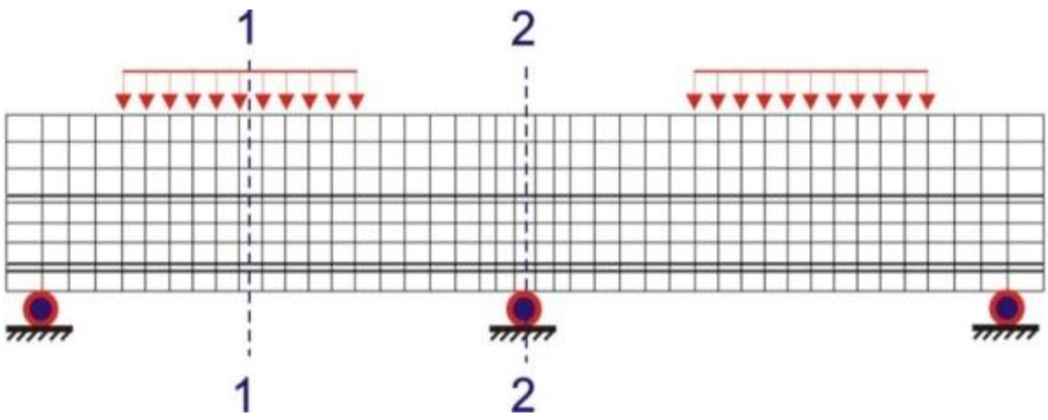

Figure 6.11 The area of concern

Figure 6.12 and Figure 6.13 below show the transversal strains $\varepsilon_{\chi\chi}$ recorded during the static tests along the thickness of the tested beam. As it can be seen all tested beams produce higher strain values at 10^0C than at -5^0C, specially on the PA. The influence of temperature on the strain of the steel deck plate is not significant. Maximum tensile strain for all tested beams recorded on the top face of PA and maximum compressive strain on the bottom of PA close to the top membrane. Figure 6.11, indicating the two cross sections where the strains have been recorded.

Cross section 1-1

Beam 2 was found to be the most vulnerable with higher strain amplitude compared with the other tested beams at 10^0C. High strain concentration also recorded on beam 4 with high tensile strain at the bottom of GA at 10^0C. Beam 3 was found to have the lower strain concentration especially at the area close to steel plate both at 10^oC and -5^oC. Finally, beam 1 has also shown good response with low strain values particularly at -5^0C.

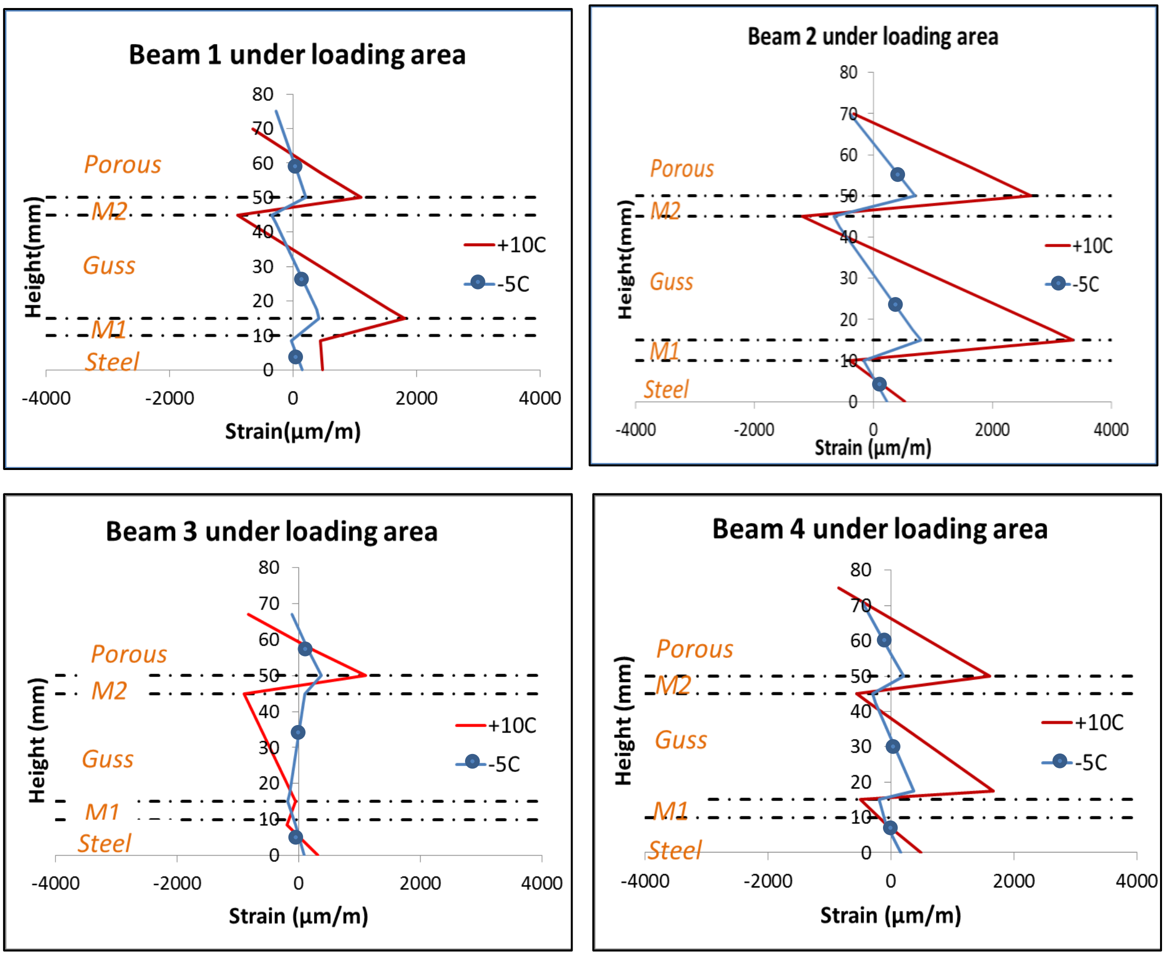

Figure 6.12 Strain distribution below the loading area, cross section 1-1

Cross section 2-2

The same observation can be made at the location above the central support, Figure 6.13. Beam 2 was found to have higher strain both in compression and tension at 10^{0}C. The influence of temperature is obvious for all cases. Beam 3 and 4 were found to be in the same range in term of the strain distribution. At -5^{o}C beam 3 was found to have the lower strain values in GA.

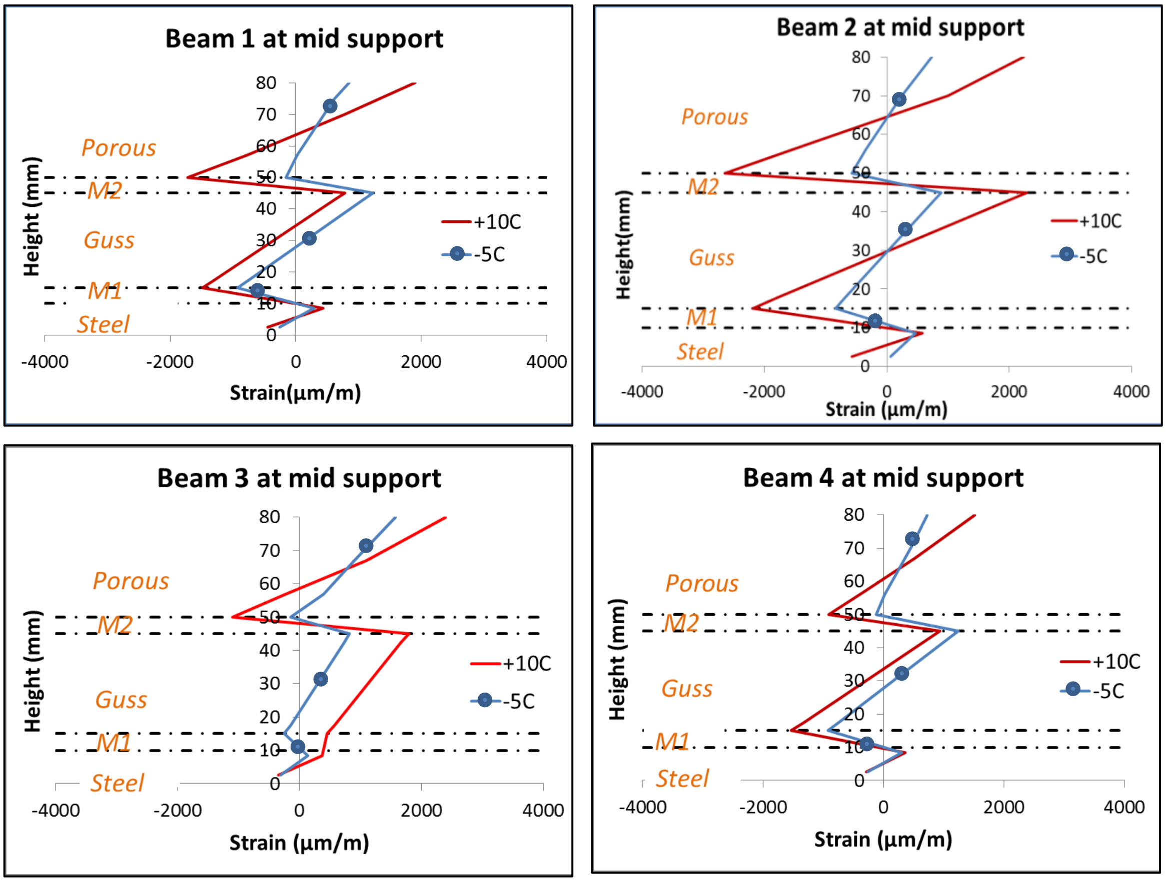

Figure 6.13 Strain distribution above the middle support, cross section 2-2

6.6 Fatigue tests

6.6.1 Strain measurements

Cross section 1-1

The strain concentration at the lateral side of the GA below the loading area both close to top (RK007) and bottom membrane (RK008) was recorded, Figure 6.8. From Figure 6.14, during the first 500 cycles it can be observed that all tested beams produced compressive strain. Maximum strain values was found on beam 2 around 800μm/m. However after the first 1000 cycles an evolution of strain from compression to tension is observed. Beam 3 kept its amplitude constant after the first 500,000 cycles close to zero though beam 2 and 4 after the first 1000 cycles re-distribute their strain amplitude to tensile obtaining 600μm/m and 1200μm/m respectively. Beam 1, while during the first 500,000 cycles showed the same response with all other tested beams. After that until the end of the test, the strain amplitude on beam 1 re-distributed and compressive strain around 200μm/m was recorded.

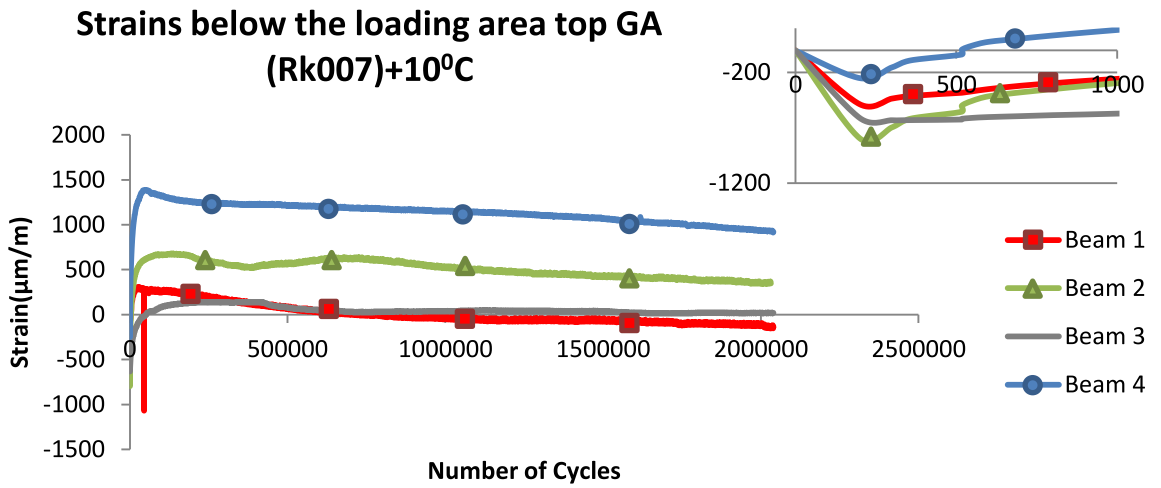

Figure 6.14 Strain distribution on GA at 10^{0}C (RK007)

At the area close to bottom membrane higher strain concentration observed on beam 1 and 2, Figure 6.15. During the first 1000 cycles beam 2 has reached its maximum tensile strain value close to 3500 µm/m then strain is suddenly decreased to amplitude around 1500µm/m and then gradually decreased until the completion of the test. Beam 3 has showed no significant deformation at this location. The same observation can be made for beam 1 and 4 with maximum strain values around 2200 and 1300 respectively.

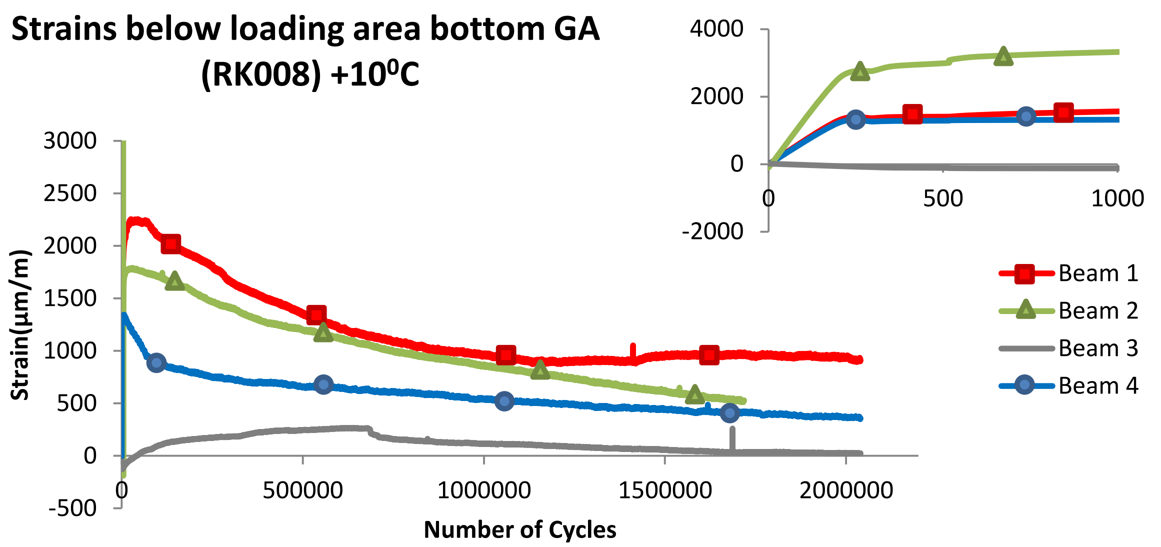

Figure 6.15 Strain distribution on GA at 10^{0}C (RK008)

In Figure 6.16 the results from the measurements on GA below the loading area at -5^{0}C are presented. The evolution of the strain amplitude from compression to tension is recorded for all four beams. The strain amplitude for beam 3 has been increased during the first 250.000 and it was kept constant until the completion of the entire test around 200µm/m in compression. However, with the number of load cycle increasing, the strain development of beam 1, 2 and 4 are changed from compression to tension. Beam 1 and 2 have followed the same trend and reached maximum strain amplitudes around 400μm/m.

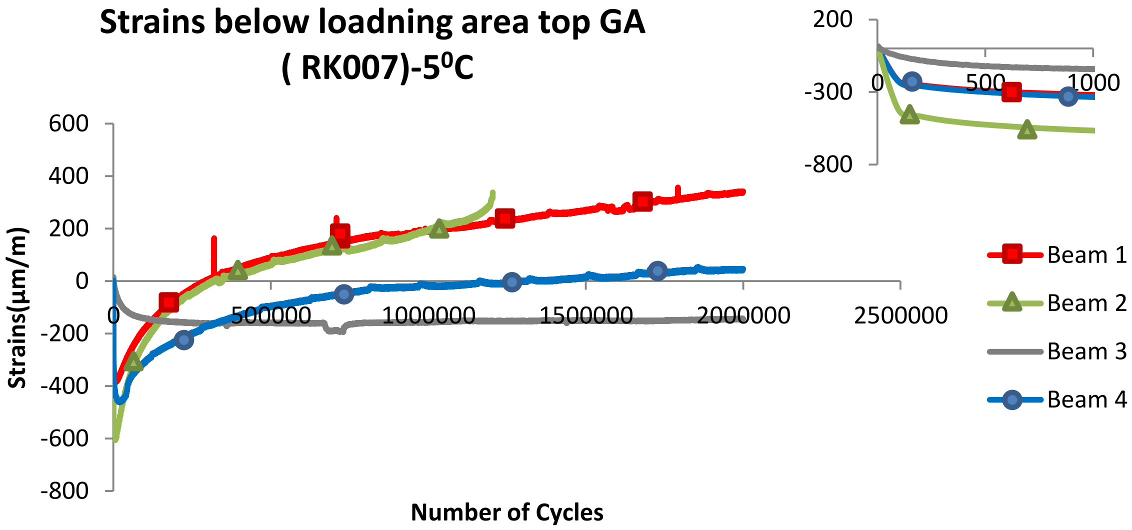

Figure 6.16 Strain distribution on GA at -5^{0}C (RK007)

The strain distribution below the loading area close to the bottom membrane is presented in Figure 6.17. As it was observed in Figure 6.16, beam 3 indicates the development of compression strain on both locations of RK007 and RK008. This proves that the bonding strength between the bottom membrane and the GA are quite high in this sample that resulting the neutral axis close to the steel plate so that compressive strains are observed at both location. It is noticed that beam 1 and 4 followed the same trend reaching their maximum values after the first 250,000 cycles and kept constant until the completion of the test. Finally beam 2 was found to be the one with maximum tensile strain concentration since the beginning of the test.

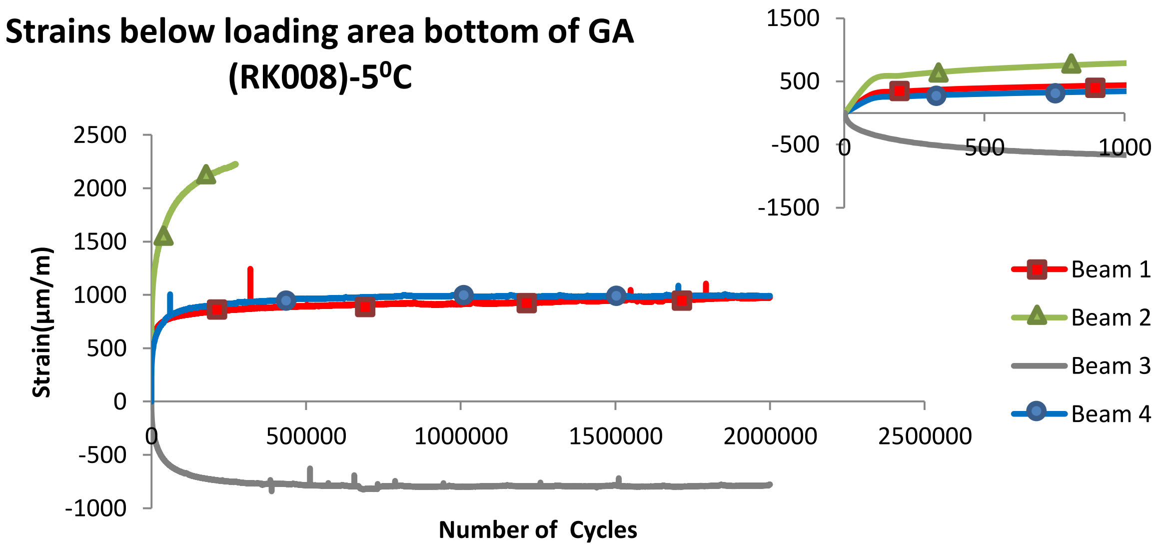

Figure 6.17 Strain distribution on GA at -5^{0}C (RK008)

Cross section 2-2

Rk001 is the strain gauge glued on the GA area close to the top membrane, see Figure 6.8, above the middle support. The recordings on beam 2 at this specific location was lost after 2000 cycles due to sensitivity of the strain gauges without any visual damage on the sample. Even though, it can be observed that during the first 1000 cycles beam 2 was found to have the higher strain concentration reaching 2000μm/m and then slightly droped but not significant, Figure 6.18. Beam 1 and 3 were found to have the lowest values in terms of strain amplitude. However during the first 1000 cycles beam 3 reached 1000μm/m though Beam 1 has significant less strain concentration around 500μm/m. Finally on beam 4 the evolution of strain from tension to compression is observed. During the first 1000 cycles beam 4 almost reached 1000μm/m in tension, nevertheless at the end of the test this amount decreased significant to 500μm/m in compression.

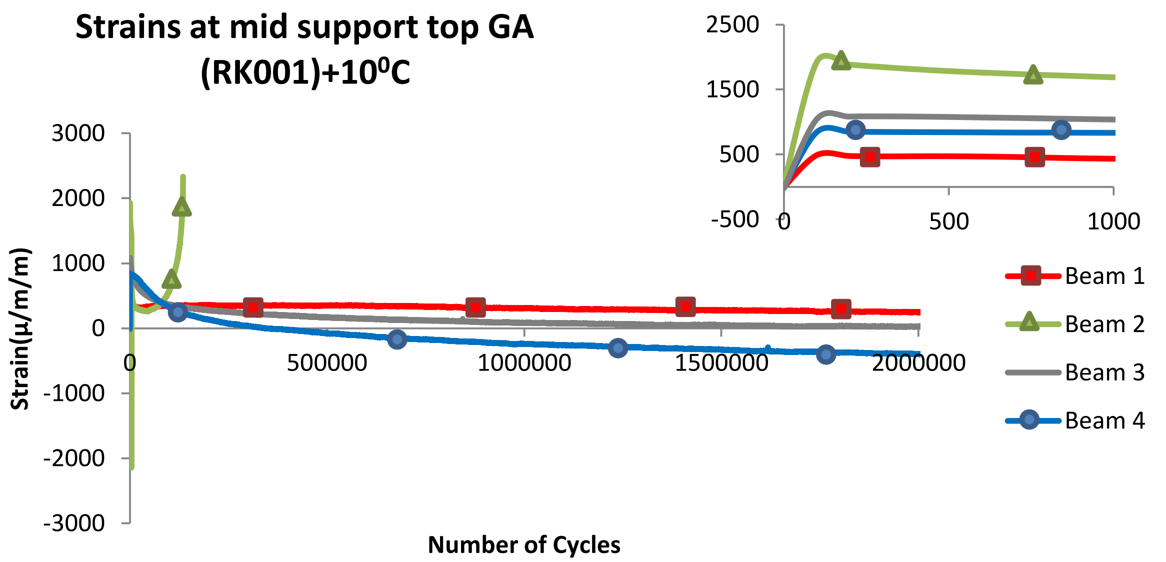

Figure 6.18 Strain distribution on GA at 10^{0}C (RK001)

Rk002 was applied on the GA close to the bottom membrane above the central support, Figure 6.8. As it can be observed during the first 1000 cycles, there are two different strain responses, Figure 6.19. Beam 3 was found to have positive values (tension) immediately after loading though all the other beams have negative values (compression). This can be explained due to the bonding characteristics of the bottom membrane. When the bonding strength between the bottom membrane and the steel plate is high the neutral axis is shifted close to the steel plate so that itresults tension strains distrbution for both location (Rk001 and Rk002). On the other hand all other beams show the same response during the first 1000 cycles producing compressive strain at this this location. Beam 1 and 2 were found to be the ones with the highest compressive strain around 1100μm/m. Beam 4 reached its maximum value during the first 1000 cycles around 1200μm/m and then decreased up to 500000 cycles and became constant around 600μm/m until the end of the test.

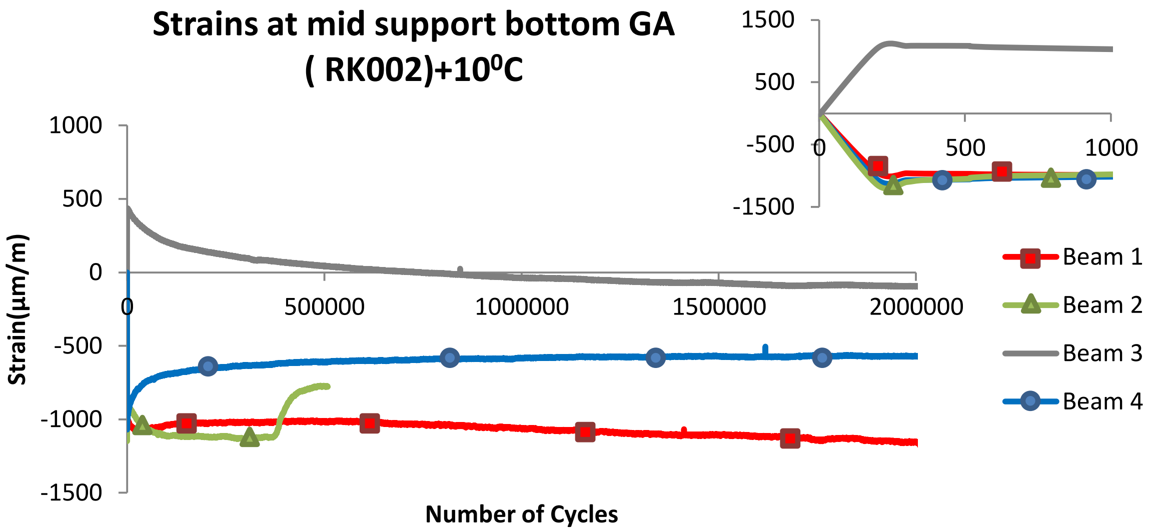

Figure 6.19 Strain distribution on GA at 10^0C (RK002)

Figure 6.20 shows the results recorded at the location close to top membrane on GA (RK001) at -5^0C. In this case the maximum amount of strain amplitude observed on beam 3 around 2000µm/m at the end of the fatigue test. As it can be seen during the first 1000 cycles all other tested samples follow the same trend reaching 500µm/m. The same observation can be made during the last 500,000 cycles where again all tested beams follow the same trend with almost the same strain values around 500µm/m. However after the first 1000 cycles all tested samples show an increase in terms of strain. The maximum tensile strain value on beam 2 at this location was 1100µm/m. Beam 1 was found to have the lowest tensile strain development around 300µm/m, it kept constant until the end of the test. Finally on beam 4 although the strain values kept increasing to 700 µm/m after the first 1000 cycles, it decreased gradully until the end of the test to the value of 500µm/m.

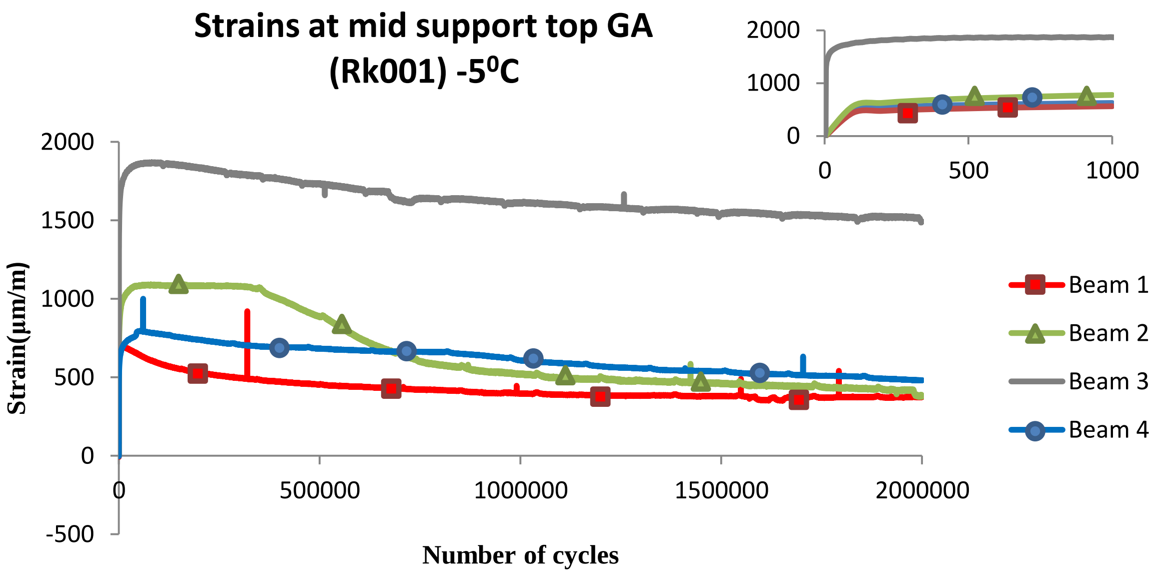

Figure 6.20 Strain distribution on GA at -5^0C (RK001)

The same observation can be made at -5^{0}C with beam 3 to produce positive values (tension) though beam 1,2, 4 to produce negative values (compression),Figure 6.21. Beam 3 produced tensile strains at this specific location due to the bonding characteristics of the bottom membrane. When the bonding strength is high, the neutral axis is shifted and closed to the steel interface that results the development of tension on both locations (Rk001 and Rk002). The beam 4 showed the higher compressive strain development around 1500μm/m at the completion of the fatigue test. Beam 1 and 2 kept strains at this location constant around 1000μm/m during the entire test.

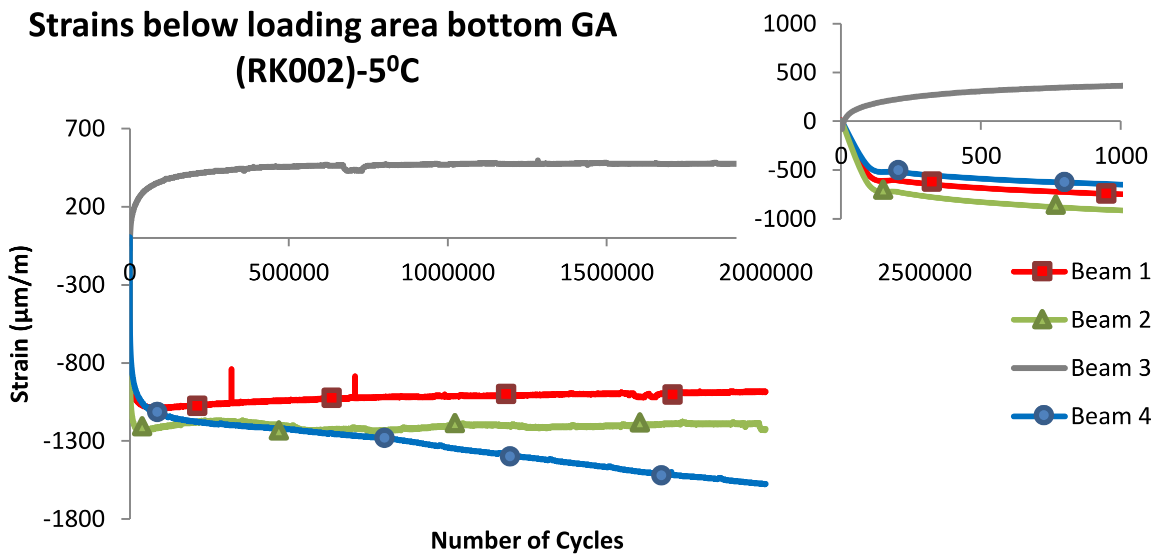

Figure 6.21 Strain distribution on GA at -5^{0}C (RK002)

Strain measurements on top face of (PA)

Figure 6.22 shows the strain development on the top of PA for all samples at 10^0 C. On the top right corner of Figure 6.22, the measurements from the first 500 cycles are presented in order to study the evolution of the strain development and better understand the response of the top PA layer in the 5PB beam .

During the entire fatigue tests beam 3 was found to have a more constant response compared with the other three beams with strain values around 900μm/m. Dduring the first 500 cycles beam 4 showed a constant response with maximum strain values around 1500μm/m, however, at the completion of the test, the strain values decreased and dropped to 1000μm/m after 2 million cycles. During the first 300 cycles, beam 1 was found to have high tensile starin values around 1300μm/m but then it is gradually increased and stopped to record.

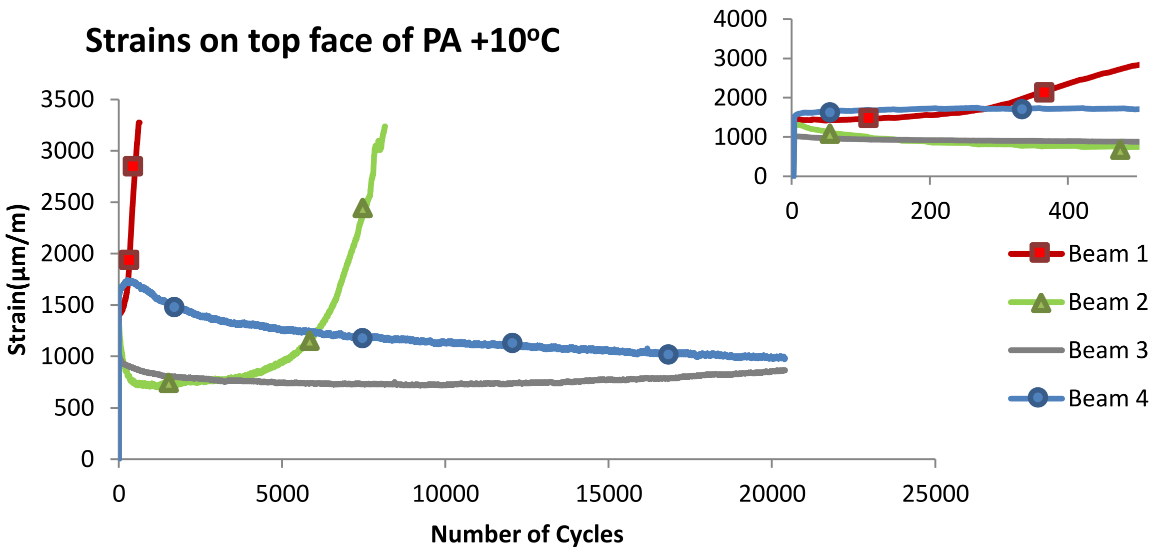

Figure 6.22 Strain evolution on PA at 10^0C

Figure 6.23 presents the strain evolution on the top face of PA at -5^0C. As it was expected higher strain amplitude is recorded at this temperature due to viscoelastic response of the asphalt layers and the membrane products. In contrast to the test at 10^0C, beam 3 showed the maximum tensile values around 3000 µm/m at -5^0C. However during the entire fatigue test the strain values dropped around 2400µm/m. Beam 2 was found to have the lowest tensile strain around 800µm/m at the beginning of the test even though it was lost early due to. Beam 1 was found to have a constant response after the first 5000 cycles with maximum value around 1300µm/m. The tensile strain at the top of PA of beam 4 was increased gradually to the amount of 2300µm/m at the end of the test.

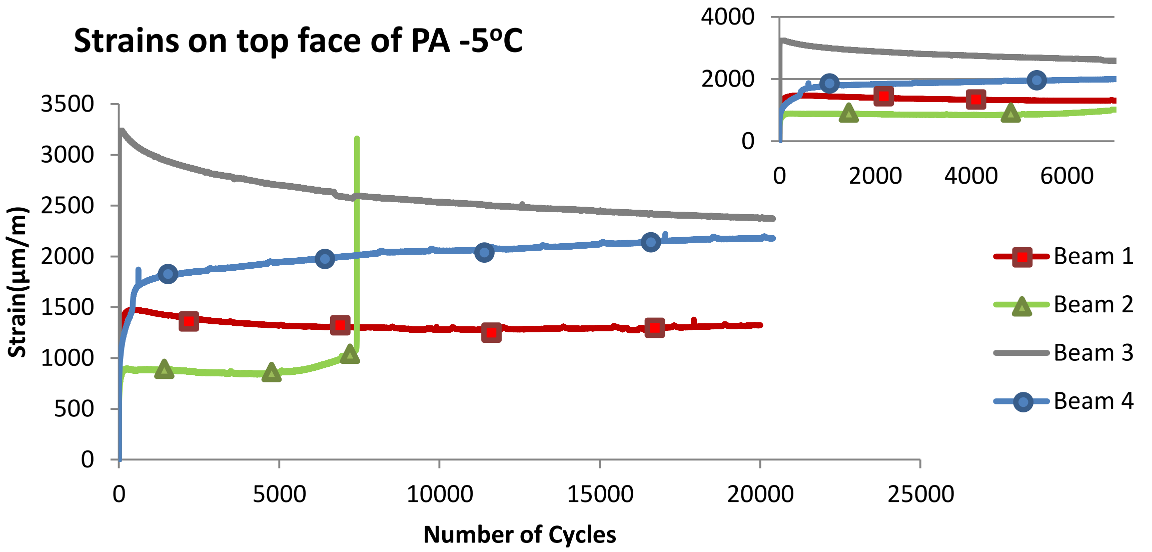

Figure 6.23 Strain evolution on PA at -5^0C

6.6.2 Displacement measurements

Four sets of LVDTs have been installed at both sides of the samples to measure the relative displacement between the asphalt layers and also the shear displacement between the GA and the steel deck,Figure 6.24. An average value from the both side of movement measurements has been used for the graphical representation.

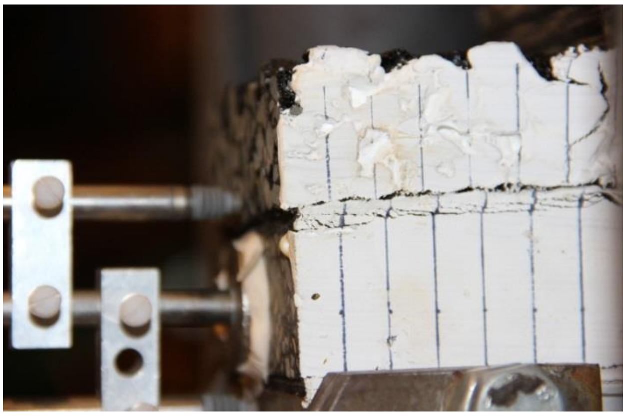

Figure 6.24 Side LVDT's

At 10^{0}C beam 3 was found to have the lower shear displacement between steel and GA. This shear displacement value is also constant during the entire fatigue test, Figure 6.25. Beam 1 has the maximum relative displacement values around 0.6mm. Beam 3 and 4 showed maximum value of 1mm after 100,000 cycles. However during the first 60000 cycles beam 2 has already reached its maximum value though beam 4 reached its maximum value after 250,000cycles.

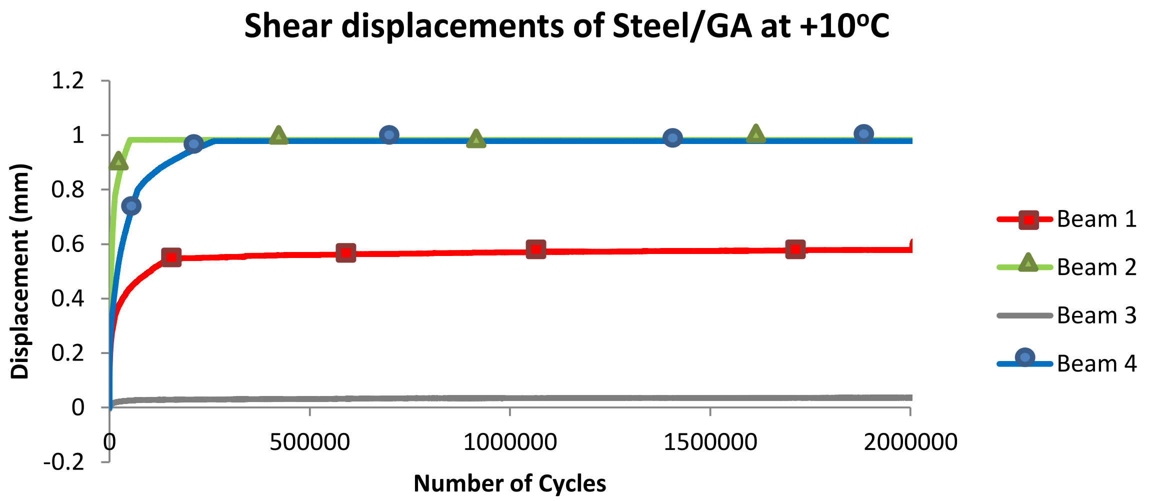

Figure 6.25 Shear displacement between steel/GA interface at 10^{0}C

Due to the higher bonding strength, beam 3 showed very low values of shear displacement between steel and GA at -5^{0}C,Figure 6.26. Beam 1 was found to have the higher values of 0.6mm after the completion of the first 100000 cycles and then it remained constant. Both beam 2 and 4 showed an increase in the shear displacement at the steel/GA interface during the entire test. After 2.0 million cycles maximum shear displacement between steel and GA was reached 0.5 mm for beam 2 and 0.3mm for beam 4.

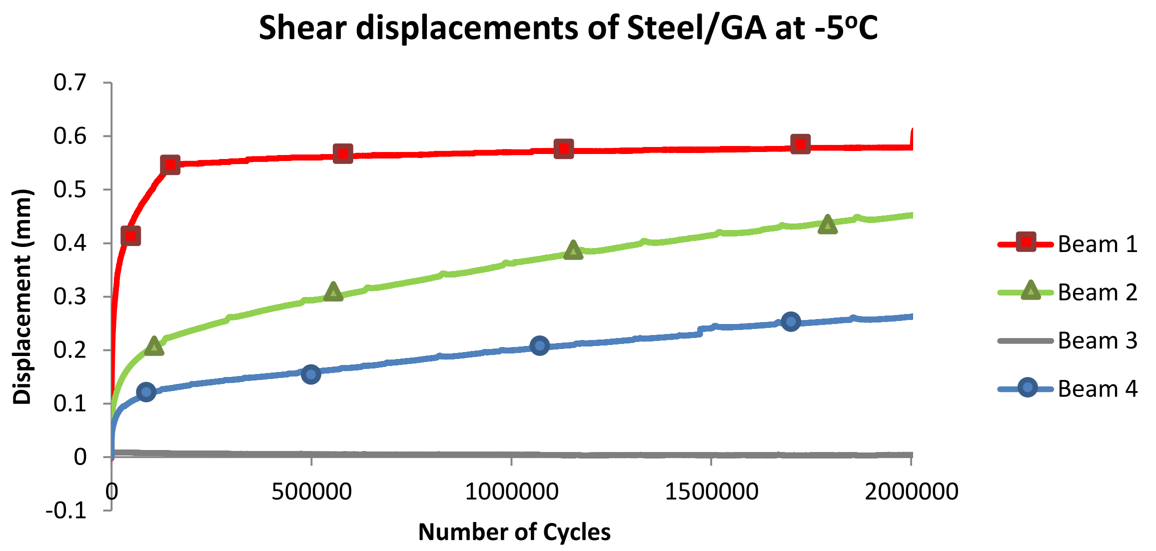

Figure 6.26 Shear displacement on steel/GA interface at -5^{0}C

The shear displacements at the interface between GA and PA are presented in Figure 6.27 and Figure 6.28 . In this case significant influence of the temperature is observed for all tested samples. At 10^{0}C beam 4 showed better behavior with maximum shear displacement of 0.35 mm,Figure 6.27. Beam 3 and 1 had the highest shear displacements values around 0.6mm.

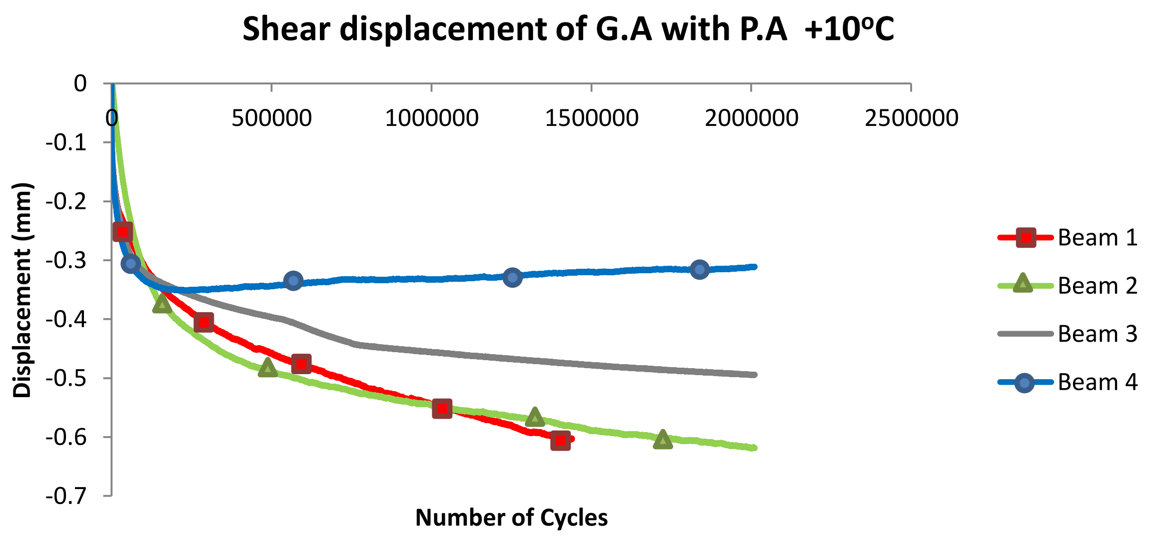

Figure 6.27 Shear displacement on GA/PA interface at 10^{0}C

The similar observations can be made at -5^{0}C, with beam 4 having the lower shear displacement values around 0.15mm, Figure 6.28. Beam 1 and 3 have the same trend up to 1 million cycles but then beam 1 had slightly increased shear displacement 0.2mm. Beam 2 was the only tested sample with maximum shear displacement between GA and PA interface more than 0.2 mm.

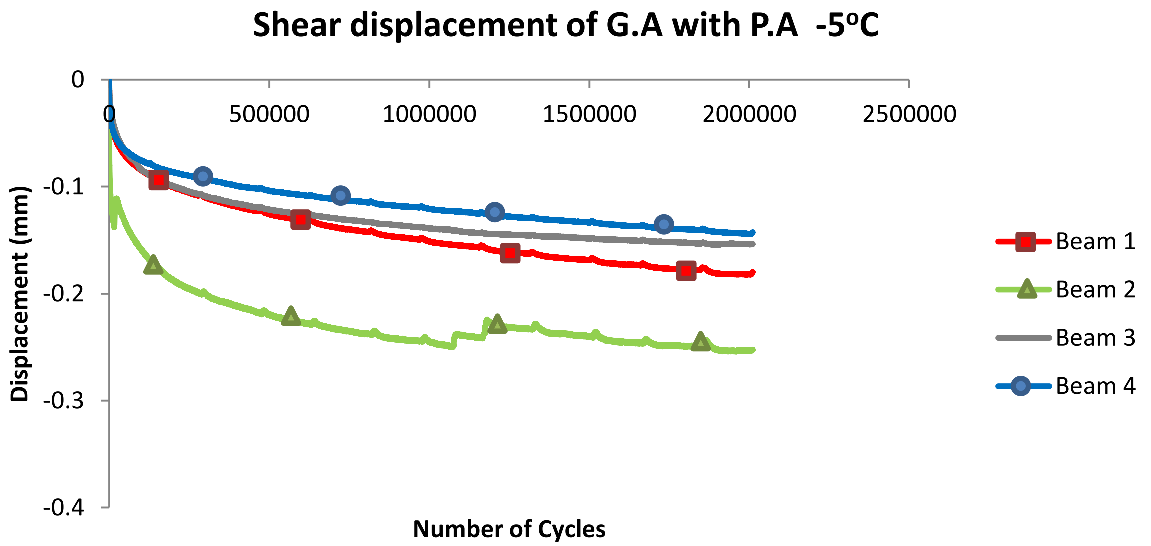

Figure 6.28 Shear displacement on GA/PA interface at -5^{0}C

6.7 Dissipated work and ratio of dissipated work measurements

Similar as the MAT cyclic loading test in Chapter 5, dissipated work approach was used as an indicator of damage in the 5PB beam. The damage in the 5PB beam was related to the rate of change in dissipated energy from one cycle to the next.

In the past, extensive effort was directed towards using dissipated work/energy in the study of fatigue behaviour of asphalt concrete. The dissipated work/energy approach has many advantages. For example, it is simple in principle and easy to use, requiring only the dissipated work/energy in each force cycle.

The 5PB test is essential for the design of the asphalt layers on steel orthotropic decks: essential because the metallic structure is very flexible, and as a consequence, the asphalt concrete is submitted to very high levels of strains under traffic force as compared to asphalt on classic roads. The main advantage of 5PB test is the ability to safely represent the conditions on a real steel deck applying negative moments at the alignment of the stiffener web when each of the wheels of a double tyre is positioned at each side of the web. The disadvantage is that, due to the multi-surfacing layer structure and the presence of the middle support, the shear stress in the centre of the beam cannot be neglected. This makes the analysis required more complex than one required for the 4PB beam test. Moreover the fatigue damage can occur not only at asphalt concrete surfacing layers but also at the interface between the membrane bonding layers and the surfacing layers.

In this investigation, the fatigue damage of the 5PB beam is related to the amount of dissipated work computed by using the measurement of actuator force and the loading plate deformation during the loading cycle. The ratio of dissipated work, which is equivalent to the lost part of the total potential energy of the beam, can be used to explain the incremental damage during the testing. The definition of the dissipated work and ratio of dissipated work are the same as Eq. 5.2 and 5.4 in Chapter 5.

Under the controlled load mode of the 5PB tests, with a limited number of load cycles, the development of dissipated work in the four types of 5PB beams show two distinctive stages in Figure 6.29 and Figure 6.30: (I) dissipated work increases with decreasing dissipated work reduction rate, (II) dissipated work increase gradually with an almost constant slope (constant energy change rate). At higher temperature, under same loading condition, all of 5PB beams show higher dissipated work than those with lower temperature condition. Since the value of the dissipated work can be used to explain the incremental damages during the testing, thus the beam 3 with membrane product C1&C2 shows less damages than the other three beams. The higher damage occurs in the beam 2 with membrane product B&B at higher temperature.

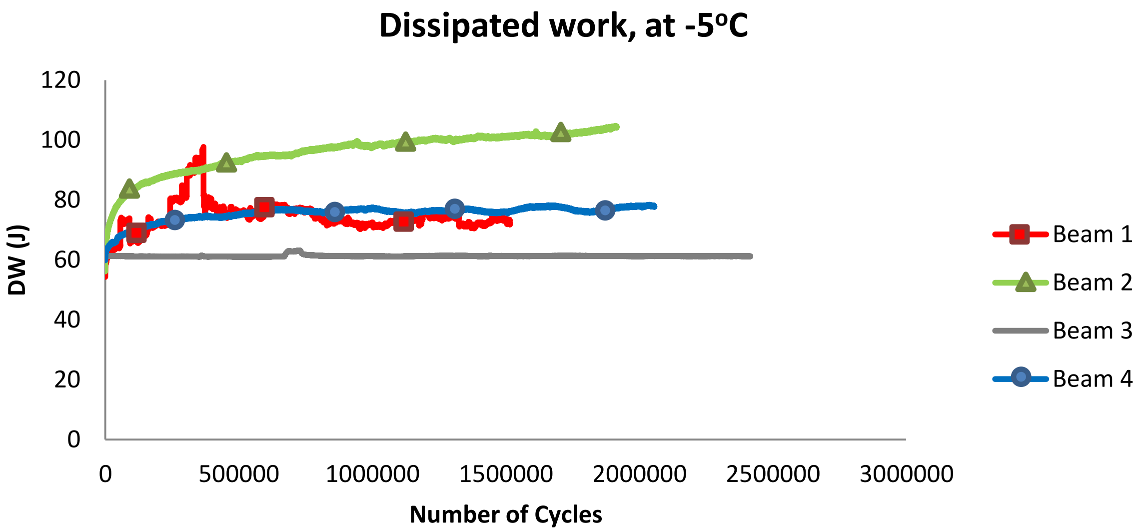

Figure 6.29 Comparison of dissipated work of 5PB beams at -5^{o}C

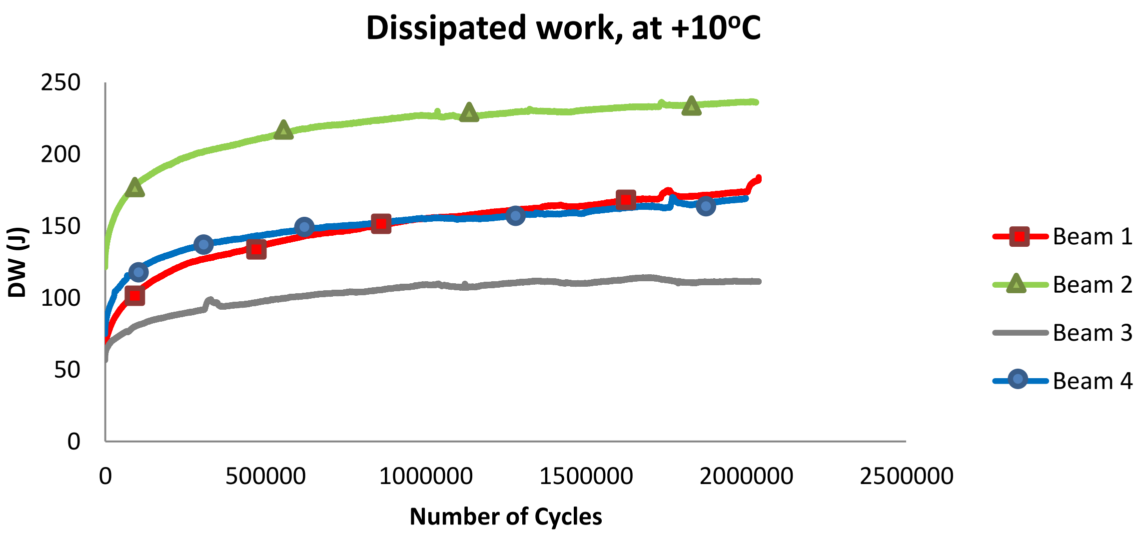

Figure 6.30 Comparison of dissipated work of 5PB beams at +10^{o}C

It is notified in Figure 6.31 and Figure 6.32 that RDWC values for four types of beam at two different temperature are almost constant after 8000 load cycle. Although slightly different from the RDWC for beam with different membrane products, it is typical that second stage is a plateau stage. This plateau value characterizes a period where there is a constant percentage of input energy being turned into beam damage. The analysis of the testing data indicates that such plateau stage starts from approximately the 80% initial structure stiffness reduction until the 50% initial structure stiffness reduction. At higher temperature, the 5PB beams show higher RDWC values than those with lower temperature condition. Beam 3 with membrane product C1&C2 at lower temperature shows almost no energy being turned into beam damage.

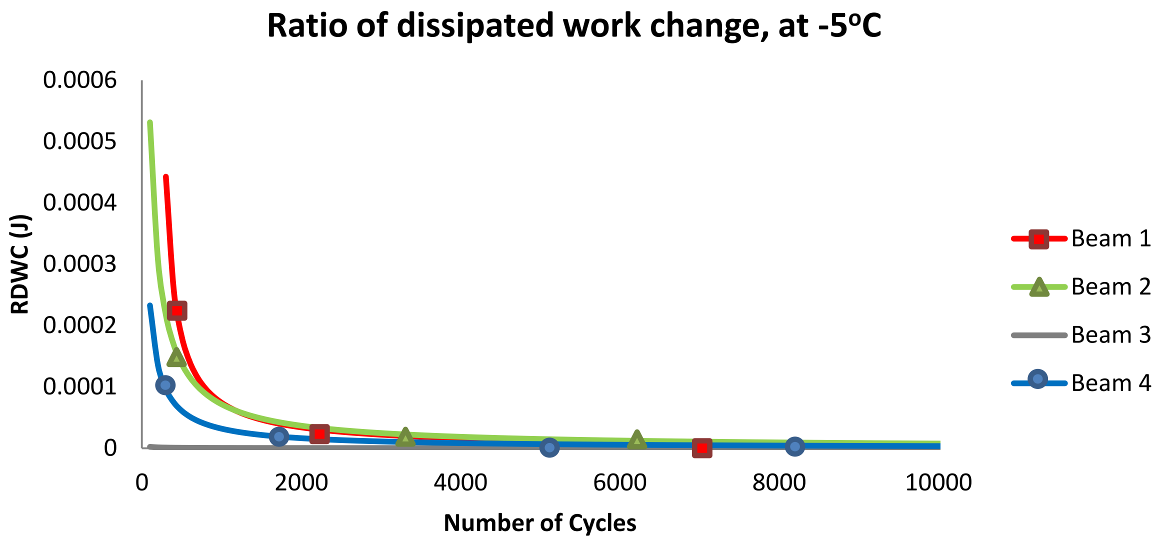

Figure 6.31 Comparison of ratio of dissipated work change of 5PB Beams at -5^{o}C

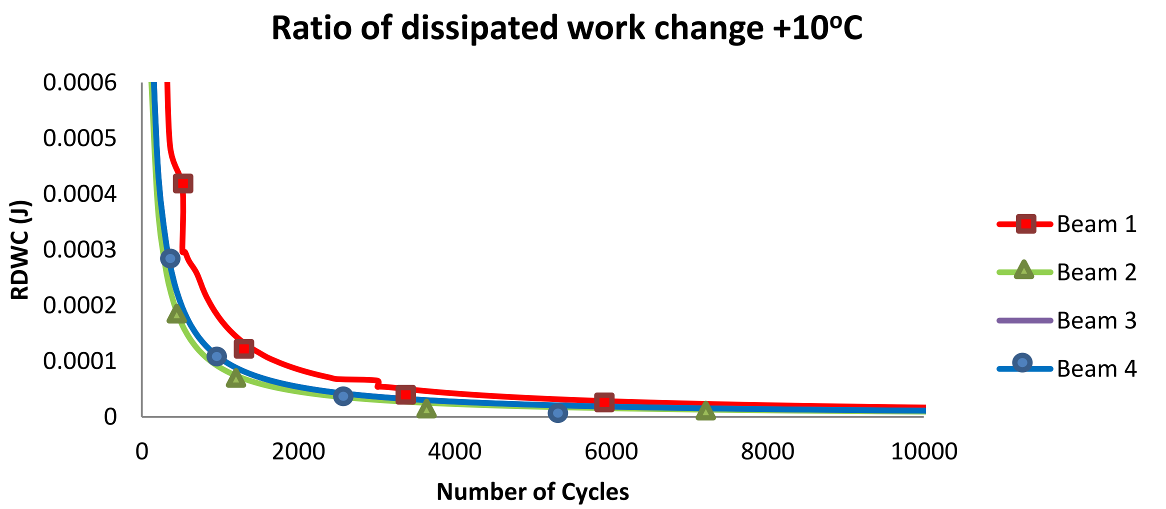

Figure 6.32 Comparison of ratio of dissipated work change of 5PB beams at +10^{o}C

In this study, similar as the traditional failure definition, the structure stiffness of the 5PB beam is used instead of the material complex modulus. Figure 6.33 and Figure 6.34 show the decreasing structure stiffness of the 5PB beam with increasing the number of load cycles. The structure stiffness of the 5PB beam is calculated by using the total load measured from the actuator divided by the load platen deformation during the loading cycle. It can be observed that temperature has important effects on the structure stiffness of the 5PB beams. At higher temperature, the asphalt concrete layers together with its membrane layers becomes more flexible. The structure stiffness of 5PB beam decreases faster than the one in the lower temperature.

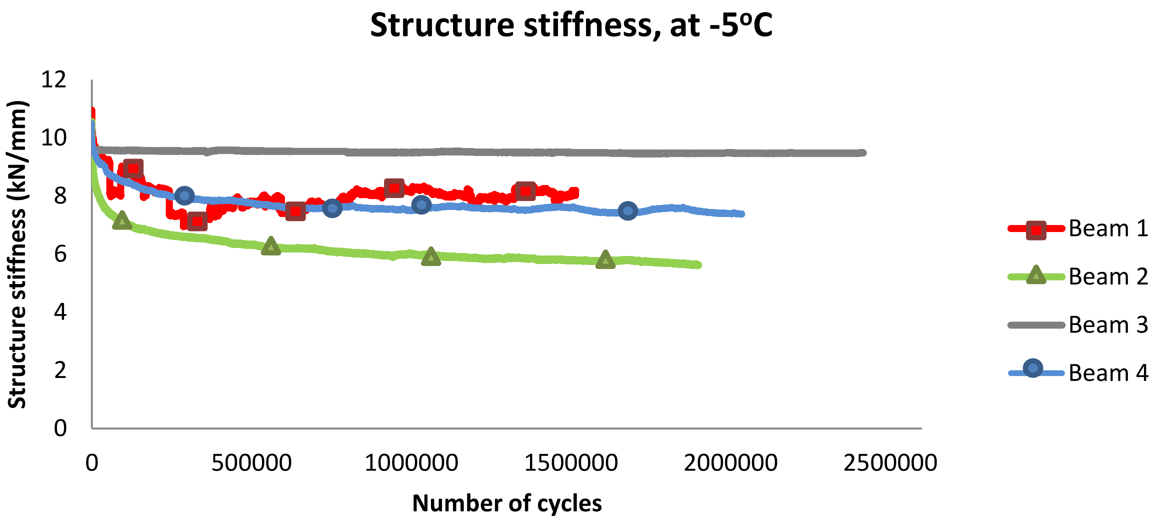

Figure 6.33 Comparison of structure stiffness in four types of 5PB beams at -5°C

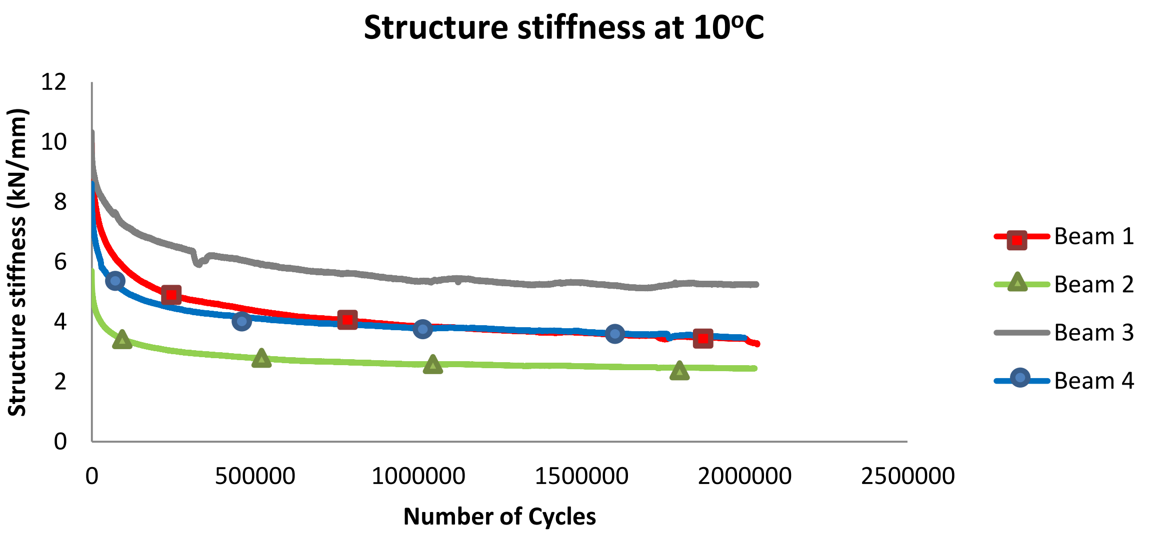

Figure 6.34 Comparison of structure stiffness in four types of 5PB beams at +10°C

By a reasonable testing data extrapolation, Table 6-3 and Table 6-4 show the cycles to failure of the 5PB beams with four types of membrane products at temperature of 10 °C and -5 °C. The corresponding values of DW and RDWC at failure are also presented in these tables. It is noticed that using the traditional stiffness approach the fatigue life of the 5PB beam predicts from less than 260000 to 2 million load repetitions at temperature of 10 °C. Greater load repetitions are predicted for 5PB beam tested at -5 °C.

Table 6-3 Comparison of fatigue life of 5PB beams at temperature of 10^{o}C

Failure criterion	Nf_{50}	DW (J)	RDWC (J)
Beam 1	300000	126.95	5.35e-07
Beam 2	260000	197.91	3.65e-07
Beam 3	2000000	114.52	5.83e-08
Beam 4	350000	137.69	3.25e-07

Table 6-4 Comparison of fatigue life of 5PB beams at temperature of -5^{o}C

Failure criterion	Nf_{50}	DW (J)	RDWC (J)
Beam 1	2.5e+12	97.34	2.47e-14
Beam 2	6.0e+06	112.22	1.34e-08
Beam 3	1.0e+100	65.4	1.2e-102
Beam 4	1.0e+10	103.36	4.03e-12

By comparing Figure 6.29 through Figure 6.34 together with Table 6-3 and, it can be observed that the beam 3 with membrane product C1&C2 performs better than other membrane types at all temperatures, thus the combination of multi-surfacing asphalt concrete layers with membrane product C1&C2 can be chosen as the best performed multi-surfacing layer system for Dutch orthotropic steel bridge.

6.8 Conclusions

The main findings that can be drawn from the results presented in this chapter are summarized as follows:

- The five-point bending (5PB) beam test offers a good tool in studying the composite behavior of the multilayer surfacing system on orthotropic steel deck bridges.
- The response of the 5PB beam with different surfacing systems differs significantly with temperature due to the high temperature sensitivity of the asphaltic materials and the membranes.
- The results of the 5PB beam tests can be utilized for calibration and validation of the finite element tools and allow additional insight into the overall ranking of multilayer surfacing systems.
- 5PB beam 3 with membrane products C1&C2 has shown the longer fatigue life in comparison to the other three beams with different surfacing systems. Beam 1 and 4 can be recommend as second option.
- Due to the high void ratio in the PA layer of the beam, cracks on the top side of the PA at the central location between the loading area are difficult to be visualized. Hence the criteria of judgment of specimen failure at the location where it is subjected to negative moments is not applicable for this type surfacing system.

7 Conclusions and recommendations

An asphalt surfacing applied on a steel bridge deck is a multifunctional structure. Its function is to provide a suitable running surface with adequate skid resistance, to reduce and disperse stresses/strains by composite actions, and to provide a waterproofing layer. The ultimate goal of this research work was to evaluate the influence of various membrane products on the response of multilayer asphalt surfacing of orthotropic steel bridges.

A multi-scale approach consisting of three study phases was followed: 1) MAT monotonic tests, 2) MAT fatigue tests 3) 5PB tests. The main conclusions of each research phase are presented and recommendations for future work are drawn in the final section.

7.1 Phase 1: behaviour of membranes under monotonic loading

- The MAT setup is capable of characterizing the adhesive bonding strength of the various membranes with the surrounding materials. MAT results will allow a better understanding of the performance of the membrane on the bridge structure allowing thus optimization of maintenance activities.
- The mechanical response of a membrane product is influenced not only by the surrounding substrate but also by the environmental temperatures and loading rates.
- The critical energy release rate G is a fundamental physical quantity that can be utilized to quantify the membrane adhesive bonding strength with different substrates.
- The material maximum reaction force consists of the combination of both the membrane material response and the membrane bonding response. It is not an objective measure of the membrane bonding quality.
- By comparing the strain energy release rate (G-values) of different membranes at the same test condition, it can be concluded that product B and C1 perform quite well as the bottom membrane, and product A2 and C2 are considered as the best choices for the top membrane in Dutch OSDBs.
- In most cases, debonding happens at interfaces (adhesive layers) either at the top or at the bottom of a membrane layer, rather than the material failure of the membrane layer itself.
- Three key issues need to be considered as an integral group when evaluating a membrane layer: 1) the mechanical properties of the membrane material itself; 2) the behaviour of the bonding layer between the membrane and its upper material layer; 3) the behaviour of the bonding layer between the membrane and its underneath layer. A qualified membrane product should meet demands of all these three aspects.
- An overqualified material selection may result in diseconomy especially when the interfacial failure happens much earlier than a material failure.

7.2 Phase 2: behaviour of membranes under fatigue loading

- The MAT set up is capable of characterizing the fatigue response of the various membranes bonded on the different substrates. The test results allow a better understanding of performance of the membrane on the bridge structure allowing thus optimization of maintenance activities;
- The fatigue response of a membrane product is influenced not only by the surrounding substrate but also by the environmental temperature and loading level applied on the membrane;
- The concept of dissipated energy/work provides a fundamental and expedient means to evaluate the fatigue life of membrane products on different substrates;
- As damage accumulates in a specimen, the dissipated work varies depending on the rate of membrane debonding;
- The observations from the MAT cyclic loading tests are coincident to the observations from MAT monotonic static loading tests in the previous report. It means that the findings of this report is a further proof that the methodology utilized in this research project is adequate for ranking the bonding characteristics of various membrane products on different substrates for OSDB construction.
- The MAT set up can be used for determination of the compliance of a membrane system to the requirements of Advies Niveau III.
- The methodology developed in this research project is adequate not only for ranking the bonding characteristics of various membrane products on different substrates but also for predicting the actual fatigue life of membrane products on OSDB construction.
- The fatigue response of a membrane product is influenced both by the load level and the environmental conditions
- The asymptotic model used has been found to represent well the load-repetition curve when certain curve fitting rules are followed, however more sophisticated models might give more accurate results.
- Accuracy of results can be improved if tests are conducted at lower load levels. Restrictions of the set up limited the minimum applied load to 100N on this research.

7.3 Phase 3: behaviour of surfacing in 5PB tests

- Withstanding the differences in loading conditions, boundary conditions and structural stiffness characteristics between a 5PB beam test and a steel bridge deck, the 5PB beam test offers an expedient tool in investigating the composite behaviour of multilayer surfacing systems on OSDBs.

- The role of the membrane layers in ensuring the composite action and hence the integrity of the surfacing system is crucial. It is extremely important to use a membrane product with good bonding strength, high stiffness and strength in order to obtain good composite behaviour.

- The concept of dissipated energy/work provides a means to quickly estimate the fatigue life of a laboratory 5PB fatigue tests. The procedure introduced, presents a simply method of fatigue behaviour analysis at different temperatures based on an energy approach.

- The response of the surfacing systems differs significantly with temperature due to the high temperature sensitivity of the asphaltic materials and the membranes.
- The results of the 5PB beam tests can be utilized for calibration and validation of the finite element tools and allow additional insight into the overall ranking of multilayer surfacing systems.
- Surfacing system 3 with membrane products C1 and C2 has shown better integral response in comparison to the other three surfacing systems. Surfacing systems 1 and 4 can be recommended as second option.

7.4 Recommendations for future research

- A minimum standard of bonding requirements for membrane products with other surfacing material layers need to be investigated. Material performances such as the energy release rate G, basic mechanical properties of membranes like viscoelastic features, perforation stability, ageing stability and flexibility, tensile and shear adhesion strengths of bonding layers need to be included.
- Further study should be done on the development of experimental methods that are able to determine the associated model parameters of the adhesive contact interface element for simulating the fatigue damage at interfaces.
- Comparative study between the multilayer asphalt surfacing systems within this research scope and other surfacing types such as systems without membrane layers or with just a single asphalt material layer creates much interest and deserves further investigation.
- By reproducing in-service conditions, accelerated loading tests by means of the LINTRACK facility available at TU Delft, will provide an additional and conclusive means for verification of the capabilities of the MAT device in ranking the field response of membrane products.
- Lintrack tests (De Jong, 2007) of full-size bridge section are considered to evaluate the behaviour and influence of the surfacing systems on OSDBs. This extensive research program is being carried out as an extend study of this work.

References

Al-Khateeb, G. and Shenoy, A. (2004). *A Distinctive Fatigue Failure Criterion*, Journal of the Association of Asphalt Paving Technologists, 73: 585-622.

Baburamani, P. (1999). *Asphalt Fatigue Life Prediction Models*, A Literature Review. Research Report ARR 344, Australia.

Brown, J. R., 1973. *Pervious Bitumen- Macadam Surfacing Laid to Reduce Splash and Spray at Stonebridge, Warwickshire* .TRL Laboratory Report LR563. Crowthorne, UK.

Carpenter, S. H., and M. Jansen.. *Fatigue Behavior Under New Aircraft Loading Conditions*. In Aircraft/Pavement Technology: In the Midst of Change, Seattle, Washington, 17-21 August 1997. Edited by F.V. Hermann. American Society of Civil Engineers, New York. pp. 259-271. 1997.

Carpenter, S. H., Ghuzlan, K, and Shen, S. *Fatigue Endurance Limit for Highway and Airport Pavements*, In Transportation Research Record: Journal of the Transportation Research Board, No. 1832, TRB, National Research Council, Washington D.C., 2003, pp. 131-138. 2003.

Carpenter, S. H. and Shen, S. *A Dissipated Energy Approach to Study Hot-Mix Asphalt Healing in Fatigue*. Transportation Research Record (TRR): Journal of the Transportation Research Board, No. 1970, pp.178-185. 2006.

Clough, G. W., & Duncan, J. M. (1973). Finite element analysis of retaining wall behavior. *Journal of Soil Mechanics & Foundations Div*, *99*(sm 4).

Daines, M.E., 1992. *Trials on Porous Ashalt and Rolled Asphalt on the A38 at Burton*. TRRL Supplementary Report 323. Wokingham, UK: Transport Research Lanboratory

Dannenberg, H. (1961). Measurement of adhesion by a blister method.*Journal of Applied Polymer Science*, *5*(14), 125-134.

Decoene, Y., (1989). *Knowledge acquired after 10 years of research on Porous Asphalt in Belgium*. Proceedings of the 4th Eurobitume Symposium, p.762. Madrid, Spain.

Desai, C. S., Zaman, M. M., Lightner, J. G., & Siriwardane, H. J. (1984). Thin-layer element for interfaces and joints. *International Journal for Numerical and Analytical Methods in Geomechanics*, *8*(1), 19-43.

Fini, E. H., Al-Qadi, I. L., & Masson, J. F. (2010). Interfacial fracture energy: an indicator of the adhesion of bituminous materials. Journal of the Association of Asphalt Paving Technologists, 77, 827-850.

Gent, A. N., & Lewandowski, L. H. (1987). Blow-off pressures for adhering layers. *Journal of Applied Polymer Science*, *33*(5), 1567-1577.

Ghuzlan, K. *Fatigue Damage Analysis in Asphalt Concrete Mixtures Based upon Dissipated Energy Concept*. PHD thesis. University of Illinois at Urbana-Champaign, August, 2001.

Ghuzlan, K, and S. H. Carpenter. *Energy-Derived/Damage-Based Failure Criteria for Fatigue Testing*, In Transportation Research Record: Journal of the Transportation Research Board, No.1723, TRB, National Research Council, Washington D.C. pp. 141-149. 2000.

Goodman, R. E., Taylor, R. L., & Brekke, T. L. (1968). A model for the mechanics of jointed rock. *Journal of Soil Mechanics & Foundations Div*.

Günther, G. H., Bild, S., & Sedlacek, G. (1987). Durability of asphaltic pavements on orthotropic decks of steel bridges. *Journal of Constructional Steel Research*, *7*(2), 85-106.

Gurney, T. (1992). *Fatigue of steel bridge decks* (No. 8). HMSO Publication Centre: London. 1992, pp. 165.

Hadley, W. O., Hudson, W. R., & Kennedy, T. W. (1971). Evaluation and Prediction of the Tensile Properties of Asphalt-Treated Materials. *Highway Research Record*.

Hameau, G., Puch, C., Ajour, A.M*: Fatigue Behaviour due to Negative Bending Moments (in French),* Revêtments de Chaussées sùr platelages métalliques, 1981.

Héritier, B., Olard, F., Saubot, M., & Krafft, S. (2005, June). Design of a specific bituminous surfacing for orthotropic steel bridge decks: application to the Millau Viaduct. In *7th Symposium on bearing capacity of roads, railways and airfields*.

Heukelom, W.(1966). Observations on the Rheology and Fracture of Bituments and Asphalt Mixes. Shell Bitumen Reprint , No.19, Shell Laboratorium Koninklijke.

Hopman, P.C., Kunst, P.A.J.C. and Pronk, A.C. (1989). *A Renewed Interpretation Method for Fatigue Measurements*, Verification of Miner’s Rule. In: 4th Eurobitume Symposium in Madrid, Vol. 1, pp. 557-561.

Houel, A., & Arnaud, L. (2008). A five point bending test for asphalt cracking on steel plates. *Pavement Cracking: Mechanisms, Modeling, Detection, Testing and Case Histories*, 261.

Houel, A., T.L. N'Guyen, and L. Arnaud. *Monitoring and Designing of Wearing Courses for Orthotropic Steel Decks Throughout the Five-point Bending Test*. Advanced Testing and Characterisation of Bituminous Materials, Vol. 1 and 2, pp. 433-442. 2009

Huang, W., & , CL, M. (1995). Study into fatigue performances of . *China Journal of Highway and Transport*,*8*(001), 56-62.

Huang, W., Zhang, X., & Hu, G. (2002). New advance of theory and design on pavement for long-span steel bridge. *Dongnan Daxue Xuebao/Journal of Southeast University(Natural Science Edition)*, *32*(3), 480-487.

Irwin, L.H. and Gallaway, B.M. (1974*). Influence of Laboratory Test Method on Fatigue Results for Asphaltic Concrete. Fatigue and Dynamic Testing of Bituminous Mixtures,* ASTM STP, 561: 12-46.

Kim, Y. R. and Little, D. N. (1990). One-dimensional Constitutive Modelling of Asphalt Concrete." *Journal of Engineering Mechanics*, 116(4), pp.751-772

Lee, H. J., & Kim, Y. R. (1998). Viscoelastic constitutive model for asphalt concrete under cyclic loading. *Journal of Engineering Mechanics*, *124*(1), 32-40.

Lee, H.J., Daniel, J.S. and Kim, Y.R. (2000). *Continuum Damage Mechanics Based Fatigue Model of Asphalt Concrete*, American Society of Civil Engineering (ASCE) Journal of Materials in Civil Engineering, 12: 105-112.

Li, J. (2015). *Optimum design of Multilayer Ashpalt Surfacing System for Orthotropic Steel Deck Bridges. Doctoral thesis.* Delft University of Technology.

Liu, X. (2003). Numerical modelling of porous media response under static and dynamic load conditions.

Liu, X., Medani, T.O., Scarpas, A., Huurman, M. and Molenaar, A.A.A. *Experimental and Numerical Characterization of a Membrane Material for Orthotropic Steel Deck Bridges: Part 2 - Development and Implementation of a Nonlinear Constitutive Model*," Finite Elements in Analysis and Design, vol. 44, pp. 580-594, 2008.

Liu, X., Scarpas, A., Li, J., Tzimiris, G., Hofman, R. and Voskuilen, J. *Test Method to Assess Bonding Characteristics of Membrane Layers in Wearing Course on Orthotropic Steel Bridge Decks*. In Transportation Research Record: Journal of the Transportation Research Board, No. 2360, Transportation Research Board of the National Academies, Washington, D.C., 2013, pp. 77–83.

Liu, X., and A. Scarpas. *Experimental and Numerical Characterization of Membrane Adhesive Bonding Strength on Orthotropic Steel Deck Bridges*, Part 1. Project report CITG2012-1, Delft University of Technology, The Netherlands, 2012.

Liu, X., & Scarpas, T. (2012). Experimental and Numerical Characterization of Membrane Adhesive Bonding Strength on Orthotropic Steel Deck Bridges. *Project report*. Delft University of Technology.

Liu, X., Tzimiris, G. & Scarpas, T. (2013). Experimental Investigation of Membrane Fatigue Response. *Project report*. Delft University of Technology.

Lundstrom, R. and Isacsson, U. (2003). *Asphalt Fatigue Modelling using Viscoelastic Continuum Damage Theory*, Road Materials and Pavement Design, 4: 51-75.

Malyshev, B. M., & Salganik, R. L. (1965). The strength of adhesive joints using the theory of cracks. *International Journal of Fracture Mechanics*, *1*(2), 114-128.

Mangus, A.R. and Sun, S., *Orthotropic Bridge Decks. Bridge Engineering Handbook, ed*. W. Chen and L. Duan, Boca Raton: C.R.C. Press. 1999.

Martin, R. H., & Murri, G. B. (1990). Characterization of mode I and mode II delamination growth and thresholds in AS4/PEEK composites. *ASTM STP,1059*, 251-270.

Maycock, G., (1966). *The Problem of Water Thrown up by vehicles on Wet Roads.* LR4. Wokingham, UK: Transport Research Laboratory.

Medani, T. O. (2001). Asphalt surfacing applied to orthotropic steel bridge decks. *Faculty of Civil Engineering and Geosciences Road and Railroad Research Laboratory & Steel and Timber Structures*.

Medani, T. O. (2006). Design principles of surfacings on orthotropic steel bridge decks. PhD thesis, Delft University of Technology.

Miner, M. A. (1945). "Cumulative Damage In Fatigue." *Applied Mechanics*, Vol. 12(9).

Nicholls, J.C. (1997). *Review of UK Porous Ashalt Trials. TRL264*. Crowthorne, UK: Transport Research Laboratory.

Nicholls, J.C. (2001). *Material Performance of Porous Asphalt, Including when Laid over Concrete. TRL499*. Crowthorne, UK: Transport Research Laboratory.

Nikolaides, A., (2015). *Highway Engineering, Pavements, Materials and Control of Quality,* 257-268

Nishizawa, T., Himeno, K., Nomura, K., & Uchida, K. (2001). Development of a new structural model with prism and strip elements for pavements on steel bridge decks. *International Journal of Geomechanics*, *1*(3), 351-369.

Nunn, D. E., & Morris, S. A. H. (1974). *Trials of experimental orthotropic bridge deck panels under traffic loading* (No. TRRL LR 627 Series).

Park, S. W., Richard Kim, Y., & Schapery, R. A. (1996). A viscoelastic continuum damage model and its application to uniaxial behavior of asphalt concrete. *Mechanics of Materials*, *24*(4), 241-255.

Pell, P.S. and Cooper, K.E. (1975). *The Effect of Testing and Mix Variables on the Fatigue Performance of Bituminous Materials*, Journal of the Association of Asphalt Paving Technologists, 44: 1-37.

Phillips, S.M., PM. Nelson and G. Abbott. (1995). *Reducing the Noise from Motorways: The Acoustic Performance of Porous Asphalt on the M4 at Cardiff*. Paper to Acoustics '95. Volume 17: Part 4

Porter, B.W. and Kennedy, T.W. (1975). *Comparison of Fatigue Test Methods for AsphaltMaterials*. Research Report 183-4, Project 3-9-72-183, Center for Highway Research, University of Texas at Austin.

Pronk, A.C. and Hopman, P.C. (1990*). Energy Dissipation: The Leading Factor of Fatigue. Highway Research: Sharing the Benefits*, Proceedings of the Conference, the United States Strategic Highway Research Program, London.

Ramsamooj, D.V. (1991). *Fatigue Cracking of Asphalt Concrete Pavements*, Journal of Testing and Evaluation, 19: 231-239.

Ramsamooj, D.V. (1999). *Prediction of Fatigue Performance of Asphalt Concrete Mixes*, Journal of Testing and Evaluation, 27: 343-348.

Rodrigues, R.M. (2000). *A Model for Fatigue Cracking Prediction of Asphalt Pavements Based on Mixture Bonding Energy*, International Journal of Pavement Engineering, 1: 133-149.

Rowe, G.M. (1993). *Performance of Asphalt Mixtures in the Trapezoidal Fatigue Test,* Journal of the Association of Asphalt Paving Technologists, 62: 344-384.

Rowe, G.M. and Bouldin, M.G. (2000). *Improved Techniques to Evaluate the Fatigue Resistance of Asphaltic Mixtures.* In: Proceedings of 2nd Eurasphalt & Eurobitume Congress, Barcelona, Spain.

Russell, H. G. (2012). *Waterproofing Membranes for Concrete Bridge Decks*. Transportation Research Board.

Shen, S., Carpenter, S.: *Dissipate Energy concept for HMA Performance: Fatigue and Healing, Department of Civil and Environmental Engineering*. University of Illinois at Urbana-Champaign: Urbana, Illinois. 2007.

Smith, J. W., & Cullimore, M. S. G. (1987). Stress reduction due to surfacing on a steel bridge deck. *Steel Structures--Advances, Design and Construction*, 806-814.

Storåkers, B., & Andersson, B. (1988). Nonlinear plate theory applied to delamination in composites. *Journal of the Mechanics and Physics of Solids,36*(6), 689-718.

Tayebali, A.A., Rowe, G.M. and Sousa, J.B. (1992). *Fatigue Response of Asphalt-Aggregate Mixtures,* Journal of the Association of Asphalt Paving Technologists, 61: 333-360.

Tayebali, A.A., Deacon, J.A., Coplantz, J.S. and Monismith, C.L. (1993). *Modeling Fatigue Response of Asphalt-Aggregate Mixes*, Journal of the Association of Asphalt Paving Technologists, 62: 385-421.

Touran, A., & Okereke, A. (1991). Performance of orthotropic bridge decks.*Journal of performance of constructed facilities*, *5*(2), 134-148.

Van Dijk, W. *Practical Fatigue Characterization of Bituminous Mixes.* Proceedings of the Association of Asphalt Paving Technologists, vol. 44, pp. 38-74. 1975.

Van Dijk, W. and W. Visser.The *Energy Approach to Fatigue for Pavement Design*. Proceedings of the Association of Asphalt Paving Technologists, vol. 46, pp. 1-40. 1977.

Vincent, R. B., & Ferro, A. (2004, August). A new orthotropic bridge deck: design, fabrication and construction of the Shenley Bridge incorporating an SPS orthotropic bridge deck. In *2004 Orthotropic Bridge Conference* (pp. 201-223).

Wan, K. T., Guo, S., & Dillard, D. A. (2003). A theoretical and numerical study of a thin clamped circular film under an external load in the presence of a tensile residual stress. *Thin Solid Films*, *425*(1), 150-162.

Wang, C. S., Feng, Y. C., & Duan, L. (2009). Fatigue Damage Evaluation and Retrofit of Steel Orthotropic Bridge Decks. *Key Engineering Materials,413*, 741-748.

Williams, M. L. (1969). The continuum interpretation for fracture and adhesion. *Journal of Applied Polymer Science*, *13*(1), 29-40.

Xu, X., Shearwood, C., & Liao, K. (2003). A shaft-loaded blister test for elastic response and delamination behavior of thin film–substrate system.*Thin solid films*, *424*(1), 115-119.

Zaman, M. M. U., Desai, C. S., & Drumm, E. C. (1984). Interface model for dynamic soil-structure interaction. *Journal of Geotechnical Engineering*,*110*(9), 1257-1273.

Zhang, T. and Raad, L. (1999). *Numerical Methodology in Fatigue Analysis: Basic Formulation*, Journal of Transportation Engineering, 125: 552-559.

Zhang, T. and Raad, L. (2001). *Numerical Methodology in Fatigue Analysis Applications*, Journal of Transportation Engineering, 127: 59-66.

Zhu, X. Q., & Law, S. S. (2000). Identification of vehicle axle loads from bridge dynamic responses. *Journal of sound and vibration*, *236*(4), 705-724.

Zong-Ze, Y., Hong, Z., & Guo-Hua, X. (1995). A study of deformation in the interface between soil and concrete. *Computers and Geotechnics*, *17*(1), 75-9

Appendix I

Observation after 2million cycles

Specimen with membrane product A at +10^{o}C

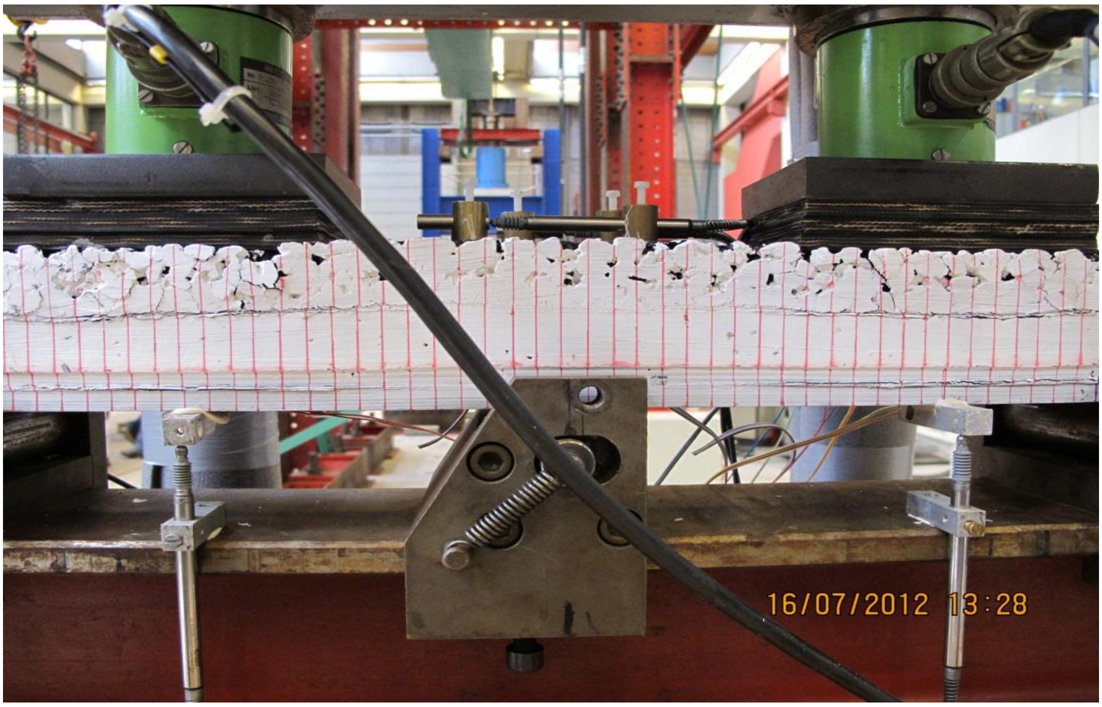

Figure A-1 Overview of damage on the entire speciment

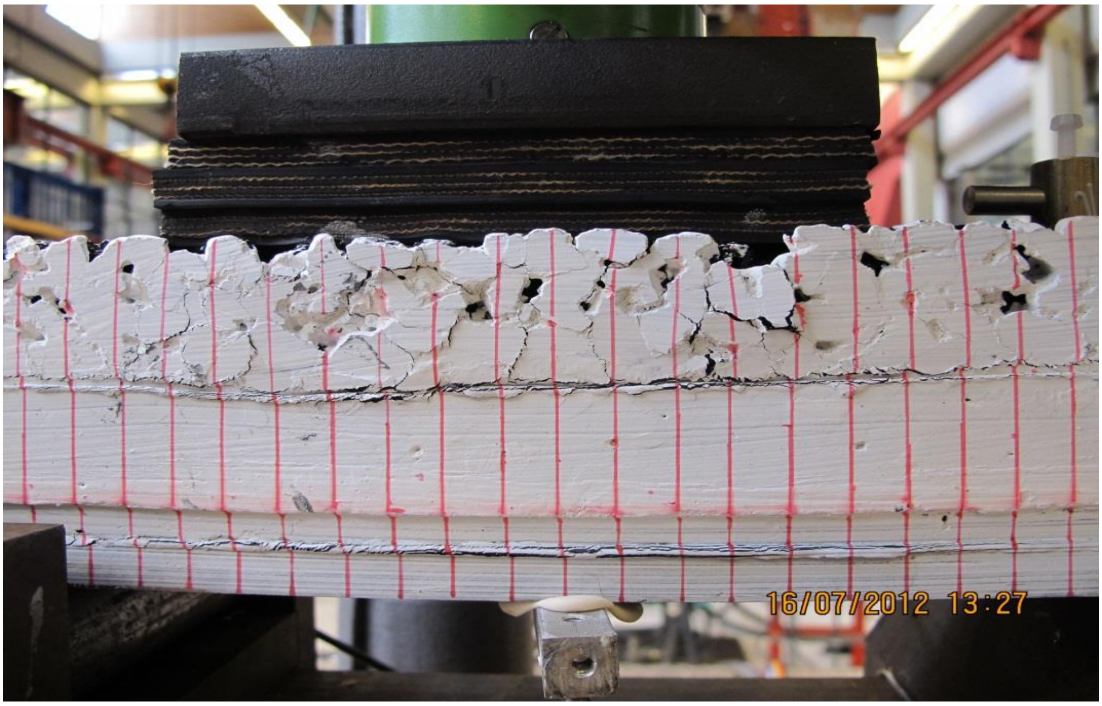

Figure A-2 Damage on the specimen under the left side of the load cell

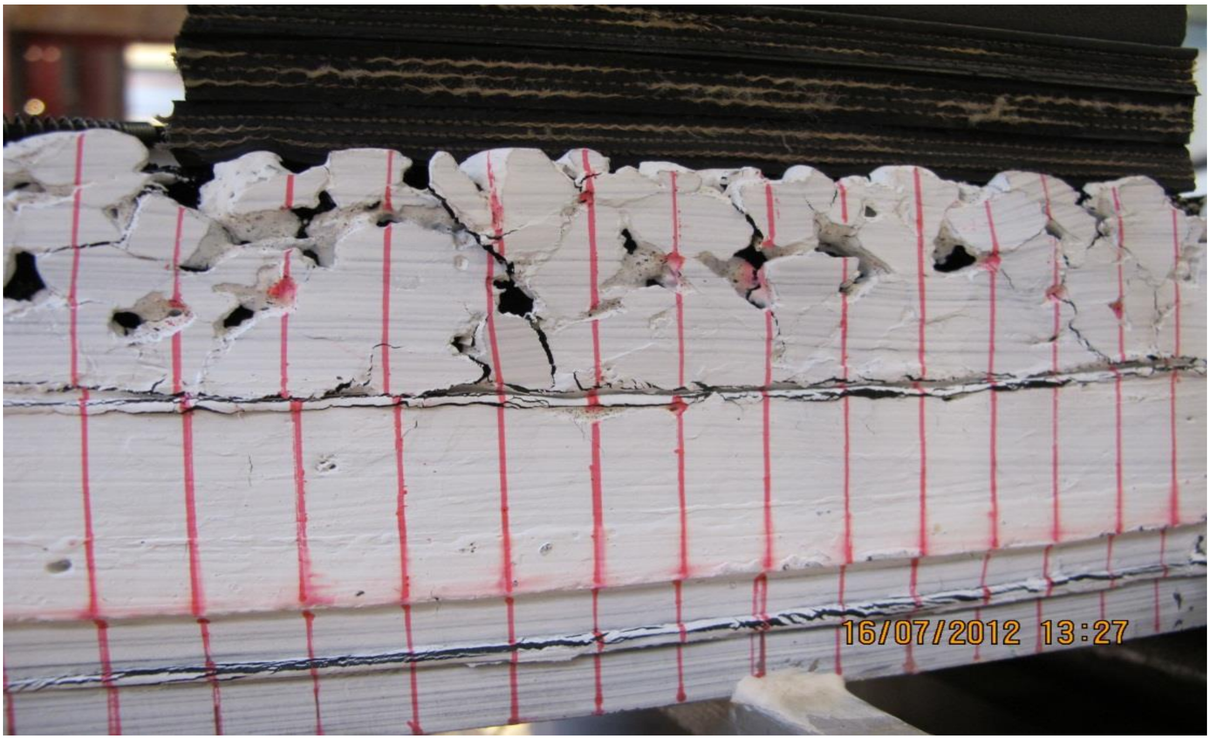

Figure A-3 Damage on the specimen under the right side of the load cell

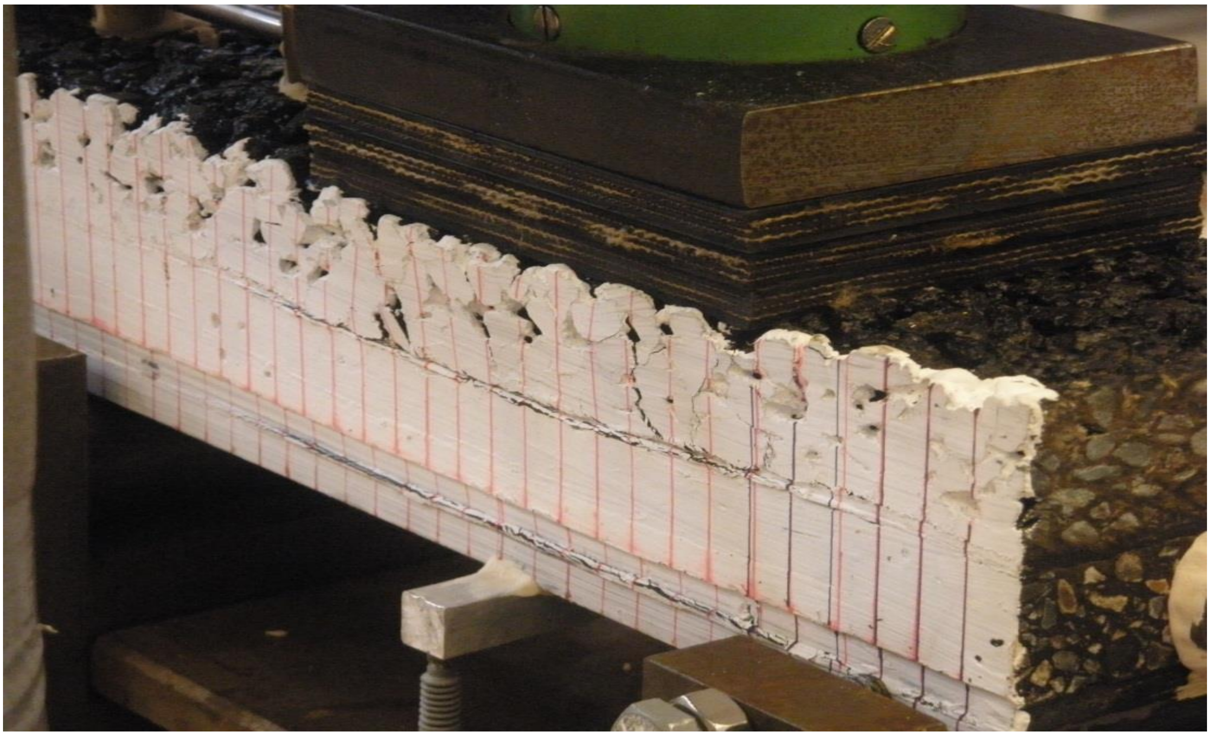

Figure A-4 Zoom on the right end of the specimen

Specimen with membrane product A at -5^{o}C

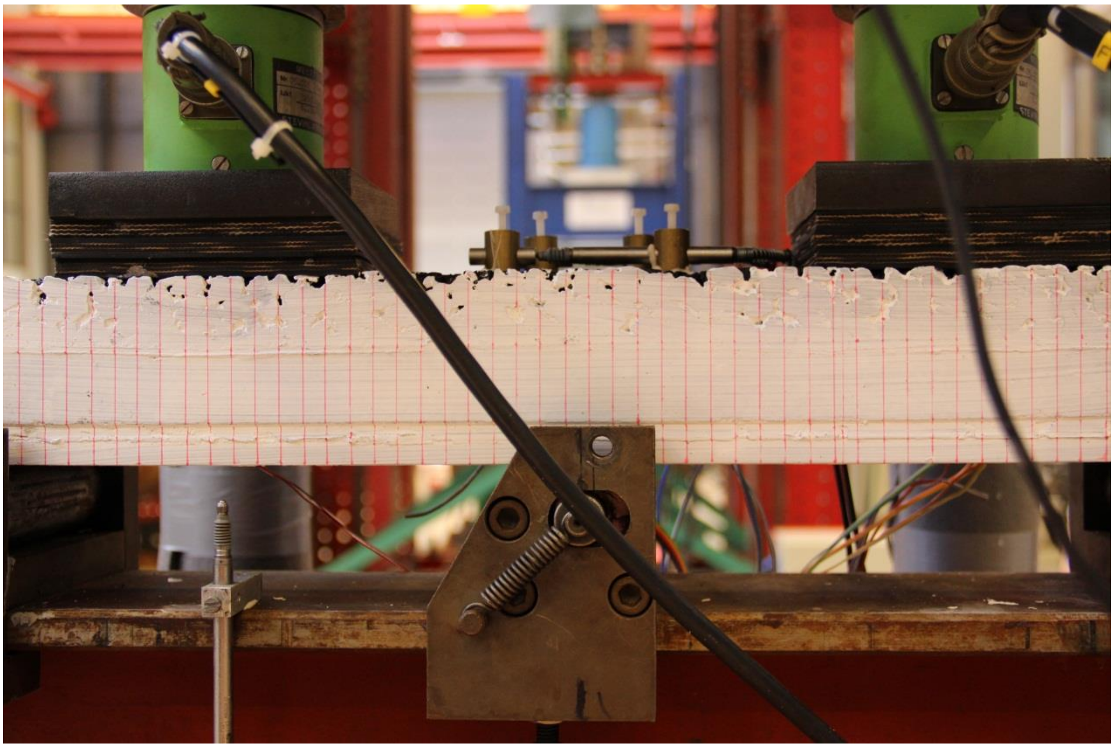

Figure A-5 Overview of damage on the entire specimen

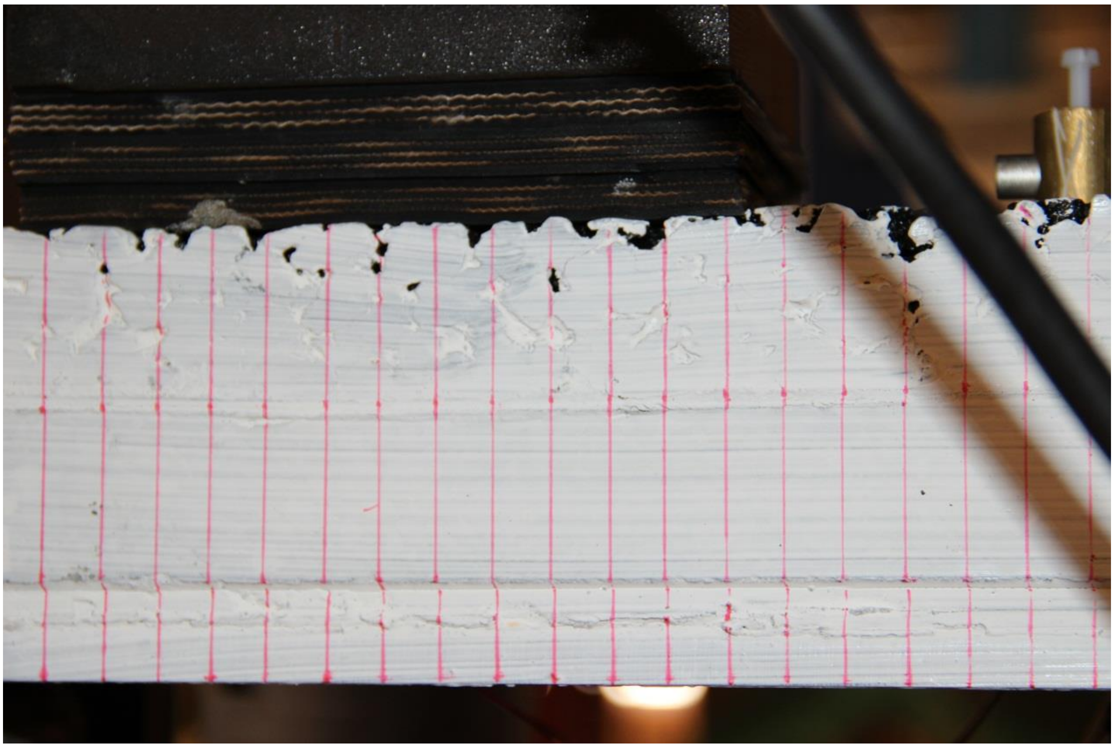

Figure A-6 Zoom on the specimen under the left side of the load cell

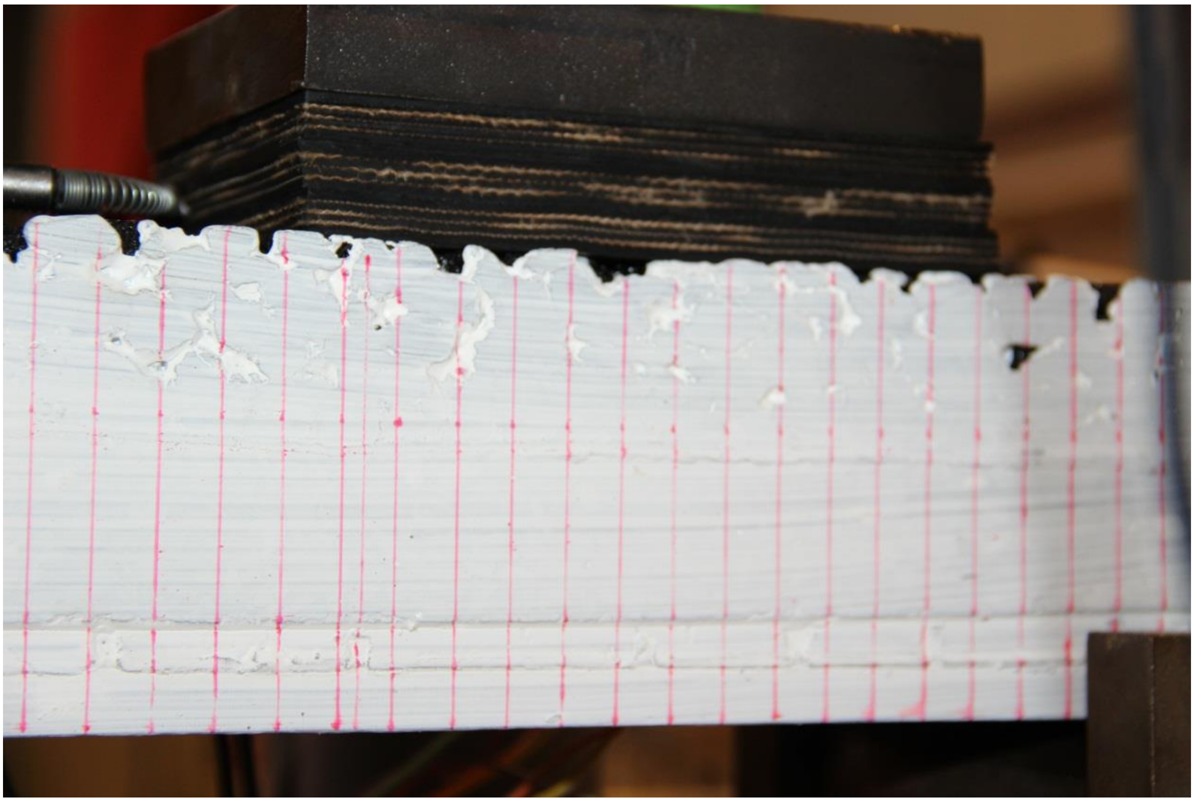

Figure A-7 Zoom on the specimen under the right side of the load cell

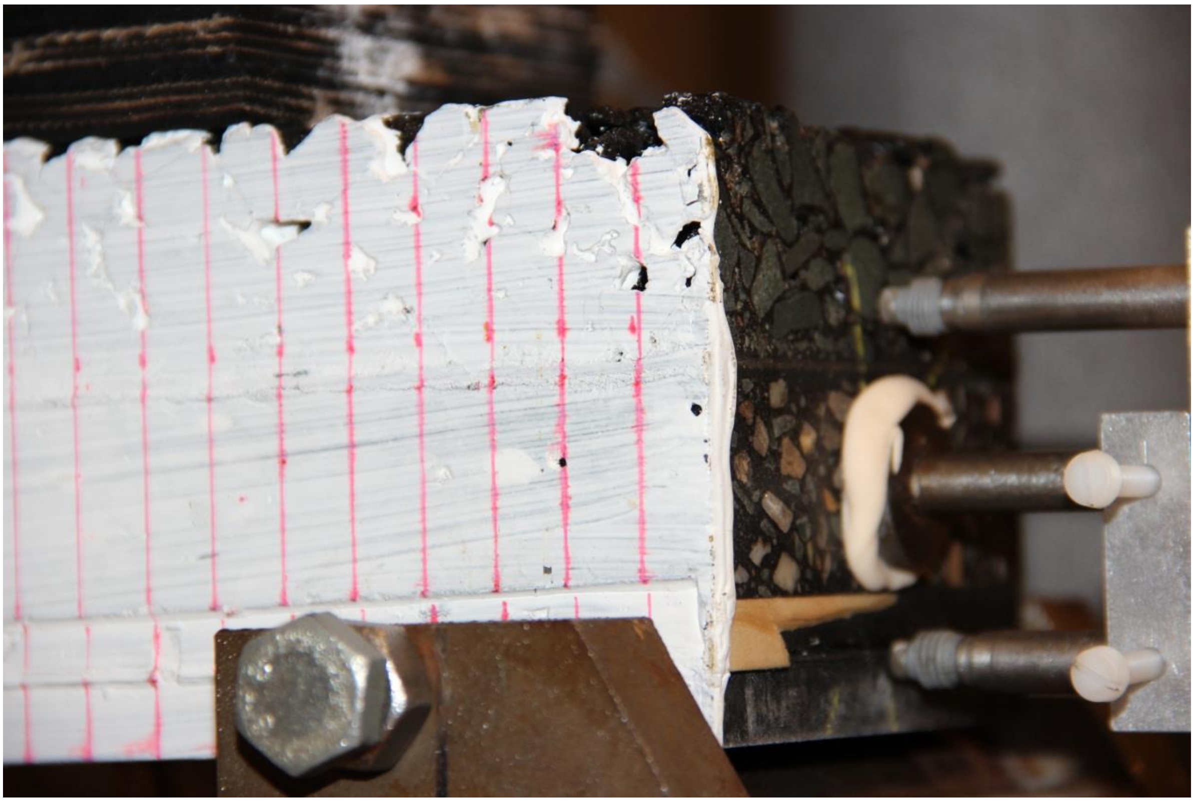

Figure A-8 Zoom on the right end of the specimen

Specimen with membrane product B at 10^{o}C

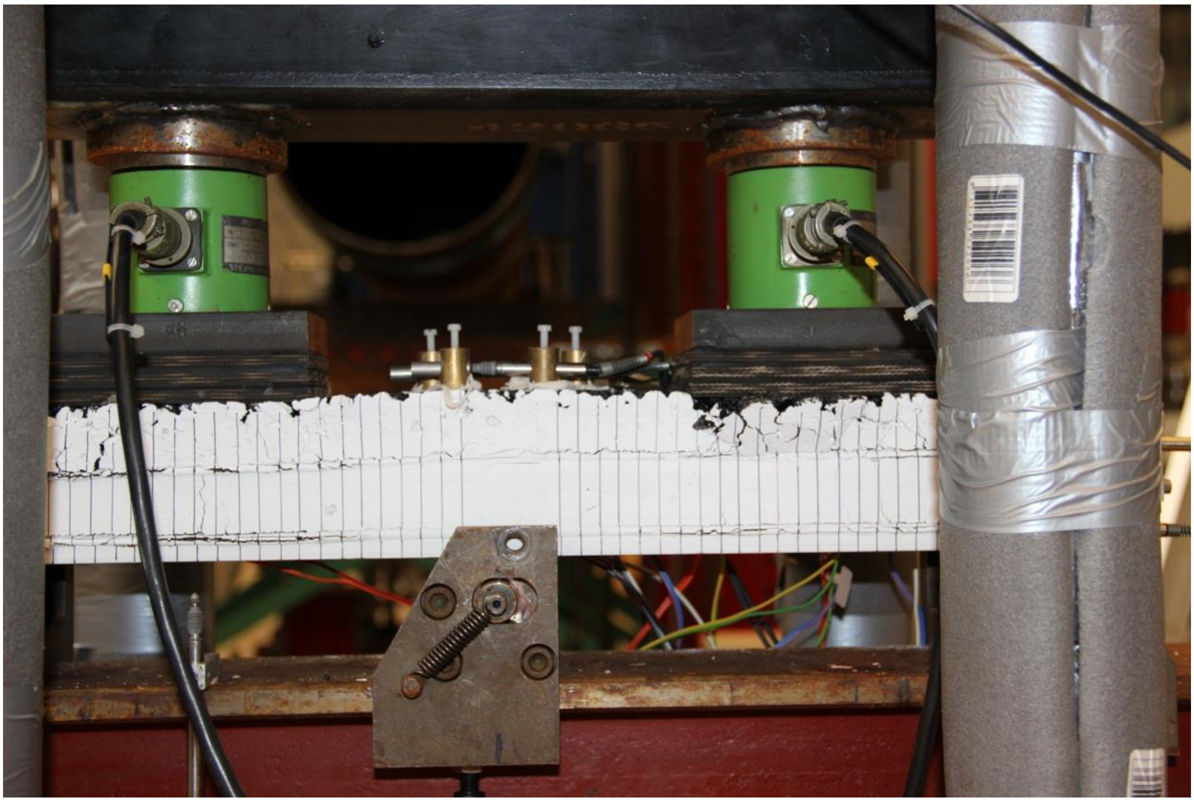

Figure A-9 Overview of damage on the entire specimen

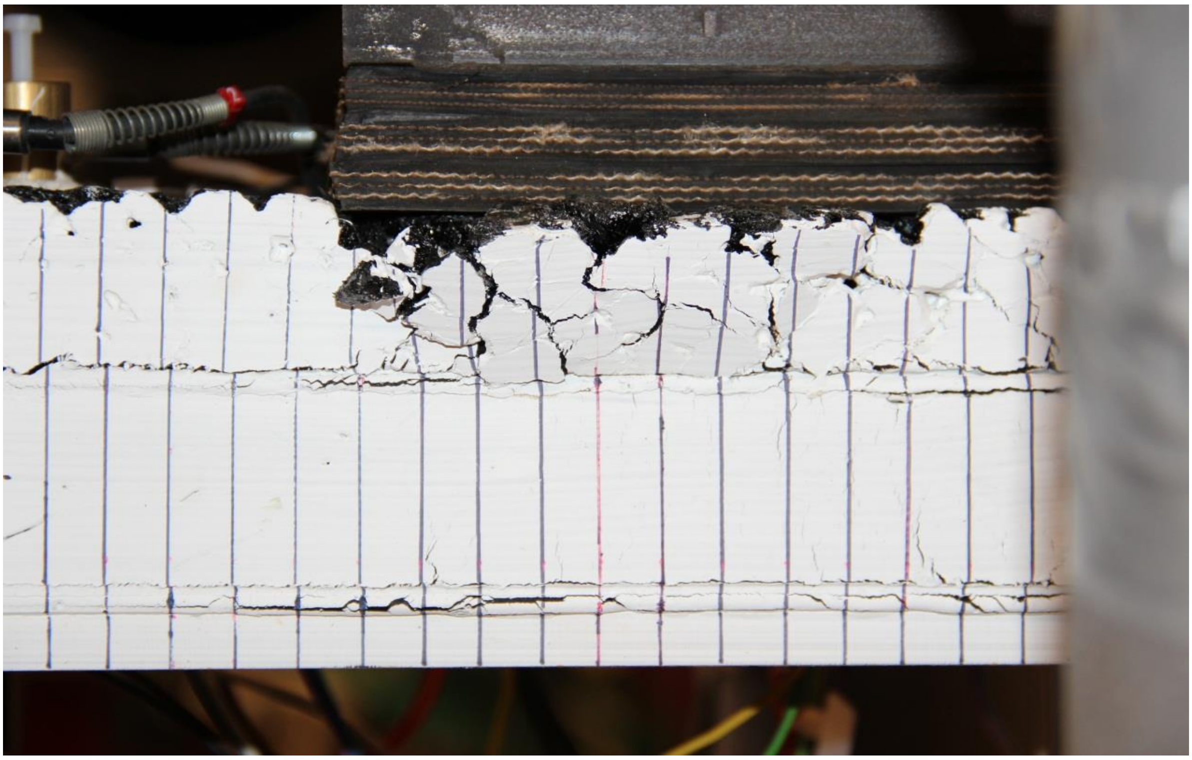

Figure A-10 Damage on the specimen under the right side of the load cell

Figure A-11 Zoom on the left end of the specimen

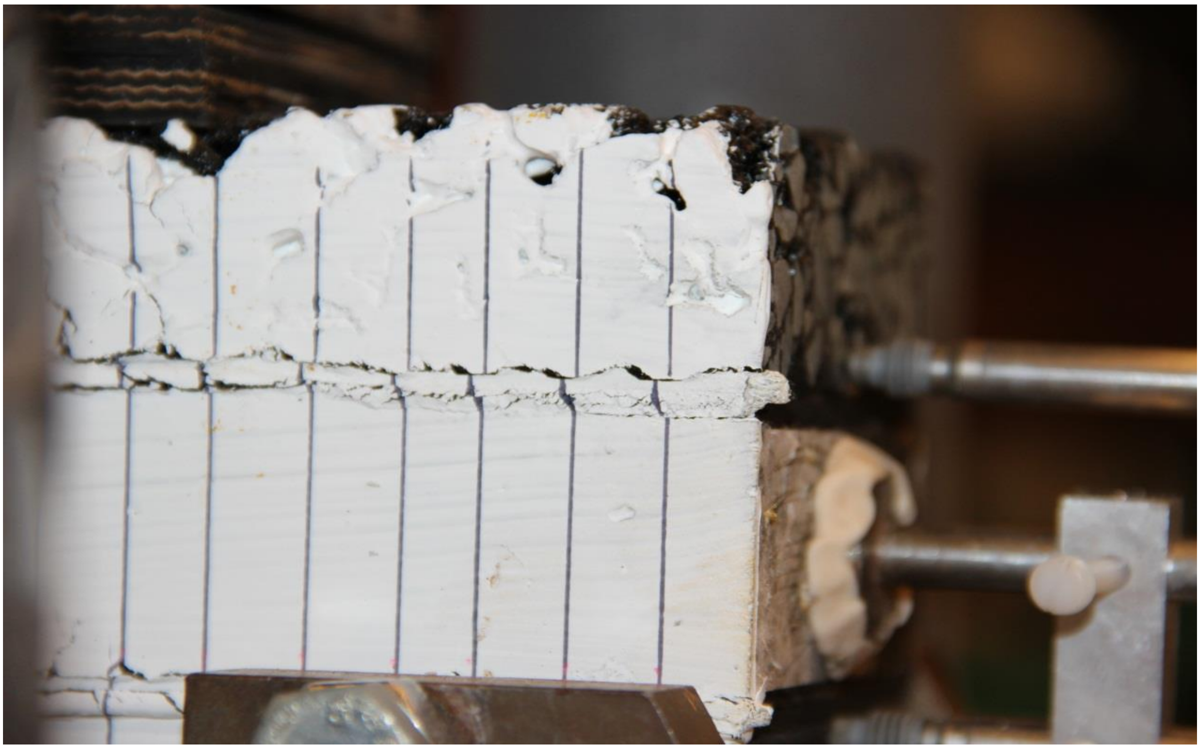

Figure A-12 Zoom on the right end of the specimen

Specimen with membrane product B at -5^{o}C

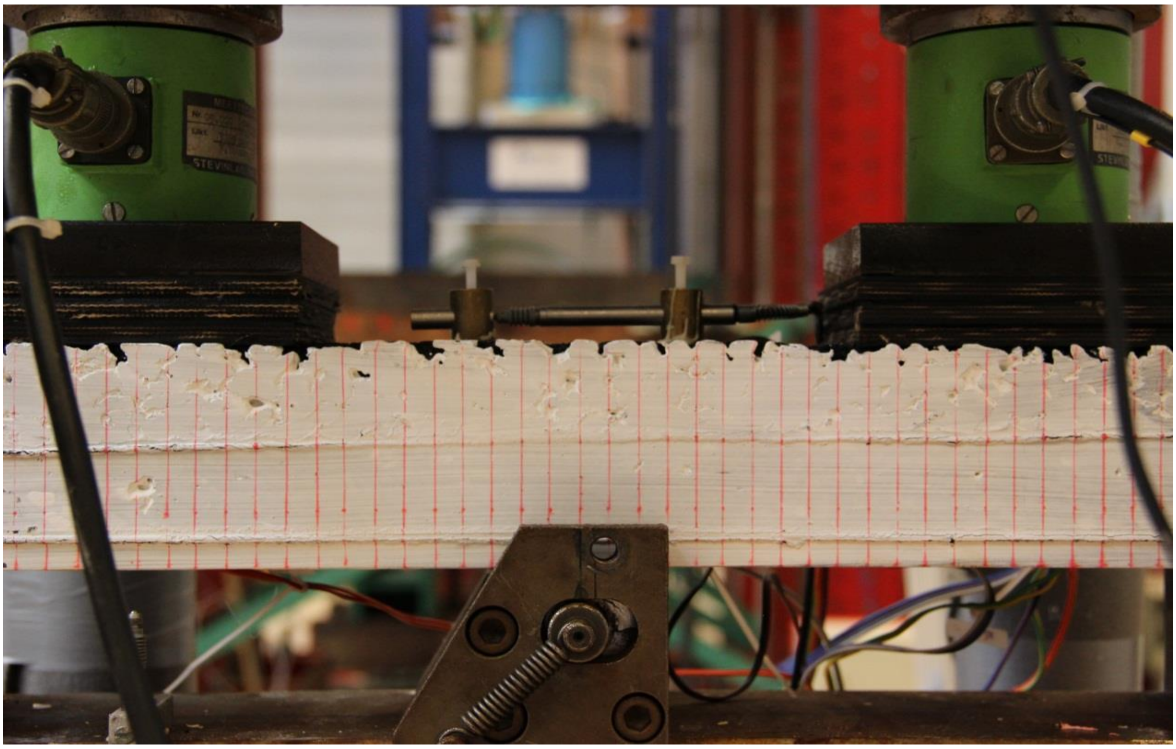

Figure A-13 Overview of damage on the entire specimen

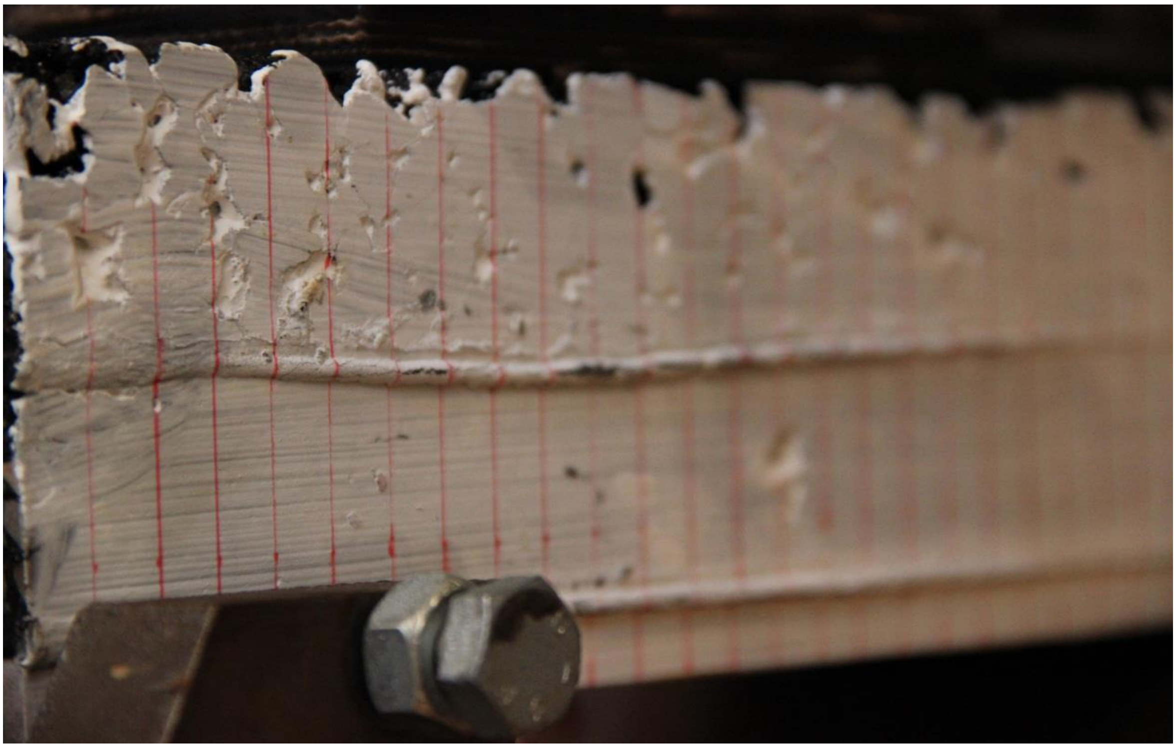

Figure A-14 Zoom on the left end of the specimen

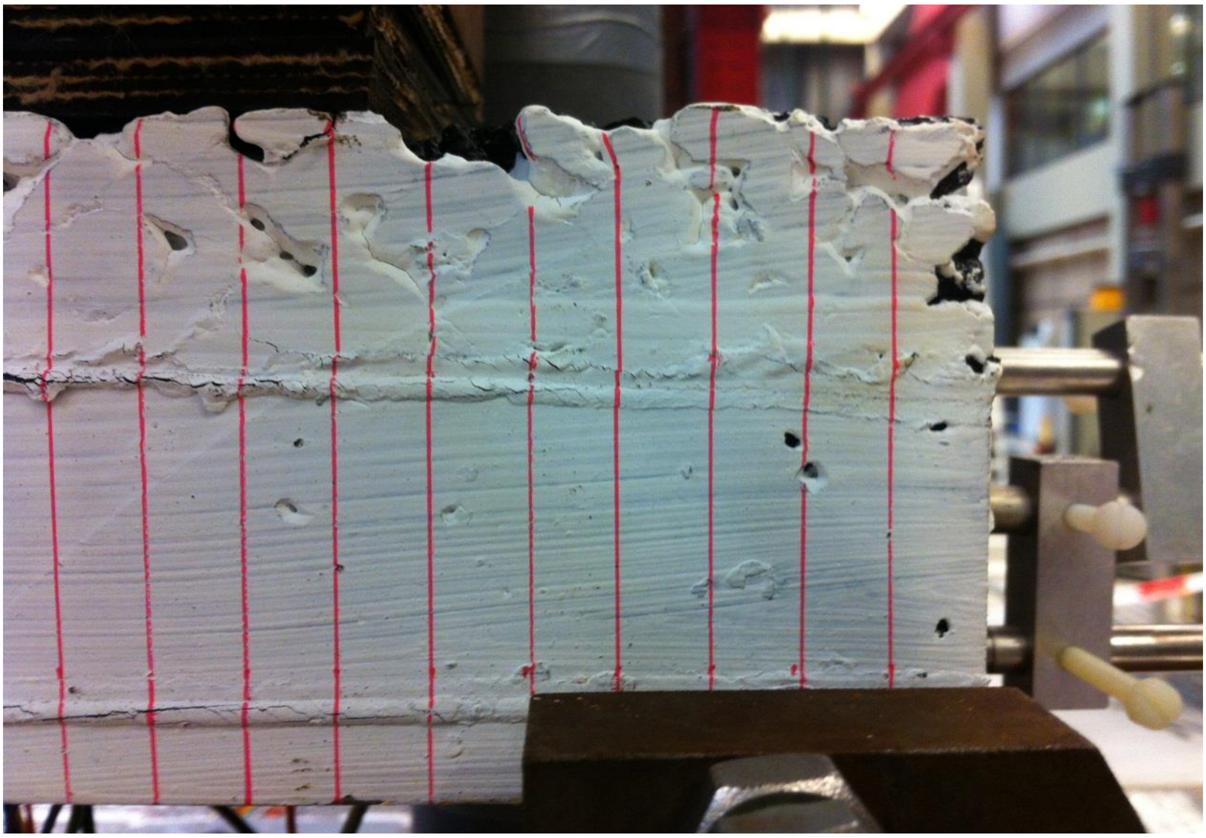

Figure A-15 Zoom on the right end of the specimen

Specimen with membrane productC1 at +10^{o}C

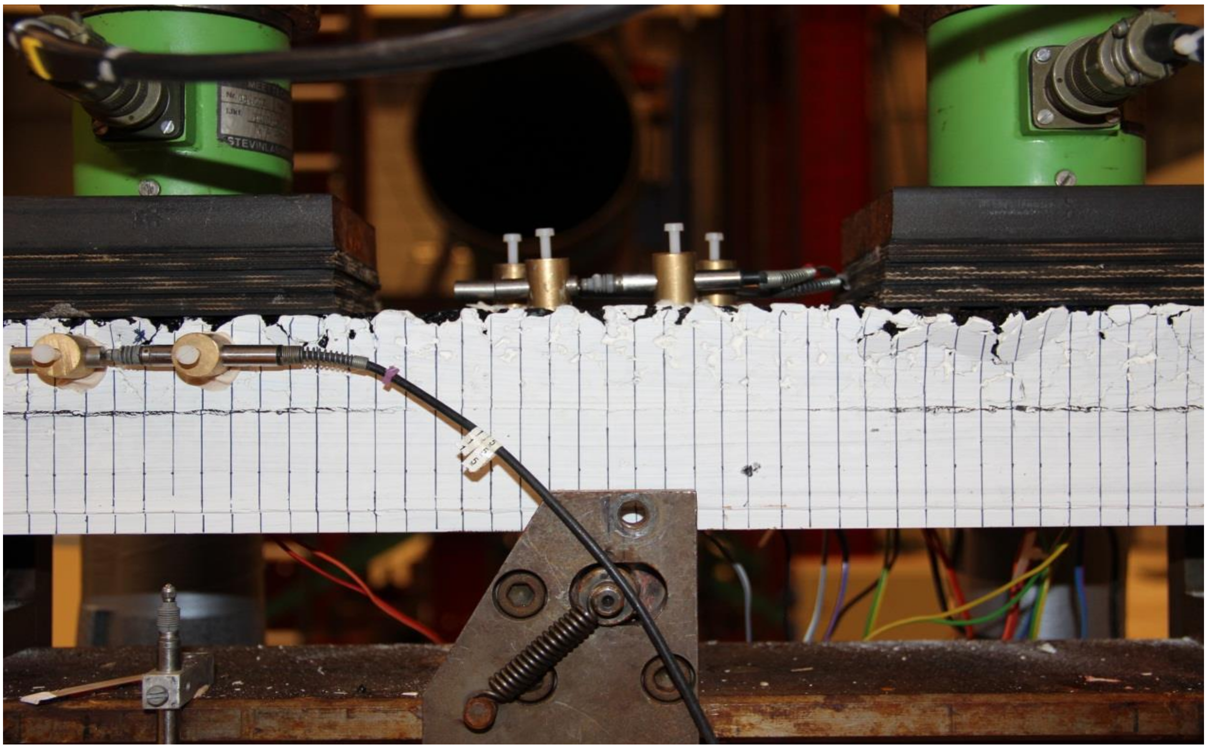

Figure A-16 Overview of damage on the entire specimen

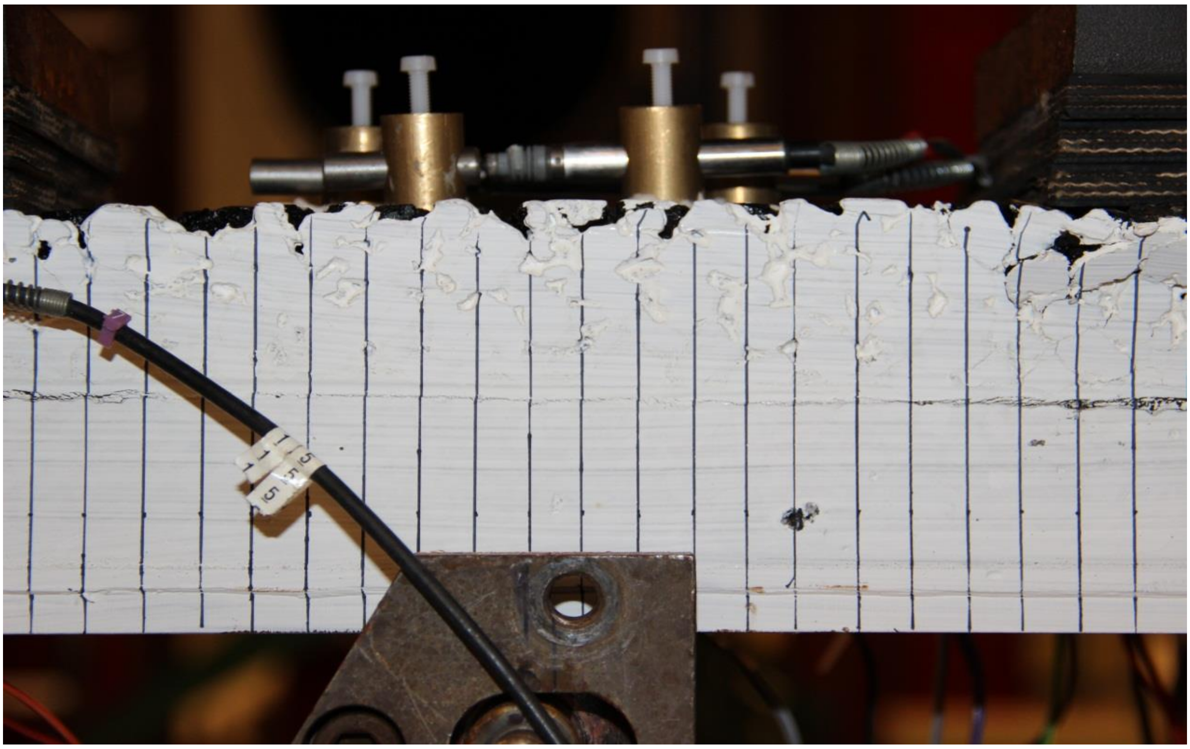

Figure A-17 Zoom on the mid support of the specimen

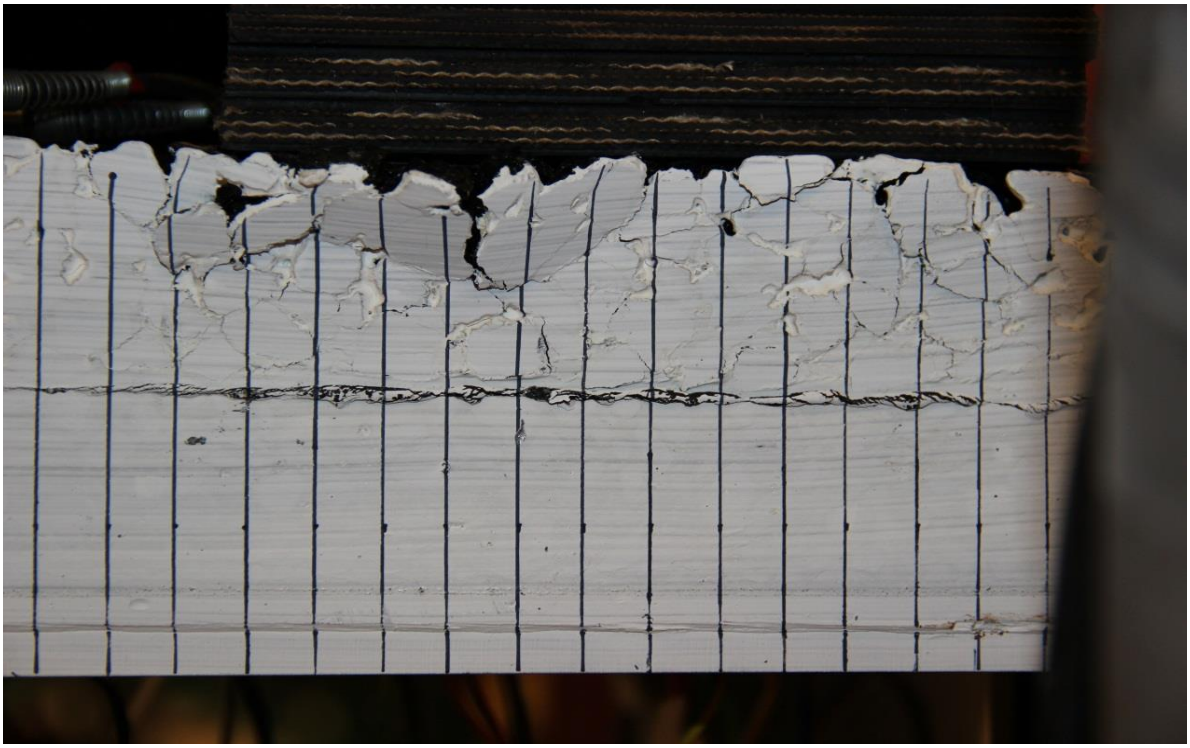

Figure A-18 Damage on the specimen under the right side of the load cell

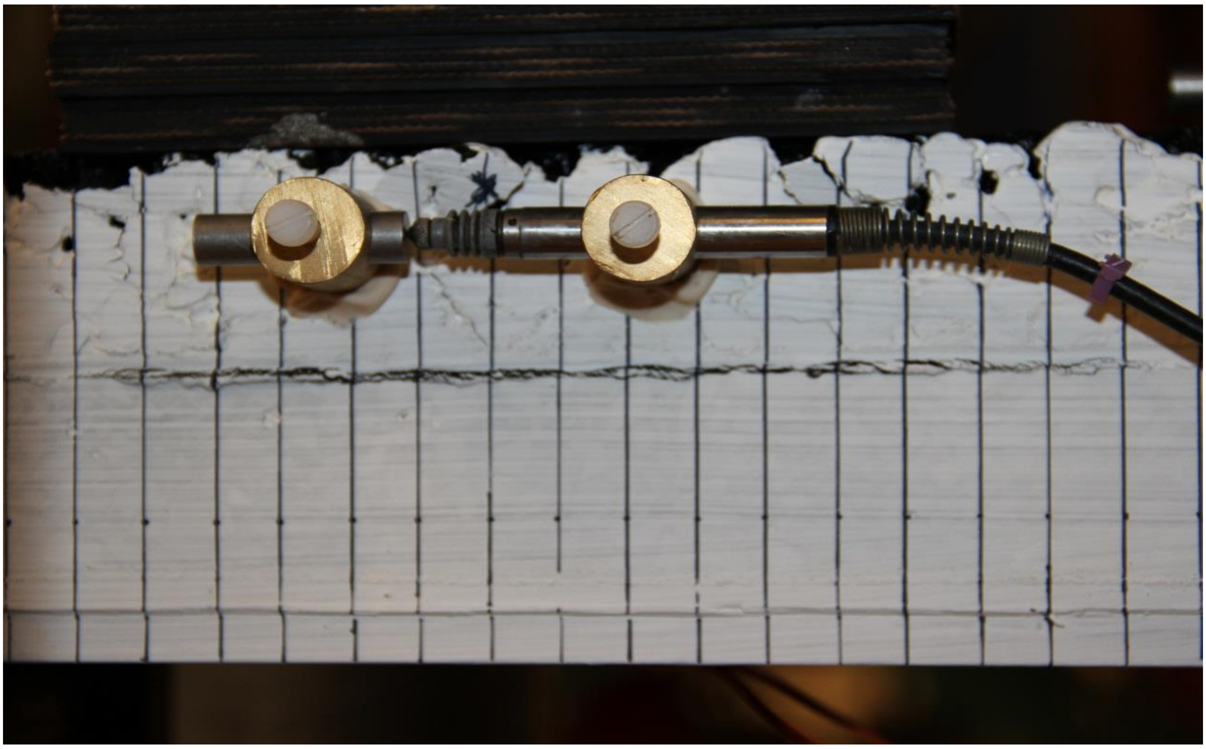

Figure A-19 Damage on the specimen under the left side of the load cell

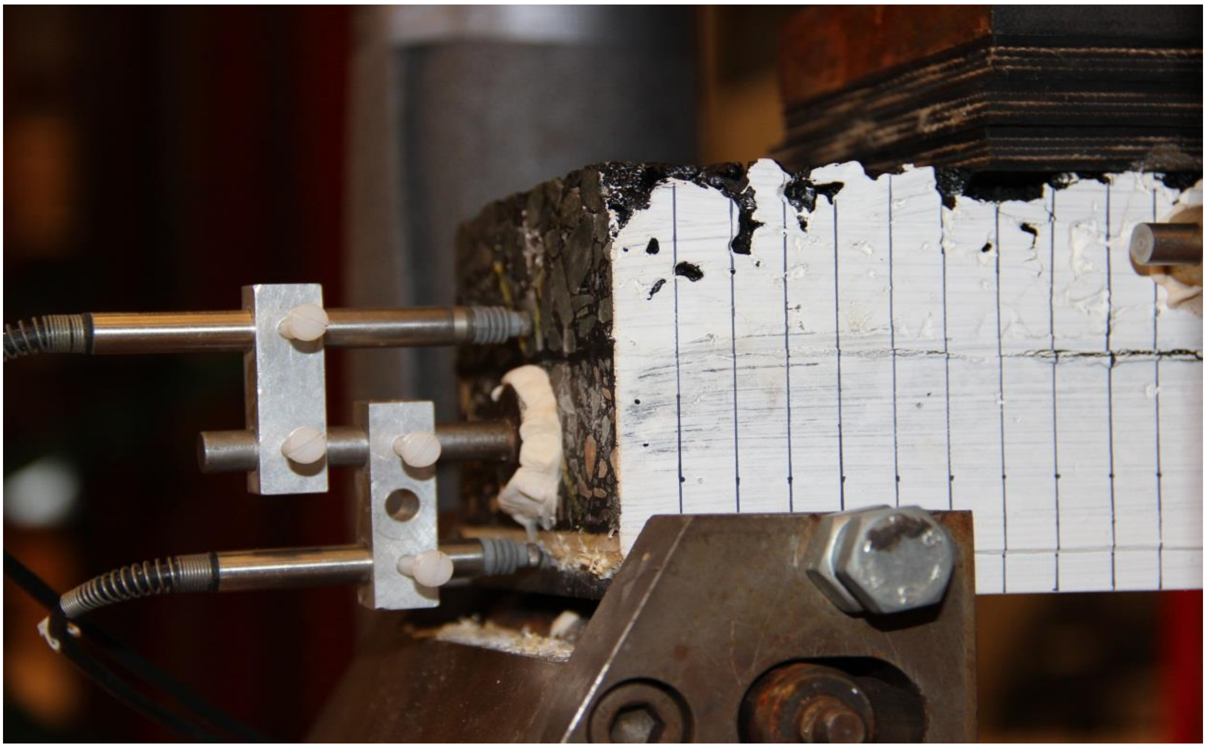

Figure A-20 Zoom on the left end of the specimen

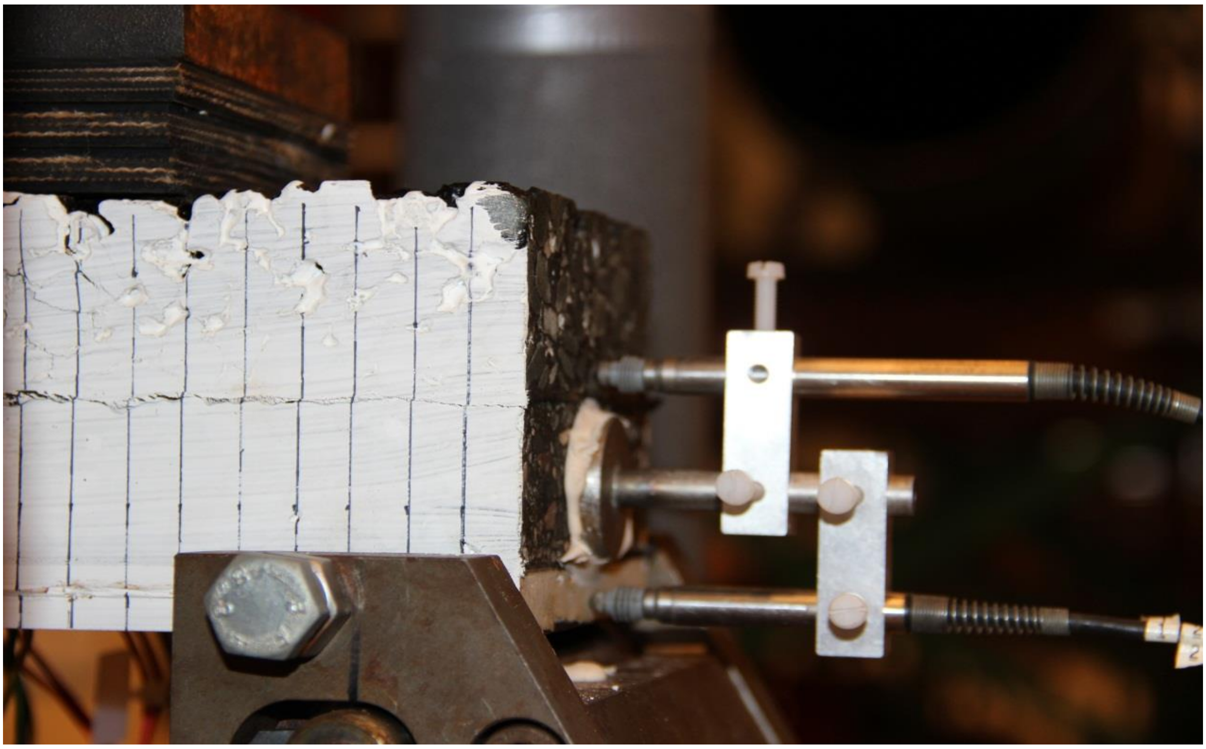

Figure A-21 Zoom on the right end of the specimen

Specimen with membrane productC1 at -5^{o}C

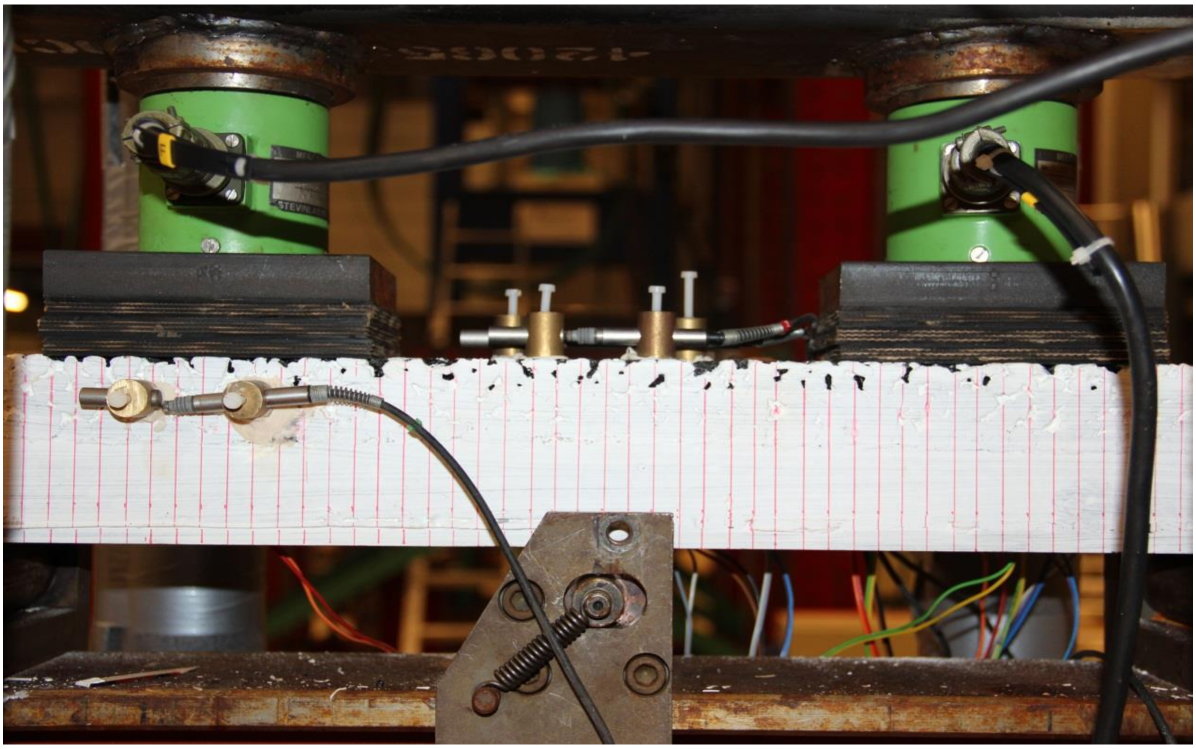

Figure A-22 Overview of damage on the entire specimen

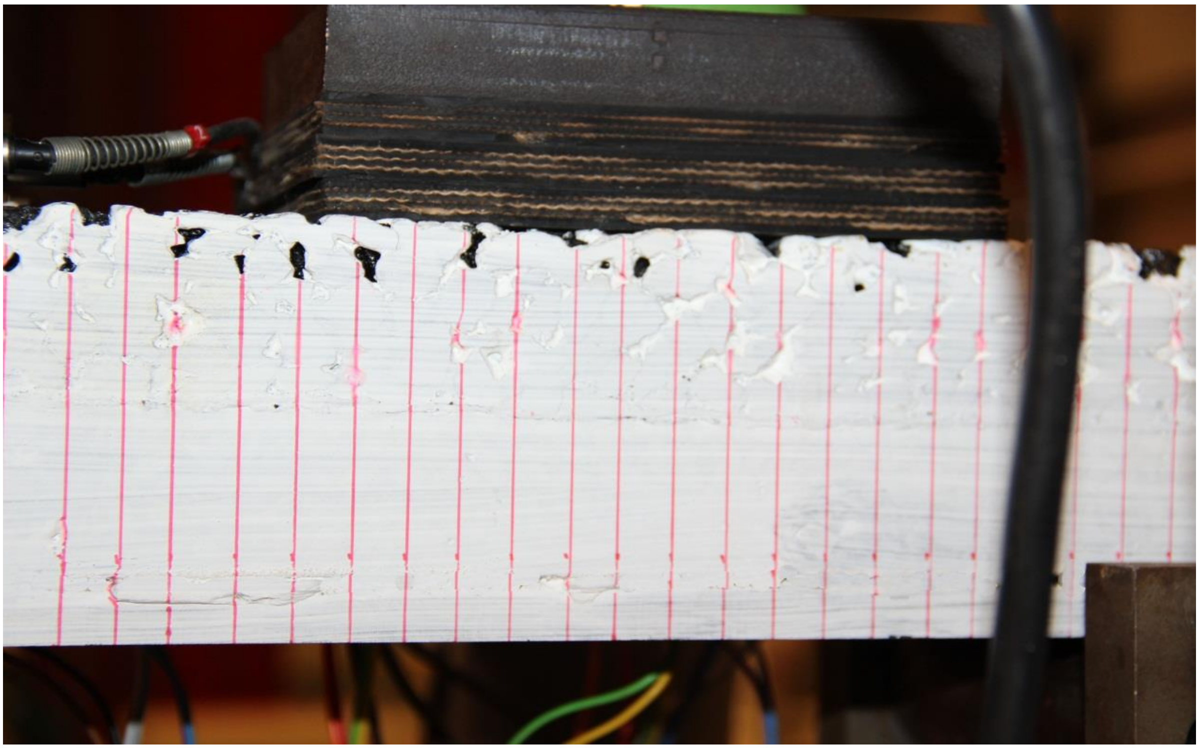

Figure A-23 Zoom on the specimen under the right side of the load cell

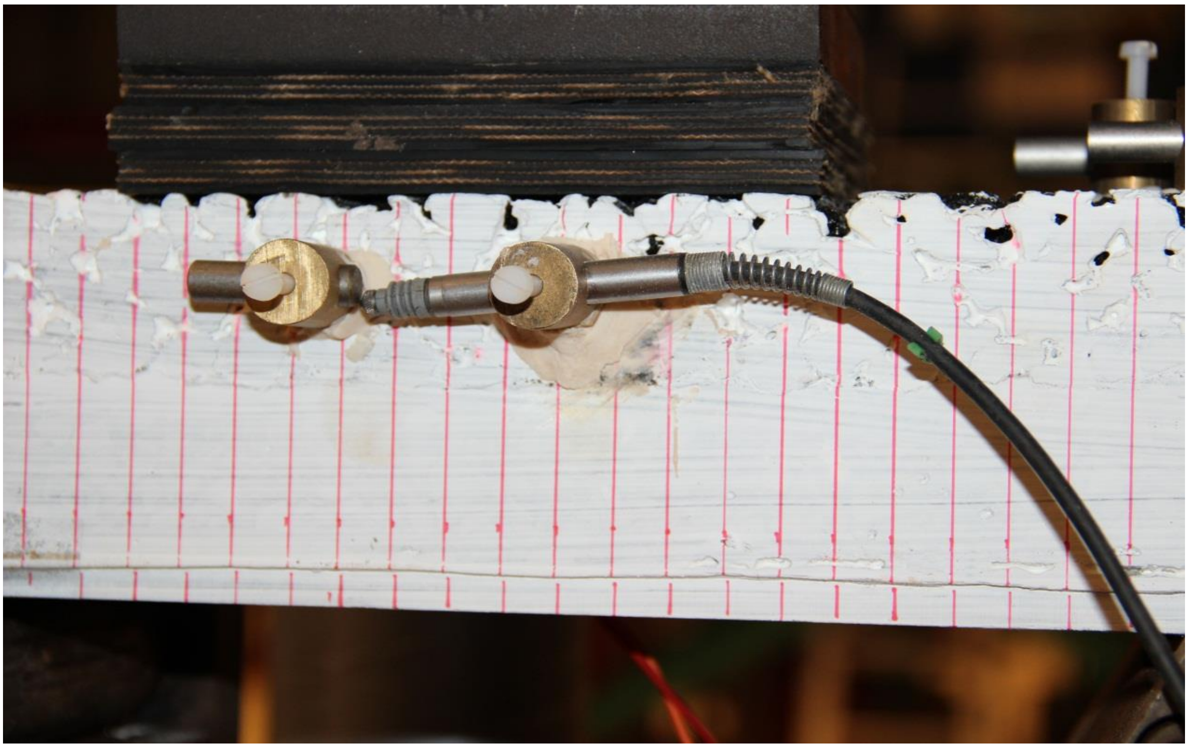

Figure A-24 Zoom on the specimen under the left side of the load cell

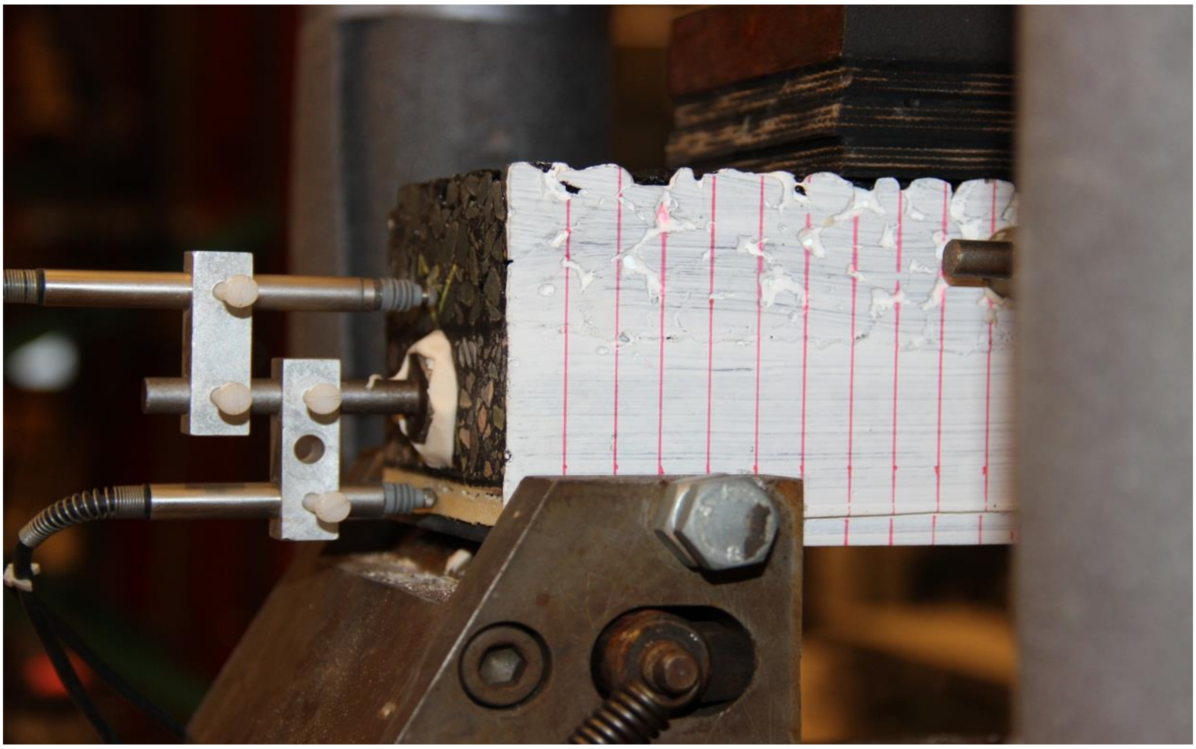

Figure A-25 Zoom on the left end of the specimen

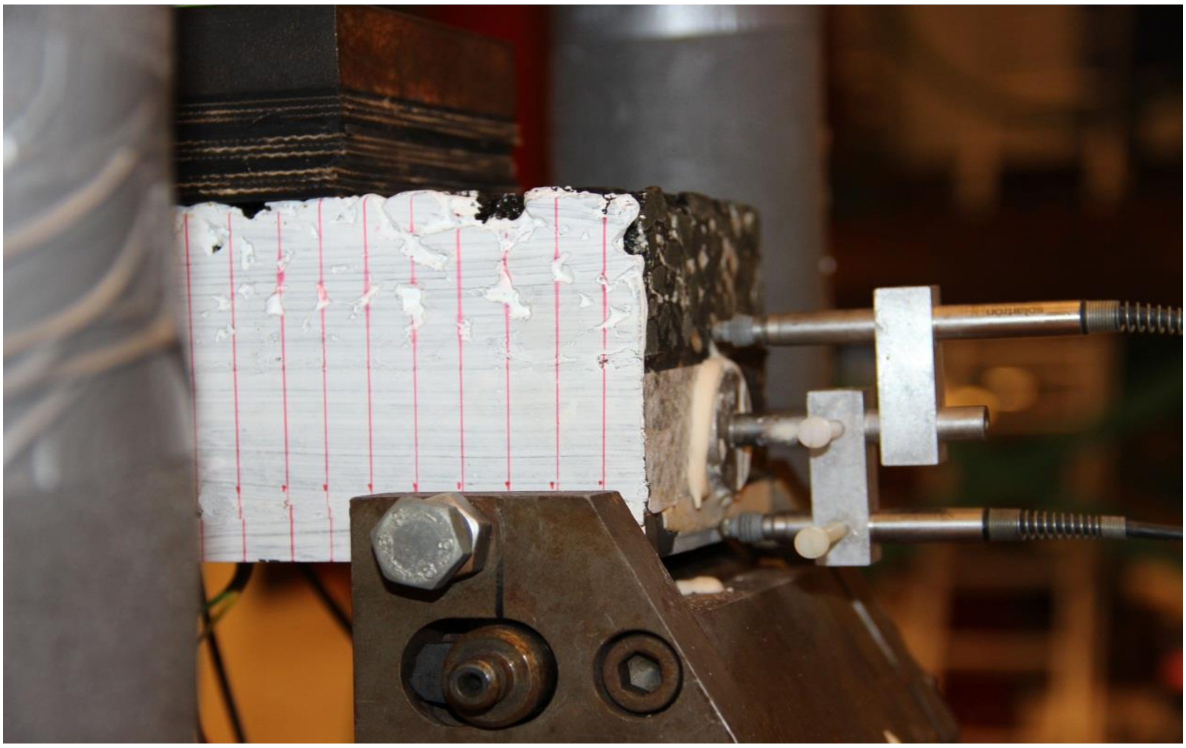

Figure A-26 Zoom on the right end of the specimen

Specimen with membrane product C2 at -5^{o}C

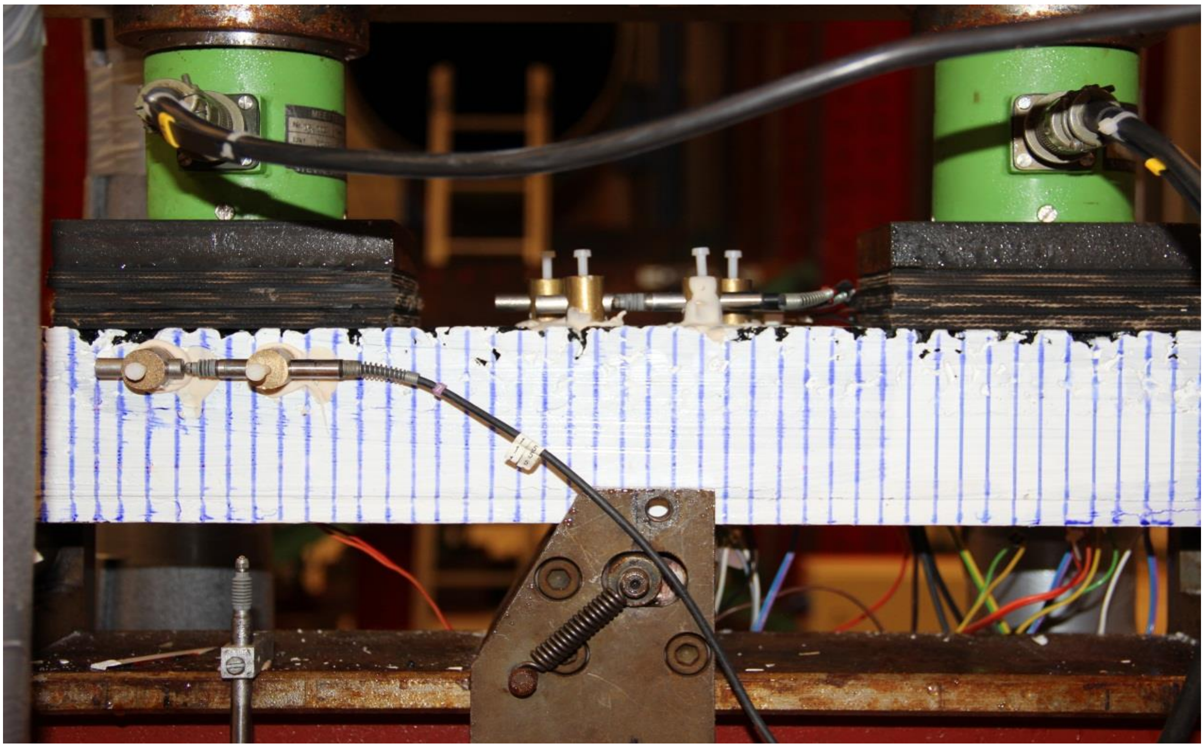

Figure A-27 Overview of damage on the entire specimen

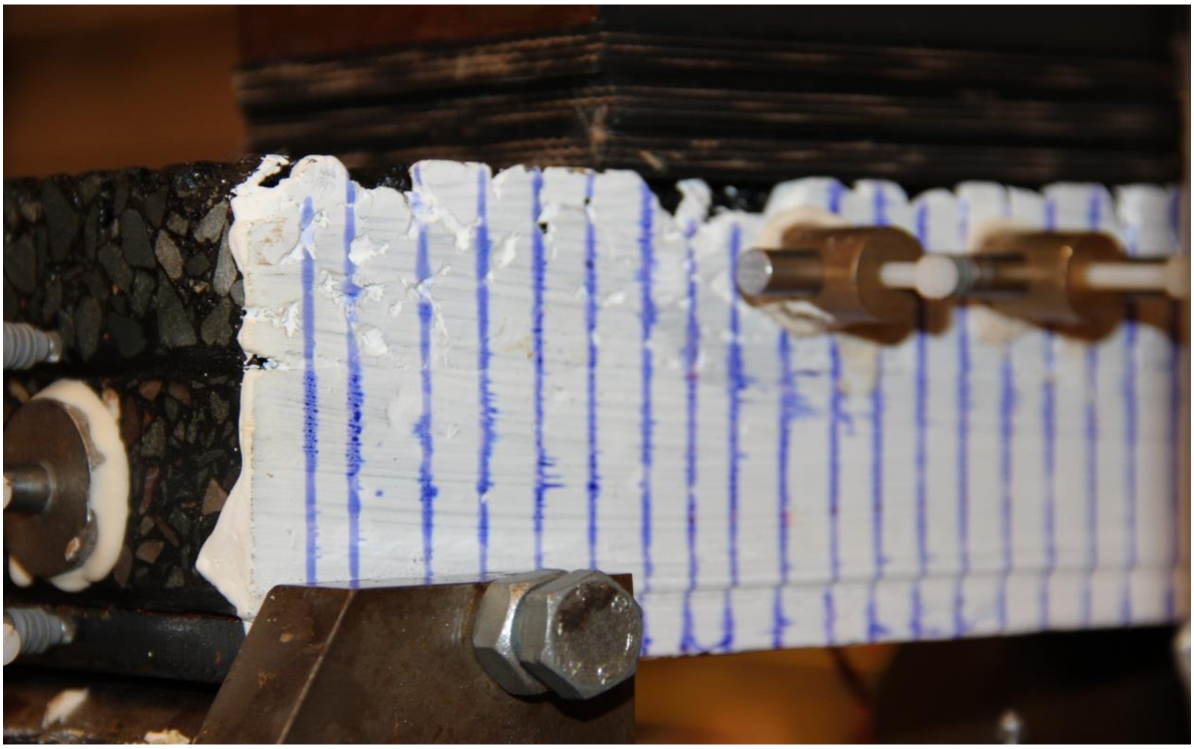

Figure A-28 Zoom on the left end of the specimen

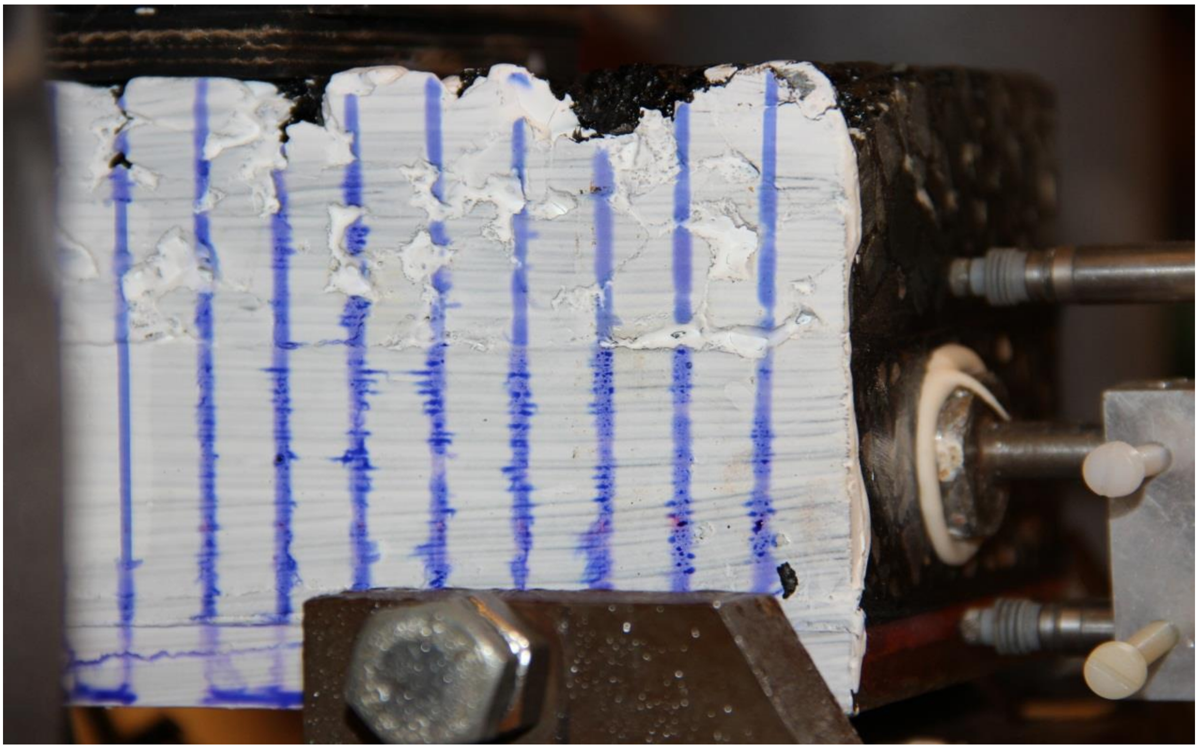

Figure A-29 Zoom on the right end of the specimen

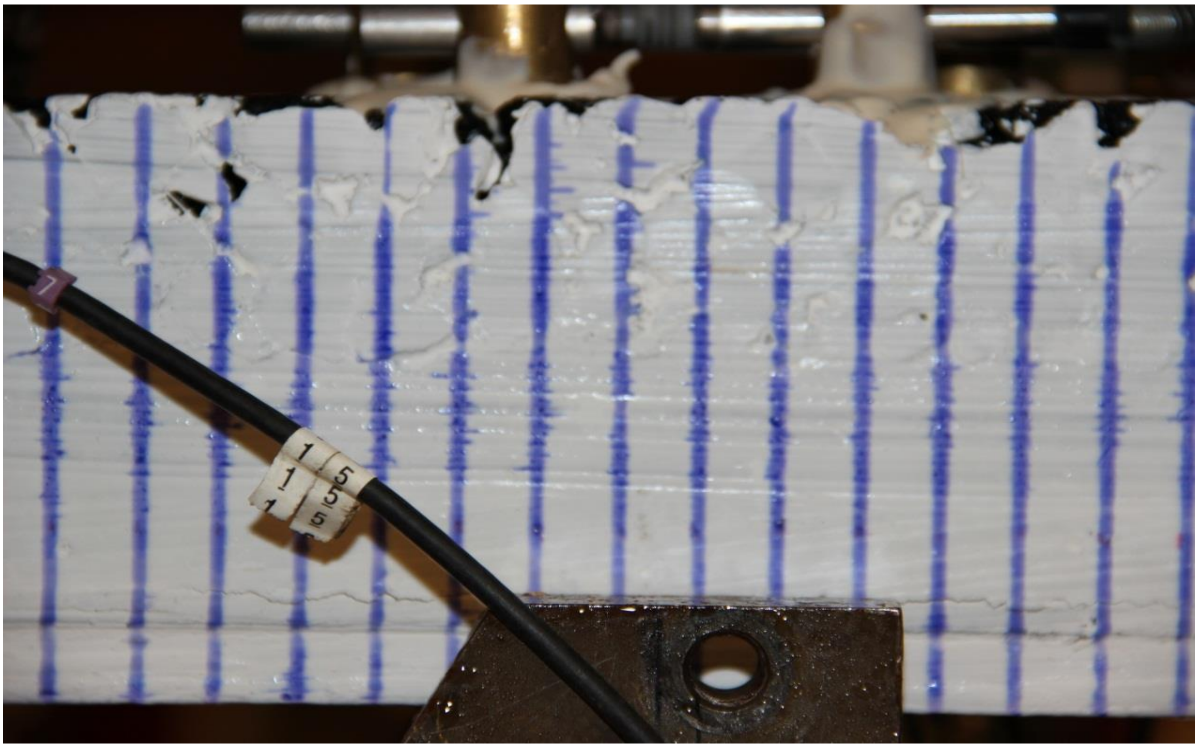

Figure A-30 Zoom on the mid support of the specimen

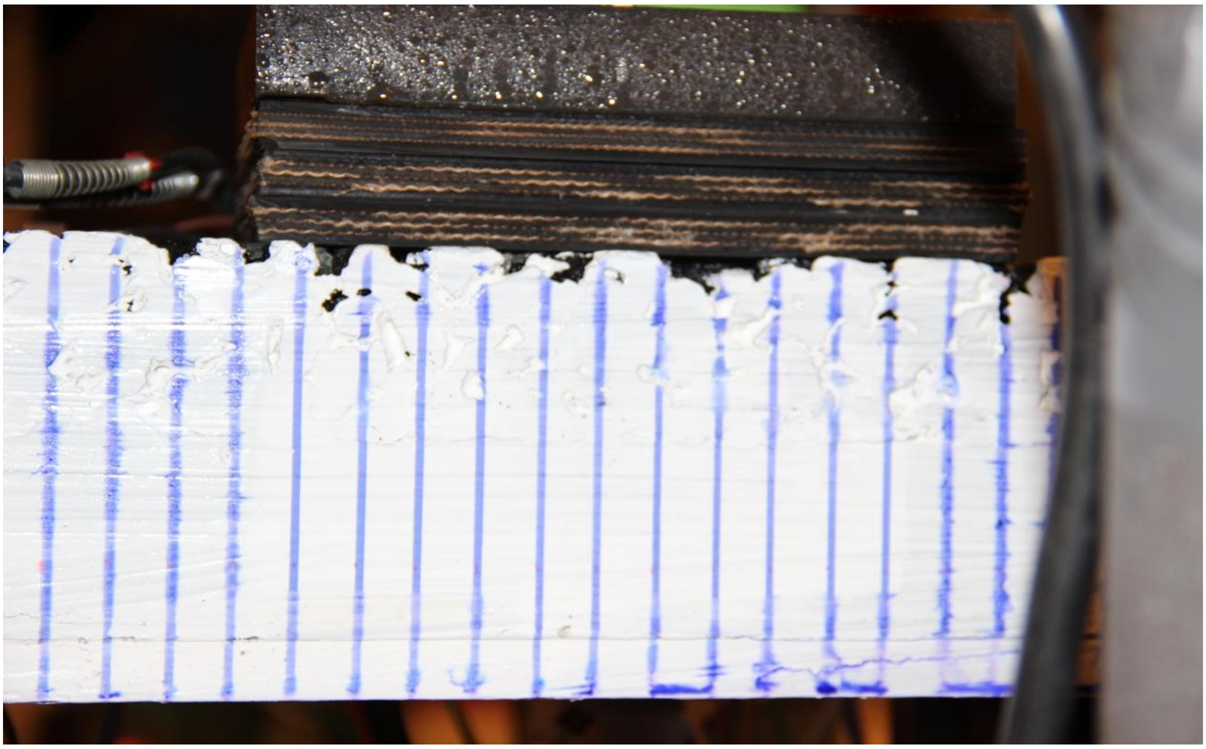

Figure A-31 Zoom on the specimen under the right side of the load cell

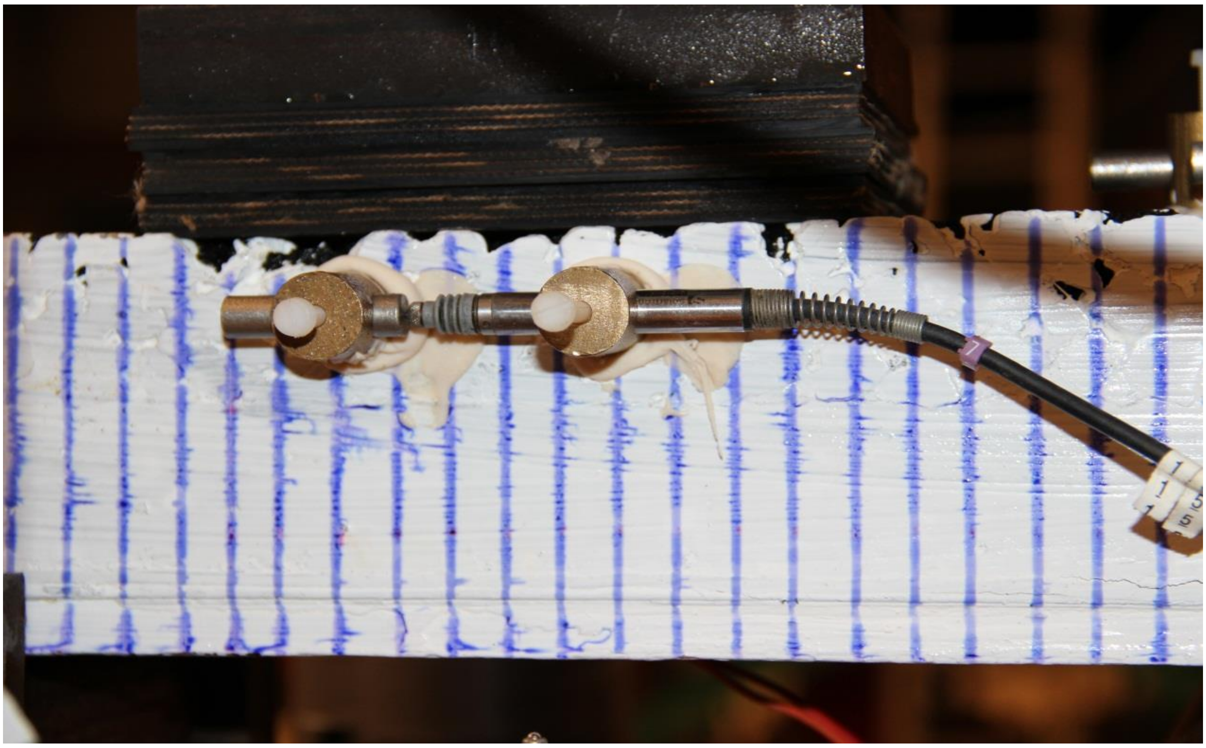

Figure A-32 Zoom on the specimen under the left side of the load cell

Specimen with membrane product C2 at +10°C

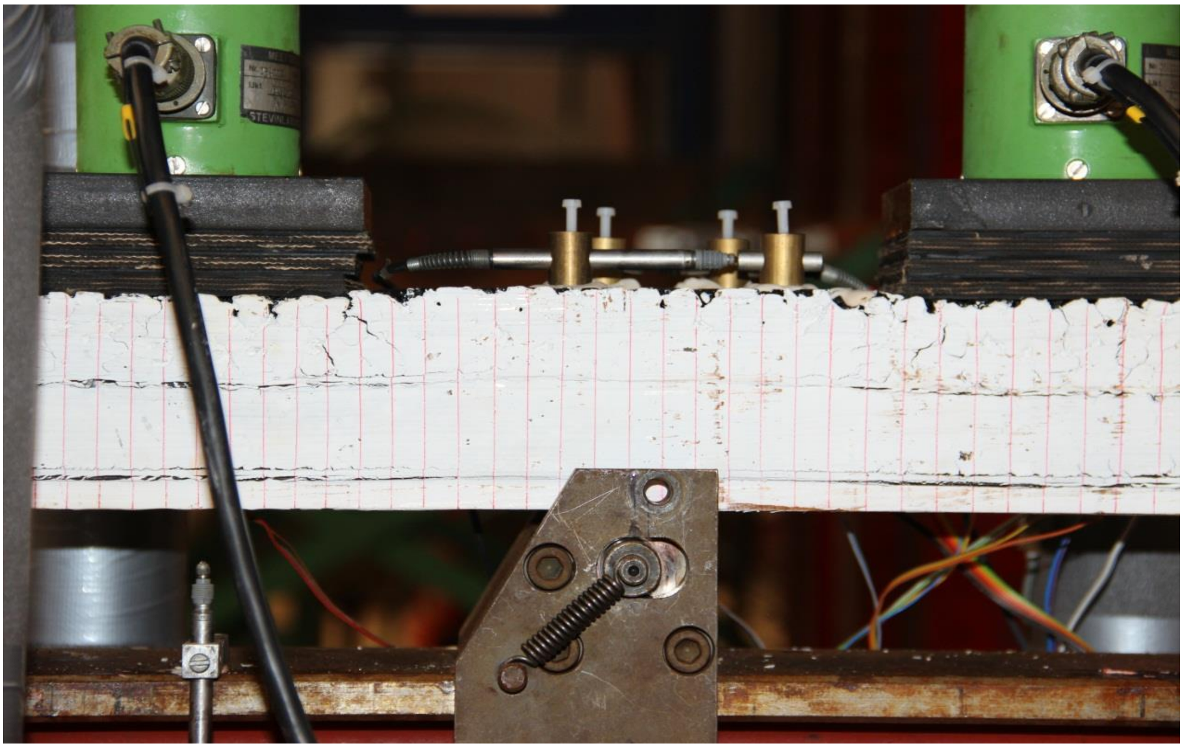

Figure A-33 Overview of damage on the entire specimen

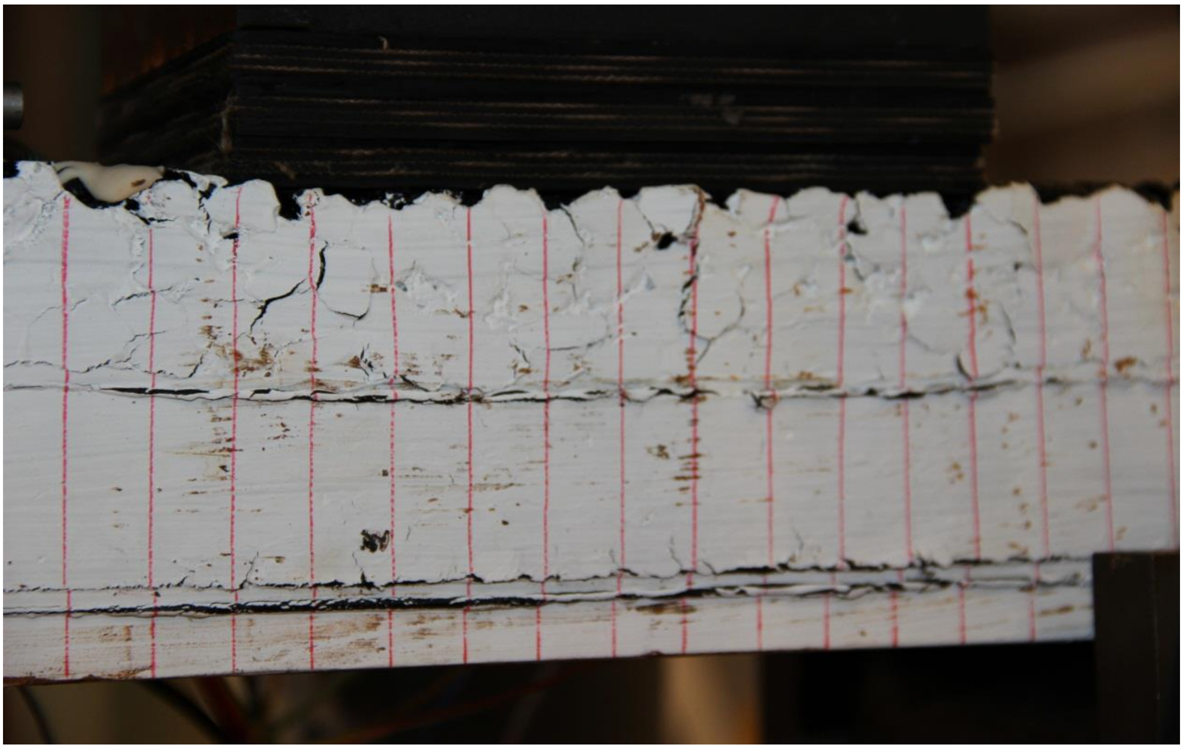

Figure A-34 Zoom on the specimen under the right side of the load cell

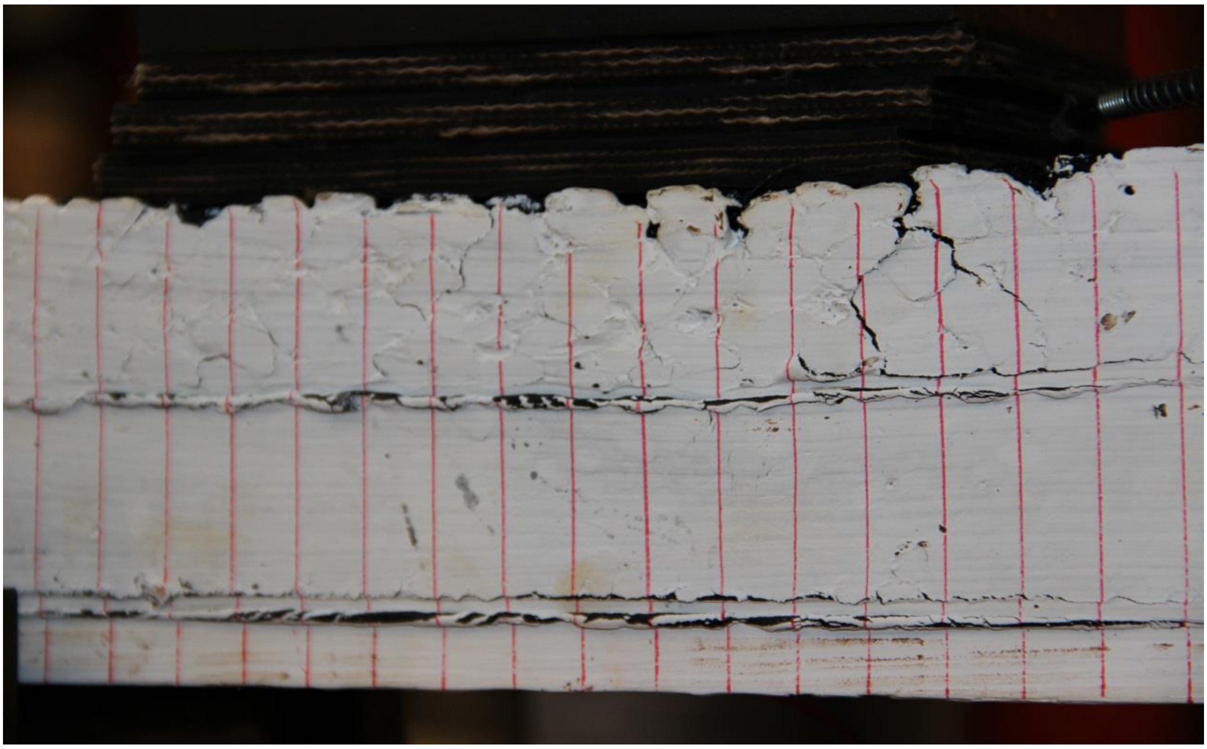

Figure A-35 Zoom on the specimen under the left side of the load cell

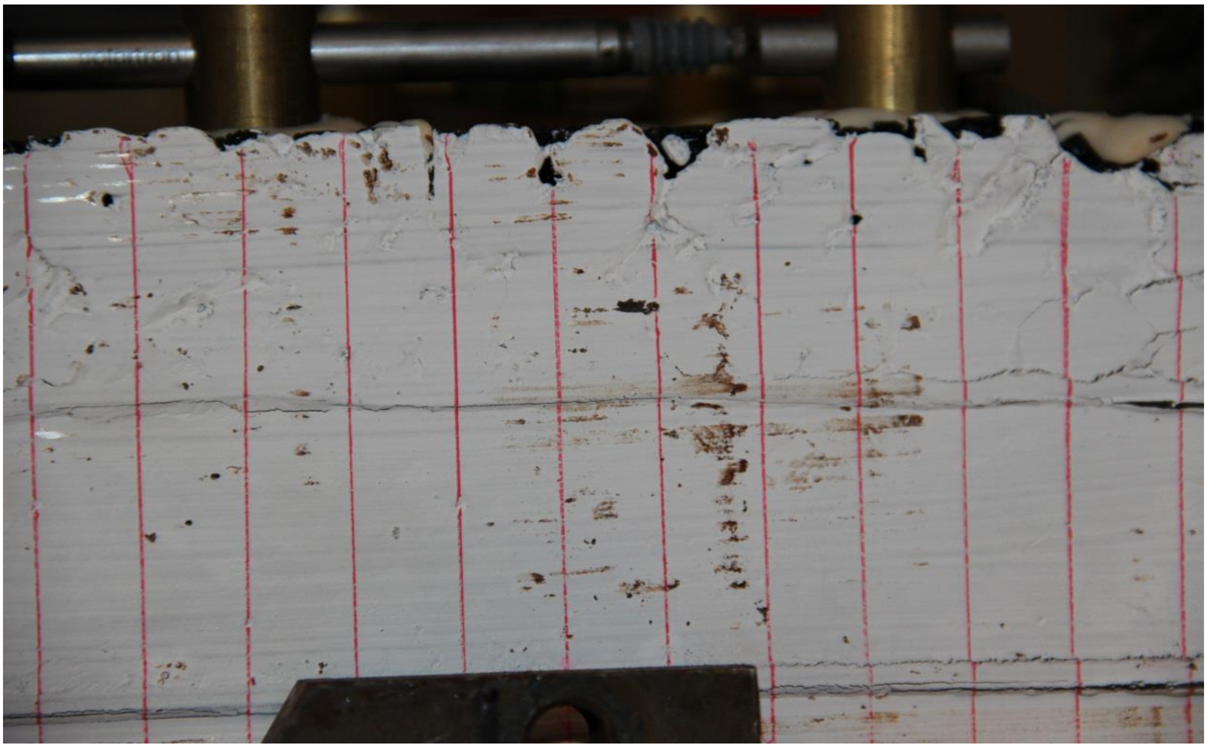

Figure A-36 Zoom on the mid support of the specimen

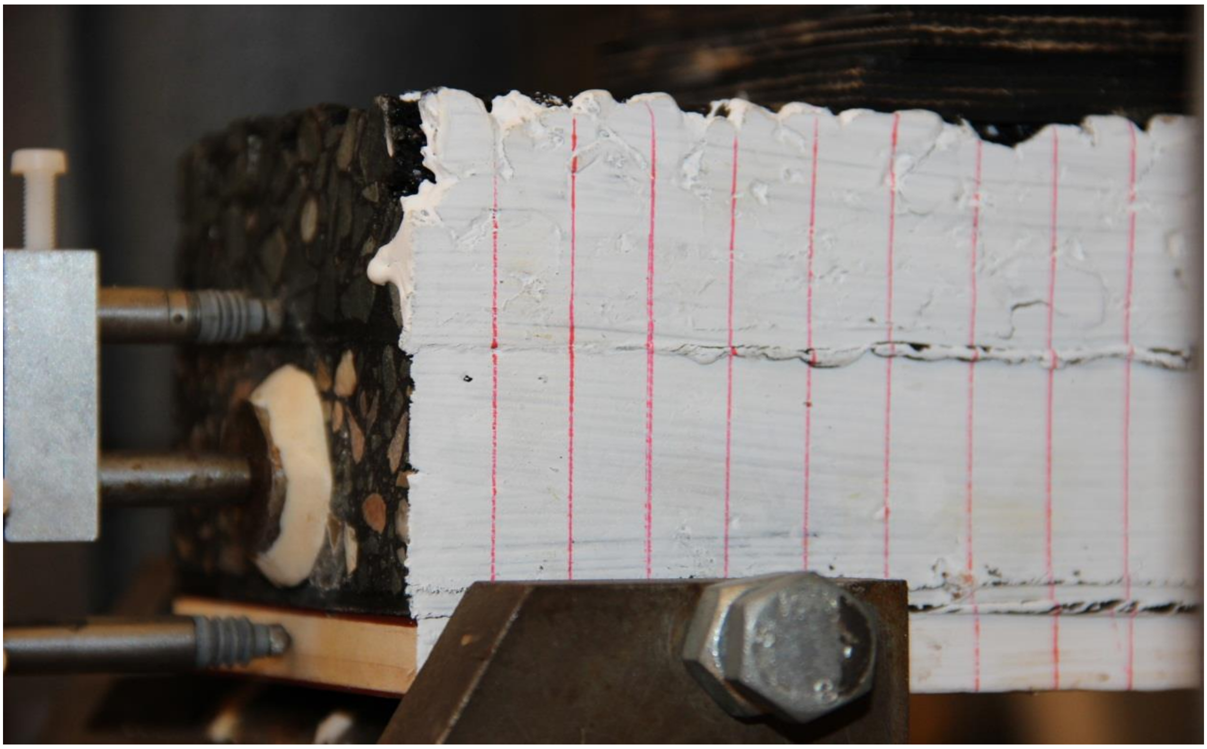

Figure A-37 Zoom on the left end of the specimen

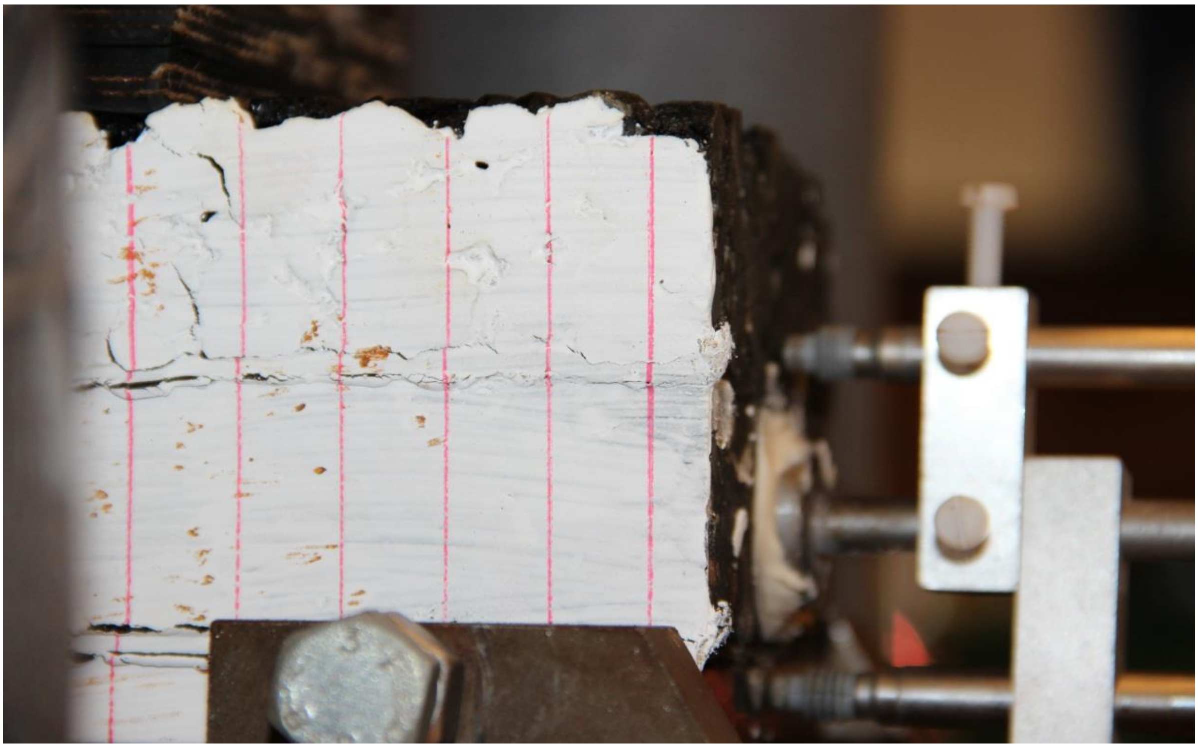

Figure A-38 Zoom on the right end of the specimen

Appendix II

In Appendix II the bonding characteristic of the selected the membrane products for 5PB beam tests are presented. The bonding properties were obtained by using MAT device and reported by Liu & Scarpas (2012).

Company A

Table 1 MAT test results of membrane A1 and A2

Interface	Temp (^oC)	Code	G_c (J/m^2)	Debonding Force (N)	δ_{max} (mm)
Steel/A1	-5	S03	1106.85	1017.13	2.73
		S04	1055.23	1080.07	
	+5	S01	1381.21	1154.52	2.45
		S02	1217.28	1120.58	
	+10	S05	1186.59	1079.36	4.77
		S06	1328.57	1129.79	
A1/G-asphalt	-5	GM1-01	1680.45	1534.85	1.58
		GM1-02	1568.00	1331.78	
	+5	GM1-03	2133.67	1240.86	4.58
		GM1-04	2258.76	1507.07	
	+10	GM1-05	2150.84	1275.69	5.90
		GM1-06	2048.47	1282.20	
G-asphalt/A2	-5	GM2-03	2302.15	1784.20	1.54
		GM2-04	2470.65	1759.57	
	+5	GM2-05	2411.75	1653.26	1.00
		GM2-06	2560.82	1838.77	
	+10	GM2-01	2130.90	1751.74	2.45
		GM2-02	1965.24	1377.38	
A2/P-asphalt	-5	PM2-01	3730.00	1926.49	7.75
		PM2-02	3554.05	1957.71	
	+5	PM2-03	2409.94	1786.13	3.01
		PM2-04	2332.50	1588.80	
	+10	PM2-05	2534.00	1413.13	2.33
		PM2-06	2613.09	1755.90	

Company B

Table 2 MAT test results of membrane B

Interface	Temp (^oC)	Code	G_c (J/m^2)	Debonding Force (N)	δ_{max} (mm)
Steel/B	-5	S04	3129.21	2216.99	1.76
		S06	3373.41	2335.68	
	+5	S02	3941.27	2312.14	3.22
		S05	3760.65	2190.45	
	+10	S09	5427.31	2135.44	4.06
		S10	5509.85	2401.86	
B/G-asphalt	-5	GM1-05	2952.76	2365.96	2.45
		GM1-06	2880.23	2332.71	
	+5	GM1-03	3120.86	2269.85	1.65
		GM1-04	3120.76	2215.18	
	+10	GM1-01	2892.20	2168.59	2.20
		GM1-02	2892.20	2168.59	
G-asphalt/B	-5	GM2-01	751.26	1061.31	1.76
		GM2-02	705.48	886.90	
	+5	GM2-03	1901.22	1374.85	3.00
		GM2-04	2321.04	1682.59	
	+10	GM2-05	2931.78	1774.79	3.39
		GM2-06	2823.08	2058.48	
B/P-asphalt	-5	PM2-05	3846.39	2575.41	6.80
		PM2-06	3927.07	2074.86	
	+5	PM2-03	3463.01	1928.98	5.93
		PM2-04	3677.13	2131.38	
	+10	PM2-01	2874.29	2166.79	5.26
		PM2-02	2830.27	1891.14	

Company C

Table 3 MAT test results of membrane C1

Interface	Temp (^oC)	Code	G_c (J/m^2)	Debonding Force (N)	δ_{max} (mm)
Steel/C1	-5	S01	4804.32	3374.05	4.19
		S02	4416.74	3599.76	
	+5	S03	4207.97	3127.70	2.92
		S04	4494.59	3267.41	
	+10	S05	4744.09	3112.04	3.99
		S06	4949.96	2977.43	
C1/G-asphalt	-5	GM-05	3012.46	2193.50	7.26
		GM-06	3146.68	2384.01	
	+5	GM1-03	3337.69	2102.73	6.21
		GM1-04	3591.27	2561.11	
	+10	GM1-01	3233.12	2231.41	6.00
		GM1-02	3132.66	2237.18	

Table 4 MAT test results of membrane C2

Interface	Temp (^oC)	Code	G_c (J/m^2)	Debonding Force (N)	δ_{max} (mm)
Steel/C2	-5	S01	816.83	1079.80	4.18
		S02	825.51	1050.89	
	+5	S04	2008.46	1426.80	2.31
		S07	2110.00	1746.06	
	+10	S05	2478.89	1813.98	1.50
		S06	2516.67	2217.57	
C2/G-asphalt	-5	GM1-05	3185.59	2426.57	2.95
		GM1-06	3178.34	2360.02	
	+5	GM1-03	3799.45	2506.77	5.45
		GM1-04	3977.85	2637.79	
	+10	GM1-01	3438.94	2373.34	3.22
		GM1-02	3414.79	2511.30	
G-asphalt/C2	-5	GM2-01	1813.59	1959.91	1.53
		GM2-02	1943.54	1867.63	
	+5	GM2-03	3079.18	2311.07	2.18
		GM2-04	2812.33	2339.97	
	+10	GM2-06	3614.82	2331.04	4.01
		GM2-05	3614.82	2331.04	
C2/P-asphalt	-5	PM2-05	2113.69	2098.90	4.31
		PM2-06	2336.65	2183.92	
	+5	PM2-03	3567.56	2604.93	5.53
		PM2-04	3023.89	2211.96	
	+10	PM2-01	4485.72	2650.84	6.16
		PM2-02	4236.49	2581.03	

Appendix III

The comparisons of the test results among different interfaces with different membrane products are summarized in the following tables:

Product A1

Interface	10°C						30°C	
	150N		250N		350N		100N	
	DW(N.mm)	Debonding length (mm)	DW (N.mm)	Debonding length (mm)	DW (N.mm)	Debonding length (mm)	DW (N.mm)	Debonding length (mm)
SM1	1100	9	7100	81	1850	8	1334	38
GM1	2940	51	9700	50	-	-	2243	82
GM2	-	-	-	-	-	-	-	-
PM2	-	-	-	-	-	-	-	-

Product A2

Interface	10°C						30°C	
	150N		250N		350N		100N	
	DW(N.mm)	Debonding length (mm)	DW (N.mm)	Debonding length (mm)	DW (N.mm)	Debonding length (mm)	DW (N.mm)	Debonding length (mm)
SM1	-	-	-	-	-	-	-	-
GM1	-	-	-	-	-	-	-	-
GM2	1792	5	10000	94	-	-	1335	22
PM2	3250	12	14000	72	-	-	2361	92

Product C1

Interface	10°C						30°C	
	150N		250N		350N		100N	
	DW(N.mm)	Debonding length (mm)	DW (N.mm)	Debonding length (mm)	DW (N.mm)	Debonding length (mm)	DW (N.mm)	Debonding length (mm)
SM1	1538	0	3275	0	4874	0	1111	0
GM1	1021	0	2134	0	11167	0	2168	44
GM2	-	-	-	-	-	-	-	-
PM2	-	-	-	-	-	-	-	-

Product C2

Interface	10°C						30°C	
	150N		250N		350N		100N	
	DW(N.mm)	Debonding length (mm)	DW (N.mm)	Debonding length (mm)	DW (N.mm)	Debonding length (mm)	DW (N.mm)	Debonding length (mm)
SM1	1070	16	3817	42	10856	9	1157	90
GM1	2094	14	4855	8	8866	16.5	1779	74
GM2	2091	4	4845	5	8850	16.5	1776	58
PM2	3588	20.56	7178	19	-	-	1311	85

A series of pictures with the debonded tested samples:

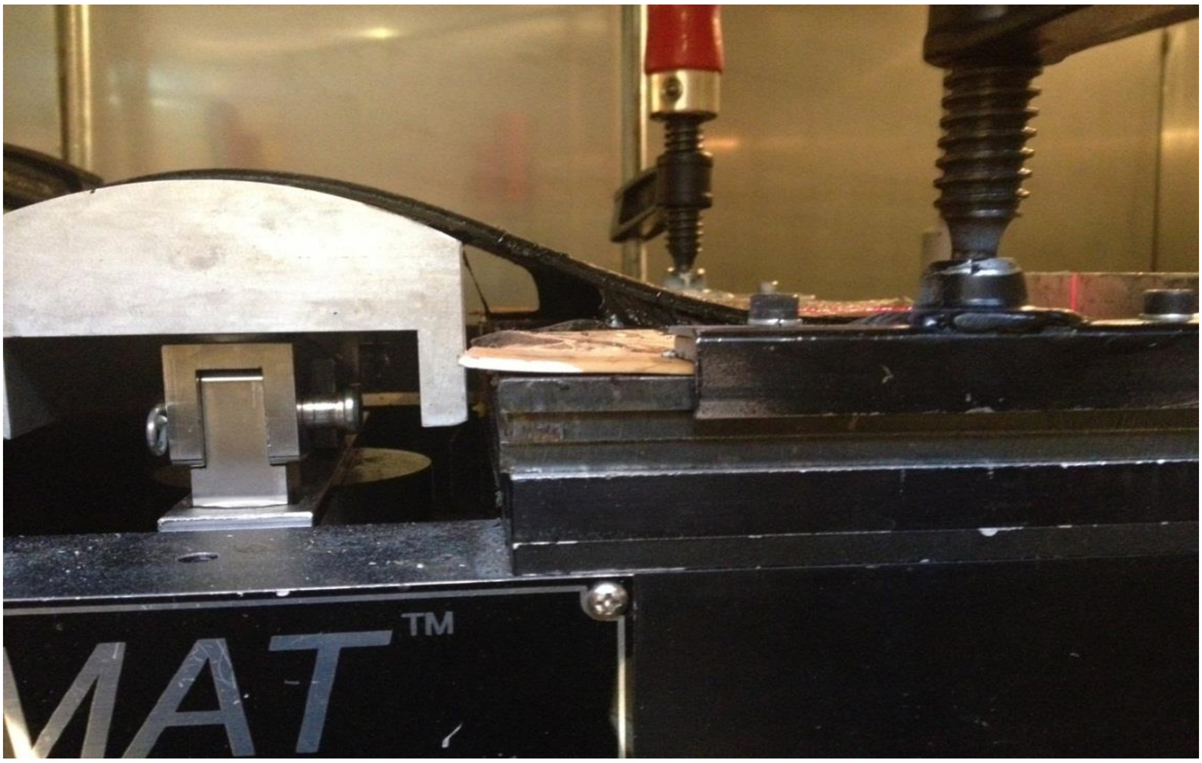

FigureA-1 Product A1 at 10^0C P_{max}=350N SM1 interface for 432,000 load cycles

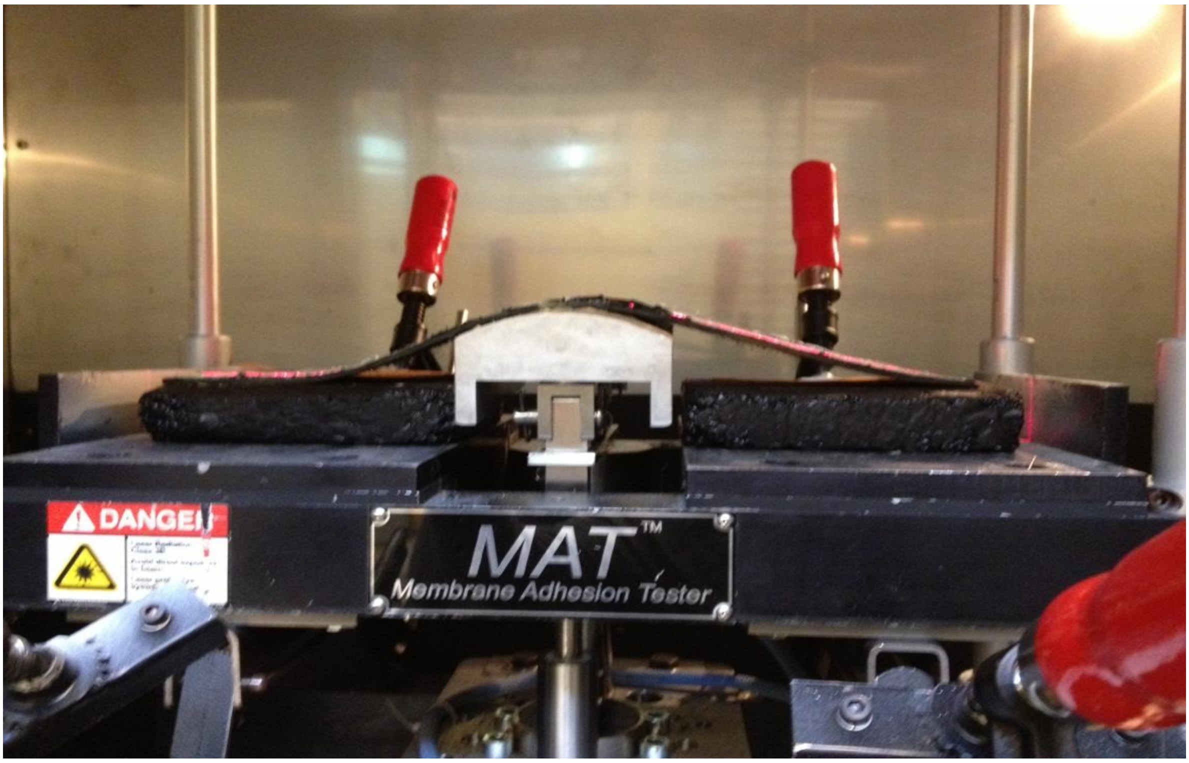

Figure A-2 Product A1 at 10^0C P_{max}=350N GM1 interface for 432,000 load cycles

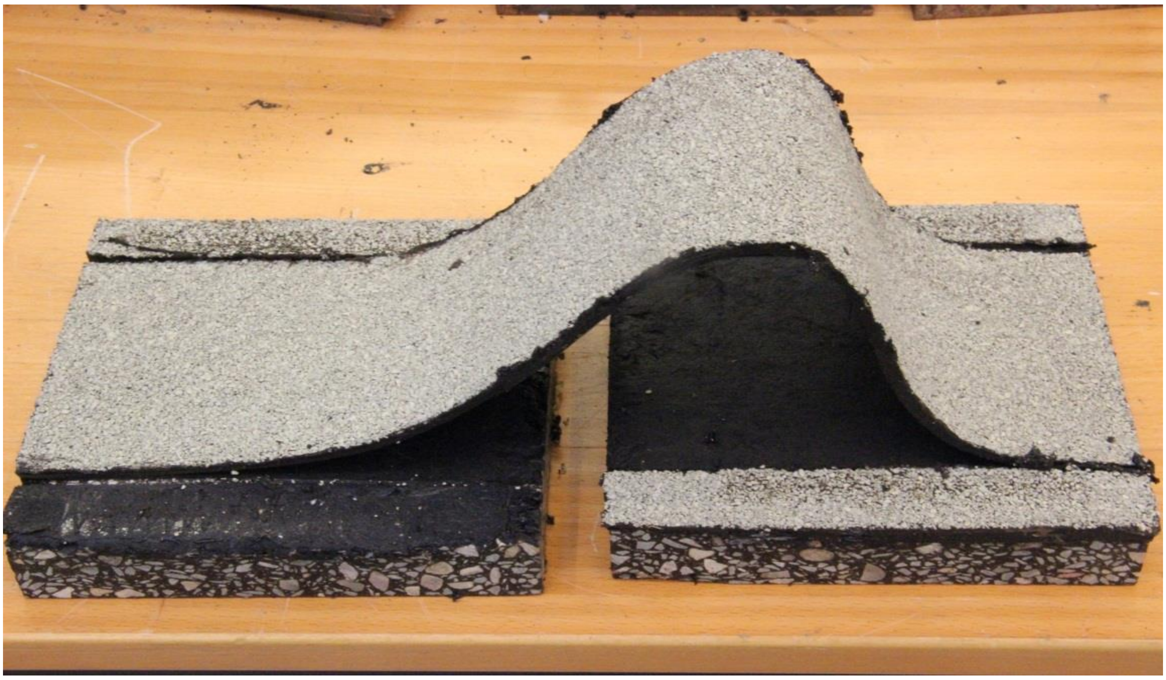

Figure A-3 Product A2 at 10^0C P_{max}=350N GM2 interface for 432,000 load cycles

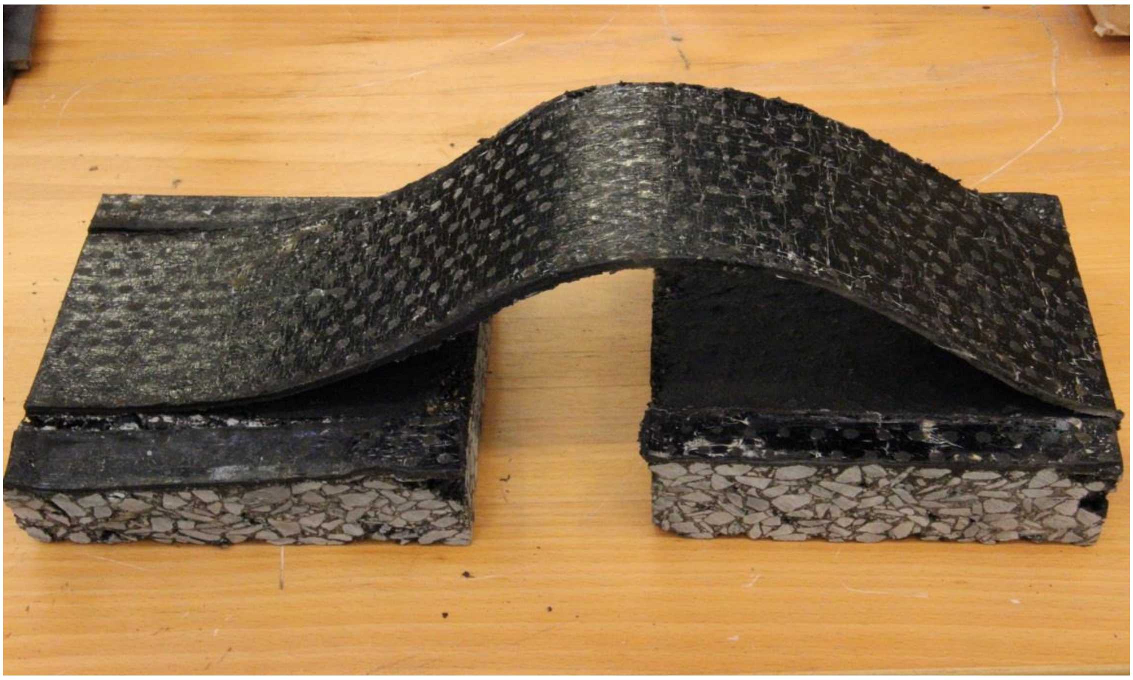

Figure A-4 Product A2 at 10^0C P_{max}=350N PM2 interface for 432,000 load cycles

Figure A-5 Product C1 at 10^0C P_{max}=350N SM1 interface for 432,000 load cycles

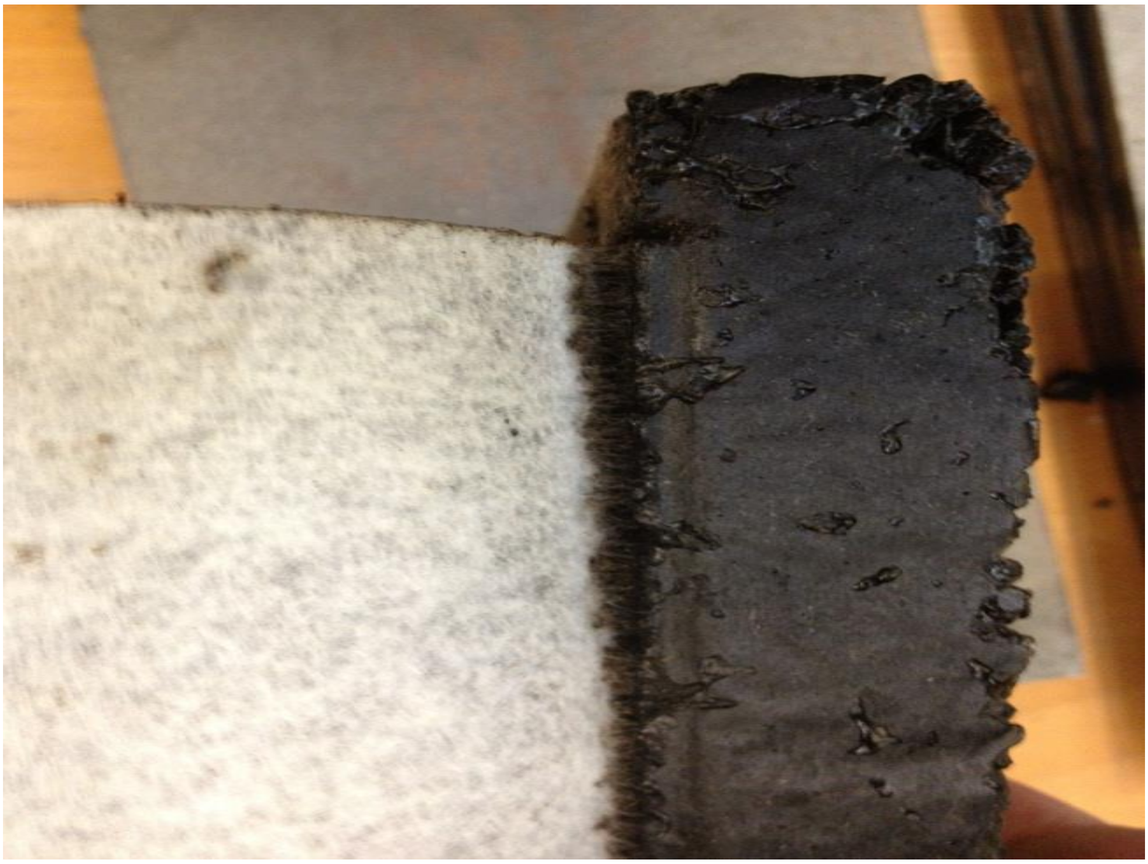

Figure A-6 Product C1 at 10^0C P_{max}=350N GM1 interface for 432,000 load cycles

Figure A-7 Product C2 at 10^0C P_{max}=350N GM2 interface for 432,000 load cycles

Figure A-8 Product C2 at 10^0C P_{max}=350N GM1 interface for 432,000 load cycles

Figure A-9 Product C2 at 10^0C P_{max}=350N GM2 interface for 432,000 load cycles

Figure A-10 Product C2 at 30^0C P_{max}=100N PM2 interface for 864,000 load cycles

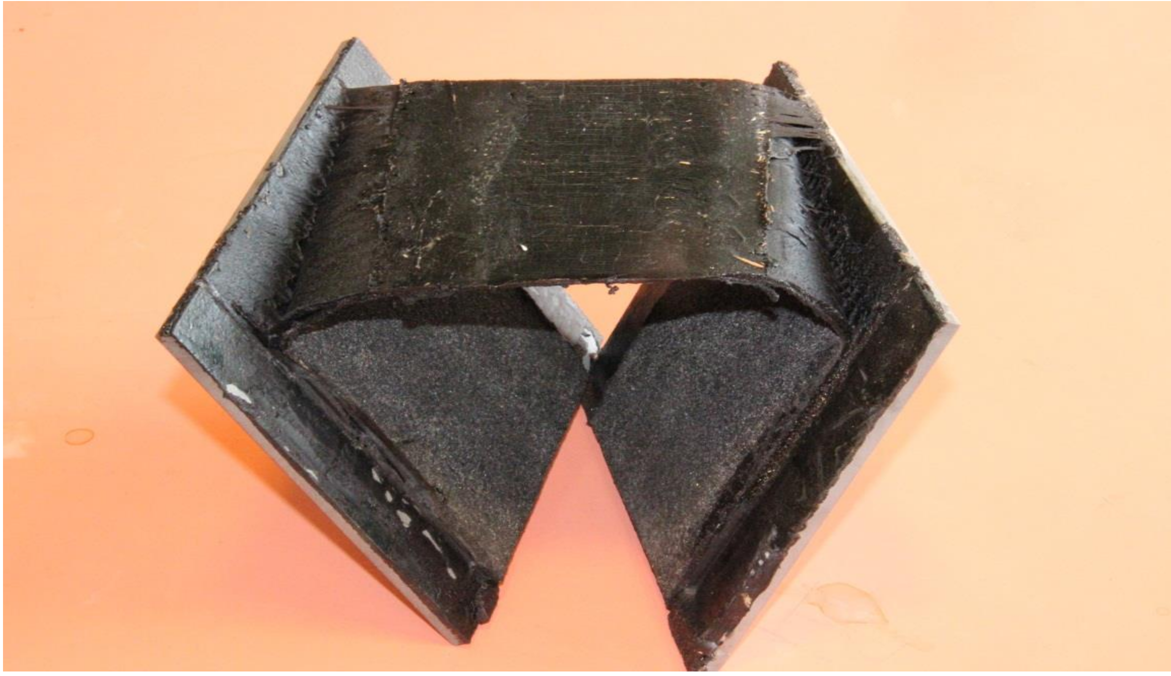

Figure A-11 Product A1 at 10^0C P_{max}=100N SM1 interface for 864,000 load cycles

Figure A-12 Product A1 at 30^0C P_{max}=100N PM2 interface for 864,000 load cycles

Figure A-13 Product A2 at 30^{0}C P_{max}=100N GM2 interface for 864,000 load cycles

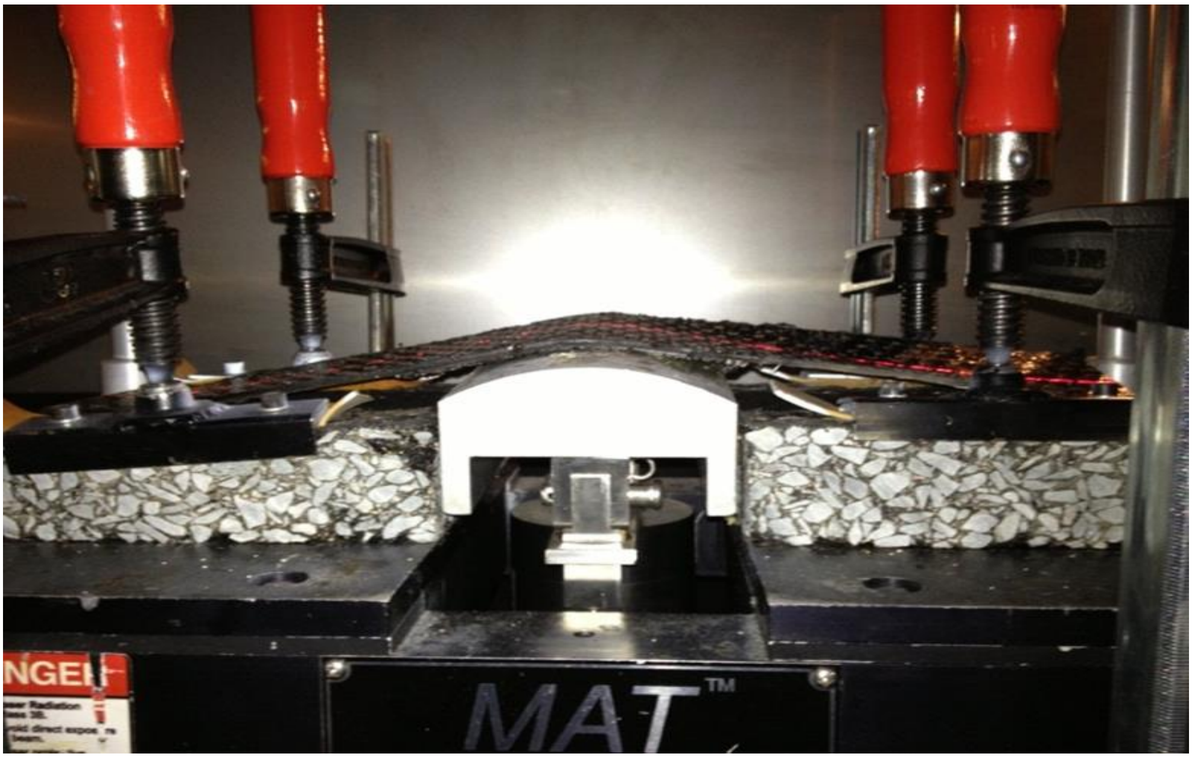

Figure A-14 Product A1 at 30^{0}C P_{max}=100N PM2 interface for 864,000 load cycles

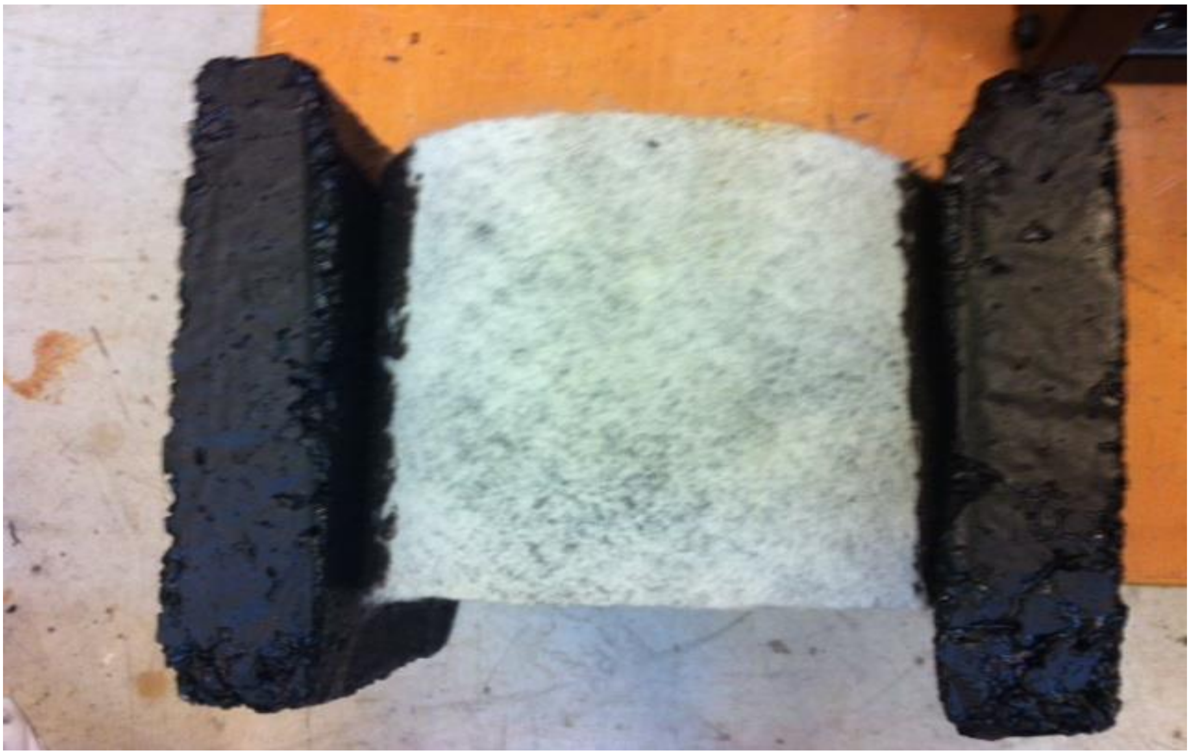

Figure A-15 Product C1 at 30^0C P_{max}=100N GM1 interface for 864,000 load cycles